Tailoring electrolyte additives for advanced Mg-based anodes in primary aqueous Mg-air battery

Dissertation

zur Erlangung des akademischen Grades

Doktorin der Ingenieurwissenschaften

(Dr.-Ing.)

der Technischen Fakultät

der Christian-Albrechts-Universität zu Kiel

Linqian Wang

aus

Sichuan, VR China

Kiel, 2022

Gutachtern der Dissertation:

1. Gutachter: Prof. Dr. Mikhail Zheludkevich

2. Gutachter: Prof. Dr. Fabio La Mantia

3. Gutachter: Prof. Dr. rer. nat. Rainer Adelung

4. Gutachter: Prof. Dr. rer. nat. Franz Faupel

Vorsitzender des Promotionsausschusses:

Prof. Dr. rer. nat. Franz Faupel

Tag der mündlichen Prüfung:

11th April 2022

Eidesstattliche Erklärung

Hiermit erkläre ich, dass die beigefügte Dissertation, abgesehen von der Beratung durch die Betreuerin, nach Inhalt und Form meine eigene Arbeit ist.

Die Arbeit, ganz oder zum Teil, wurde nie schon einer anderen Stelle im Rahmen eines Prüfungsverfahrens vorgelegt und ist abgesehen, von den im Anhang angegebenen Veröffentlichungen, nicht anderweitig zur Veröffentlichung vorgelegt worden.

Außerdem ist die Arbeit unter Einhaltung der Regeln guter wissenschaftlicher Praxis der Deutschen Forschungsgemeinschaft entstanden.

Unterschrift: Lingjian Wang

Geesthacht, den 22.11.2021

Abstract

Owing to the remarkable theoretical discharge performance and eco-friendliness, aqueous Mg-air batteries (AMABs) are considered as promising power sources for next-generation electronics. However, the extensive commercialization of AMABs has still hampered by the dissatisfied practical battery performance, namely, relative low cell voltage and specific energy in comparison with the theoretical values (3.1 V and 6.8 kWh kg^{-1}), which are mainly driven by the sluggish reaction kinetics and serious self-discharge of Mg anode in aqueous electrolyte. Therefore, addressing these issues becomes the top priority in the research filed on AMABs.

This doctoral work proposes new approaches to boost discharge performance of AMABs via tailoring electrolyte additives for newly developed Mg-Ca anodes. Micro-alloyed Mg-Ca anode exhibits negative discharge potential and high utilization efficiency (UE) compared to other commercial Mg alloys. With the addition of suitable Mg^{2+} complexing agent into electrolyte, the discharge performance of Mg-Ca is able to be further improved. Therefore, the effect of Mg^{2+} complexing agents on the corrosion and discharge performance of Mg-Ca anode was investigated, indicating the potential of Mg^{2+} complexing agents to regulate the interfacial condition of the Mg anode/electrolyte and to enhance the specific energy of AMABs. In order to reveal the working mechanism of electrolyte additives, the evolution of interfacial condition between Mg anode and electrolyte was traced by electrochemical impedance spectroscopy. Nevertheless, the interpretation of impedance spectra has been still controversial, which may affect the accurate understanding of the additive working mechanism. Therefore, the physical interpretations of high frequency and middle frequency time constants in Mg impedance spectra were thoroughly investigated, revealing the high frequency time constant is originated form the barrier effect of surface film and the middle frequency time constant is related to charge transfer process and the electric double layer. Based on a better understanding about Mg impedance spectra, EIS measurements during discharge interval were applied to study the working mechanism of selected electrolyte additives. 2,6-dihydroxybenzoate (2,6-DHB) shows the possibility to simultaneously improve the discharge activity and UE of Mg-Ca anode. Thus, the working mechanism of 2,6-DHB with different concentrations was studied by EIS and real-time hydrogen evolution test during discharge. Meanwhile, 2,6-DHB was evaluated and tested as a versatile electrolyte additive for AMABs based on diverse commercial Mg anodes, which yielded the performance enhancement for all tested AMABs under 5 and 10 mA cm^{-2} current densities. Additionally to Mg^{2+} complexing agents, $InCl_3$ was also studied as a potential electrolyte additive for Mg-Ca based aqueous Mg-air battery (AMAB). The working

mechanism of different concentrations $InCl_3$ was explored by EIS, real-time hydrogen evolution during discharge, and local pH measurements. The addition of $InCl_3$ delays the alkalization of the electrolyte through the hydrolysis reaction of In^{3+} ions, mitigates the self-discharge of Mg-Ca anode, and promotes its homogeneous dissolution, thereby improving the discharge activity and UE of Mg-Ca anode. Summarizing, suitable chemical compounds in electrolyte are capable of improving the discharge performance of AMABs. This work proposes two different types of electrolyte additives for AMABs based on a deep understanding of their working mechanisms, which could be indicative for the discovery of other potential electrolyte additives and would greatly facilitate the development and widespread applications of high-performance AMAB systems.

Zusammenfassung

Aufgrund der hohen theoretischen Entladeleistung sowie sehr guter Umweltverträglichkeit gelten wässrige Mg-Luft-Batterien (AMABs) als vielversprechende Energiequellen für elektrische Technologien der nächsten Generation. Die umfassende Kommerzialisierung von AMABs wird jedoch immer noch durch eine unzureichende Batterieleistung im Realbetrieb behindert. Dies betrifft insbesondere die relativ niedrige Zellspannung und erzielte spezifische Energie im Vergleich zu den theoretischen Werten (3,1 V und 6,8 kWh kg^{-1}), die hauptsächlich durch eine ungünstige Reaktionskinetik sowie massive Selbstentladungseffekte an der Mg-Anode in wässrigen Elektrolyten verursacht werden. In der Forschung zu AMABs sind daher die beiden genannten Aspekte zu adressieren sowie zu priorisieren.

In dieser Doktorarbeit wird eine neue Strategie zur Steigerung der Entladeleistung von AMABs durch maßgeschneiderte Elektrolytzusätze zur Verwendung mit zuletzt neu entwickelten Mg-Ca-Anoden vorgeschlagen. Mikrolegierte Mg-Ca-Anoden weisen im Vergleich zu anderen kommerziellen Mg-Legierungen, ein besseres negativeres Entladungspotenzial bei gleichzeitig hohem Nutzungsgrad (Utilization efficiency (UE)) auf. Durch die Zugabe eines geeigneten Mg^{2+}-Komplexbildners in den Elektrolyten kann die Entladeleistung von Mg-Ca basierten Anoden messbar verbessert werden. Daher wurde die Wirkung von Mg^{2+}-Komplexbildnern auf das Korrosionsverhalten sowie die Entladungsleistung von Mg-Ca-Anoden untersucht. Dezidierte Experimente zeigten direkt, dass Mg^{2+}-Komplexbildner das Potenzial haben, die Grenzflächenbedingungen zwischen Mg-Anode und Elektrolyt zu regulieren und die spezifische Energie von AMABs zu erhöhen. Um den Wirkmechanismus der Elektrolytzusätze zu erforschen, wurde das Verhalten der Grenzfläche zwischen Mg-Anode und Elektrolytsystemen mittels elektrochemischer Impedanzspektroskopie (EIS) untersucht. Die Interpretation der Impedanzspektren ist jedoch schwierig. Nach wie vor ist in der Forschung umstritten, wie der Wirkmechanismus der Additive die EIS Ergebnisse beeinträchtigen kann. Aus diesem Grund wurden die physikalischen Interpretationen der hoch- und mittelfrequenten Zeitkonstanten in den Mg-Impedanzspektren detailliert hinterfragt und Untersuchungen durchgeführt. Es stellte sich heraus, dass die hochfrequente Zeitkonstante der entsprechenden Spektren auf den Barriere-Effekt sich bildender Schichten zurückzuführen ist und die mittelfrequente Zeitkonstante mit dem Ladungstransferprozess sowie der elektrischen Doppelschicht zusammenhängt. Basierend auf dem erlangten besseren Verständnis der Mg-Impedanzspektren wurden EIS-Messungen während Entladungsexperimenten durchgeführt, um gezielt, den Wirkmechanismus ausgewählter Elektrolytzusätze zu untersuchen. 2,6-

Dihydroxybenzoat (2,6-DHB) zeigte hier früh gute Ergebnisse. Es ermöglicht, gleichzeitig die Entladungsaktivität und Nutzungsgrad der Mg-Ca-Anoden zu verbessern. Daher wurde der Wirkmechanismus von 2,6-DHB bei verschiedenen Konzentrationen mittels EIS als auch mittels Messungen zur Wasserstoffentwicklung während der Entladung untersucht. Parallel wurde 2,6-DHB als vielseitiger Elektrolytzusatz für AMABs auf Basis verschiedener kommerzieller Mg-Anoden bzw. Legierungen bewertet und gezielt getestet. Eine elektrische Leistungssteigerung für alle AMAB Systeme bei Stromdichten von 5 und 10 mA cm^{-2} wurde beobachtet. Alternativ zu den Mg^{2+}-Komplexbildnern wurde auch $InCl_3$ als potenzieller Elektrolytzusatz für Mg-Ca-basierte wässrige Mg-Luft-Batterien (AMAB) untersucht. Der Wirkmechanismus bei unterschiedlichen $InCl_3$-Konzentrationen wurde durch EIS, Wasserstoffentwicklungstest während der Entladung als auch mittels lokaler pH-Messungen erforscht. Die Zugabe von $InCl_3$ verzögert aufgrund einer Hydrolysereaktion von In^{3+}-Ionen die Alkalisierung des Elektrolyten. Es vermindert die Selbstentladung der Anoden und es fördert eine homogene Anodenauflösung, wodurch die Entladungsaktivität und die UE messbar verbessert werden. Die Ergebnisse beweisen final, dass geeignete chemische Verbindungen im Elektrolyten die Entladeleistung von AMABs erheblich verbessern können. Diese Arbeit schlägt, basierend auf einem tiefen Verständnis der Wirkmechanismen zwei verschiedene Arten von Elektrolytzusätzen für AMABs, vor. Die Ergebnisse bilden einen Anhaltspunkt für die Entdeckung anderer potenzieller Elektrolytzusätze. Die Entwicklung in Richtung breite Anwendung von Hochleistungs-AMAB-Systemen wurde beschleunigt.

Table of Contents

1 Introduction

Aqueous metal-air batteries refer to the electrochemical power sources composed of metallic anode, aqueous electrolyte and air cathode, which exhibit many prominent features in comparison with Li-ion batteries (LIBs), such as superior theoretical specific energy, environmental benignity, great safety and cost-effectiveness [1-4]. The active materials in aqueous metal-air batteries are metallic anode and oxygen from air. Hence, the total weight of the system is reduced and the theoretical specific energy is 3 to 30 times higher than that of LIBs. The theoretical specific energy (excluding the molar loss of O_2) of aqueous metal-air batteries varies with the different anode types, from 1.3 to 13.0 kWh kg^{-1} [5, 6]. Hence, they have been widely used in a variety of equipment in different scales, ranging from micro-implantable devices to energy storage of smart grids. Aqueous Mg-air batteries (AMABs) as desirable energy conversion and storage options attracted much attention among existing metal-air battery systems in recent five years [7-15]. The negative standard electrode potential and low density of Mg anode enable AMABs a relatively high theoretical cell voltage, 3.1 V, and superior energy density, 6.8 kWh kg^{-1} based on Mg anode [16, 17]. Nevertheless, the severe self-corrosion of Mg anode amid discharge and the sluggish oxygen reduction reaction kinetics on cathode limit the practical performance and commercialization of AMABs. Besides, AMABs can only be mechanically recharged by replacing active materials and are not electrochemically rechargeable. Numerous efforts have been made to boost the discharge performance of AMABs focusing on optimizing the properties of each component and battery design [18-21]. Electrolyte as one of the key components is decisive for defining the electrochemical and chemical reactions inside the system. Consequently, the properties of electrolyte (i.e. composition, pH and concentration) determine the practical performance of anode, cathode and fully assembled AMABs. Nevertheless, only limited works have covered this subject and most of them have focused on alleviating the self-discharge of Mg anode via adopting corrosion inhibitors or surfactants as electrolyte additives, which resulted in the sacrifice of anode discharge activity [22-25]. The most prominent electrolyte system for AMABs should possess the capability of inhibiting self-discharge and promoting anode activity concurrently. To fulfill these two criteria, new strategies based on a deep understanding of self-discharge and discharge behavior of Mg in aqueous electrolyte should be developed. Hence, the work presented in this dissertation focuses on performance boosting of AMABs from electrolyte side via tailoring the electrolyte chemical properties and regulating the Mg anode/electrolyte interfacial condition.

INTRODUCTION

This dissertation is composed of seven chapters. Chapter 2 presents an overview of the electrolyte systems for different aqueous metal-air batteries, including the existing problems, approaches to tackle these issues and perspectives for future works. The motivation of this work and objectives are explicated in Chapter 3, whilst the details regarding all experimental methods adopted in this work are given in Chapter 4. The experimental results are displayed in Chapter 5 in form of 5 published scientific papers. A general discussion on all presented results is given in Chapter 6. Summary and perspectives are drawn and described in Chapter 7.

Electrolyte for Aqueous Metal-Air Batteries

1. Introduction

The first (1760-1830) and second (1870-1914) industrial revolution introduced fossil fuels (coal, petroleum, natural gas and oil) as energy sources, which greatly promoted the progress in different aspects of human life. However, with the increasing demand for energy, non-renewable fossil fuels will encounter a shortage in supply in the future, which will definitely trigger the worldwide energy crisis. In addition, the continuous consumptions of fossil fuels arise serious environmental issues, especially the emission of greenhouse gases. The levels of greenhouse gases in the atmosphere reached a new record in 2019 [1]. The international community is increasingly advocating reduce greenhouse gases emission and the concept of carbon neutrality [2-4], which refers to the net-zero CO_2 emission. With the aim to address the emerging problems caused by over-commitment to fossil fuels and to reduce CO_2 emission, much effort has been devoted to develop alternative energy conversion technologies like photovoltaic solar or wind turbine energy production technologies, and energy storage devices, such as metal-ion batteries, metal-air batteries, redox-flow batteries, fuel cells, super-capacitors, etc.

Among the existing energy storage devices, rechargeable Li-ion batteries (LIBs) are mature and representative technologies for our daily applications. LIBs possess high voltage, superior capacity and impressive cycling life. However, LIBs possess some inherent safety problems. Li is a volatile metal and exhibits extremely negative electrode potential. Meanwhile, the organic electrolytes used for LIBs are also highly flammable, leading to the potential exploding issue of LIBs. The recent news about the explosion of Samsung Galaxy Note 7 and the ban event of Boeing 787s raises public concerns regarding the safety of LIBs. The byproducts during mining and manufacturing process of LIBs lead to certain environment problems and the recycling of pollutants in waste LIBs is still a big issue. In addition, rechargeable LIBs are not able to completely fulfill the demands for some high energy density applications, such as long-range pure electric vehicles (EVs) [5], unmanned aerial vehicle (UAV) [6], and other off-grid applications [7]. Moreover, the prices of raw materials for LIBs (Li, Co and Ni) and the associated production costs are high. Thus, LIBs are not always optimal candidates for large-scale energy storage systems. In view of the above, searching and developing other reliable energy storage systems is an urgent task.

Owing to the superior theoretical specific energy densities, safety and environmental benignity, metal-air batteries evoke ubiquitous attention latterly. Metal-air batteries rely on the dissolution of the metallic anode and the oxygen reduction reaction at the cathode, which are also known as semi-fuel cells given the O_2 adopted as cathodic reactant (Fig. 1a). The O_2 consumed on the cathode is mostly from the air. It dramatically reduces the weight of these battery systems, and thus increases the theoretical energy densities. Fig. 1b listed the theoretical energy densities of several conventional metal-air batteries based on different anode materials, namely, Al-air batteries (AABs), Mg-air batteries (MABs), Zn-air batteries (ZABs) and Fe-air batteries (FABs). The theoretical energy densities of those metal-air batteries in the range 0.8-8.1 kWh kg^{-1} (excluding O_2), some of which are close to the theoretical energy density of gasoline, ~13 kWh kg^{-1} and higher than that of LIBs, 4 kWh kg^{-1}. In comparison with traditional fuel cell and LIBs, metallic anodes, such as Mg and Zn, are normally less combustible than H_2 and Li. Hence, no strict manufacturing conditions, special storage or transportation methods are needed. All actions can be proceed under ambient environment, making metal-air batteries easier to be manufactured and reducing the production costs. Besides, metal-air batteries have long shelf life under dry condition. Nevertheless, even with the mentioned merits, the development of metal-air batteries has been downplayed in the past decades.

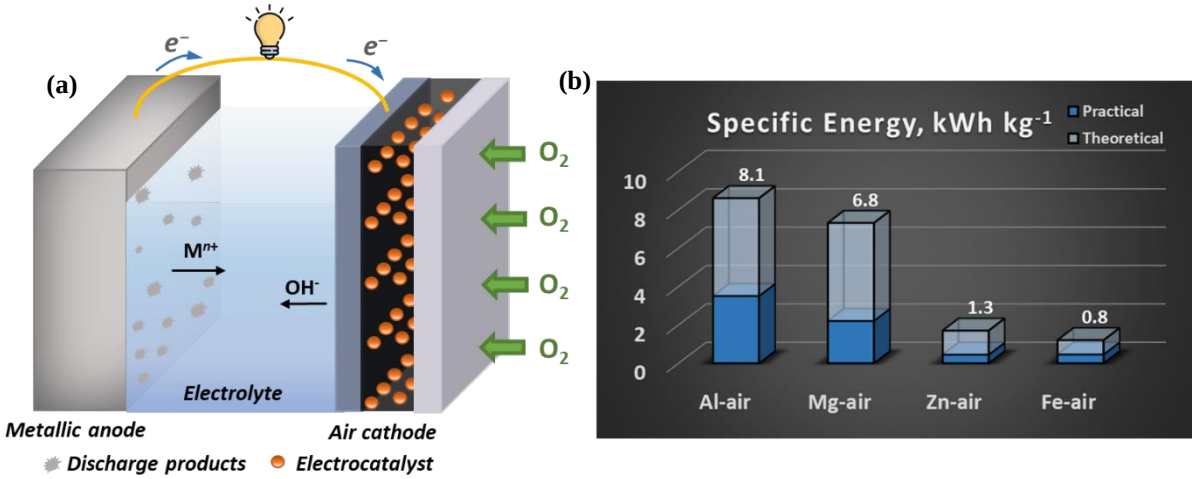

Fig. 1. (a) Illustration of metal-air battery and (b) theoretical and practical specific energy for metal-air batteries.

The investigation of metal-air battery has a longer history than LIBs. The first metal-air battery can be traced back to 1878, when Maiche designed the first primary Zn-air battery [8]. In 1932, the first commercialized metal-air battery entered the market [9]. Following that, Fe-air [10], Al-air [11], and Mg-air batteries were developed in 1960s [12]. In the 1960s and early

1970s, the investigation of metal-air batteries ushered the first bloom [13]. However, several relevant technique issues retarded the pace of the development of metal-air batteries in that period, especially the lack of air cathode with adequate efficiency. In the past years, along with the development of fuel cell, the stability and efficiency of air cathode have been improved greatly [14-16]. Hence, metal-air batteries are confronted with new opportunities.

According to the adopted electrolyte, metal-air batteries can be sorted to two types, aqueous and non-aqueous metal-air batteries. The common problem of aqueous metal-air batteries is the self-corrosion of metallic anodes, especially for Al-based and Mg-based anodes. The adoption of organic electrolyte is able to alleviate the corrosion of anode in electrolyte and hence contributes to longer cell life. However, as above introduced, organic electrolyte is one of the major causes for the safety and environmental issues of LIBs due to its flammability and toxicity. Furthermore, the ionic conductivity of organic electrolyte is normally lower than that of aqueous electrolyte, resulting in the inferior power density of non-aqueous metal-air batteries. Aqueous electrolyte is nonflammable and environmentally friendly, which fundamentally addresses the relevant issue of organic electrolyte and offers the possibility to be used as grid-scale energy storage [17]. Besides, aqueous electrolytes also exhibit other merits, such as relatively low price and plain manufacturing processes. Unlike ZABs and FABs, AABs and MABs are only mechanically rechargeable due to intrinsic reactions of metallic anodes in aqueous electrolytes. Comparing to electrochemically rechargeable metal-air batteries, mechanically rechargeable aqueous metal-air batteries possess some unique advantages, including the capability of supplying full power instantly without a waiting period for charging process, less requirement for air cathode (oxygen reduction reaction (ORR) happened only), and high anodic efficiency (e.g. anode materials are inserted into the electrolyte only during operation). Besides, they are good options as standby emergency power supplies where charging is not possible and exhibit high capability under extreme environments. Taking into account the aforementioned traits, the research on aqueous metal-air batteries experiences an astounding increase in recent decade.

The most conventional metallic anode used in aqueous metal-air battery systems are Zn [18], Al [19], and Mg [20]. There are also emerging research adopting Fe [21] as anode material for aqueous metal-air batteries. Due to the various inherent properties of anode materials, aqueous metal-air batteries face different roadblocks, but there are several common challenges for all metal-air batteries impeding the achievement of the theoretical performance and retarding their broad practical applications. Fig. 2 lists the common and special issues of common aqueous

ZABs, AABs, and MABs. All of them possess the balance issue regarding battery life span and discharge activity. Metallic anodes undergo serious self-corrosion under working condition, which shortens the battery capacity. Meanwhile, anode materials also suffer from surface passivation caused by the accumulation of discharge products. In addition, although a great improvement has been achieved, the efficiency of air cathode is still a limiting factor for metal-air batteries. The discharge performance of rechargeable aqueous ZABs is limited not only by the sluggish ORR but also the sluggish oxygen evolution reaction (OER) on the air cathode. Moreover, the dendrite formation and the electrode shape change after cycling significantly reduce the battery life of ZABs. For aqueous AABs and MABs, they are suffering from negative difference effect (NDE) and chunk effect. Both of these effects are detrimental to anode utilization efficiency and will also shorten the battery life. NDE and chunk effect refer to the anomalous hydrogen evolution during discharging process (anodic polarization) and the detachment of small metal pieces from anode surface, respectively. To overcome these issues, many attempts have been done from different aspects, including novel anode, efficient air cathode, functionalized electrolyte development, and rational cell design. Especially, much attention has been paid on the development of novel anode and cathode materials. The cathode is also an issue but will be not touch it here. More detailed overview about anode and cathode materials for aqueous metal-air batteries can be found on the following references [22-24].

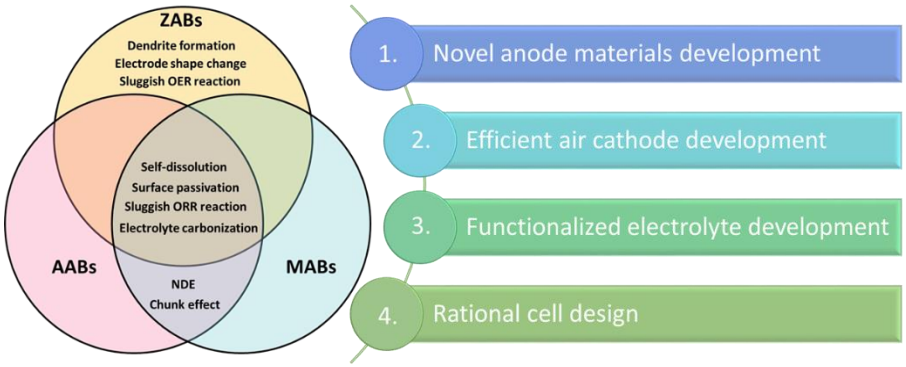

Fig. 2. Illustration of issues and possible solutions of aqueous metal-air batteries.

Comparatively little concern is addressed to the electrolyte development. However, it is in fact controlling the electrochemical reaction inside the metal-air batteries. The electrochemical properties of electrodes vary as the change of electrolyte composition, concentration, and pH. Therefore, the research on electrolyte modification is indeed the key factor for achieving superior discharge performance of aqueous metal-air batteries and facilitating the large-scale commercialization for industrial deployment. In order to further stimulate the investigation on

the electrolyte modification of aqueous metal-air batteries, the recent progress on electrolyte development for aqueous metal-air batteries is reviewed and the state-of-art strategies for choosing electrolyte additives is summarized herein. The basic working mechanism of different conventional aqueous metal-air batteries (Zn, Al and Mg-based) and clarity on the existing problems for each system are introduced. The design tactics of suitable electrolyte system for one sort of metal-air batteries may also inspire or be readily transplanted to other metal-air batteries. Hence, some perspectives on the future research directions of aqueous metal-air batteries are proposed.

2. Working principle for aqueous metal-air batteries

As illustrated in Fig. 1a, the basic configuration of metal-air battery is composed of the metallic anode, the electrolyte, and the air cathode. Some other components can be added in for special purpose, such as functional membranes as the separator. The main reactions of aqueous metal-air batteries during discharging process are the dissolution of metallic anode and the reduction of O_2. The involved reactions depend on the pH of the electrolyte,

In acidic environment,

$$\textit{Anodic reactions: } M \rightarrow M^{n+} + n\,e^{-} \tag{1}$$

$$\textit{Cathodic reactions: } \frac{n}{2}\,O_2 + n\,H^{+} + n\,e^{-} \rightarrow \frac{n}{2}\,H_2O \tag{2}$$

$$\textit{Overall reactions: } M + \frac{n}{2}\,O_2 + n\,H^{+} \rightarrow M^{n+} + \frac{n}{2}\,H_2O \tag{3}$$

In neutral environment,

$$\textit{Anodic reactions: } M \rightarrow M^{n+} + n\,e^{-} \tag{4}$$

$$\textit{Cathodic reactions: } \frac{n}{4}\,O_2 + \frac{n}{2}\,H_2O + n\,e^{-} \rightarrow n\,OH^{-} \tag{5}$$

$$\textit{Overall reactions: } M + \frac{n}{4}\,O_2 + \frac{n}{2}\,H_2O \rightarrow M(OH)_n \tag{6}$$

In alkaline environment,

$$\textit{Anodic reactions: } M + x\,OH^{-} \rightarrow M\,(OH)_x^{y-} + (x-y)\,e^{-} \tag{7}$$

$$\textit{Cathodic reactions: } \frac{x}{4}\,O_2 + \frac{x}{2}\,H_2O + x\,e^{-} \rightarrow x\,OH^{-} \tag{8}$$

$$\textit{Overall reactions: } M + \frac{x}{4}\,O_2 + \frac{x}{2}\,H_2O \rightarrow M(OH)_x \tag{9}$$

Except for the anodic and cathodic reactions, the parasitic hydrogen evolution reaction between metallic anode (*M*) and water also happens, which presents as following,

$$\textit{Parasitic reaction: } M + xH_2O \rightarrow M(OH)_x + \frac{x}{2}H_2 \quad (10)$$

Since the anodic reaction of aqueous metal-air batteries is the metal dissolution, understanding the thermodynamic equilibrium of the corresponding metal-water system is beneficial to understand the aqueous metal-air battery systems. Pourbaix diagram elucidates the thermodynamic equilibrium of metal-water system, which is indicative to show the theoretical condition of metallic anode materials in simple aqueous electrolyte under certain electrochemical potential and pH. Fig. 3 presents the theoretical conditions of Zn, Al and Mg metals at 25 °C in presence of 10^{-6} M soluble species [25]. The potential is versus standard hydrogen electrode (SHE). As shown in Fig. 3, the upper dash line refers to the equilibrium of O_2 evolution reaction and the lower dash line refers to the equilibrium of H_2 evolution reaction. The region in between is the electrochemical stability window of water. As presented in Fig. 3a, the zone of immunity represents the area where metallic state is the most stable state of Zn and Zn is totally immune from corrosion. With the increase of pH or potential, the corrosion zone is reached and the most stable state of Zn changes to the soluble ionic state. In other words, corrosion reaction of the metal happens. The zone of passivation depicts that the formed oxide or hydroxide layer on Zn surface prevents the contact of Zn with the solution. Zn and Al are amphoteric metals and, thus, both of them possess two corrosion zones. For Mg, there is only one corrosion zone, but it almost dominates the whole region when the environmental pH is less than 12. According to Fig. 3, the conventional anode materials for aqueous metal-air batteries corrode severely in acidic electrolyte, which may lead to anode utilization efficiency loss. Neutral and alkaline electrolytes may therefore be more preferable with regard to this issue. Nevertheless, Zn and Al anodes suffer from surface passivation in near neutral electrolytes, which is detrimental to the sustainability of anode discharge activity and practical output voltage. By contrast, for Mg anode, the surface passivation occurs only in alkaline electrolyte. Hence, for different anode materials, the favorable pH range of the electrolyte is different.

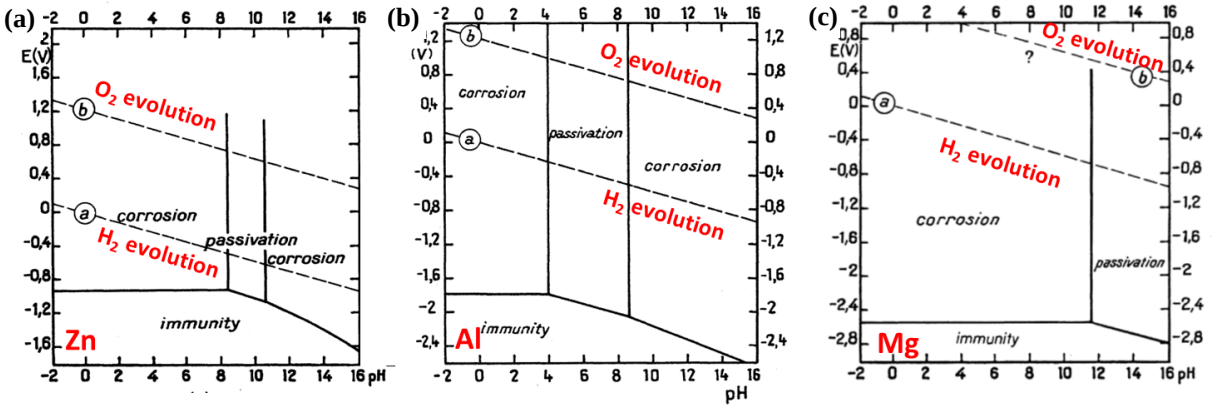

Fig. 3. Theoretical domains of corrosion, immunity and passivation of (a) Zn, (b) Al, and (c) Mg at 25 °C in presence of 10^{-6} M soluble species reproduced with permission from Ref. 25.

It is noteworthy that Fig. 3 only shows the condition in simple aqueous electrolyte in presence of 10^{-6} M soluble species. The real system is dynamic and influenced by the concentration of soluble species, the anions and cations in the background electrolyte (e.g. those induce precipitates formation), the existence of other additives (e.g. complexing reagents), etc. Thus, the composition and pH of the electrolyte are decisive and critical for the development of novel aqueous metal-air batteries with superior discharge performance. Note that the requirements on the electrolyte are diverse for different metal-air battery systems. Therefore, in the following, the basis and advances in the electrolyte for conventional metal-air batteries based on different anodes are introduced.

3. Aqueous Zn-air batteries

As aforementioned, Zn-air battery is the oldest metal-air battery. The concept of Zn-air battery was proposed in 1840s and the first primary Zn-air battery was developed in 1878 with further practical commercialization in 1930s, like electric vehicles and hearing-aids [26]. Despite that the theoretical energy density of Zn-air battery is not competitive in comparison to other aqueous metal-air batteries (Fig. 1b), Zn anode exhibits one most appealing merit, namely the electrochemical reversibility of discharge reaction in aqueous electrolyte, which enables the implementation of rechargeable ZABs. However, the first commercial rechargeable ZAB from NantEnergy was launched in 2012 with limited energy density, ~ 35 Wh kg^{-1} [27]. Hence, much effort have been devoted to achieve rechargeable ZABs with fairly good cycle life and energy efficiency in the last decade. The discharge reactions happened in conventional aqueous alkaline ZABs are:

$$\textit{Anodic reactions: } Zn + 4\,OH^- \leftrightarrow Zn(OH)_4^{2-} + 2\,e^-\ E_0 = -1.25\,V \textit{ vs. SHE} \qquad (11)$$

$$Zn(OH)_4^{2-} \leftrightarrow ZnO + H_2O + 2\,OH^- \quad (12)$$

$$Cathodic: O_2 + 2\,H_2O + 4\,e^- \leftrightarrow 4\,OH^- \quad E_0 = 0.41\,V\ vs.\ SHE \quad (13)$$

$$Overall: 2\,Zn + O_2 \leftrightarrow 2\,ZnO \quad E_0 = 1.66\,V\ vs.\ SHE \quad (14)$$

As shown in Eq. 11, the anodic reaction is the oxidation of Zn to soluble zincate $Zn(OH)_4^{2-}$. When zincate ions are supersaturated in the electrolyte, they decompose via Eq. 12 and form insoluble ZnO, which may induce surface passivation for both anode and cathode depending on the solubility of zincate ion in the specified electrolyte and the properties of the precipitates film. If a dense and compact ZnO film is formed, the precipitated ZnO is not able to be completely reduced to Zn during charging process. Thus, the discharge capacity and cycle life of ZABs are reduced significantly. The dense ZnO film also gives rise to the increase of internal resistance and consequently influences the output voltage of ZABs. As presented in Fig. 4a, with the prolongation of discharge, the precipitated ZnO cover the surface of metallic Zn sponge anode and leads to the decrease of cell voltage. Therefore, it is crucial to hinder the formation of a dense ZnO film. Many researchers have attempted to clarify the nucleation and growth mechanism of ZnO with discrepant morphologies via modeling and experimental investigations [28-30].

Soluble zincate ions formed during discharge are supposed to be reduced and plated on Zn anode during charging process. Nevertheless, the free zincate ions may diffuse away from the vicinity of anode and reluctant to be redeposited back to the same place with the same arrangement during charge, leading to the change of electrode shape. Accordingly, preferential redepostion is triggered, which is influenced by many factors, including the difference in overpotential along Zn electrode, local current density, electric field, local concentration of zincate ions, and so on [18, 31-33]. Continuously preferential redeposition of zincate ions eventually turns to the growth of dendrite, as shown in Fig. 4b-d [34, 35]. Dendrite formation and electrode shape change during charge are detrimental to the cycle life of ZABs and even induces short-circuit between anode and cathode. Much effort have been made to reveal the mechanism of Zn dendrite formation and to alleviate the preferential redeposition [35-38].

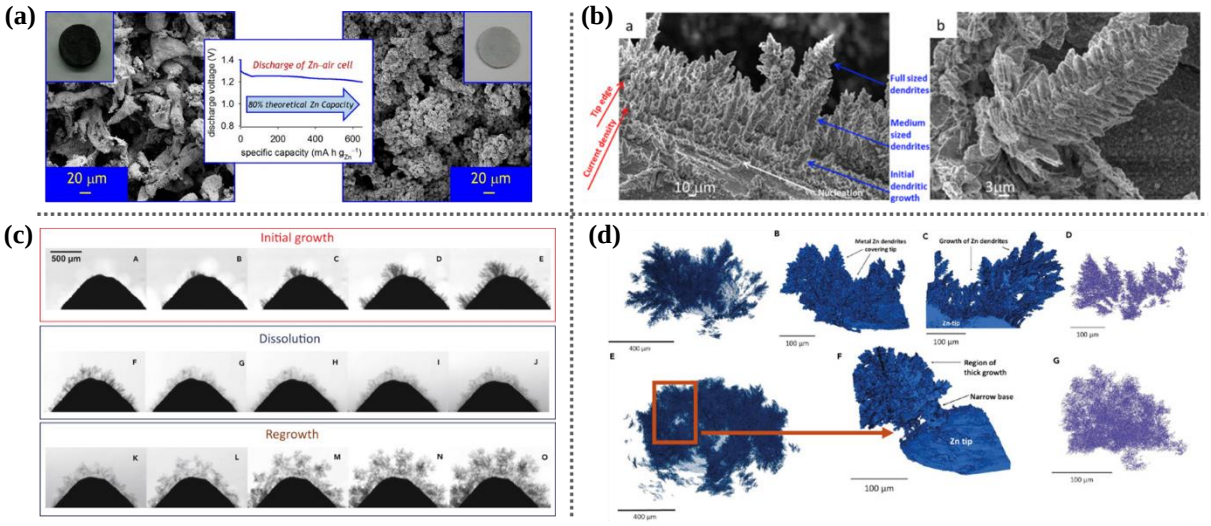

Fig. 4. Surface morphologies of Zn anode after cycling: (a) Surface morphologies of Zn sponge anode before and after discharge reproduced with permission from Ref. 29; (b) Second electron SEM images of Zn dentrite formed on Zn anode reproduced with permission from Ref. 34; (c) *Operando* synchrotron X-ray computed tomography of Zn dendrite evolution and (d) 3D reconstruction of Zn dendrite reproduced with permission from Ref. 35.

Self-dissolution or self-corrosion of Zn anode in aqueous electrolyte is another drawback, which leads to undesirable loss of utilization efficiency and energy density of aqueous ZABs. Eq. 15 is the parasitic hydrogen evolution reaction, which occurs on Zn electrode in aqueous electrolyte though Zn possesses relative low overpotential of the hydrogen evolution reaction. This issue also shortens the shelf-life and cycle life of aqueous ZABs since the hydrogen evolution reaction is a spontaneous reaction over the whole pH range during charge/discharge (Fig. 3a).

$$\textit{Parasitic reaction on anode: } Zn + 2\,H_2O \rightarrow Zn(OH)_2 + H_2 \qquad (15)$$

Except for the passivation, dendrite formation and self-dissolution of Zn anode, there are several other challenges hindering the further commercialization of rechargeable aqueous ZABs, such as electrolyte carbonation, evaporation of aqueous electrolyte, etc. Several approaches have been explored for addressing these problems. Hereinto, adopting suitable electrolyte system and relevant modification with effective electrolyte additives are considered as promising ways to control Zn anode dissolution, regulate zincate ions plating and hinder dendrite formation. Besides, using ammonia or other electrolyte compositions is able to moderate electrolyte carbonation, etc. The adopted electrolyte decides the electrochemistry of the battery. According to the pH of the electrolyte, aqueous ZABs can be sorted into two types:

alkaline and non-alkaline ZABs. Hence, thereinafter the research progress of electrolyte modification for aqueous ZABs in different pH ranges is introduced.

3.1 Alkaline electrolytes

The most commonly used electrolytes for aqueous ZABs are alkaline solutions based on KOH, NaOH, LiOH, etc., due to the high ionic conductivity [39-41]. KOH electrolyte is more favorable since it has lower viscosity, higher oxygen diffusion coefficient, and better ionic conductivity (73.50 Ω^{-1} cm^2 equiv^{-1} for K^+ vs. 50.11 Ω^{-1} cm^2 equiv^{-1} for Na^+) [40, 42]. The ionic conductivity can be enhanced by increasing the concentration of KOH. Nevertheless, high concentration of KOH results in the increase of viscosity and the formation of ZnO. Hwang and co-workers [43] investigated the influence of KOH concentration on the electrochemical reactions of ZABs, indicating that 4 M KOH solution shows the most efficient corrosion inhibition effect for Zn anode among the solutions with 2-8 M KOH. 6 M KOH solution is also considered as the optimal concentration due to its high conductivity. However, the practical application of alkaline ZABs is still limited due to issues like the formation of insoluble carbonates, unfavorable dendrite growth, and self-dissolution of Zn anode as well as the hydrogen evolution reaction.

Electrolyte carbonation and relevant side effects are major issues for alkaline ZABs. The reaction is as follows,

$$CO_2 + 2\,OH^- \rightarrow H_2O + CO_3^{2-} \quad (16)$$

CO_2 from the ambient environment reacts with OH^- in electrolyte and forms CO_3^{2-}. It may induce the precipitation of insoluble carbonates, which deteriorates the performance via blocking active sites of air cathode. Besides, the increase of CO_3^{2-} decreases the ionic conductivity of the electrolyte and complicates the diffusion of O_2 by increasing viscosity of the electrolyte. As indicated by Drillet et al. [44], with the increase of CO_2 concentration, the life time of air cathode dramatically decreases from 2500 h (pure O_2 atmosphere) to 60 h (10000 ppm CO_2-containing atmosphere). Thus, they proposed to use solid adsorbents to capture CO_2 in the feed gas. Cheng and Tan [45] suggested to adopt amine-based aqueous electrolyte combining piperazine (PZ) and its mixture with 2-(2-aminoethylamino) ethanol (AEEA) and monoethanolamine (MEA) as CO_2 absorbents for ZABs. The results indicated that the CO_2 concentration in the feed gas can be controlled below 20 ppm with such treatment. As proposed by Kucka et al. [46], the increase of CO_3^{2-} concentration in the electrolyte leads to the decrease of carbonation reaction rate. The addition of 28.6 mol% K_2CO_3 into 6 M KOH marginally

influence the discharge performance of ZAB [47]. Hence, the addition of K_2CO_3 into KOH electrolyte was proposed to be an efficient method to alleviate the side effect of electrolyte carbonation.

3.2 Near-neutral electrolytes

Employing near-neutral electrolytes is another direction for high performance aqueous ZABs. First, the aforementioned electrolyte carbonation is diminished due to a lack of OH^-. Further, according to Pourbaix diagram (Fig. 3a), the dissolution of Zn in non-alkaline solutions does not give rise to a stable ZnO passive film, and thus the problem of surface passivation could be solved. Besides, the dendrite formation could be mitigated via using non-alkaline solutions [18]. However, only few works adopted acidic solution as the electrolyte for aqueous ZABs [48, 49], because the acidic environment induces severe corrosion of Zn anode. Meanwhile, there is a lack of suitable catalysts and support materials that possess desirable performance in acidic electrolyte. Hence, the pH range of non-alkaline electrolyte is normally around 5-7 depending on the salts added into the electrolyte. The anodic reactions happened in non-alkaline aqueous ZABs during discharge are as follow:

$$\textit{Anodic reaction: } Zn \leftrightarrow Zn^{2+} + 2\,e^-, E_0 = -0.76\ V \textit{ vs. SHE} \quad (17)$$

$$\textit{Cathodic: } O_2 + 4\,H^+ + 4\,e^- \leftrightarrow 2\,H_2O \quad E_0 = 1.23\ V \textit{ vs. SHE} \quad (18)$$

$$\textit{Overall: } 2\,Zn + O_2 + 4\,H^+ \leftrightarrow 2\,Zn^{2+} + 2\,H_2O \quad E_0 = 1.99\ V \textit{ vs. SHE} \quad (19)$$

Widely investigated neutral electrolytes for aqueous ZABs are mainly chloride-based and ammonium-based solutions [50, 51]. However, chloride-based electrolytes have been demonstrated undesirable for rechargeable ZABs, because the charging process of ZABs in chloride-based electrolytes gives rise to the chlorine evolution reaction, which is even more favored than oxygen evolution reaction [52],

$$2\,Cl^- \rightarrow Cl_2 + 2\,e^-, E_0 = 1.36\ V \textit{ vs. SHE} \quad (20)$$

$$2\,H_2O \rightarrow O_2 + 4\,H^+ + 4\,e^-, E_0 = 1.23\ V \textit{ vs. SHE} \quad (21)$$

The side reaction decreases the charging efficiency and may further lead to the formation of chloric acids. In order to tackle these side effects, namely the chlorine and/or hypochlorite formation, urea were suggested to be introduced into chloride-based electrolytes, because it can reacts with chlorine and releases innocuous gases (i.e. N_2) [39].

The cation types of chloride salts also make great impact on the discharge/charge performance of Zn-air batteries. Bi^{3+}, Pb^{2+}, Hg^{2+} and Sn^{2+} chloride salts are able to enhance the hydrogen evolution overpotential and suppress unwanted hydrogen evolution reaction [52]. $ZnCl_2$-NH_4Cl electrolyte is well-known as the electrolyte for Leclanche batteries (Zn-MnO_2/C batteries). The concentration of NH_4Cl plays a vital role on deciding which Zn-based species are to be formed in the discharging process [53]. Low NH_4Cl-containing electrolyte favors the formation of amorphous $ZnCl_2 \cdot 4Zn(OH)_2 \cdot H_2O$, whilst high NH_4Cl-containing electrolyte leads to the formation of crystalline $ZnCl_2 \cdot 2NH_3$ and may result in the surface passivation due to the dense structure of crystalline $ZnCl_2 \cdot 2NH_3$ [54]. Except for these two Zn-based species, ZnO, $Zn(OH)_2$, $Zn(NH_3)_2Cl_2$ and other Zn-complexes are able to be formed depending on pH, Cl^- concentration, temperature and water amount [53, 55]. Goh and co-authors developed a $ZnCl_2$-NH_4Cl based electrolyte for a secondary ZAB, which enabled the battery to sustain hundreds of charge/discharge cycles and cycle life of more than 1000 h [56]. Polyethylene glycol (PEG) and thiourea were added into the $ZnCl_2$-NH_4Cl based electrolyte, showing inhibitory effects on Zn deposition. The further work from this team reported the combination of neutral chloride-based electrolyte and directly grown MnO_x catalyst boosts the cycling stability and cell voltage of a secondary ZAB [57]. The performance enhancement is due to the reduced electrolyte carbonization and suppressed carbon corrosion in cathode. Except for chloride-based and ammonium-based electrolytes, carbonate-based, sulfate-based, nitrate-based and perchlorate-based solutions have also been reported as possible electrolyte systems for ZABs [52, 58]. However, near-neutral electrolytes indeed suppress the activity of catalysts and exhibit less ionic conductivity in comparison with alkaline electrolytes. Therefore, more attention should paid to tackle these drawbacks of near-neutral electrolytes to facilitate the practical utilization of these promising electrolytes in aqueous ZABs.

3.3 Additives-containing electrolytes

As above mentioned, some inorganic and organic additives were added into chloride-based neutral electrolyte to eliminate the side reactions. The strategy of adding inorganic or organic compounds with specific properties into the electrolyte has been proven to be an efficient way to address some typical issues of aqueous ZABs. As shown in Fig. 5, the common issues of aqueous ZABs include surface passivation, dendrite growth and self-corrosion, which could be alleviated via various functional electrolyte additives.

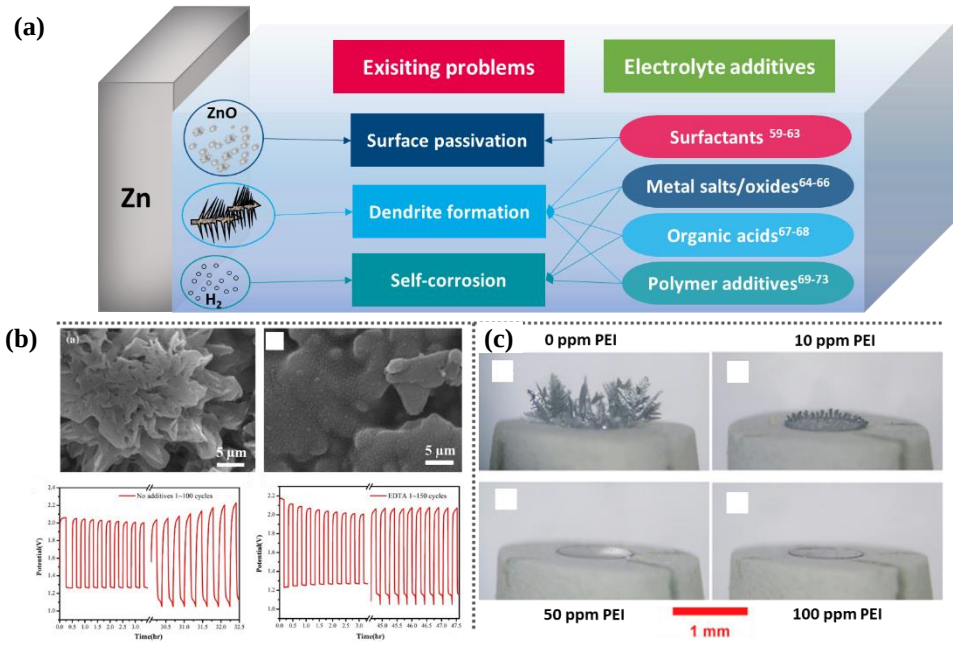

Fig. 5. (a) Illustration of Zn anode: existing problems and solutions; (b) SEM images of Zn anode after 1000 CV cycles and discharge performance of ZABs in blank KOH solution and EDTA-containing KOH solution reproduced with permission from Ref. 68; (c) *In-situ* optical images of Zn electrode in PEI-containing electrolytes reproduced with permission from Ref. 69.

As mentioned before, *surface passivation* is one of the biggest obstacles limiting ZABs performance in alkaline electrolytes. A high salt concentration in alkaline electrolytes is capable of increasing the solubility of ZnO film and consequently decreasing the passivation effect. However, high solubility also induces the unwanted diffusion of zincate ions and electrode shape change. Adding gel to aqueous electrolytes has been suggested to enhance the overall performance of ZABs. The addition of gel to aqueous electrolytes increases the viscosity of the electrolyte resulting in the suspension of zinc powder. Yang et al. [59] reported that the addition of a surfactant, i.e. sodium dodecyl benzene sulfonate (SDBS), to KOH solution suppressed the surface passivation via the adsorption effect and consequently enhanced the discharge capacity of Zn anode. Except for the adsorption effect of the surfactant, Ghavami and co-author [60] found that the negative charged head group of SDBS is more effective to tailor the precipitation of ZnO in comparison with the positive charged head group of cationic surfactant, cetyl trimethyl ammonium bromide (CTAB), and thus is beneficial for prolonging the service life of ZABs.

The physical adsorption of surfactants on the dendrite sites of Zn anode is a possible strategy to hinder the dendrite growth. Tetrea-alkyl ammonium hydroxides (TAAHs) and some surfactants [61], such as sodium dodecyl sulfate (SDS) [62] and Triton-X [63], were reported

possessing the effect to diminish Zn dendrite formation. The inhibition effect of TAAHs for dendrite formation enhances with the increase of the alkyl group size and concentration of TTAHs due to the increase of steric hindrance and polarity [61]. Metal salts and oxides, such as $BiCl_3$ [64], PbO [65] and SnO [66], were also reported as suitable electrolyte additives for inhibiting Zn dendrite formation. Wang and co-authors [64] found that the synergistic effect of Bi^{3+} and tetrabutylammonium bromide (TBAB) greatly suppressed the formation of dendrite at high cathodic overpotential. Organic acids, such as citric acids, with higher amount of polar groups effectively prevented dendrite formation, whilst tartaric acids with lower amount of polar groups increased the hydrogen overpotential and consequently suppressed self-dissolution of Zn electrode [67]. Huang et al. [68] found that the addition of ethylenediaminetetraacetic acid (EDTA) into 6 M KOH electrolyte not only suppresses the Zn dendrite formation but also alleviates the corrosion of Zn anode. As shown in Fig. 5b, Zn anode after 1000 cycles of cyclic voltammetry (CV) measurements in EDTA-containing solution elucidates surface morphology without dendrite, distinctly different from that in blank KOH solution. Moreover, EDTA increases the discharge/charge cycling stability of Zn anode.

Polymer additives, such as polyethylenimine (PEI), can adsorb onto propagating dendrite tips and serve as a physical barrier to dendrite formation [69]. As shown in Fig. 5c, with the increase of PEI concentration, the growth of Zn dendrite is significantly suppressed. Other polymer additives, such as PEG, are also proposed as effective corrosion inhibitors for Zn electrode in strong alkaline electrolyte [70]. Poly(ethylene glycol) bis (carboxymethyl) ether (PEG DiAcid) shows even better corrosion inhibition effect for Zn electrode than PEG and polyoxyethylene alkyl phosphate ester acid (GAFAC RA), because the introduction of PEG DiAcid is capable of forming a protective layer on Zn electrode [71]. The combination of imidazole (IMZ) and PEG 600 in 3M KOH also shows corrosion inhibition effect for Zn anode [23]. IMZ suppresses the anodic reaction whilst PEG works on inhibiting the cathodic reaction. The composite of PEG 600 and poly-sorbate 20 (Tween 20) shows the similar effect as reported [72] as well as some inorganic acid salts, silicates and borates [73].

All in all, in spite of numerous efforts have been put on searching suitable electrolytes for aqueous ZABs, the practical performance of ZABs is still unsatisfactory. There is a lack of universal electrolyte system which can tackle all issues. One solution to a problem may lead to the occurrence of other problems. For instance, non-alkaline electrolytes solve the problem of electrolyte carbonation, but they give rise to other issues, such as low ionic conductivity and sluggish reaction kinetics. Thus, further investigations on understanding interfacial reactions

and selecting efficient additives for alkaline and non-alkaline electrolytes are still required to alleviate surface passivation, reduce dendrites formation, decrease self-dissolution of Zn anode and consequently to achieve more advances in aqueous ZABs.

4. Aqueous Al-air batteries

The investigation of Al-air batteries can be traced back to 1962. According to previous research regarding Al as anode material, Zaromb firstly proposed the alkaline primary Al-air battery [11]. The basic chemistry for Al-air batteries (AABs) is the oxidation of Al on the anode (Eq. 22) and the reduction of O_2 on the cathode (Eq. 13). The standard electrode potential of Al is much lower than the hydrogen evolution potential. Hence, electrochemically rechargeable AABs is not feasible in aqueous electrolytes. Notwithstanding, AABs possess several advantages. The theoretical specific energy of AABs is 8140 Wh kg^{-1}, which is much higher than that of Li-ion battery, 631 Wh kg^{-1} [74]. Al as anode material is cost-efficient since it is the most abundant metal in the earth crust and the reaction products are easy to be recycled. Moreover, the volumetric capacity of Al anode is much higher than that of Zn anode (2981 mAh g^{-1} vs. 820 mAh g^{-1}) [23], since Al^{3+} ion is trivalent and the anodic reaction of AABs involves the transfer of three electrons. The discharge and parasitic reactions of conventional alkaline AABs are as follows [75]:

$$\text{Anodic reaction: } Al + 4\,OH^- \rightarrow Al(OH)_4^- + 3\,e^- \qquad E_0 = -2.35\,V \text{ vs. } SHE \tag{22}$$

$$\text{Overall: } 4\,Al + 3\,O_2 + 6\,H_2O + 4\,OH^- \rightarrow 4\,Al(OH)_4^- \qquad E_0 = 2.76\,V \text{ vs. } SHE \tag{23}$$

$$\text{Parasitic: } 2\,Al + 6\,H_2O \rightarrow 2\,Al(OH)_3 + 3\,H_2 \tag{24}$$

As above shown, the theoretical voltage of AABs is also higher than that of ZABs. However, the parasitic reaction of Al anode (Eq. 24) leads to the deposition of $Al(OH)_3$ and H_2 evolution, which is an irreversible reaction and certainly decreases the cell voltage and discharge capacity of AABs. Furthermore, Al-based anode materials suffer from the negative difference effect (NDE), which is the intrinsic property of Al-based and Mg-based materials. It refers to the anomalous accelerated hydrogen evolution reaction happened on electrode surface during anodic polarization in aqueous solutions, which dramatically decreases the utilization efficiency of Al-based anode materials. Hence, the utilization efficiency of Al-based anodes in aqueous electrolytes could never achieve 100%. There are many discussion and interpretations with respect to the origin of NDE on Al-based materials [76], including the occurrence of low valence species [77], the breakdown of passive film and the detachment of small metallic pieces

from electrode, termed as “chunk effect”. The parasitic reaction leads to the big difference between the theoretical and practical discharge performance of aqueous AABs (Fig. 1b). In addition, the compact native oxide layer of Al is detrimental to the discharge activity of aqueous AABs. As presented in Fig. 3b, this film rarely dissolves in a wide pH range from 4.0-8.5, but it breaks down easily in very alkaline and acidic environment [78]. This is also the reason why Al anodes in alkaline electrolytes suffer from sever self-corrosion, leading to unsatisfied anode efficiency and discharge capacity. The formation of hydrated alumina in aqueous electrolytes as parasitic reaction products also decreases the discharge capacity of aqueous AABs.

In the preliminary stage, much more attention was paid on the development of Al-based anode materials [19]. Recently, increasing attention is given to the modification of electrolyte and the optimization of Al-air battery design. The most common aqueous electrolytes for AABs are neutral NaCl solution, sea water and alkaline electrolytes such as KOH or NaOH solutions [79]. Nevertheless, as above mentioned, there is an insoluble oxide layer covering the Al anode surface in neutral electrolyte, which may be detrimental to the discharge activity of Al anode. The pros and cons of adopting electrolytes of different pH and the relevant investigations are comprehensively introduced in the following part.

4.1 Alkaline electrolytes

Alkaline electrolyte are favorable for aqueous metal-air batteries because alkaline environment is in favor of oxygen reduction reaction to achieve an ideal energy density. The regular alkaline electrolytes for aqueous AABs are NaOH [80, 81] and KOH [82] solutions because both of them possess relatively high conductivity. Fan et al. [83] compared the discharge performance of AABs in 2 M NaCl, 4 M KOH, and 4 M NaOH electrolytes. The NaOH solution renders the battery with the highest cell voltage and the lowest utilization efficiency, whereas the battery with KOH-based electrolyte shows the highest energy density. The NaCl-based electrolyte is beneficial to the anodic efficiency but inimical to the cell voltage. Al as an amphoteric metal can dissolve rapidly in alkaline electrolytes leading to the evolution of hydrogen, since Al_2O_3 and $Al(OH)_3$ are both soluble in concentrated alkaline electrolyte via the following reactions,

$$Al(OH)_3 + OH^- \leftrightarrow Al(OH)_4^- \quad (25)$$

$$Al_2O_3 + 2\,OH^- \leftrightarrow 2AlO_2^- + H_2O \quad (26)$$

From one side, the alkaline electrolytes mitigate the surface passivation of Al-based anode materials. However, from other side, the alkaline environment leads to the decrease of corrosion resistance of Al anodes and results in the efficiency loss during discharge and standby stage. Therefore, the main emphasis on developing novel alkaline AABs with superior performance is the improvement of the *corrosion resistance* and utilization efficiency of Al anodes. As above mentioned, doping Al with other alloying elements is one of the common methods to solve the relevant issues. Apart from that, the employment of electrolyte additives is also an efficient and economical strategy for the performance enhancement of alkaline AABs. Na_2SnO_3 is one of the most common inorganic corrosion inhibitors for Al anodes in alkaline electrolytes [84]. SnO_3^{2-} can deposit on the anode surface and block the active sites for hydrogen evolution reaction. However, the deposited film of stannate is relatively porous. Therefore, Nie and co-authors [85] proposed to adopt casein to regulate the deposition of stannate and consequently to form a uniform protective layer on Al anode surface. This hybrid additives of stannate with casein results in an 83% inhibition efficiency for hydrogen evolution reaction and an 89% increment of discharge capacity. As shown in Fig. 6a and Fig. 6b, Wu and co-authors [86] employed alkyl polyglucoside (APG) to promote and tailor the deposition of K_2SnO_3 to form a uniform layer. The combination of APG and K_2SnO_3 yields a superior specific capacity of AABs, which is 2.5 times higher than that in blank KOH electrolyte. Kapali and co-authors [80] indicated the usage of 4 M NaOH based alkaline citrate cum stannate electrolyte is also capable of reducing the corrosion rate of Al-based anode materials and simultaneously maintaining relatively negative OCP.

ZnO has also been reported as an effective inorganic corrosion inhibitor for Al-based anode materials in alkaline electrolytes based on the similar working mechanism with SnO_3^{2-} [11, 87]. Sun and co-authors [88] compared the effect of ZnO and Na_2SnO_3 as electrolyte additives for alkaline AABs, indicating that both additives are capable of inhibiting the corrosion rate of Al-In anode and improving its utilization efficiency via the deposition of Zn and Sn:

$$ZnO + H_2O + 2\,OH^- \rightarrow Zn(OH)_4^{2-} \quad (27)$$

$$3\,Zn(OH)_4^{2-} + 2\,Al \rightarrow 3\,Zn + 2Al(OH)_4^- + 4\,OH^- \quad (28)$$

$$3\,SnO_3^{2-} + 4\,Al + 9\,H_2O \rightarrow 3\,Sn + 4\,Al(OH)_4^- + 2\,OH^- \quad (29)$$

The inhibition efficiency of ZnO could be further improved through mixing with organic additives, such as dimethyl amine epoxy propane (DE) [89], polyaniline (PANI) [90],

carboxymethyl cellulose (CMC) [91], and 8-hydroxyquinoline (8-HQ) [92]. Jiang and co-authors [93] studied the inhibition effect of ZnO with organic acids (EDTA, citric acid ($C_6H_8O_7$) and acetic acid ($C_2H_4O_2$)) for Al foam based on the experimental results and computational simulation. They proposed that these organic acids can adsorb on the surface of Al and Zn to form a composite protective film (RCOO-Al and RCOO-Zn) (Fig. 6c) and thus suppresses the corrosion of the Al anode. Fig. 6d shows that the solely addition of organic acid only induces minor improvement in specific capacity of AABs but the combination of citric acid with ZnO contributed to a remarkable improvement from 763 mAh g^{-1} to 1902 mAh g^{-1}. Furthermore, the aforementioned PEG and PEG derivatives, which are extensively used as electrolyte additives for alkaline ZABs [71, 94], are also applicable for alkaline AABs. According to the work of Wang and co-authors [95], the combination of 0.2 M ZnO with 2 mM PEG leads to a 98.8% corrosion inhibition efficiency for Al anode in alkaline electrolyte and around -1 $V_{HgO/Hg}$ discharge potential at 40 mA cm^{-2} [95]. The effect of hybrid inhibitors (ZnO/ PEG di-acid) was also investigated in 5 M KOH electrolyte, showing considerable enhancement of the corrosion resistance of Al anode and the battery capacity [96] owning to the adsorption of PEG di-acid on the deposited Zn layer to protect Al anode. The addition of halide ions is beneficial for the adsorption of organic molecules [97, 98]. Hence, Umoren and co-authors [99] investigated the synergistic effect of PEG and halide ions (Cl^-, Br^-, and I^-) and found that the addition of halide ions enhances the inhibition effect of PEG for Al in NaOH solution with different extent ($I^- > Br^- > Cl^-$). For instance, the addition of 0.05 M KI and KCl increase the inhibition efficiency of 0.7 mM PEG from 43.8% to 55.7% and 49.9%, respectively.

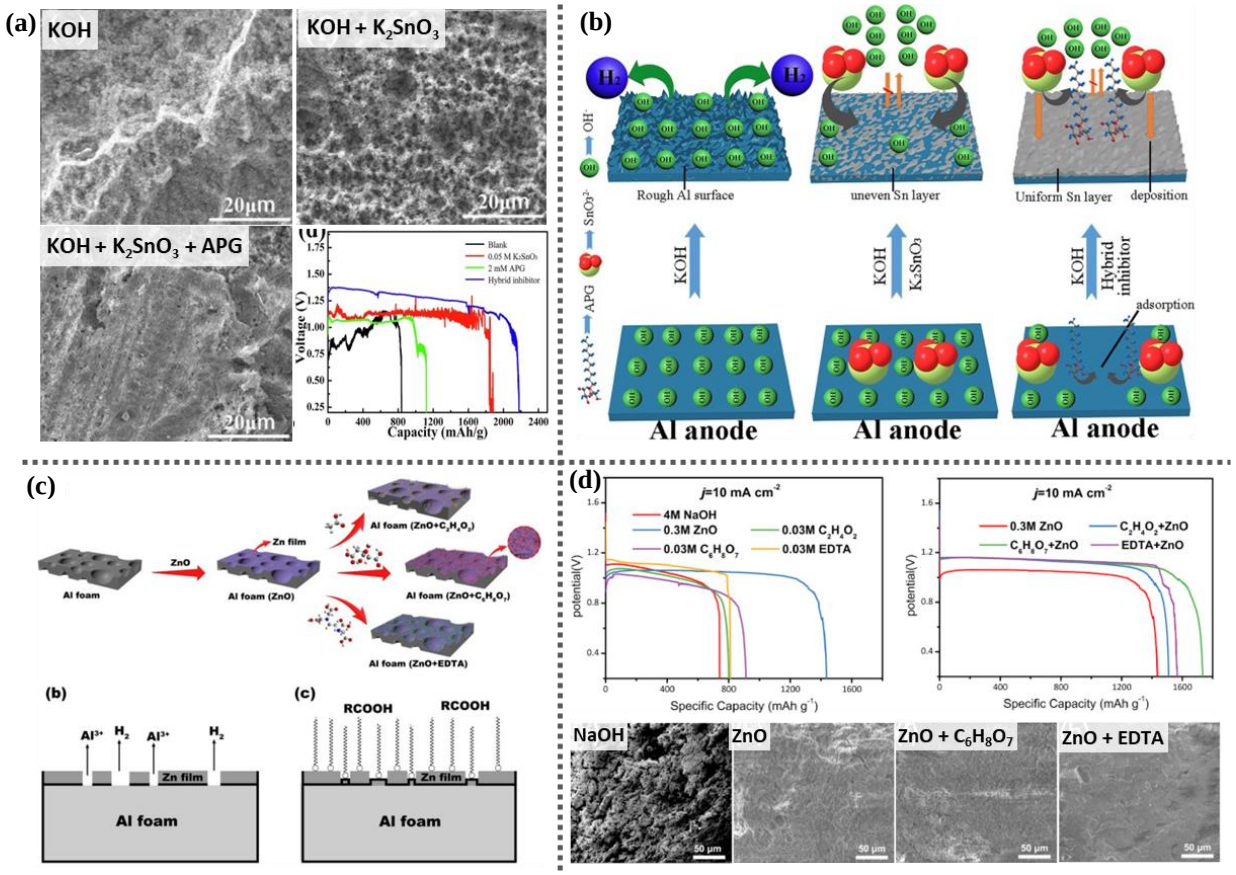

Fig. 6. (a) Surface morphologies of Al anode after 2 h immersion in 4 M KOH with and without additives and the discharge performance of AABs in these electrolytes at 100 mA cm^{-2}, (b) schematic of working mechanism of K_2SnO_3 and APG as electrolyte additives for Al anode reproduced with permission from Ref. 86; (c) illustration of inhibition mechanism of ZnO and ZnO/organic acid as electrolyte additive for AABs, (d) discharge performance of alkaline AABs with various electrolyte additives and surface morphologies of Al foam electrode after 1 h immersion in different solutions reproduced with permission from Ref. 93.

CaO is also considered as a good electrolyte additive for alkaline AABs. Albert et al. [100] compared the synergistic effects of sodium citrate with CaO and $CaCl_2$, demonstrating that the addition of CaO or $CaCl_2$ with sodium citrate both alleviates the corrosion rate of Al anode. The mixed electrolyte of 20% sodium citrate and 2.5% $CaCl_2$ shows the best inhibition effect [100]. Shao et al. [101] found the addition of Ca^{2+} ion into 4 M KOH can increase the corrosion resistance of pure Al, which can be further improved by the synergistic effect of Ca^{2+} and tartrate ion. They suggest the synergistic effect of the hybrid additives is based on the complexation of Ca^{2+} with tartrate ion, which makes the adsorption of Ca^{2+} on Al surface easier. Kang and co-authors [102] adopted experimental methods and quantum chemical calculation to investigate the working mechanism of CaO/ L-aspartic as an electrolyte additive for AABs, elucidating that CaO can react with water to form $Ca(OH)_2$ on the top of Al surface and L-

aspartic is able to adsorb on $Ca(OH)_2$ layer and the rest bare Al surface, which therefore retards the anode self-corrosion reaction. Other sorts of hybrid additives for alkaline AABs based on similar working mechanism have been reported as well. Wang and co-authors [103] demonstrated that L-cysteine and $Ce(NO_3)_3$ as a hybrid additive owns the capability of preventing the hydrogen evolution reaction of AA5052 anode in 4 M NaOH electrolyte. The addition of Ce^{3+} ion gives arise to the deposition of CeO_2 and $Ce(OH)_4$ via the following reactions:

$$Ce^{3+} + 3\,OH^- \rightarrow Ce(OH)_3 \quad (30)$$

$$2\,Ce(OH)_3 \rightarrow Ce_2O_3 + 3\,H_2O \quad (31)$$

$$4\,Ce(OH)_3 + O_2 + 2\,H_2O \rightarrow 4\,Ce(OH)_4 \quad (32)$$

$$Ce(OH)_4 \rightarrow CeO_2 + 2\,H_2O \quad (33)$$

Meanwhile, L-cysteine adsorbs on the anode surface and then interacts with Ce^{3+} ion to form a composite film, further retarding the anode corrosion reaction. Similarly, the combination of L-glutamic acid and cerium acetate show a 77.85% corrosion inhibition efficiency for Al-Mg-Sn-Ga anode in 4 M NaOH electrolyte [104]. Besides, this additives mixture is also beneficial to the cell voltage and discharge capacity of the battery, attributed to the formation of a complex film on Al anode.

Since the adsorption of organic inhibitors is able to block the active sites on the anode surface and consequently mitigate the corrosion of Al anodes, the sole addition of organic inhibitors is also considered as an efficient and economical way to improve the discharge performance of AABs. Liu and co-authors [105] proposed three quaternary ammonium-type surfactants, i.e. dodecyl dimethyl benzyl ammonium bromide (DDBAB), cetyl trimethyl ammonium bromide (CTAB), and dihexadecyl dimethyl ammonium bromide (DDAB), as electrolyte additives for alkaline AABs. Among the tested systems, alkaline AABs with DDBAB additive shows the highest specific capacity and cell voltage (2430 mAh g^{-1} and 1.34 V at 20 mA cm^{-2}). Deyab [106] reported an nonionic surfactant (i.e. Nonoxynol-9) with the capability of mitigating the cathodic reaction of Al anode in 4 M NaOH, which consequently exhibits a 92.8% corrosion inhibition efficiency. Except for surfactants, some carboxylic acids also attract great interest. Wysocka and co-authors [107] found the minor addition of citric, tartaric and tricarballylic acid achieved corrosion inhibition efficiencies exceeds 99% on Al anode, which were determined via galvanostatic dynamic EIS measurements. Other organic additives, such as gluconic acid

[108], urea and thiourea [109], and 6-thioguanine [110], have also been studied as electrolyte additives for alkaline AABs.

Except for using different electrolyte additives, some researchers divert their attention from solutes to solvents. Comparing to water, methanol and other organic solvents possess less protic activity, thus *hydrogen evolution* reaction in those solvents is more difficult. Replacing a part of water to other solvents is beneficial for decreasing the self-corrosion rate of Al in alkaline media. Hence, alkaline methanol solutions were proposed to be suitable electrolyte systems for AABs [111-113]. Wang et al. [111] investigated 4 M KOH methanol solution with different water contents, revealing that the corrosion rate of Al anode increases with the increase of water content but the proper discharge performance requires adequate amount of water (20%) in the electrolyte. The addition of Na_2SnO_3 into 4 M KOH methanol-20% water electrolyte further improves the inhibition efficiency and discharge potential of Al anode [113]. Ma et al. [114] compared the discharge performance of Al-based anodes in 4 M NaOH ethanol-10% water with that of Zn anode in 4 M NaOH. 4M NaOH ethanol-10% water as the electrolyte for alkaline AABs can effectively inhibit parasitic hydrogen evolution reaction of Al anodes and simultaneously maintain the anode discharge activity. Apart from alcohols, ionic liquids are also considered as possible substituents of water as electrolyte solvents. Wang and co-authors [115] systematically studied the influence of 1-butyl-3-methyl imidazolium tetrafluoroborate ($BMIMBF_4$) content and KOH concentration on the electrochemical behavior of pure Al. The results indicate that 2 M KOH $BMIMBF_4$-H_2O mixed electrolyte with 60% water is a promising electrolyte system for AABs in which Al anode exhibits moderate corrosion rate and good discharge potential. Moreover, the work of Deyab elucidates that the addition of 1.5 mM 1-Allyl-3-methylimidazolium bis(trifluoromethylsulfonyl)imide) into 4 M NaOH is able to suppress the HER reaction and thus increase the discharge capacity of AABs [116].

Even though many achievements have been made for alkaline Al-air battery system, the *electrolyte carbonation* is still a main obstacle to the application of alkaline electrolytes for Al-air batteries. The CO_3^{2-} generated via Eq. 16 may react with the alloying elements or impurities in Al based anode and form insoluble carbonate, which is detrimental to air cathode and can block the active sites of air cathode. As reported in literature [23, 117], carbon-based air cathode is subject to corrosion in highly concentrated alkaline electrolyte via the following reaction,

$$C + 6\,OH^- \rightarrow CO_3^{2-} + 3\,H_2O + 4\,e^- \quad (34)$$

Besides, the working temperature, the concentration of the electrolyte and the ratio of electrode surface area to the electrolyte volume also have impact on the performance of AABs [118, 119]. The working temperature is decisive for the corrosion behavior and discharge performance of Al anodes. The discharge reaction of AABs is an exothermic reaction, leading to the increment of electrolyte temperature inevitably. Wilhelmsen and co-authors [120] investigated the corrosion behavior of super pure Al and Al-In alloy in 4 M KOH electrolyte under different temperatures (-20 to 60 °C). The results show that the corrosion rates of Al and Al-In alloy increases with the increment of temperature, but Al-In alloy possesses excellent corrosion resistance even at 60 °C. Similar conclusion were also conducted in the work of Chu et al. [119], reporting that higher working temperature and concentration of KOH induce faster dissolution of Al anode. By contrast, Ilyukhin and co-authors [121] found that, in concentrated NaOH electrolyte with minor addition of Na_2SnO_3 (8 M NaOH + 0.015 M Na_2SnO_3), the rise of working temperature increases the faradaic efficiency of Al anode. 60 °C is proposed as the optimal working temperature for efficient reaction activity of pure Al anode. It should also be remarked that battery testing performed at high temperatures are essential in order to simulate the real working condition [122]. In case of the relatively high working temperatures, the thermal management for Al-air batteries should also be taken into account for further development.

4.2 Neutral salt-based electrolytes

Al anodes possess better corrosion resistance and more uniform dissolution in neutral electrolyte than in acidic and alkaline electrolytes (as shown in Fig. 7). Hence, Ma et al. [123, 124] proposed that neutral solution could be the most suitable electrolyte for aqueous AABs. Moreover, the adoption of neutral electrolytes is one feasible solution to get rid of the electrolyte carbonization issue. Among the neutral electrolytes for aqueous AABs, NaCl solution has been widely investigated as well as seawater [125, 126]. Akmal and co-authors [125] compared the performance of AAB in seawater and in NaCl solution of various concentrations (0.5-7 M), demonstrating that the battery exhibits the best discharge performance in 4 M NaCl electrolyte. Nevertheless, the discharge performance of AAB in seawater can be enhanced via adopting open-cell configuration, which is related to the ratio of exposed electrode area to the volume of electrolyte. Moreover, the work of Despic and co-authors [76] concerning the influence of various cations in the electrolyte (Li^+, Na^+, Ca^{2+}, Sr^{2+}, Ba^{2+}, K^+, and NH_4^+) indicate that the cations also impart significant effect on the loss of Al

anode during anodic polarization. In Na^+-based electrolyte, the loss of Al is moderate and could be further decreased via the dilution of NaCl concentration.

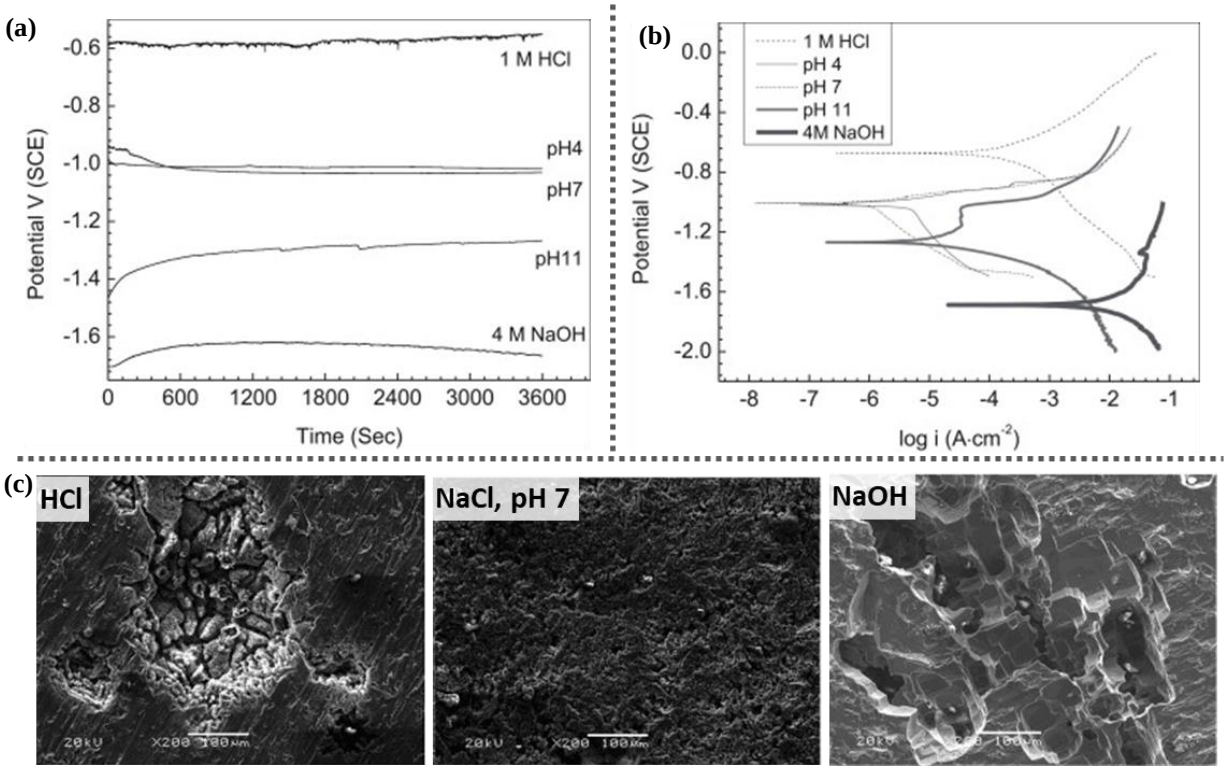

Fig. 7. (a) OCP and (b) polarization curves of Al-Zn-Mg alloy in HCl, NaCl with different pH, and NaOH solutions, reproduced with permission from Ref. 123; (c) surface morphologies of Al-Zn-In alloy after cyclic polarization test in in HCl, NaCl with different pH, and NaOH electrolytes, reproduced with permission from Ref. 124.

Notwithstanding several merits attributed to neutral electrolytes, the cell voltage and energy density of neutral AABs are relatively low in comparison with alkaline AABs, because the passive oxide film is stable in neutral electrolytes [114]. The *surface passivation* of Al-based anodes in neutral electrolytes is the main obstacle for AABs to achieving superior discharge performance. In order to tackle this problem, Al-based anode materials with various active alloying elements have been developed and tested in neutral electrolytes. A series of alloying elements and ternary Al alloys [76, 127, 128], such as Al-In, Al-Ga, Al-Ti, Al-Mg, Al-Sn, Al-In-Ga and Al-Mg-Ga alloys were adopted as anode materials for neutral AABs. Al-In anode shows -1.2 V vs. SCE discharge potential and 95.4% utilization efficiency in 2 M NaCl solution at 20 mA cm^{-2} discharge current density [128]. These works clarify that neutral solutions could be suitable electrolytes for AABs providing high-performance anodes are adopted in the battery system.

Similar to anode alloying of these elements, the addition of sole or combined cations of these metallic elements, such as In^{3+} [129], Fe^{3+} [130], Zn^{2+} [131], Ga^{3+} [132], Sn^{2+} [133], etc., as electrolyte additives is also beneficial for the activation of Al anodes. The electrochemical behavior of Al-In alloy in neutral 0.5 M NaCl with various concentrations of $ZnCl_2$ was investigated by Tang and co-authors [134], elucidating that the addition of Zn^{2+} restrains the parasitic hydrogen evolution reaction and improves the anode potential. It should be noted that the activation effect of these cations is dependent on the adopted anode. For instance, the work of Shayeb et al. [133] indicates that the addition of $SnCl_2$ into 0.6 M NaCl solution only imparts activation effect to Al-Zn-based anodes rather than pure Al and Al-Sn anodes. The activation mechanism of Sn^{2+} is attributed to the deposition of Sn on the Al surface, which changes the structure of the surface film. Only Al-Zn-based alloys allow the diffusion of Sn^{2+} into the interface because the $ZnAl_2O_4$ formed on Al-Zn alloys leads to defects and cracks of the surface film, which act as channels for penetration of the active metal cations through the interface between the oxide film and alloy matrix. Consequently, the deposited Sn results in the surface activation. The addition of In^{3+} as an electrolyte additive possesses similar effect to Sn^{2+}, which shows more superior activating effect on Al-Zn alloy than pure Al and Al-Zn-Sn alloy [129]. Carroll and Breslin [135] investigated the activation mechanism of In^{3+} and Hg^{2+} on Al passive film formed in aqueous halide solutions. As concluded, the activation mechanism of In^{3+} is incorporated with halide ions, while the activation caused by Hg^{2+} is independent on the presence of halide ions but relies on the oxide detachment.

Although the corrosion rate of Al-based anodes in neutral electrolyte is relatively moderate, the addition of corrosion inhibitors as electrolyte additives may be also helpful to improve the discharge performance of neutral AABs. Further investigations are indeed needed to explore the existing corrosion inhibitors as promising additives for neutral AABs.

4.3 Acidic electrolytes

The conventional acidic electrolytes for aqueous Al-air battery systems are sulfuric acid and hydrochloric acid. However, concentrated sulfuric acid leads to the formation of passive layer on Al anodes, which is detrimental to the output cell voltage. Except for the anode passivation, the slow kinetics of air cathode in acidic electrolyte is another issue hindering the utilization of acidic electrolyte.

Rota and co-authors [136] compared the discharge performance of AABs with bipolar configuration in alkaline electrolyte and acidic electrolyte. The mixture electrolyte of 0.04 M

HCl and 3 M H_2SO_4 gives rise to higher power output 35 W (at 170 mA cm^{-2}) than the highest power output 30 W (at 110 mA cm^{-2}) achieved in 4 M NaOH electrolyte. Nevertheless, the voltage of alkaline Al-air batteries is higher than that in acidic electrolyte. Their follow-up work exhibits that the faradaic efficiency of Al-Zn-In anode in 3 M H_2SO_4 + 0.04 M HCl reachs up to 84%. The highest power density, 120 mW cm^{-2}, is achieved by the combination of Al-Zn-Sn anode in the same acidic electrolyte [137]. Flamini and Saidman [138] compared the electrochemical behavior of Al-In-Ga and Al-Zn-Ga alloys in 0.5 M acidic NaCl solution and in 0.5 M HAc solution of pH 3. The results indicate that aggressive Cl^- ions result in more negative OCP than that of the same alloy in HAc solution with the same acidity. The possible reason as proposed is the formation of a passive film via the reaction of oxidized Al and acetate ion. Therefore, similar to neutral AABs, *activation of the Al anodes* in acidic environment is needed. Accordingly, the aforementioned metal cations have also been evaluated as electrolyte additives for acidic AABs. The electrochemical behavior of Al anodes in acidic NaCl and NaCl solution with inorganic additives was investigated in 1990s [139, 140]. The addition of $InCl_3$, $ZnCl_2$ and $HgCl_3$ into acidic NaCl solution is beneficial to the enhancement of anode discharge activity. Saidman et al. [141] investigated the dissolution behavior of Al in acidic NaCl solution with $In_2(SO_4)_3$, indicating the concentration of In^{3+} is decisive for the activation of Al in acidic solutions. The research work from Holzer and co-authors [142] shows the addition of Cl^-, Zn^{2+}, and In^{3+} can moderate the passivation of Al anode in sulfuric acid.

In summary, aqueous AABs in different pH environment are confronted with diverse problems which could be alleviated via adopting specific electrolyte additives or various Al alloy anode materials. Novel aqueous AABs with superior discharge performance could be achieved by the combination of a high performance anode with a tailored electrolyte system supported by battery design. Mokhtar et al. [143] summarized conventional electrolytes and Al anodes for Al-air batteries. They proposed that Al-In-based anodes, Al-Sn-based anodes, and Al-Zn-based anodes are suitable anode materials for acidic, neutral, and alkaline electrolytes, respectively. With the development of separator and battery design, dual-electrolyte or even tri-electrolyte aqueous AABs are emerging in recent years, which can improve the drawbacks of conventional aqueous AABs and are worthy of further development. Chen and co-authors [144] proposed a dual-electrolyte membrane less AAB adopted H_2SO_4 as catholyte and KOH as anolyte (Fig. 8b). The maximum power density of this dual-electrolyte system is 104.6% higher than that of the single electrolyte system under the same condition. As shown in Fig. 8a, the theoretical voltage of dual electrolyte system is much higher than that of single electrolyte

alkaline system due to the following favorable cathodic reaction in acidic catholyte different from that described in Eq. 13.

Cathodic (acidic environment): $O_2 + 4H^+ + 4e^- \rightarrow 2H_2O \quad E_0 = 1.23\,V\ vs.SHE$ (35)

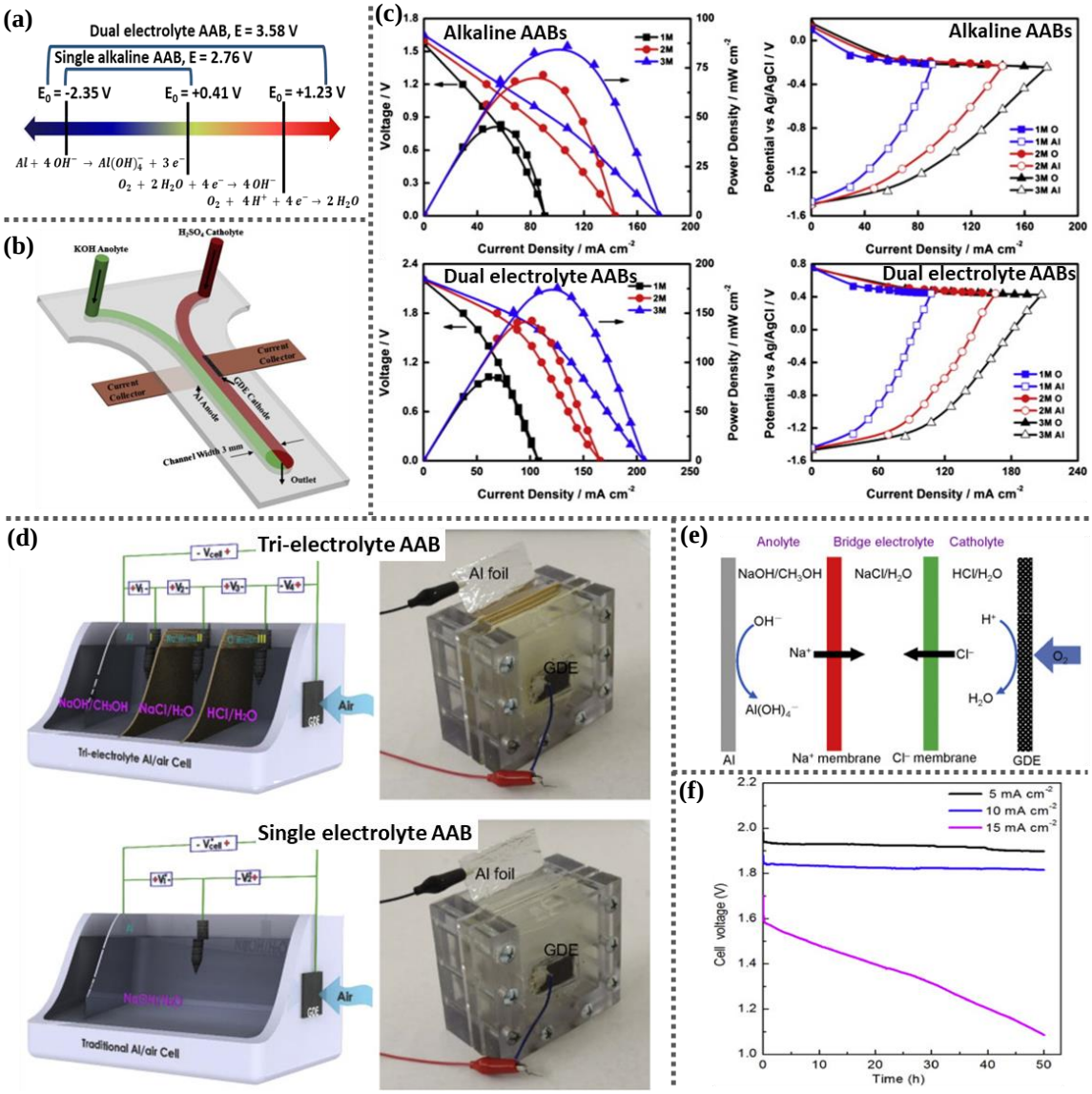

Fig. 8. (a) illustration of the theoretical voltage of alkaline and dual-electrolyte AABs; (b) schematic of dual-electrolyte membraneless AAB; (c) discharge performance of alkaline AABs and dual-electrolyte AABs; (d) schematic and real prototype of tri- and single electrolyte AABs; (e) illustration of ion migration in tri-electrolyte AAB and (f) discharge curves of tri-electrolyte AAB under different load ((b) and (c) are reproduced with permission from Ref. 144; (e), (f) and (g) are reproduced with permission form Ref. 147.

Therefore, the dual-electrolyte AABs exhibit higher cell voltage and power density than that of single alkaline AABs (Fig. 8c). Feng et al. [145] designed a recirculating dual-electrolyte Al-air cell based on a composite polytetrafluoroethylene/polyethylene/ polytetrafluoroethylene (PTFE/PE/PTFE) membrane, which is capable of simultaneously prolonging the electrolyte

utilization and maintaining high cell voltage after several cycles. Except for mixed-pH dual-electrolyte system, dual-electrolyte or even tri-electrolyte systems based on the combination of aqueous and non-aqueous for Al-air batteries are emerging in recent years. For instance, Wang et al. [146] developed a dual-electrolyte system with KOH/CH_3OH as anolyte and KOH/H_2O as catholyte, showing 6000 mAh cm^{-3} discharge capacity at 30 mA cm^{-2}. The researchers also proposed a tri-electrolyte Al-air battery system, which is composed of organic solvent-based alkaline anolyte (4 M NaOH/CH_3OH), a cation membrane, an aqueous bridging electrolyte, an anion membrane and an air-breathing cathode in an aqueous acidic catholyte (Fig. 8d). The OCV of this tri-electrolyte system achieves 2.2 V and the cell voltage of this system under 5 mA cm^{-2} current density is stable at ~1.95 V (Fig. 8f) [147]. All these works show the importance of selecting suitable electrolyte and battery prototype design for achieving high-performance Al-air batteries.

5. Aqueous Mg-air batteries

Comparing to aqueous ZABs and AABs, aqueous Mg-air batteries (MABs) are less noticed in the last few decades due to the non-electrochemical rechargeable property and the most severe self-corrosion in aqueous electrolytes. Nevertheless, in recent years, there is a resurgence of the research interest in aqueous MABs due to the demand of lightweight and high specific energy systems. The specific energy density (excluding O_2) and the faradic capacity of MABs are 6.8 kWh kg^{-1} and 2205 mA h/g, respectively [20]. Besides, the theoretical voltage of common aqueous MABs is the highest, 3.1 V vs. 1.66 V for ZABs and 2.76 V for AABs. The reactions involved in aqueous MABs are as follows:

$$\text{Overall: } 2\,Mg + O_2 + 2\,H_2O \rightarrow 2\,Mg(OH)_2 \quad E_0 = 3.1\,V \tag{36}$$

$$\text{Parasitic: } Mg + 2\,H_2O \rightarrow Mg(OH)_2 + H_2 \tag{37}$$

Additionally, Mg is abundant in seawater and earth crust with low toxicity, good bio-compatibility and high safety. Therefore, Mg-air battery is a promising electrochemical energy storage and conversion device, which shows good feasibility to supply power for marine equipment and implantable medical devices [148, 149]. As early as the 1960s, General Electric (GE, United State) obtained a neutral Mg-air fuel cell, which adopted NaCl solution as the electrolyte. MagPower Systems Inc. (Canada) also developed a Mg-air full cell adopting saline solution with electrolyte additive, which possesses 136.19 Wh kg^{-1}. In 1993, Norwegian Defence Research Establishment (FEI, Norway) invented Mg/seawater/O_2 cell for autonomous underwater vehicle (AUV) [150]. In 2004, CLIPPER battery system for AUV was created

cooperatively by FEI, Direction Generale Armanment (DGA, France), and Bassin d'Essais des Carenés (BEC, France). It allows the undersea vehicle to advance 1600 nautical miles with a speed of 2 m/s [151].

Even with these successful examples, the wide range practical application of aqueous MABs is still plagued by problems associated with the following issues. Fig. 9 presents the existing problems of aqueous MABs. The parasitic reaction of Mg anode (Eq. 37) in standby condition or under anodic polarization in aqueous electrolyte is serious due to the relatively high reaction activity of Mg with H_2O, partially protective film and the intrinsic property of NDE, resulting in the decreased utilization efficiency and the shortened service life. The origin of NDE is controversial and there are many possible explanations for NDE of Mg [152-154]. The prevailing views regarding the mechanism of NDE include the univalent Mg^+ mechanism [155-157], the mechanism based on the enhanced cathodic catalytic activity [158-160], the mechanism based on the partially protective film [161], and the existence of MgH_2 [162, 163]. NDE is one of the main causes for the unsatisfactory utilization efficiency of Mg-based anode materials. Besides, the detachment of metallic particles from matrix (Fig. 9), namely "chunk effect", also leads to the loss of utilization efficiency. The "chunk effect" mainly refers to the detachment of undissolved matrix, second phases and impurities. According to the work of Deng et al. [164], the efficiency loss of Mg-based anodes caused by "chunk effect" can exceed the loss due to NDE for some Mg alloys under low current densities, such as WE43 and ZE41 Mg alloys. Adding alloying elements is one of the strategies to alleviate the self-corrosion of Mg-based anode materials. However, a large amount of second phases may induce serious "chunk effect". Hence, many research adopt thermo-mechanical treatment to tailor the microstructure of Mg-based anode materials to further reduce the self-corrosion and "chunk effect" [165-167]. A more detailed overview on the recent development about Mg-based anode materials can be found in other literature reviews [168, 169]. Besides, as the products of discharge reaction and parasitic reaction, a large amount of $Mg(OH)_2$ forms and stably precipitates on the anode surface when the pH of electrolyte exceeds 10.4 in the ambient environment. The formed discharge product film blocks the anode surface and passivates anodic reactions, leading to large potential drop and energy loss. The large amount of H_2, as

the by-products of the parasitic reaction, may provoke several technical issues, especially for closed systems [170].

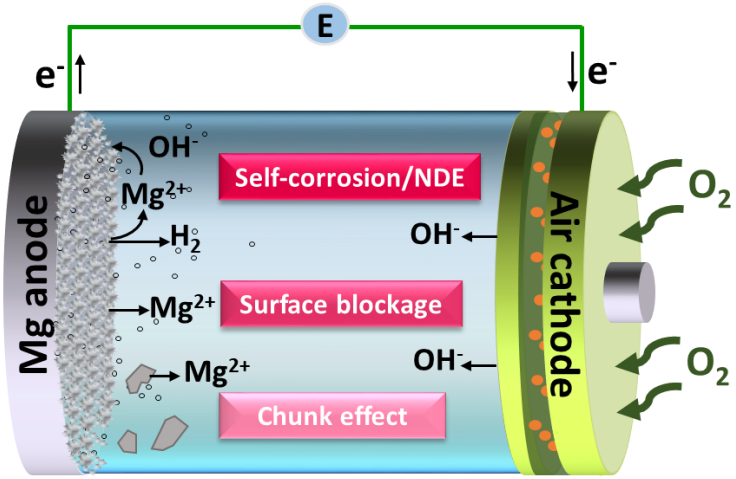

Fig. 9. Illustration of aqueous Mg-air battery.

Electrolyte, as one of the key components for aqueous MABs, greatly influences the battery performance and may remedy the drawbacks of aqueous MABs if suitable electrolyte is applied. Mg anodes self-corrosion and the products deposition are tightly dependent on the electrolyte composition. Therefore, the modification of electrolyte is of great interest to researchers worldwide. In the following sections, different electrolytes for aqueous MABs are introduced and relevant concepts for electrolyte tailoring are discussed in detail.

5.1 Inorganic salt electrolytes

According to the Pourbaix diagram of a Mg-water system at 25 C° in presence of 1 M soluble species [171], Mg is thermodynamically stable below -2.37 V with a large pH range, which is beyond the stable region of water. Mg^{2+} is the stable form in a pH range from 0 to 10, above which $Mg(OH)_2$ forms. Consequently, in neutral and acidic aqueous environments, Mg spontaneously converts to Mg^{2+} ions, which further reacts with OH^- generated by H_2O to produce $Mg(OH)_2$. Unlike amphoteric metallic electrodes like Al and Zn, the strong alkaline environment favors the formation of stable $Mg(OH)_2$ precipitation and leads to sever surface passivation. Thus, the conventional aqueous electrolytes for MABs do not include strong alkaline electrolytes. Neutral salt solution is more favorable than alkaline and acidic solutions.

The sort of salt in the electrolyte is decisive for the electrochemistry and interface control of aqueous MABs. Chloride, nitrate/nitrite, and sulfate have been used as the main components of neutral electrolyte. Leong and co-author [172] investigated the effect of different electrolyte salt species on the discharge performance of MABs. The results indicate that MAB in NaCl

solution shows the highest cell voltage but the shortest discharge lifetime. $NaNO_3$ solution as MAB electrolyte is beneficial to prolong the discharge lifetime but it is detrimental to the cell voltage. The cell voltage of MAB in Na_2SO_4 solution is slightly higher than that in $NaNO_3$ solution when the applied current density is less than 50 mA cm^{-2} (Fig. 10a). The Coulombic efficiency of MAB in Na_2SO_4 solution is less than that in $NaNO_3$ solution. Shrestha and co-authors [173] compared the discharge behavior of pure Mg and Mg-RE (rare earth) alloy in NaCl, Na_2SO_4, and $NaNO_3$ electrolytes. Being consistent with other research, chloride-free electrolytes are beneficial for high utilization efficiency via retarding self-corrosion of Mg-based anodes. However, the IR drop caused by the discharge product film formed in chloride-free electrolytes is tremendously huge, even leading to positive discharge potential (Fig. 10b). Table 1 lists the performance of MABs in different inorganic salt solutions.

3.5 wt. % NaCl or 0.6 M NaCl solution is the most studied electrolyte for neutral MABs [174-176]. This concentration is similar to the salinity of seawater, which is a widely used electrolyte for aqueous MABs as reliable energy supplier for marine equipment. Moreover, this concentration is beneficial for achieving good comprehensive discharge performance [177]. Hamlen and coauthors [178] tested the cell voltage of AZ61 Mg alloy in NaCl and LiCl solution with different concentrations, indicating the cell voltage of MABs greatly depends on the type and concentration of salt in the adopted electrolytes. The cell voltage of MAB is higher in more concentrated NaCl solution (18%) in comparison with that in 7% NaCl or 7% LiCl solution. Nevertheless, high concentration Cl^- ions lead to severe corrosion of Mg electrode[179]. Hence, in most cases, 3.5% NaCl is used as the background electrolyte for MABs.

Table 1. Comparison of MABs performance in different inorganic salt solutions

electrolyte	concentration	anode	open circuit voltage/ potential vs. Ag/AgCl	voltage/ potential vs. Ag/AgCl	other performance	Ref
NaCl	Sat.	Mg	1.7 V	1.4 V at 20 mA cm^{-2}	*Coulombic efficiency 56%	[172]
NaCl	0.6 M	Mg	-1.53 V	-1.29 V at 10 mA cm^{-2}	hydrogen evolution rate: 3.25 ml cm^{-2} h^{-1}; **Faradaic efficiency: 44.0 ± 2.8 %	[173]
		ZE10A	-1.6 V	-1.29 V at 10 mA cm^{-2}	hydrogen evolution rate: 3.6 ml cm^{-2} h^{-1}; Faradaic efficiency: 47.5 ± 1.6 %	
		EV31A	-1.5 V	-1.29 V at 10 mA cm^{-2}	hydrogen evolution rate: 3.3 ml cm^{-2} h^{-1}; Faradaic efficiency: 38.2 ± 2.3 %	
NaCl	3.5 wt.%	Mg-0.1 wt. % Ca	2.032 V	-1.542 V at 5 mA cm^{-2}	***utilization efficiency: 58.2 ± 2.1 %	[175]
NaCl	18%	AZ61		1.28 V at 12 mA cm^{-2}	-	[178]
NaCl	7%	AZ61		1.24 V at 12 mA cm^{-2}	-	
NaCl	0.5 M	Mg	-1.61 V	-1.58 V at 3.2 mA cm^{-2}	****Mg^{2+} Faradaic efficiency: 40%	[180]
NaCl/HNa_2PO_4	0.5 M/0.05 M	Mg	-1.58 V	-1.54 V at 3.2 mA cm^{-2}	Mg^{2+} Faradaic efficiency: 31%	
LiCl	18%	AZ61		1.15 V at 12 mA cm^{-2}	-	[178]
LiCl	7%	AZ61		1.25 V at 12 mA cm^{-2}	-	
$NaNO_3$	5 M	Mg	1.7 V	0.9 V at 20 mA cm^{-2}	Coulombic efficiency 79%	[172]
$NaNO_3$	0.5 M	Mg	-1.26 V	-0.98 V at 10 mA cm^{-2}	hydrogen evolution rate: 0.55 ml cm^{-2} h^{-1}	[173]

		ZE10A	-1.38 V	-0.4 V at 10 mA cm^{-2}	hydrogen evolution rate: 0.8 ml cm^{-2} h^{-1}	
		EV31A	-1.6 V	-0.64 V at 10 mA cm^{-2}	hydrogen evolution rate: 0.66 ml cm^{-2} h^{-1}	
$NaNO_3$	0.5 M	Mg	-1.4 V	-1.35 V at 3.2 mA cm^{-2}	Mg^{2+} Faradaic efficiency based H_2 evolution reaction: 93%	[180]
$Mg(NO_3)_2$ ·$6H_2O$/$NaNO_2$	2.6 M/ 3.6 M	AZ21		1 V at 0.9 mA cm^{-2}		[181]
Na_2SO_4	1 M	Mg	1.5 V	1.1 V at 20 mA cm^{-2}	Coulombic efficiency 60%	[172]
Na_2SO_4	0.1 M	Mg	-1.5 V	-0.56 V at 10 mA cm^{-2}	hydrogen evolution rate: 1.5 ml cm^{-2} h^{-1}	[173]
		ZE10A	-1.6 V	-0.91 V at 10 mA cm^{-2}	hydrogen evolution rate: 3.1 ml cm^{-2} h^{-1}	
		EV31A	-1.66 V	-0.96 V at 10 mA cm^{-2}	hydrogen evolution rate: 2.1 ml cm^{-2} h^{-1}	
HNa_2PO_4	0.5 M	Mg	-1.52 V vs Ag/AgCl at 3.2 mA cm^{-2}	2.3 V vs Ag/AgCl at 3.2 mA cm^{-2}	Mg^{2+} Faradaic efficiency: 66%	[180]

*Coulombic efficiency =Specific capacity /Theoretical capacity

** Faradaic efficiency was calculated using the weight loss method where the mass loss was converted into charge consumed using faradaic relation and it was normalized with the charge passed during the galvanostatic tests.

***Utilization efficiency= Theoretical weight loss/ Actual weight loss

****Mg^{2+} Faradaic efficiency=$\frac{(i_{applied}-i_{H2})}{i_{applied}} \times 100$.

Sathyanarayana and Munichandraiah [182] investigated a series of inorganic salt solutions as electrolytes for MABs to evaluate the impact of different salts on the discharge performance of MABs. Mixed $Mg(NO_3)_2/NaNO_2$ solution was proposed as the best electrolyte among NaCl, $KHCO_3$, NH_4NO_3, $NaNO_3$, $NaNO_3 + HNO_3$, $NaNO_2$, Na_2SO_4, $MgCl_2$, $MgBr_2$, and $Mg(ClO_4)_2$ solutions. AZ21 Mg alloy shows superior anodic efficiency in the mixed $Mg(NO_3)_2/NaNO_2$ electrolyte. The calculation of anodic efficiency is based on the volume of anodic hydrogen evolution. This mixed electrolyte is also considered as a better electrolyte in comparison to 1.6 M $Mg(NO_3)_2$ and 14% NaCl because of the inhibition effect for hydrogen evolution reaction [181]. Nevertheless, in the work of Richey and co-authors [180], a delicate H-cell equipped with air pressure transducer and mass spectroscopy (Fig. 10a) was employed to investigate the dissolution behavior of Mg anode at OCV and during discharge in 0.5 M NaCl, $NaNO_3$, Na_2SO_4, HNa_2PO_4 and the mixed solution of 0.5 M NaCl/0.05M HNa_2PO_4. As shown in Fig. 10b, HNa_2PO_4 and $NaNO_3$, especially $NaNO_3$, as electrolytes significantly suppress the anodic hydrogen evolution, but another reduction reaction occurs in $NaNO_3$ solution,

$$NO_3^- + H_2O + 2e^- \rightarrow NO_2^- + 2OH^- \quad E_0 = 0.01\,V \tag{38}$$

After counting the efficiency loss caused by this reaction, $NaNO_3$ as electrolyte still improves the faradaic efficiency of Mg anode in comparison with that in NaCl solution. However, the passive film formed in $NaNO_3$ solution is detrimental to the anode discharge potential (-1.35 V vs Ag/AgCl), which also significantly deteriorates the anode potential in HNa_2PO_4 electrolyte (2.3 V vs Ag/AgCl). Mg anode exhibits the fastest anodic hydrogen evolution rate but the most negative discharge potential (-1.58 V vs Ag/AgCl) in NaCl solution. They proposed to adopt the mixed electrolyte (NaCl/HNa_2PO_4) to moderate the fast hydrogen evolution in blank NaCl solution. However, this strategy only works for hydrogen evolution reaction during OCV. Shrestha and co-authors [173] compared the discharge behavior of pure Mg and Mg-RE (rare earth) alloy in NaCl, Na_2SO_4, and $NaNO_3$ electrolytes. Being consistent with other research, chloride-free electrolytes are beneficial for high utilization efficiency via retarding self-corrosion of Mg-based anodes. However, the IR drop caused by the discharge product film formed in chloride-free electrolytes is tremendously huge, even leading to positive discharge potential (Fig. 10c). The work of Leong et al. [172] shows that MABs exhibits the highest peak power density in NaCl solution than that in $NaNO_3$ and Na_2SO_4 solutions (Fig. 10d).

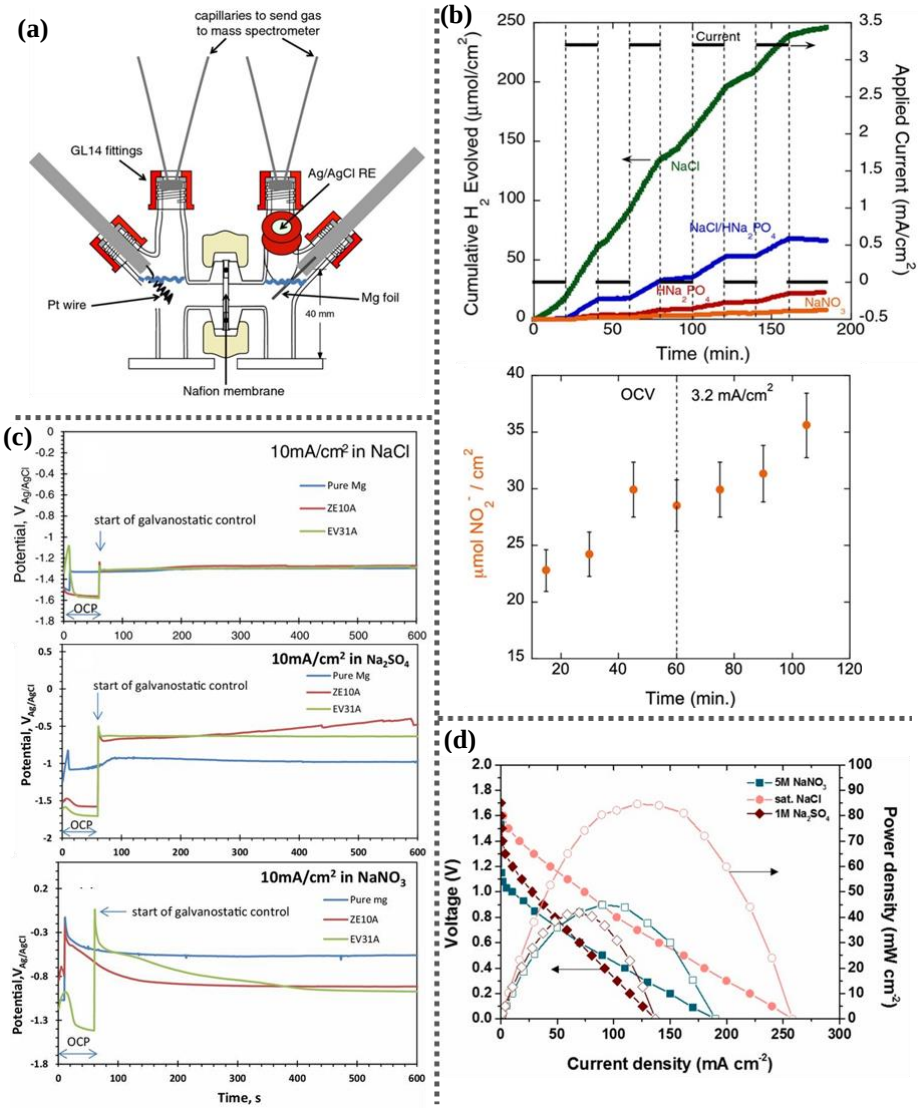

Fig. 10. (a) illustration of H-cell, (b) anodic hydrogen evolution of Mg anode in different salt solutions and NO_2^- titration results of Mg in $NaNO_3$ solution, reproduced with permission from Ref. 180; (c) discharge curves of pure Mg and Mg alloys in NaCl, Na_2SO_4, and $NaNO_3$ electrolytes, reproduced with permission from Ref. 173; (d) polarization curves and power density of MABs in NaCl, Na_2SO_4, and $NaNO_3$ electrolytes, reproduced with permission from Ref. 172.

5.2 Additives-containing electrolytes

Adding corrosion inhibitors as electrolyte additives is also an effective strategy to alleviate self-corrosion of Mg anode from electrolyte aspect. Low corrosion resistance is the key obstacle for Mg-based materials for their broad applications. Hence, a high amount of research has been done to screen efficient corrosion inhibitors for Mg-based materials via experimental studies and computing-assisted methods [183-186]. Diverse corrosion inhibitors have been investigated to reduce the efficiency loss of Mg anodes and to simultaneously maintain the negative discharge potential of Mg anodes in chloride-containing electrolytes.

5.2.1 Inorganic additives

Several inorganic corrosion inhibitors for Mg-based materials were employed and tested as electrolyte additives for aqueous MABs. 0.1 wt.% $LiCrO_4$ as an corrosion inhibitor added into 3.5 wt.% NaCl electrolyte improves the anodic efficiency of AZ31 anode during intermittent discharge tests [187]. The possible working mechanism for the inhibition effect is proposed to be the formation of passive $Cr(OH)_3/Cr_2O_3$ film on anode surface. However, species containing Cr (VI) is tremendously dangerous for human and other creatures. Thus, inhibitors containing Cr (VI) should be constrained in using and replaced by other environmentally benign inhibitors [188]. Cao and co-authors [189] proposed Ga_2O_3 as an electrolyte additive for Mg-Li-based anode materials. The addition of 0.05 mM Ga_2O_3 improves the discharging current and anodic efficiency of Mg-Li-based alloys. The possible mechanism for the improvement is that the Ga_2O_3 addition promotes the peel-off of oxidation products and inhibits parasitic reactions. In the work of Zhao et al. [190], $NaVO_3$ and Na_3PO_4 were selected from commercial available Mg corrosion inhibitors as electrolyte additives for MABs owing to their corrosion inhibition efficiency and capability of keeping the electrochemical activity of Mg alloys. The sole addition of $NaVO_3$ or Na_3PO_4 enhances the utilization efficiency of AZ31 anode. However, both of them induce negligible improvement of cell voltage, whilst the cell voltage in the intermittent discharge tests is even reduced. The working mechanism of Na_3PO_4 as electrolyte additives for AZ91-based [191] and AZ31-based [192] MABs is related to the much smaller solubility product constant of $Mg_3(PO_4)_2$ than $Mg(OH)_2$. The addition of Na_3PO_4 leads to the formation of phosphate-containing surface film and consequently reduces the corrosion rate of AZ-series Mg alloys under OCP. Nevertheless, the improvement for discharge performance of AZ-series Mg anode based MABs is limited. Moreover, the possibility of silicate as an electrolyte additive for MABs has been evaluated [193]. The XRD results reveal that silicate participates in the formation of discharge products film on AZ91 anode, which may hinder the prolongation of pitting corrosion and improve the anodic efficiency. Gore and co-authors [194] found the minor addition of $InCl_3$ alleviated the NDE effect of Mg in 0.1 M NaCl and suggested it can be used as an electrolyte additive for aqueous Mg batteries. Afterwards, Wang and co-authors [195] systematically evaluated $InCl_3$ with different concentrations as electrolyte additives for MABs. The strong hydrolysis reactions of In^{3+} shift the pH of 3.5 wt. % NaCl electrolyte to around 4. In the acidic $InCl_3$-containing electrolyte, the cell voltage of MAB is much better than that in blank NaCl solution as expected. However, something surprising is

that the utilization efficiency of the Mg-0.15Ca anode is also higher due to reduced self-corrosion and alleviated chunk effect.

Graphene is considered as potential materials for fuel cell and batteries owing to the superior conductivity and high specific area [196-198]. Meanwhile, the possibility of graphene as an electrolyte additive for aqueous MABs has also been reported [177]. The addition of water soluble graphene (WSG) into 3.5 wt. % NaCl solution shows the capability to extend the operating life of a MAB and increase the anode capacity to 1030.71 mAh g^{-1}. However, the discharge voltage of MAB in WSG-containing electrolyte is lower than that in NaCl electrolyte. Ma and co-authors [199] evaluated the addition of reduced graphene oxide as an electrolyte additive to improve the discharge performance of MABs based on Mg-6 wt. % Al-1 wt. % In anode [200] and Mg-6 wt. % Al-1 wt. % In- 1 wt. % Ce anode. The improvement induced by the addition of poly (sodium 4-styrenesulfonate)/reduced graphene oxide (PSS/RGO) for the cell voltage and anodic utilization of MABs with commercial air cathode is not significant, whilst the combination of PSS/RGO-containing electrolyte and RGO/Mn_3O_4-containing air cathode increase the anodic utilization of Mg-Al-In anode from 52 to 82%. However, the latter combination deteriorates the cell voltage from 0.952 to 0.878 V. Except for graphene, another quasi-two-dimensional material, MoS_2, were synthesized and used as electrolyte additives for MABs [201]. The OCV of MAB in nano MoS_2 powder-containing electrolyte reaches 1.61V, which is 130 mV higher than that in blank $MgCl_2$ electrolyte.

5.2.2 Organic additives

Owing to the adsorption effect, surfactants are always considered as one type of conventional corrosion inhibitors for Mg-based materials. In 2004, Oehr et al. reported the improvement of discharge performance of MABs via dithiobiuret, stannate, quaternary ammonium salt or the mixture of stannate with quaternary ammonium salt as electrolyte additives [202]. Recently, Deyab [203] investigated the feasibility of non-ionic surfactant, e.g. decyl glucoside (DG), indicating that 2.5 mM DG addition shows 94.2% inhibition effect for Mg corrosion at OCP and also improves the anode utilization efficiency during discharge. Sodium dodecylbenzenesulfonate [191, 192] has also been proposed as a potential electrolyte additive for MABs with the capability of adsorbing on Mg anode and thus enhancing the utilization efficiency. On the contrary, sodium alginate (SA), which is also able to adsorb on Mg surface and can serves as a corrosion inhibitor for AZ-series Mg alloy [204], leads to the reduction of utilization efficiency of AZ61 alloy in 0.6 M NaCl electrolyte [193]. Meanwhile, it introduces negative effect on the operating cell voltage of an AZ61-based MAB, which is attributed to the

formation of “coal cinder” SA-Mg composite film. The above mentioned works elucidate that the physical adsorption effect of organic additives is not always beneficial to the discharge performance of aqueous MABs. In some cases, the adsorption layer may lead to the increase of internal resistance and thus the decrease of cell voltage.

Recently, Höche and co-authors [160] revealed that the NDE effect of Mg-based materials greatly depends on the re-deposition of Fe, which is one of the most common impurities in Mg-based materials. Accordingly, Lamaka et al. [205] suggested to adopt Fe^{3+} complexing agents to suppress the hydrogen evolution reaction (HER) of Mg. Among the selected compounds, potassium cyanide and sodium salicylate (SAL) exhibits superior corrosion inhibition effect. Based on the observed HER inhibition effect of Fe^{3+} complexing agents on Mg, in their following work [206], they proposed to use organic complexants as electrolyte additives for aqueous MABs. As illustrated in Fig. 11a, this kind of organic additives possess strong complexing ability with Fe^{3+} ions and are simultaneously able to form soluble complexes with Mg^{2+} ions. Hence, they are capable of suppressing self-corrosion of Mg anodes and retarding the precipitation of discharge products. As shown in Fig. 11b, the cell voltages of MABs in the solutions containing strong Mg^{2+} complexing agents are significantly improved, such as that in nitrilotriacetic acid disodium salt (NTA)- or 4,5-dihydroxy-1,3-benzenedisulfonic acid disodium salt monohydrate (Tiron)-containing electrolytes. However, the addition of NTA and Trion leads to the decrease of utilization efficiency, especially at low current densities. Therefore, moderate Mg^{2+} complexing agents, such as SAL, are suggested. For strong Mg^{2+} complexing agents, Vaghefinazari et al. [207] concluded that the concentration is an important factor for their efficiency according to the study of the concentration effect of NTA and Trion on the discharge performance of 220 ppm Fe-containing pure Mg anode. The results manifests that diluted Trion (0.005 M) addition imparts not only more negative discharge potential but also the improvement of anodic efficiency in comparison with that in 0.5 wt. % NaCl electrolyte. The concept of adopting Fe^{3+} complexing agents to increase the anodic efficiency is proven to be more effective for pure Mg anode with a high Fe content (Fig. 11c) [208]. For Mg alloy anode with a low Fe content, Mg^{2+} complexing agents with different complexing abilities are also effective but the effectiveness is tightly dependent on the discharge load as demonstrated by the work of Wang et al. [209], in which citrate, SAL, 5-sulfoSAL, 2,6-, and 3,4-dihydroxybenzoate were tested as electrolyte additives for aqueous MABs under different current densities. As reported, Mg^{2+} complexing agents are able to improve the anodic efficiency by decreasing the occurrence of “chunk effect”. The highest specific energy of

aqueous MAB in that work, 3 kWh kg^{-1} (calculated based on the weight loss of Mg-Ca anode), is achieved by adding 0.1 M sodium citrate. The recent work of Wang and co-author [210] reported the self-corrosion inhibition effect of 2,6-DHB for Mg-Ca anode during discharge.

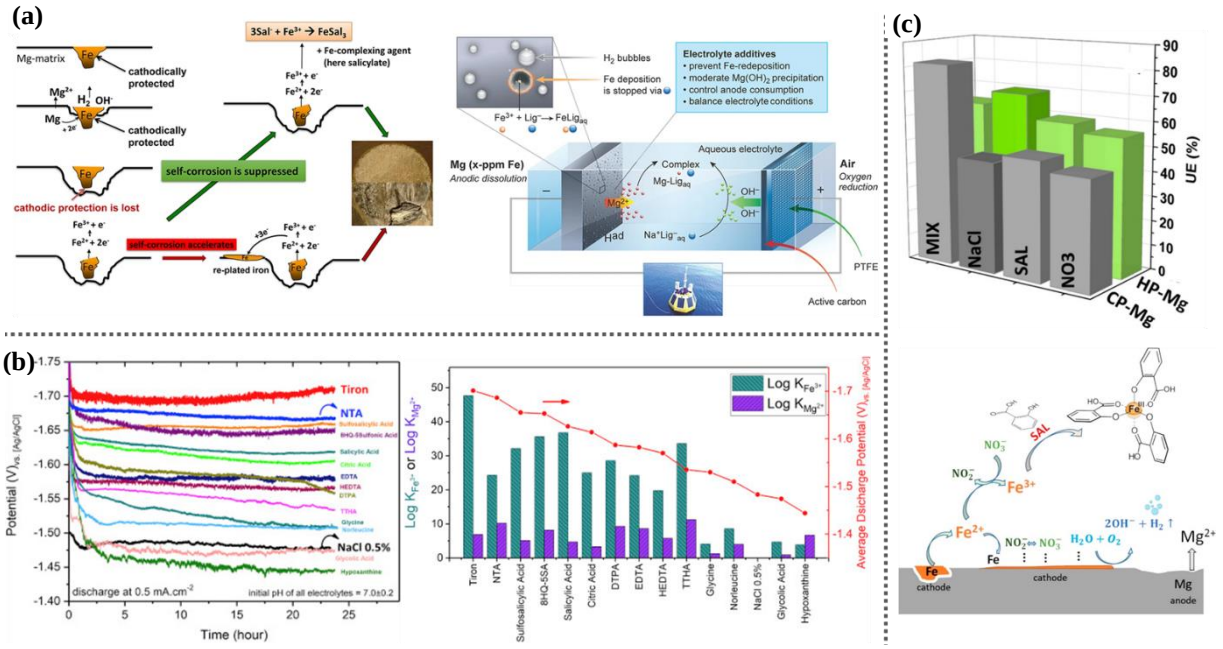

Fig. 11. (a) illustration of working mechanism of Fe^{3+} complexing reagents as electrolyte additives for MABs, reproduced with permission from Ref. 206; (b) discharge performance of CP-Mg in NaCl solution in presence and absence of Fe^{3+} and Mg^{2+} complexing reagents with variant stability constants (logK), reproduced with permission from Ref. 207; (c) utilization efficiency of pure Mg anodes in SAL-, NO_3-, SAL/NO_3-containing and blank NaCl electrolytes and possible working mechanism of hybrid SAL/NO_3 additives, reproduced with permission from Ref. 208.

5.2.3 Mixture of additives

Research regarding the application of hybrid additives in aqueous MABs is relatively rare. Li and Ma reported a series of works related to the influence of hybrid additives composed of surfactant and inorganic additive on the discharge performance of aqueous MABs [191-193]. The hybrid additives normally yield better performance than sole additive addition and the working mechanism is related to co-deposition of hybrid additives. Snihirova and co-authors [208] found the mixture of nitrate and SAL improved the utilization efficiency of commercial purity Mg (CP-Mg) from 45 % to 82 % via their synergistic effect. The possible mechanism of this synergistic effect is attributed to that the existence of nitrate promotes the oxidation of Fe^{2+} to Fe^{3+} and SAL as iron-complexing reagent is more sufficient to form complexes with Fe^{3+} rather than Fe^{2+} (Fig. 11c).

The significance of suitable electrolyte system for high performance aqueous MABs is being noticed recently. However, the investigation of electrolyte and electrolyte additive screening for aqueous MABs is still limited. Meanwhile, there are still several unclarified points concerning the discharge behavior of Mg and its alloys, including the NDE effect, chunk effect, etc., which also requires much effort. The adoption of Fe^{3+} complexing agents as electrolyte additive is a successful example for the strategical selection based on Mg intrinsic property. With a better understanding on the discharge mechanism of Mg, efficient selection of electrolyte systems and thus improvement for MABs could be expected.

6. Summary and perspective

As environmentally friendly and inherently safe energy storage systems, aqueous metal-air batteries evoke high attention during the last decade. However, common and special issues of aqueous metal-air batteries based on different anode materials (Fig. 2) retard their broad practical applications and thus more advances are urgently required. Suitable electrolytes and electrolyte additives are crucial to the accomplishment of excellent discharge performance for aqueous metal-air batteries. Nevertheless, the research on electrolyte and electrolyte additives for aqueous metal-air batteries has been downplayed and is less intensive in comparison with the development of anode and cathode materials. On the other hand, it reflects that there is still a lot of potential and room to be further explored from the aspect of electrolyte systems.

Aqueous ZABs, AABs and MABs possess same problems, e.g. self-dissolution, surface passivation and sluggish ORR reaction. In response to self-dissolution, the common solution is employing corrosion inhibitors as electrolyte additives. Many researchers have proposed the adoption of surfactants, organic acids, metal salts and oxides to alleviate the self-dissolution of anodes. The self-dissolution inhibition effect of surfactants is attributed to their adsorption effect. Computational approaches are proposed to study the mechanism behind the adsorption effect from additives. For instance, quantum chemistry calculation is applied to study the adsorption behavior and inhibition effect of EDTA, citric and acetic acid in combination with ZnO as electrolyte additives for AABs [93]. Thermodynamic descriptors are adopted to screen electrolyte components for ZABs [211]. Moreover, the possibility of efficiently screening potential corrosion inhibitors for Mg-based materials via machine learning modelling based on quantum chemistry calculation has been demonstrated [186, 212-214]. The combination of quantum chemical methods with machine learning-based quantitative structure property relationship (QSPR) methods has been used to predict the corrosion inhibition efficiency of

organic compounds, which enables the selection of potential corrosion inhibitors without deep understanding of the inhibition mechanism. This "*in silico*" screening method could be a powerful tool to efficiently screen and predict promising electrolyte additives for aqueous metal-air batteries. More importantly, the fundamental research is still needed. Strategical selection of electrolyte additives based on the intrinsic problems of metal-air battery is proven to be an efficient way. For instance, iron complexing agents as electrolyte additives boost the discharge performance of aqueous MABs, which is targeting at hindering the re-precipitation of iron impurities inside Mg anode and inhibiting the NDE effect of Mg anode. It is noteworthy that both AABs and MABs suffer from the NDE and chunk effect, which aqueous ZABs suffer from dendrite formation, electrode shape alteration. Hence, the fundamental research regarding these issues and the interfacial condition between electrodes and electrolyte must be further conducted.

Regarding the surface passivation during discharge, one of the solutions is to choose electrolyte with suitable pH. For amphoteric metallic anodes, like Zn and Al anodes, employing alkaline electrolytes is able to moderate the surface passivation, which however has exactly the opposite effect on Mg anode. Nevertheless, the electrolyte carbonation is a critical issue for alkaline ZABs and AABs. Even though several solutions have been proposed as aforementioned, the electrolyte carbonation happens inevitably and deteriorates the performance of both anode and cathode. For Mg anode, non-alkaline electrolyte is more favorable since the surface passivation in this case is less significant. Another possibility is to adopting Mg^{2+} complexing agent to hinder the formation of $Mg(OH)_2$. This method has been proven effective in literature [207-209]. The concept of adopting metal chelating agents may also work identically for ZABs and AABs. Successful strategies and brilliant ideas established for one specific system may also shed lights on other metal-air systems. For example, employing PEG and combining it with ZnO as hybrid electrolyte additives for AABs [95] is inspired by the application of PEG and its derivatives in ZABs batteries [71, 94]. Thus, the interaction between different metal-air batteries or even fuel cells in the future should be encouraged.

In terms of the sluggish ORR or OER reaction, the most effective method is to develop novel catalysts for both reactions. At the meantime, the investigation regarding the catalyst efficiency and the electrolyte environment might be an interesting topic for future work, since the existing catalysts are more efficient in alkaline electrolyte and show dependence on the electrolyte environment. Much efforts are needed to study the interaction between each component of

metal-air batteries and the battery design. Rational prototype design is decisive for the realistic discharge performance of aqueous metal-air batteries. Great advances on metal-air batteries have been achieved with emerging battery designs, such as dual- or tri-electrolyte systems [147, 172, 215], hybrid system to collect the parasitic reaction product hydrogen for fuel cell [216] and Al-air flow battery with oil displacement systems [7]. All in all, aqueous metal-air batteries are promising energy storage and conversion systems, which are worthy of more attentions for a more sustainable future.

References

[1] The sustainable development goals, https://www.un.org/sustainabledevelopment/development-agenda/.

[2] *United Nations Framework Convention on Climate Change* (UNFCCC, 1992).

[3] C.-F. Schleussner, J. Rogelj, M. Schaeffer, T. Lissner, R. Licker, E.M. Fischer, R. Knutti, A. Levermann, K. Frieler, W. Hare, Science and policy characteristics of the Paris Agreement temperature goal, Nature Climate Change, 6 (2016) 827-835.

[4] J. Cheng, D. Tong, Q. Zhang, Y. Liu, Y. Lei, G. Yan, L. Yan, S. Yu, R.Y. Cui, L. Clarke, G. Geng, B. Zheng, X. Zhang, S.J. Davis, K. He, Pathways of China's PM2.5 air quality 2015–2060 in the context of carbon neutrality, National Science Review, (2021).

[5] S. B. Sherman, Z. P. Cano, M. Fowler, Z. Chen, Range-extending Zinc-air battery for electric vehicle, AIMS Energy, 6 (2018) 121-145.

[6] A. Kindler, L. Matthies, High specific energy and specific power aluminum/air battery for micro air vehicles, in: Micro-and Nanotechnology Sensors, Systems, and Applications VI, International Society for Optics and Photonics, 2014, pp. 90831V.

[7] B.J. Hopkins, Y. Shao-Horn, D.P. Hart, Suppressing corrosion in primary aluminum–air batteries via oil displacement, Science, 362 (2018) 658-661.

[8] M. L, French patent 127,069, (1878).

[9] G.W. Heise, Air-depolarized primary battery, in, Google Patents, 1933.

[10] L. Öjefors, L. Carlsson, An iron-air vehicle battery, Journal of Power Sources, 2 (1978) 287-296.

[11] S. Zaromb, The use and behavior of aluminum anodes in alkaline primary batteries, Journal of the Electrochemical Society, 109 (1962) 1125.

[12] Y. Li, J. Lu, Metal–Air Batteries: Will They Be the Future Electrochemical Energy Storage Device of Choice?, ACS Energy Letters, 2 (2017) 1370-1377.

[13] K.F. Blurton, A.F. Sammells, Metal/air batteries: their status and potential—a review, Journal of Power Sources, 4 (1979) 263-279.

[14] Y. Takeshita, S. Fujimoto, M. Sudoh, Design of Rechargeable Air Diffusion Cathode for Metal-Air Battery Using Alkaline Solution, ECS Transactions, 50 (2013) 3.

[15] M.-J. Kim, J.E. Park, S. Kim, M.S. Lim, A. Jin, O.-H. Kim, M.J. Kim, K.-S. Lee, J. Kim, S.-S. Kim, Y.-H. Cho, Y.-E. Sung, Biomass-Derived Air Cathode Materials: Pore-Controlled S,N-Co-doped Carbon for Fuel Cells and Metal-Air Batteries, ACS Catalysis, 9 (2019) 3389-3398.

[16] J. Yu, B.Q. Li, C.X. Zhao, J.N. Liu, Q. Zhang, Asymmetric Air Cathode Design for Enhanced Interfacial Electrocatalytic Reactions in High-Performance Zinc-Air Batteries, Advanced Materials, 32 (2020) 1908488.

[17] W.J.W. Manalastas, S. Kumar, V. Verma, L. Zhang, D. Yuan, M. Srinivasan, Water in rechargeable multivalent-ion batteries: an electrochemical Pandora's box, ChemSusChem, (2018).

[18] S. Hosseini, S. Masoudi Soltani, Y.-Y. Li, Current status and technical challenges of electrolytes in zinc-air batteries: An in-depth review, Chemical Engineering Journal, 408 (2021) 127241.

[19] R. Mori, Recent Developments for Aluminum-Air Batteries, Electrochemical Energy Reviews, 3 (2020) 344-369.

[20] T. Zhang, Z. Tao, J. Chen, Magnesium-air batteries: from principle to application, Materials Horizons, 1 (2014) 196-206.

[21] X. Yu, A. Manthiram, A Voltage-Enhanced, Low-Cost Aqueous Iron-Air Battery Enabled with a Mediator-Ion Solid Electrolyte, ACS Energy Letters, 2 (2017) 1050-1055.

[22] C. Wang, Y. Yu, J. Niu, Y. Liu, D. Bridges, X. Liu, J. Pooran, Y. Zhang, A. Hu, Recent progress of metal-air batteries—a mini review, Applied Sciences, 9 (2019) 2787.

[23] Q. Liu, Z. Pan, E. Wang, L. An, G. Sun, Aqueous metal-air batteries: Fundamentals and applications, Energy Storage Materials, 27 (2020) 478-505.

[24] M. Deng, L. Wang, B. Vaghefinazari, W. Xu, C. Feiler, S.V. Lamaka, D. Höche, M.L. Zheludkevich, D. Snihirova, High-energy and durable aqueous magnesium batteries: recent advances and perspectives, Energy Storage Materials, (2021).

[25] M. Pourbaix, Atlas of electrochemical equilibria in aqueous solutions, National Association of Corrosion Engineers, Houston, Texas, 1974.

[26] F. Cheng, J. Chen, Metal-air batteries: from oxygen reduction electrochemistry to cathode catalysts, Chem Soc Rev, 41 (2012) 2172-2192.

[27] H. Wang, R. Tan, Z. Yang, Y. Feng, X. Duan, J. Ma, Stabilization Perspective on Metal Anodes for Aqueous Batteries, Advanced Energy Materials, 11 (2020) 2000962.

[28] J. Stamm, A. Varzi, A. Latz, B. Horstmann, Modeling nucleation and growth of zinc oxide during discharge of primary zinc-air batteries, Journal of Power Sources, 360 (2017) 136-149.

[29] J.F. Parker, E.S. Nelson, M.D. Wattendorf, C.N. Chervin, J.W. Long, D.R. Rolison, Retaining the 3D framework of zinc sponge anodes upon deep discharge in Zn-air cells, ACS Appl Mater Interfaces, 6 (2014) 19471-19476.

[30] H.-I. Kim, E.-J. Kim, S.-J. Kim, H.-C. Shin, Influence of ZnO precipitation on the cycling stability of rechargeable Zn-air batteries, Journal of Applied Electrochemistry, 45 (2015) 335-342.

[31] K. Popov, P. Zivkovic, N. Nikolic, Electrochemical aspects of formation of dendrites, Zastita materijala, 57 (2016) 55-62.

[32] L. Guo, H. Guo, H. Huang, S. Tao, Y. Cheng, Inhibition of zinc dendrites in zinc-based flow batteries, Frontiers in Chemistry, 8 (2020).

[33] J.-C. Riede, T. Turek, U. Kunz, Critical zinc ion concentration on the electrode surface determines dendritic zinc growth during charging a zinc air battery, Electrochimica Acta, 269 (2018) 217-224.

[34] M. Biton, F. Tariq, V. Yufit, Z. Chen, N. Brandon, Integrating multi-length scale high resolution 3D imaging and modelling in the characterisation and identification of mechanical failure sites in electrochemical dendrites, Acta Materialia, 141 (2017) 39-46.

[35] V. Yufit, F. Tariq, D.S. Eastwood, M. Biton, B. Wu, P.D. Lee, N.P. Brandon, Operando Visualization and Multi-scale Tomography Studies of Dendrite Formation and Dissolution in Zinc Batteries, Joule, 3 (2019) 485-502.

[36] J. Diggle, A. Despic, J.M. Bockris, The mechanism of the dendritic electrocrystallization of zinc, Journal of The Electrochemical Society, 116 (1969) 1503.

[37] W. Lu, C. Xie, H. Zhang, X. Li, Inhibition of Zinc Dendrite Growth in Zinc-Based Batteries, ChemSusChem, 11 (2018) 3996-4006.

[38] J. Cao, D. Zhang, X. Zhang, M. Sawangphruk, J. Qin, R. Liu, A universal and facile approach to suppress dendrite formation for a Zn and Li metal anode, Journal of Materials Chemistry A, 8 (2020) 9331-9344.

[39] A.R. Mainar, E. Iruin, L.C. Colmenares, A. Kvasha, I. de Meatza, M. Bengoechea, O. Leonet, I. Boyano, Z. Zhang, J.A. Blazquez, An overview of progress in electrolytes for secondary zinc-air batteries and other storage systems based on zinc, Journal of Energy Storage, 15 (2018) 304-328.

[40] A. R. Mainar, O. Leonet, M. Bengoechea, I. Boyano, I. de Meatza, A. Kvasha, A. Guerfi, J. Alberto Blázquez, Alkaline aqueous electrolytes for secondary zinc-air batteries: an overview, International Journal of Energy Research, 40 (2016) 1032-1049.

[41] F.R. McLarnon, E.J. Cairns, The secondary alkaline zinc electrode, Journal of the Electrochemical Society, 138 (1991) 645.

[42] Y. Li, H. Dai, Recent advances in zinc-air batteries, Chem Soc Rev, 43 (2014) 5257-5275.

[43] B. Hwang, E.-S. Oh, K. Kim, Observation of electrochemical reactions at Zn electrodes in Zn-air secondary batteries, Electrochimica Acta, 216 (2016) 484-489.

[44] J.F. Drillet, F. Holzer, T. Kallis, S. Müller, V.M. Schmidt, Influence of CO_2 on the stability of bifunctional oxygen electrodes for rechargeable zinc/air batteries and study of different CO_2 filter materials, Physical Chemistry Chemical Physics, 3 (2001) 368-371.

[45] H.-H. Cheng, C.-S. Tan, Reduction of CO_2 concentration in a zinc/air battery by absorption in a rotating packed bed, Journal of Power Sources, 162 (2006) 1431-1436.

[46] L. Kucka, E.Y. Kenig, A. Gorak, Kinetics of the gas-liquid reaction between carbon dioxide and hydroxide ions, Industrial & engineering chemistry research, 41 (2002) 5952-5957.

[47] D. Schröder, N.N. Sinai Borker, M. König, U. Krewer, Performance of zinc air batteries with added K_2CO_3 in the alkaline electrolyte, Journal of Applied Electrochemistry, 45 (2015) 427-437.

[48] P.K. Leung, C. Ponce-de-León, C.T.J. Low, F.C. Walsh, Zinc deposition and dissolution in methanesulfonic acid onto a carbon composite electrode as the negative electrode reactions in a hybrid redox flow battery, Electrochimica Acta, 56 (2011) 6536-6546.

[49] P.K. Leung, C. Ponce-de-León, F.J. Recio, P. Herrasti, F.C. Walsh, Corrosion of the zinc negative electrode of zinc-cerium hybrid redox flow batteries in methanesulfonic acid, Journal of Applied Electrochemistry, 44 (2014) 1025-1035.

[50] J. Jindra, J. Mrha, M. Musilová, Zinc-air cell with neutral electrolyte, Journal of Applied Electrochemistry, 3 (1973) 297-301.

[51] A. Velichenko, J. Portillo, M. Sarret, C. Muller, Zinc dissolution in ammonium chloride electrolytes, Journal of applied electrochemistry, 29 (1999) 1119-1123.

[52] S. Amendola, M. Binder, P.J. Black, S. Sharp-Goldman, L. Johnson, M. Kunz, M. Oster, T. Chciuk, R. Johnson, Electrically rechargeable, metal-air battery systems and methods, in, Google Patents, 2012.

[53] H. Cao, Z. Zhang, L. Wu, G. Zheng, A novel approach of preparing ZnO from ammoniacal leaching solution with high chlorine levels based on thermodynamic analysis, Hydrometallurgy, 171 (2017) 306-311.

[54] S. Zhao, H. An, S. Chen, A study of a high-power, ammonium chloride zinc/manganese dioxide dry battery, Journal of power sources, 76 (1998) 218-220.

[55] S. Clark, A. Latz, B. Horstmann, Rational development of neutral aqueous electrolytes for zinc-air batteries, ChemSusChem, 10 (2017) 4735.

[56] F.T. Goh, Z. Liu, T.A. Hor, J. Zhang, X. Ge, Y. Zong, A. Yu, W. Khoo, A near-neutral chloride electrolyte for electrically rechargeable zinc-air batteries, Journal of The Electrochemical Society, 161 (2014) A2080.

[57] A. Sumboja, X. Ge, G. Zheng, F.W.T. Goh, T.S.A. Hor, Y. Zong, Z. Liu, Durable rechargeable zinc-air batteries with neutral electrolyte and manganese oxide catalyst, Journal of Power Sources, 332 (2016) 330-336.

[58] H.H. Hassan, Perchlorate and oxygen reduction during Zn corrosion in a neutral medium, Electrochimica Acta, 51 (2006) 5966-5972.

[59] H. Yang, Improved discharge capacity and suppressed surface passivation of zinc anode in dilute alkaline solution using surfactant additives, Journal of Power Sources, 128 (2004) 97-101.

[60] R.K. Ghavami, Z. Rafiei, S.M. Tabatabaei, Effects of cationic CTAB and anionic SDBS surfactants on the performance of Zn–MnO_2 alkaline batteries, Journal of Power Sources, 164 (2007) 934-946.

[61] C.J. Lan, C.Y. Lee, T.S. Chin, Tetra-alkyl ammonium hydroxides as inhibitors of Zn dendrite in Zn-based secondary batteries, Electrochimica Acta, 52 (2007) 5407-5416.

[62] K.E. Sun, T.K. Hoang, T.N. Doan, Y. Yu, X. Zhu, Y. Tian, P. Chen, Suppression of Dendrite Formation and Corrosion on Zinc Anode of Secondary Aqueous Batteries, ACS Appl Mater Interfaces, 9 (2017) 9681-9687.

[63] J. Kan, H. Xue, S. Mu, Effect of inhibitors on Zn-dendrite formation for zinc-polyaniline secondary battery, Journal of Power Sources, 74 (1998) 113-116.

[64] J. Wang, L. Zhang, C. Zhang, J. Zhang, Effects of bismuth ion and tetrabutylammonium bromide on the dendritic growth of zinc in alkaline zincate solutions, Journal of power sources, 102 (2001) 139-143.

[65] Y.-h. Wen, J. Cheng, L. Zhang, X. Yan, Y.-s. Yang, The inhibition of the spongy electrocrystallization of zinc from doped flowing alkaline zincate solutions, Journal of Power Sources, 193 (2009) 890-894.

[66] H.-I. Kim, H.-C. Shin, SnO additive for dendritic growth suppression of electrolytic zinc, Journal of Alloys and Compounds, 645 (2015) 7-10.

[67] C.W. Lee, K. Sathiyanarayanan, S.W. Eom, H.S. Kim, M.S. Yun, Novel electrochemical behavior of zinc anodes in zinc/air batteries in the presence of additives, Journal of Power Sources, 159 (2006) 1474-1477.

[68] M.-C. Huang, S.-H. Huang, S.-C. Chiu, K.-L. Hsueh, W.-S. Chang, C.-C. Yang, C.-C. Wu, J.-C. Lin, Improved electrochemical performance of Zn-air secondary batteries via novel organic additives, Journal of the Chinese Chemical Society, 65 (2018) 1239-1244.

[69] S.J. Banik, R. Akolkar, Suppressing Dendritic Growth during Alkaline Zinc Electrodeposition using Polyethylenimine Additive, Electrochimica Acta, 179 (2015) 475-481.

[70] Y. Ein-Eli, M. Auinat, D. Starosvetsky, Electrochemical and surface studies of zinc in alkaline solutions containing organic corrosion inhibitors, Journal of power sources, 114 (2003) 330-337.

[71] T. Cohen-Hyams, Y. Ziengerman, Y. Ein-Eli, In situ STM studies of zinc in aqueous solutions containing PEG DiAcid inhibitor: Correlation with electrochemical performances of zinc-air fuel cells, Journal of Power Sources, 157 (2006) 584-591.

[72] M. Liang, H. Zhou, Q. Huang, S. Hu, W. Li, Synergistic effect of polyethylene glycol 600 and polysorbate 20 on corrosion inhibition of zinc anode in alkaline batteries, Journal of Applied Electrochemistry, 41 (2011) 991-997.

[73] N. Diomidis, J.-P. Celis, Anodic film formation on zinc in alkaline electrolytes containing silicate and tetraborate ions, Journal of The Electrochemical Society, 154 (2007) C711.

[74] S. Yang, H. Knickle, Design and analysis of aluminum/air battery system for electric vehicles, Journal of power sources, 112 (2002) 162-173.

[75] Q. Li, N.J. Bjerrum, Aluminum as anode for energy storage and conversion: a review, Journal of power sources, 110 (2002) 1-10.

[76] A. Despić, D. Dražić, M. Purenović, N. Ciković, Electrochemical properties of aluminium alloys containing indium, gallium and thallium, Journal of Applied Electrochemistry, 6 (1976) 527-542.

[77] E. McCafferty, Sequence of steps in the pitting of aluminum by chloride ions, Corrosion Science, 45 (2003) 1421-1438.

[78] D. Mercier, M.G. Barthés-Labrousse, The role of chelating agents on the corrosion mechanisms of aluminium in alkaline aqueous solutions, Corrosion Science, 51 (2009) 339-348.

[79] D. Linden, T.B. Reddy, Handbook of Batteries, McGraw-Hill, New York, 2002.

[80] V. Kapali, S.V. Iyer, V. Balaramachandran, K. Sarangapani, M. Ganesan, M.A. Kulandainathan, A.S. Mideen, Studies on the best alkaline electrolyte for aluminium/air batteries, Journal of power sources, 39 (1992) 263-269.

[81] C. Zhang, Z. Cai, R. Wang, P. Yu, H. Liu, Z. Wang, Enhancing the Electrochemical Performance of Al-Mg-Sn-Ga Alloy Anode for Al-Air Battery by Solution Treatment, Journal of The Electrochemical Society, 168 (2021) 030519.

[82] P. Zhang, X. Liu, J. Xue, K. Jiang, The role of microstructural evolution in improving energy conversion of Al-based anodes for metal-air batteries, Journal of Power Sources, 451 (2020) 227806.

[83] L. Fan, H. Lu, J. Leng, Performance of fine structured aluminum anodes in neutral and alkaline electrolytes for Al-air batteries, Electrochimica Acta, 165 (2015) 22-28.

[84] M. Doche, F. Novel-Cattin, R. Durand, J. Rameau, Characterization of different grades of aluminum anodes for aluminum/air batteries, Journal of Power Sources, 65 (1997) 197-205.

[85] Y. Nie, J. Gao, E. Wang, L. Jiang, L. An, X. Wang, An effective hybrid organic/inorganic inhibitor for alkaline aluminum-air fuel cells, Electrochimica Acta, 248 (2017) 478-485.

[86] S. Wu, Q. Zhang, D. Sun, J. Luan, H. Shi, S. Hu, Y. Tang, H. Wang, Understanding the synergistic effect of alkyl polyglucoside and potassium stannate as advanced hybrid corrosion inhibitor for alkaline aluminum-air battery, Chemical Engineering Journal, 383 (2020) 123162.

[87] M. Paramasivam, G. Suresh, B. Muthuramalingam, S.V. Iyer, V. Kapali, Different commercial grades of aluminium as galvanic anodes in alkaline zincate solutions, Journal of applied electrochemistry, 21 (1991) 452-456.

[88] Z. Sun, H. Lu, Performance of Al-0.5In As Anode for Al-Air Battery in Inhibited Alkaline Solutions, Journal of the Electrochemical Society, 162 (2015) A1617.

[89] X. Wang, J. Wang, H. Shao, J. Zhang, C. Cao, Influences of zinc oxide and an organic additive on the electrochemical behavior of pure aluminum in an alkaline solution, Journal of applied electrochemistry, 35 (2005) 213-216.

[90] A. Elango, V. Periasamy, M. Paramasivam, Study on polyaniline-ZnO used as corrosion inhibitors of 57S aluminium in 2 M NaOH solution, Anti-Corrosion Methods and Materials, (2009).

[91] J. Liu, D. Wang, D. Zhang, L. Gao, T. Lin, Synergistic effects of carboxymethyl cellulose and ZnO as alkaline electrolyte additives for aluminium anodes with a view towards Al-air batteries, Journal of Power Sources, 335 (2016) 1-11.

[92] C. Zhu, H. Yang, A. Wu, D. Zhang, L. Gao, T. Lin, Modified alkaline electrolyte with 8-hydroxyquinoline and ZnO complex additives to improve Al-air battery, Journal of Power Sources, 432 (2019) 55-64.

[93] H. Jiang, S. Yu, W. Li, Y. Yang, L. Yang, Z. Zhang, Inhibition effect and mechanism of inorganic-organic hybrid additives on three-dimension porous aluminum foam in alkaline Al-air battery, Journal of Power Sources, 448 (2020) 227460.

[94] M. Auinat, Y. Ein-Eli, Enhanced inhibition of zinc corrosion in alkaline solutions containing carboxylic acid modified PEG, Journal of the Electrochemical Society, 152 (2005) A1158.

[95] X.Y. Wang, J.M. Wang, Q.L. Wang, H.B. Shao, J.Q. Zhang, The effects of polyethylene glycol (PEG) as an electrolyte additive on the corrosion behavior and electrochemical performances of pure aluminum in an alkaline zincate solution, Materials and Corrosion, 62 (2011) 1149-1152.

[96] D. Gelman, I. Lasman, S. Elfimchev, D. Starosvetsky, Y. Ein-Eli, Aluminum corrosion mitigation in alkaline electrolytes containing hybrid inorganic/organic inhibitor system for power sources applications, Journal of Power Sources, 285 (2015) 100-108.

[97] I.L. Rozenfeld, Corrosion Inhibitors, McGraw Hill, New York, 1981.

[98] E. Oguzie, G. Onuoha, A. Onuchukwu, The inhibition of aluminium corrosion in potassium hydroxide by “Congo Red” dye, and synergistic action with halide ions, Anti-Corrosion Methods and Materials, (2005).

[99] S.A. Umoren, E.E. Ebenso, O. Ogbobe, Synergistic effect of halide ions and polyethylene glycol on the corrosion inhibition of aluminium in alkaline medium, Journal of Applied Polymer Science, 113 (2009) 3533-3543.

[100] I.J. Albert, M.A. Kulandainathan, M. Ganesan, V. Kapali, Characterisation of different grades of commercially pure aluminium as prospective galvanic anodes in saline and alkaline battery electrolyte, Journal of applied electrochemistry, 19 (1989) 547-551.

[101] H. Shao, J. Wang, Z. Zhang, J. Zhang, C. Cao, The cooperative effect of calcium ions and tartrate ions on the corrosion inhibition of pure aluminum in an alkaline solution, Materials Chemistry and Physics, 77 (2003) 305-309.

[102] Q.X. Kang, Y. Wang, X.Y. Zhang, Experimental and theoretical investigation on calcium oxide and L-aspartic as an effective hybrid inhibitor for aluminum-air batteries, Journal of Alloys and Compounds, 774 (2019) 1069-1080.

[103] D. Wang, H. Li, J. Liu, D. Zhang, L. Gao, L. Tong, Evaluation of AA5052 alloy anode in alkaline electrolyte with organic rare-earth complex additives for aluminium-air batteries, Journal of Power Sources, 293 (2015) 484-491.

[104] Q.X. Kang, T.Y. Zhang, X. Wang, Y. Wang, X.Y. Zhang, Effect of cerium acetate and L-glutamic acid as hybrid electrolyte additives on the performance of Al-air battery, Journal of Power Sources, 443 (2019) 227251.

[105] Y. Liu, H. Zhang, Y. Liu, J. Li, W. Li, Inhibitive effect of quaternary ammonium-type surfactants on the self-corrosion of the anode in alkaline aluminium-air battery, Journal of Power Sources, 434 (2019) 226723.

[106] M.A. Deyab, Effect of nonionic surfactant as an electrolyte additive on the performance of aluminum-air battery, Journal of Power Sources, 412 (2019) 520-526.

[107] J. Wysocka, M. Cieslik, S. Krakowiak, J. Ryl, Carboxylic acids as efficient corrosion inhibitors of aluminium alloys in alkaline media, Electrochimica Acta, 289 (2018) 175-192.

[108] C.-H. Wu, C.-C. Chung, K.-L. Hsueh, W.-C. Chang, Inhibiting Ability of Chelating Agent on Aluminum Corrosion in Alkaline Solution, ECS Transactions, 50 (2013) 23.

[109] Z. Moghadam, M. Shabani-Nooshabadi, M. Behpour, Electrochemical performance of aluminium alloy in strong alkaline media by urea and thiourea as inhibitor for aluminium-air batteries, Journal of Molecular Liquids, 242 (2017) 971-978.

[110] C. Hou, S. Chen, Z. Wang, G. Wang, G. Dong, Effect of 6-thioguanine, as an electrolyte additive, on the electrochemical behavior of an Al-air battery, Materials and Corrosion, 71 (2020) 1480-1487.

[111] J.-B. Wang, J.-M. Wang, H.-B. Shao, J.-Q. Zhang, C.-N. Cao, The corrosion and electrochemical behaviour of pure aluminium in alkaline methanol solutions, Journal of Applied Electrochemistry, 37 (2007) 753-758.

[112] X.X. Zeng, J.M. Wang, Q.L. Wang, D.S. Kong, H.B. Shao, J.Q. Zhang, C.N. Cao, The effects of surface treatment and stannate as an electrolyte additive on the corrosion and electrochemical performances of pure aluminum in an alkaline methanol-water solution, Materials Chemistry and Physics, 121 (2010) 459-464.

[113] X. Chang, J. Wang, H. Shao, J. Wang, X. Zeng, J. Zhang, C. Cao, Corrosion and Anodic Behaviors of Pure Aluminum in a Novel Alkaline Electrolyte, Acta Physico-Chimica Sinica, 24 (2008) 1620-1624.

[114] M. Jingling, W. Jiuba, Z. Hongxi, L. Quanan, Electrochemical performances of Al–0.5Mg–0.1Sn–0.02In alloy in different solutions for Al-air battery, Journal of Power Sources, 293 (2015) 592-598.

[115] J.M. Wang, J.B. Wang, H.B. Shao, X.X. Zeng, J.Q. Zhang, C.N. Cao, Corrosion and electrochemical behaviors of pure aluminum in novel KOH-ionic liquid-water solutions, Materials and Corrosion, 60 (2009) 977-981.

[116] M.A. Deyab, 1-Allyl-3-methylimidazolium bis(trifluoromethylsulfonyl)imide as an effective organic additive in aluminum-air battery, Electrochimica Acta, 244 (2017) 178-183.

[117] M.D. Koninck, P. Manseau, B. Marsan, Preparation and characterization of Nb-doped TiO_2 nanoparticles used as a conductive support for bifunctional $CuCo_2O_4$ electrocatalyst, Journal of Electroanalytical Chemistry, 611 (2007) 67-79.

[118] M. Nestoridi, D. Pletcher, J.A. Wharton, R.J.K. Wood, Further studies of the anodic dissolution in sodium chloride electrolyte of aluminium alloys containing tin and gallium, Journal of Power Sources, 193 (2009) 895-898.

[119] D. Chu, R.F. Savinell, Experimental data on aluminum dissolution in KOH electrolytes, Electrochimica acta, 36 (1991) 1631-1638.

[120] W. Wilhelmsen, T. Arnesen, Ø. Hasvold, N. Størkersen, The electrochemical behaviour of Al-In alloys in alkaline electrolytes, Electrochimica acta, 36 (1991) 79-85.

[121] A.V. Ilyukhina, A.Z. Zhuk, B.V. Kleymenov, A.S. Ilyukhin, M. Nagayama, The Influence of Temperature and Composition on the Operation of Al Anodes for Aluminum-Air Batteries, Fuel Cells, 16 (2016) 384-394.

[122] Z. Wu, H. Zhang, C. Guo, J. Zou, K. Qin, C. Ban, H. Nagaumi, Effects of indium, gallium, or bismuth additions on the discharge behavior of Al-Mg-Sn-based alloy for Al-air battery anodes in NaOH electrolytes, Journal of Solid State Electrochemistry, 23 (2019) 2483-2491.

[123] J. Ma, J. Wen, Q. Li, Q. Zhang, Effects of acidity and alkalinity on corrosion behaviour of Al–Zn–Mg based anode alloy, Journal of Power Sources, 226 (2013) 156-161.

[124] J. Ma, J. Wen, Q. Li, Q. Zhang, Electrochemical polarization and corrosion behavior of Al–Zn–In based alloy in acidity and alkalinity solutions, International Journal of Hydrogen Energy, 38 (2013) 14896-14902.

[125] M. Akmal, R. Othman, M.H. Ani, Comparative electrochemical performance characteristics of aluminium-air cell employing seawater and NaCl electrolytes, in: Advanced Materials Research, Trans Tech Publ, 2013, pp. 314-318.

[126] A. Mance, D. Cerović, A. Mihajlović, The effect of small additions of indium and thallium on the corrosion behaviour of aluminium in sea water, Journal of applied electrochemistry, 14 (1984) 459-466.

[127] M. Nestoridi, D. Pletcher, R.J.K. Wood, S. Wang, R.L. Jones, K.R. Stokes, I. Wilcock, The study of aluminium anodes for high power density Al/air batteries with brine electrolytes, Journal of Power Sources, 178 (2008) 445-455.

[128] I. Smoljko, S. Gudić, N. Kuzmanić, M. Kliškić, Electrochemical properties of aluminium anodes for Al/air batteries with aqueous sodium chloride electrolyte, Journal of Applied Electrochemistry, 42 (2012) 969-977.

[129] H. El Shayeb, F. Abd El Wahab, S.Z. El Abedin, Electrochemical behaviour of Al, Al–Sn, Al–Zn and Al–Zn–Sn alloys in chloride solutions containing indium ions, Journal of applied electrochemistry, 29 (1999) 473-480.

[130] H. El Shayeb, F. Abd El Wahab, S.Z. El Abedin, Role of indium ions on the activation of aluminium, Journal of applied electrochemistry, 29 (1999) 601-609.

[131] S.Z. El Abedin, F. Endres, Electrochemical Behaviour of Al, Al–In and Al–Ga–In Alloys in Chloride Solutions Containing Zinc Ions, Journal of applied electrochemistry, 34 (2004) 1071-1080.

[132] H. El Shayeb, F. Abd El Wahab, S.Z. El Abedin, Effect of gallium ions on the electrochemical behaviour of Al, Al–Sn, Al–Zn and Al–Zn–Sn alloys in chloride solutions, Corrosion Science, 43 (2001) 643-654.

[133] H. El Shayeb, F. Abd El Wahab, S.Z. El Abedin, Electrochemical behaviour of Al, Al–Sn, Al–Zn and Al–Zn–Sn alloys in chloride solutions containing stannous ions, Corrosion science, 43 (2001) 655-669.

[134] Y. Tang, L. Lu, H.W. Roesky, L. Wang, B. Huang, The effect of zinc on the aluminum anode of the aluminum–air battery, Journal of Power Sources, 138 (2004) 313-318.

[135] W. Carroll, C. Breslin, Stability of passive films formed on aluminium in aqueous halide solutions, British Corrosion Journal, 26 (1991) 255-259.

[136] M. Rota, C. Comninellis, S. Moller, F. Holzer, O. Haas, Bipolar Al/O_2 battery with planar electrodes in alkaline and acidic electrolytes, Journal of applied electrochemistry, 25 (1995) 114-121.

[137] S. Müller, F. Holzer, J. Desilvestro, O. Haas, Aluminium alloys in sulfuric acid Part II: Aluminium-oxygen cells, Journal of applied electrochemistry, 26 (1996) 1217-1223.

[138] D.O. Flamini, S.B. Saidman, Electrochemical behaviour of Al–Zn–Ga and Al–In–Ga alloys in chloride media, Materials Chemistry and Physics, 136 (2012) 103-111.

[139] G. Burri, W. Luedi, O. Haas, Electrochemical Properties of Aluminum in Weakly Acidic Sodium Chloride Solutions: Part I. Influence of the Electrolyte Additives In^{3+} and Zn^{2+}, Journal of the Electrochemical Society, 136 (1989) 2167.

[140] J.F. Equey, S. Müller, J. Desilvestro, O. Haas, Electrochemical properties of aluminum in weakly acidic sodium chloride solutions: II. Influence of the electrolyte additives Hg^{2+}, In^{3+}, Ga^{3+}, and Sn^{2+}, Journal of The Electrochemical Society, 139 (1992) 1499.

[141] S. Saidman, J. Bessone, Activation of aluminium by indium ions in chloride solutions, Electrochimica acta, 42 (1997) 413-420.

[142] F. Holzer, S. Müller, J. Desilvestro, O. Haas, Aluminium alloys in sulphuric acid Part I: Electrochemical behaviour of rotating and stationary disc electrodes, Journal of applied electrochemistry, 23 (1993) 125-134.

[143] M. Mokhtar, M.Z.M. Talib, E.H. Majlan, S.M. Tasirin, W.M.F.W. Ramli, W.R.W. Daud, J. Sahari, Recent developments in materials for aluminum-air batteries: A review, Journal of Industrial and Engineering Chemistry, 32 (2015) 1-20.

[144] B. Chen, D.Y.C. Leung, J. Xuan, H. Wang, A mixed-pH dual-electrolyte microfluidic aluminum-air cell with high performance, Applied Energy, 185 (2017) 1303-1308.

[145] S. Feng, G. Yang, D. Zheng, L. Wang, W. Wang, Z. Wu, F. Liu, A dual-electrolyte aluminum/air microfluidic cell with enhanced voltage, power density and electrolyte utilization via a novel composite membrane, Journal of Power Sources, 478 (2020) 228960.

[146] L. Wang, F. Liu, W. Wang, G. Yang, D. Zheng, Z. Wu, M.K.H. Leung, A high-capacity dual-electrolyte aluminum/air electrochemical cell, RSC Adv., 4 (2014) 30857-30863.

[147] L. Wang, R. Cheng, C. Liu, M.C. Ma, W. Wang, G. Yang, M.K.H. Leung, F. Liu, S.P. Feng, Trielectrolyte aluminum-air cell with high stability and voltage beyond 2.2 V, Materials Today Physics, 14 (2020) 100242.

[148] M. Frei, J. Martin, S. Kindler, G. Cristiano, R. Zengerle, S. Kerzenmacher, Power supply for electronic contact lenses: Abiotic glucose fuel cells vs. Mg/air batteries, Journal of Power Sources, 401 (2018) 403-414.

[149] B. Winther-Jensen, M. Gaadingwe, D.R. Macfarlane, M. Forsyth, Control of magnesium interfacial reactions in aqueous electrolytes towards a biocompatible battery, Electrochimica Acta, 53 (2008) 5881-5884.

[150] O. Hasvold, A magnesium-seawater power source for autonomous underwater vehicles, Power Sources, 14 (1993) 243-243.

[151] Ø. Hasvold, T. Lian, E. Haakaas, N. Størkersen, O. Perelman, S. Cordier, CLIPPER: a long-range, autonomous underwater vehicle using magnesium fuel and oxygen from the sea, Journal of Power Sources, 136 (2004) 232-239.

[152] G.L. Song, A. Atrens, Corrosion mechanisms of magnesium alloys, Advanced engineering materials, 1 (1999) 11-33.

[153] M. Esmaily, J.E. Svensson, S. Fajardo, N. Birbilis, G.S. Frankel, S. Virtanen, R. Arrabal, S. Thomas, L.G. Johansson, Fundamentals and advances in magnesium alloy corrosion, Progress in Materials Science, 89 (2017) 92-193.

[154] J. Huang, G.-L. Song, A. Atrens, M. Dargusch, What activates the Mg surface—A comparison of Mg dissolution mechanisms, Journal of Materials Science & Technology, 57 (2020) 204-220.

[155] Z. Shi, F. Cao, G.-L. Song, A. Atrens, Low apparent valence of Mg during corrosion, Corrosion Science, 88 (2014) 434-443.

[156] A. Atrens, W. Dietzel, The Negative Difference Effect and Unipositive Mg^{+}, Advanced Engineering Materials, 9 (2007) 292-297.

[157] G. Song, Recent Progress in Corrosion and Protection of Magnesium Alloys, Advanced Engineering Materials, 7 (2005) 563-586.

[158] G.S. Frankel, A. Samaniego, N. Birbilis, Evolution of hydrogen at dissolving magnesium surfaces, Corrosion Science, 70 (2013) 104-111.

[159] M. Taheri, J.R. Kish, N. Birbilis, M. Danaie, E.A. McNally, J.R. McDermid, Towards a Physical Description for the Origin of Enhanced Catalytic Activity of Corroding Magnesium Surfaces, Electrochimica Acta, 116 (2014) 396-403.

[160] D. Höche, C. Blawert, S.V. Lamaka, N. Scharnagl, C. Mendis, M.L. Zheludkevich, The effect of iron re-deposition on the corrosion of impurity-containing magnesium, Physical Chemistry Chemical Physics, 18 (2016) 1279-1291.

[161] G. Song, A. Atrens, D. Stjohn, J. Nairn, Y. Li, The electrochemical corrosion of pure magnesium in 1 N NaCl, Corrosion Science, 39 (1997) 855-875.

[162] J. Chen, J. Dong, J. Wang, E. Han, W. Ke, Effect of magnesium hydride on the corrosion behavior of an AZ91 magnesium alloy in sodium chloride solution, Corrosion Science, 50 (2008) 3610-3614.

[163] W.D. Mueller, H. Hornberger, The influence of MgH2 on the assessment of electrochemical data to predict the degradation rate of Mg and Mg alloys, Int J Mol Sci, 15 (2014) 11456-11472.

[164] M. Deng, L. Wang, D. Höche, S.V. Lamaka, D. Snihirova, B. Vaghefinazari, M.L. Zheludkevich, Clarifying the decisive factors for utilization efficiency of Mg anodes for primary aqueous batteries, Journal of Power Sources, 441 (2019) 227201.

[165] L. Wang, R. Wang, Y. Feng, M. Deng, N. Wang, Effect of Heat Treatment on Electrochemical Properties of Mg–9 wt.%Al–2.5 wt.%Pb Alloy in Sodium Chloride Solution, Jom, 69 (2017) 2467-2470.

[166] X. Liu, J. Xue, D. Zhang, Electrochemical behaviors and discharge performance of the as-extruded Mg-1.5 wt%Ca alloys as anode for Mg-air battery, Journal of Alloys and Compounds, 790 (2019) 822-828.

[167] J. Li, B. Zhang, Q. Wei, N. Wang, B. Hou, Electrochemical behavior of Mg-Al-Zn-In alloy as anode materials in 3.5 wt.% NaCl solution, Electrochimica Acta, 238 (2017) 156-167.

[168] M. Deng, D. Höche, D. Snihirova, L. Wang, B. Vaghefinazari, S.V. Lamaka, M.L. Zheludkevich, Aqueous Mg Batteries, in: Magnesium Batteries, 2019, pp. 275-308.

[169] X. Chen, X. Liu, Q. Le, M. Zhang, M. Liu, A. Atrens, A comprehensive review of the development of magnesium anodes for primary batteries, Journal of Materials Chemistry A, 9 (2021) 12367-12399.

[170] C.-S. Li, Y. Sun, F. Gebert, S.-L. Chou, Current Progress on Rechargeable Magnesium-Air Battery, Advanced Energy Materials, 7 (2017) 1700869.

[171] M. Pourbaix, A.d.E. Electrochimiques, Gauthier-Villars, Editeur-Imprimeur-Libraire, Paris, (1963) 256-271.

[172] K.W. Leong, Y. Wang, W. Pan, S. Luo, X. Zhao, D.Y.C. Leung, Doubling the power output of a Mg-air battery with an acid-salt dual-electrolyte configuration, Journal of Power Sources, 506 (2021) 230144.

[173] N. Shrestha, K. Raja, V. Utgikar, Mg-RE alloy anode materials for Mg-air battery application, Journal of the Electrochemical Society, 166 (2019) A3139.

[174] Y. Feng, W. Xiong, J. Zhang, R. Wang, N. Wang, Electrochemical discharge performance of the Mg–Al–Pb–Ce–Y alloy as the anode for Mg–air batteries, Journal of Materials Chemistry A, 4 (2016) 8658-8668.

[175] M. Deng, D. Höche, S.V. Lamaka, D. Snihirova, M.L. Zheludkevich, Mg-Ca binary alloys as anodes for primary Mg-air batteries, Journal of Power Sources, 396 (2018) 109-118.

[176] M. Deng, L. Wang, D. Höche, S.V. Lamaka, P. Jiang, D. Snihirova, N. Scharnagl, M.L. Zheludkevich, Ca/In micro alloying as a novel strategy to simultaneously enhance power and energy density of primary Mg-air batteries from anode aspect, Journal of Power Sources, 472 (2020) 228528.

[177] M. Mayilvel Dinesh, K. Saminathan, M. Selvam, S.R. Srither, V. Rajendran, K.V.I.S. Kaler, Water soluble graphene as electrolyte additive in magnesium-air battery system, Journal of Power Sources, 276 (2015) 32-38.

[178] R. Hamlen, E. Jerabek, J. Ruzzo, E. Siwek, Anodes for Refuelable Magnesium-Air Batteries, Journal of the Electrochemical Society, 116 (1969) 1588.

[179] M.-C. Zhao, M. Liu, G.-L. Song, A. Atrens, Influence of pH and chloride ion concentration on the corrosion of Mg alloy ZE41, Corrosion Science, 50 (2008) 3168-3178.

[180] F.W. Richey, B.D. McCloskey, A.C. Luntz, Mg anode corrosion in aqueous electrolytes and implications for Mg-Air batteries, Journal of the Electrochemical Society, 163 (2016) A958.

[181] W. Li, C. Li, C. Zhou, H. Ma, J. Chen, Metallic magnesium nano/mesoscale structures: their shape-controlled preparation and mg/air battery applications, Angew Chem Int Ed Engl, 45 (2006) 6009-6012.

[182] S. Sathyanarayana, N. Munichandraiah, A new magnesium-air cell for long-life applications, Journal of Applied Electrochemistry, 11 (1981) 33-39.

[183] S.V. Lamaka, B. Vaghefinazari, D. Mei, R.P. Petrauskas, D. Höche, M.L. Zheludkevich, Comprehensive screening of Mg corrosion inhibitors, Corrosion Science, 128 (2017) 224-240.

[184] N. Dinodi, A.N. Shetty, Alkyl carboxylates as efficient and green inhibitors of magnesium alloy ZE41 corrosion in aqueous salt solution, Corrosion Science, 85 (2014) 411-427.

[185] L. Hou, N. Dang, H. Yang, B. Liu, Y. Li, Y. Wei, X.-B. Chen, A combined inhibiting effect of sodium alginate and sodium phosphate on the corrosion of magnesium alloy AZ31 in NaCl solution, Journal of The Electrochemical Society, 163 (2016) C486.

[186] C. Feiler, D. Mei, B. Vaghefinazari, T. Würger, R.H. Meißner, B.J.C. Luthringer-Feyerabend, D.A. Winkler, M.L. Zheludkevich, S.V. Lamaka, In silico screening of modulators of magnesium dissolution, Corrosion Science, (2019) 108245.

[187] Y.-C. Zhao, G.-S. Huang, G.-l. Gong, T.-Z. Han, D.-B. Xia, F.-S. Pan, Improving the Intermittent Discharge Performance of Mg-Air Battery by Using Oxyanion Corrosion Inhibitor as Electrolyte Additive, Acta Metallurgica Sinica (English Letters), 29 (2016) 1019-1024.

[188] The Registration, Evaluation and Authorization of Chemicals ("REACH") (EU Regulation 1907/2006), https://jonesdayreach.com/substances/.

[189] D. Cao, L. Wu, Y. Sun, G. Wang, Y. Lv, Electrochemical behavior of Mg–Li, Mg–Li–Al and Mg–Li–Al–Ce in sodium chloride solution, Journal of Power Sources, 177 (2008) 624-630.

[190] Y. Zhao, G. Huang, C. Zhang, C. Peng, F. Pan, Effect of phosphate and vanadate as electrolyte additives on the performance of Mg-air batteries, Mater. Chem. Phys., 218 (2018) 256-261.

[191] Y. Li, J. Ma, G. Wang, F. Ren, Y. Zhu, Y. Song, Investigation of sodium phosphate and sodium dodecylbenzenesulfonate as electrolyte additives for AZ91 magnesium-air battery, Journal of the Electrochemical Society, 165 (2018) A1713.

[192] Y. Li, J. MA, G. WANG, Y. ZHU, Y. SONG, Effect of Sodium Phosphate and Sodium Dodecylbenzene-sulfonate on Discharge Performance of AZ31 Magnesium Air Battery, Journal of Chinese Society for Corrosion and protection, 38 (2019) 587-593.

[193] J. Ma, G. Wang, Y. Li, W. Li, F. Ren, Influence of Sodium Silicate/Sodium Alginate Additives on Discharge Performance of Mg-Air Battery Based on AZ61 Alloy, Journal of Materials Engineering and Performance, 27 (2018) 2247-2254.

[194] P. Gore, S. Fajardo, N. Birbilis, G.S. Frankel, V.S. Raja, Anodic activation of Mg in the presence of In^{3+} ions in dilute sodium chloride solution, Electrochimica Acta, 293 (2019) 199-210.

[195] L. Wang, D. Snihirova, M. Deng, C. Wang, D. Höche, S.V. Lamaka, M.L. Zheludkevich, Indium chloride as an electrolyte additive for primary aqueous Mg batteries, Electrochimica Acta, 373 (2021) 137916.

[196] K.S. Novoselov, A.K. Geim, S.V. Morozov, D. Jiang, Y. Zhang, S.V. Dubonos, I.V. Grigorieva, A.A. Firsov, Electric field effect in atomically thin carbon films, science, 306 (2004) 666-669.

[197] M. Selvam, K. Sakthipandi, R. Suriyaprabha, K. Saminathan, V. Rajendran, Synthesis and characterization of electrochemically-reduced graphene, Bulletin of Materials Science, 36 (2013) 1315-1321.

[198] L. Tang, Y. Wang, Y. Li, H. Feng, J. Lu, J. Li, Preparation, Structure, and Electrochemical Properties of Reduced Graphene Sheet Films, Advanced Functional Materials, 19 (2009) 2782-2789.

[199] J. Ma, C. Qin, Y. Li, F. Ren, Y. Liu, G. Wang, Effect of functionalized graphene on performance of magnesium/air battery, Materials Research Express, 6 (2019) 085528.

[200] J. Ma, C. Qin, Y. Li, F. Ren, Y. Liu, G. Wang, Properties of reduced graphene oxide for Mg-air battery, Journal of Power Sources, 430 (2019) 244-251.

[201] A. Prabhakaran Shyma, S. Palanisamy, N. Rajendhran, R. Venkatachalam, Enhanced discharge capacity of Mg-air battery with addition of water dispersible nano MoS_2 sheet in $MgCl_2$ electrolyte, Ionics, 25 (2018) 583-592.

[202] K.H. Oehr, S. Splinter, J.C.-y. Jung, E.L. Gyenge, C.W. Oloman, Methods and products for improving performance of batteries/fuel cells, in, Google Patents, 2004.

[203] M.A. Deyab, Decyl glucoside as a corrosion inhibitor for magnesium-air battery, Journal of Power Sources, 325 (2016) 98-103.

[204] P. Zhang, Q. Li, L.Q. Li, X.X. Zhang, Z.W. Wang, A study of environment-friendly synergistic inhibitors for AZ91D magnesium alloy, Materials and Corrosion, 66 (2015) 31-34.

[205] S.V. Lamaka, D. Höche, R.P. Petrauskas, C. Blawert, M.L. Zheludkevich, A new concept for corrosion inhibition of magnesium: Suppression of iron re-deposition, Electrochemistry Communications, 62 (2016) 5-8.

[206] D. Höche, S.V. Lamaka, B. Vaghefinazari, T. Braun, R.P. Petrauskas, M. Fichtner, M.L. Zheludkevich, Performance boost for primary magnesium cells using iron complexing agents as electrolyte additives, Scientific Reports, 8 (2018) 7578.

[207] B. Vaghefinazari, D. Höche, S.V. Lamaka, D. Snihirova, M.L. Zheludkevich, Tailoring the Mg-air primary battery performance using strong complexing agents as electrolyte additives, Journal of Power Sources, 453 (2020) 227880.

[208] D. Snihirova, L. Wang, S.V. Lamaka, C. Wang, M. Deng, B. Vaghefinazari, D. Hoche, M.L. Zheludkevich, Synergistic Mixture of Electrolyte Additives: A Route to a High-Efficiency Mg-Air Battery, Journal of Physical Chemistry Letters, (2020) 8790-8798.

[209] L. Wang, D. Snihirova, M. Deng, B. Vaghefinazari, S.V. Lamaka, D. Höche, M.L. Zheludkevich, Tailoring electrolyte additives for controlled Mg-Ca anode activity in aqueous Mg-air batteries, Journal of Power Sources, 460 (2020) 228106.

[210] L. Wang, D. Snihirova, M. Deng, B. Vaghefinazari, D. Höche, S.V. Lamaka, M.L. Zheludkevich, Enhancement of discharge performance for aqueous Mg-air batteries in 2,6-dihydroxybenzoate-containing electrolyte, Chemical Engineering Journal, (2021) 132369.

[211] S. Clark, A.R. Mainar, E. Iruin, L.C. Colmenares, J.A. Blázquez, J.R. Tolchard, Z. Jusys, B. Horstmann, Designing Aqueous Organic Electrolytes for Zinc-Air Batteries: Method, Simulation, and Validation, Advanced Energy Materials, 10 (2020) 1903470.

[212] T. Würger, D. Mei, B. Vaghefinazari, D.A. Winkler, S.V. Lamaka, M.L. Zheludkevich, R.H. Meißner, C. Feiler, Exploring structure-property relationships in magnesium dissolution modulators, npj Materials Degradation, 5 (2021).

[213] T. Würger, C. Feiler, F. Musil, G.B.V. Feldbauer, D. Höche, S.V. Lamaka, M.L. Zheludkevich, R.H. Meißner, Data Science Based Mg Corrosion Engineering, Frontiers in Materials, 6 (2019).

[214] C. Feiler, D. Mei, B.J.C. Luthringer-Feyerabend, S.V. Lamaka, M.L. Zheludkevich, Rational Design of Effective Mg Degradation Modulators, Corrosion, 77 (2020) 204-208.

[215] L. Wang, M. Jia, X. Xu, Q. Wang, Asymmetric aqueous Zn-air battery with high voltage of 2.16 V by metal organic framework derived Co-Nx based bi-functional electrocatalyst as cathode, Journal of Power Sources, 437 (2019) 226892.

[216] L. Wang, W. Wang, G. Yang, D. Liu, J. Xuan, H. Wang, M.K.H. Leung, F. Liu, A hybrid aluminum/hydrogen/air cell system, International Journal of Hydrogen Energy, 38 (2013) 14801-14809.

3 Motivation and objectives

Mitigating the gap between the theoretical and practical performance of AMABs has been the target of intense research in the past decades. Many efforts have been devoted to develop high-performance anodes [8, 26-28], high-efficiency air cathodes [29-31] and suitable electrolytes [32-34]. However, the performance of existing AMABs is far from satisfactory, which achieves scarcely half of the theoretical limit. One of the drawbacks is the voltage drop caused by the blockage of the anode surface during discharge. The discharge products ($Mg(OH)_2$/MgO) accumulate on the Mg-based anode surface, impeding the contact of active anode surface with the electrolyte. Moreover, the Mg-based anode materials suffer from self-discharge in aqueous electrolyte. Although novel Mg-based anode materials emerge rapidly in the last five years, the cell voltage of AMABs based on those anodes barely exceeds 1.6 V and the utilization efficiencies (UEs) of Mg-based anode materials are rarely higher than 50% under low current densities (e.g. 1 mA cm^{-2}) [35-37]. Therefore, it is essential to introduce other approach to intervene the discharge behavior of Mg-based anode materials. Electrolyte with functional additives has been proven to be an efficient strategy for discharge performance enhancement in other aqueous metal-air batteries [38-43], such as Zn-air and Al-air batteries. Only few works were dedicated to the development of electrolytes with functional additives for AMABs before 2016 [25, 44, 45]. However, electrolytes with functional additives have already shown the potential to be game changer in developing high-performance AMABs. Hence, one of the motivations for this dissertation is to unlock new possibilities for AMABs based on a newly developed Mg-Ca anode via tailoring suitable electrolyte additives. The usage of electrolyte additive is a simple, economical and versatile way to improve the discharge performance of AMABs.

According to the available literature, the working mechanisms of electrolyte additives are mainly based on their capabilities of regulating interaction between Mg anode and electrolyte. For instance, Deyab [34] reported the addition of 2.5 mM Decyl glucoside (DG) significantly improves the UE of pure Mg from 39.4 to 89.7% at 2 mA cm^{-2}. Furthermore, Höche et al. [7] proposed adopting complexing agents as electrolyte additives for AMABs, which improves the cell voltage of pure Mg based AMABs from 1.3 to 1.7 V at 0.5 mA cm^{-2}. The UE improvement in the former work is stem from the physisorption of DG molecules on Mg anode surface, whilst the cell voltage increment in the latter one is attributed to the alleviation of precipitates form on Mg anode surface during discharge. Hence, it is essential to clarify the influence of interfacial condition changes (Mg/electrolyte) on the discharge behavior of Mg anode, which

would be instructive for the screening of suitable electrolyte additives and beneficial for developing high-performance AMABs. In order to identify the surface conditions of Mg anode and clarify the effect of additives, the reliable, non-destructive, *in-situ* characterization techniques are needed. Electrochemical impedance spectroscopy (EIS) is a powerful non-destructive technique that has been used extensively to evaluate electrochemical systems. These make EIS an appropriate technique to detect the evolution of Mg anode surface condition during discharge. Nevertheless, the physical interpretation of Mg impedance spectra is still disputed. The controversial opinions regarding the origin of time constants in Mg impedance spectra definitely lead to diverse interpretations for the interfacial condition and electrochemical properties of Mg. Therefore, it is vital to elucidate the physical meaning of different time constants in Mg impedance spectra in order to accurately interpret the effect of electrolyte additives on the discharge behavior of Mg-based anodes. Hence, the work described in this dissertation is also encouraged by the necessity to clarify the physical interpretation of high frequency (HF) and middle frequency (MF) time constants in Mg impedance spectra (i.e. different capacitive loops in Nyquist plots).

With this work, the following objectives are anticipated to be accomplished:

1) Digging a deep understanding on the correlations between anode/electrolyte interfacial condition and the discharge behavior of Mg anode via EIS measurement.

2) Clarifying the physical interpretation of HF and MF time constants (capacitive loops) in impedance spectra of Mg in NaCl solutions.

3) Improving the discharge performance of novel Mg-Ca anode based AMABs by adopting electrolyte additives to regulate the anode/electrolyte interfacial condition.

4) Investigating the working mechanism of a selected Mg^{2+} complexing additive (i.e. 2,6-dihydroxybenzoate) on the discharge performance of Mg-Ca anode and its potential as a versatile electrolyte additive for AMABs based on diverse commercial Mg anodes.

5) Studying the influence of addition of metallic ions (In^{3+}) on the interfacial conditions and discharge properties of the Mg-Ca anode. Optimizing the concentration of In^{3+} ion with the purpose of alleviating anode self-discharge and motivating anode discharge activity.

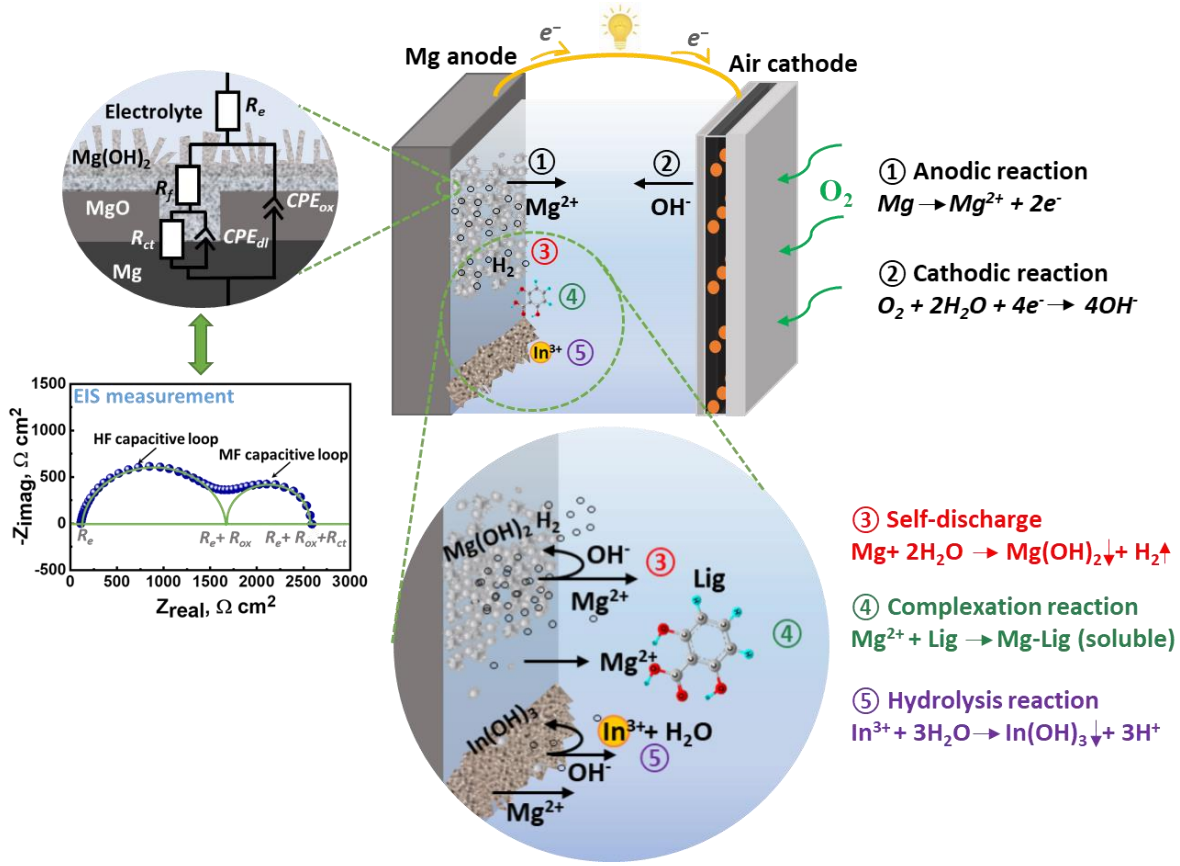

Fig. 3-1. Illustration of the works presented in this thesis.

4 Experimental

4.1 Materials and electrolytes

4.1.1 Materials

As-cast high purity Mg (HP-Mg), Mg-2.97 wt.% Al-0.73 wt.% Zn (AZ31), Mg-4.85 wt.% Al-0.43 wt.% Mn (AM50) and Mg-Ca alloys were employed as working electrodes in this work. HP-Mg, AZ31 and AM50 Mg alloy were purchased from the market. Mg-0.04 wt.% Ca (Mg-0.04Ca) and Mg-0.15 wt.% Ca (Mg-0.15Ca) were prepared via different casting procedures. For both, 99.96 wt.% pure Mg and 99.9 wt.% pure Ca were applied as raw materials and melted under protection of Ar/SF_6 gas in a boron nitride coated steel crucible at 760 °C. For Mg-0.04Ca, the molten metals were held at 760 °C for 30 min followed by a manual stirring process of 5 min to ensure composition homogeneity. Afterwards, the mixed melts were poured into cylindrical steel molds with diameter of 18 mm and cooled in air. The steel molds were pre-heated at 300 °C before casting. The melts of Mg-0.15Ca were stirred electromagnetically and then poured into a 700 °C preheated steel mold with diameter of 60 mm. After that, the mold was then immersed into a flowing water bath with a descending speed of 15 cm min^{-1} for solidification. The actual chemical compositions of aforementioned Mg-based materials were analyzed via atomic absorption spectroscopy (AAS, Agilent) and spark discharge optical emission spectrometry (SD-OES, Ametek-Spectro), which are summarized in Table 4-1.

Table 4-1 Elemental composition of Mg-based materials used in this dissertation (wt. %).

Materials	Ca	Al	Fe	Ni	Cu	Mn	Si	Zn	Mg
Mg-0.04Ca	0.041	<0.010	0.0021	0.0010	0.0012	0.019	0.0086	0.0038	Bal.
Mg-0.15Ca	0.15	0.0021	0.0014	0.0002	0.0002	0.016	0.0056	0.002	Bal.
HP-Mg-24	0.0016	0.0030	0.0024	0.0003	0.0004	0.025	0.0093	0.0018	Bal.
HP-Mg-51	<0.0001	0.0050	0.0051	<0.0001	<0.0001	0.0008	<0.0001	0.001	Bal.
AZ31	0.0011	2.97	0.0011	0.0007	0.0019	0.358	0.0309	0.732	Bal.
AM50	0.0011	4.85	0.0002	0.0005	0.0017	0.430	0.0637	0.0418	Bal.

4.1.2 Electrolytes

The electrolyte used in **Section 5.1** and **Section 5.2** was 0.05 M NaCl solution to investigate the origin of high frequency and middle frequency time constants in electrochemical impedance spectra of Mg. The electrolyte was prepared by 99.5% NaCl from Carl Roth, CAS No. 7647-14-5, with deionized water. In **Section 5.1**, all the electrochemical measurements

were carried out in 0.05 M NaCl solution with different initial pH. The initial pH of 0.05 M NaCl without any pH adjustment was 5.6 ± 0.2 (owing to naturally dissolved CO_2 from air), which is denoted as neutral NaCl solution in **Section 5.1**. In order to prevent the influence of compounds that constitute pH buffers, which may interact with Mg^{2+} ions or adsorb on Mg surface, the acidic NaCl solution (pH 3) and the alkaline NaCl solution (pH 11) were prepared by adding 0.1 M HCl and NaOH solution, respectively. The pH adjustment for all testing solutions was monitored by Hanna Metrohm-691 pH meter.

The electrolytes used in **Section 5.3** were 3.5 wt. % NaCl solutions in the presence and absence of diverse Mg^{2+} complexing agents, which were applied to investigate the influence of electrolyte additives with variant complexing abilities with Mg^{2+} ions on the corrosion and discharge performance of novel Mg-0.04Ca anode. The blank NaCl solution as the background electrolyte was prepared by adopting 99% NaCl from Fisher Chemical and deionized water. The following sodium salts were used as electrolyte additives: citrate (CIT); salicylate (SAL); 2,6-dihydroxybenzoate (2,6-DHB); 5-sulfosalicylate (5-sulfoSAL) and 3,4-dihydroxybenzoate (3,4-DHB). Their corresponding organic acids were purchased from Sigma-Aldrich. The pH of all prepared solutions except for blank NaCl solution was adjusted to 7.0 ± 0.3 by adding NaOH, monitored by Metrohm-691 pH meter.

According to the results obtained in **Section 5.3**, the concentration effects of 2,6-DHB were studied in **Section 5.4**. 3.5 wt. % NaCl solution was also utilized as the background electrolyte for all the electrochemical tests appearing in this work. 2,6-DHB with concentrations 0.05, 0.1, 0.2, and 0.3 M were added into NaCl solution as electrolyte additives. All the electrolytes were prepared with deionized water and 2,6-DHB-containing electrolytes and were neutralized by NaOH to pH 7.0 ± 0.1 under monitoring of Metrohm-691 pH meter.

$InCl_3$ was also investigated as electrolyte additives for AMABs in **Section 5.5**. $InCl_3$ with concentrations 1, 5 and 10 mM were introduced as electrolyte additives into the background NaCl solution (3.5 wt.%). The $InCl_3$-containing electrolytes were unbuffered showing pH of 4.4 ± 0.1, 4.1 ± 0.1 and 3.9 ± 0.1 corresponding to 1, 5 and 10 mM, respectively. All the electrolytes were prepared by chemical reagents purchased from Sigma-Aldrich and deionized water.

4.2 Surface and microstructure characterization

4.2.1 Scanning electron microscope (SEM)

Mg-based material surfaces and cross-sectional morphologies were characterized by scanning electron microscope (SEM, TESCAN VEGA 3) equipped with an energy dispersive spectrometer (EDS, IXRF systems). The morphology images were obtained under secondary electron (SE) mode and backscattered-electron (BSE) mode, as demonstrated in Fig. 4-1. the elemental information was carried out under 12-18 kV accelerating voltage with 15 mm working distance. Gold sputtering was employed for samples with insulated surface film to ensure good conductivity for high-quality and high-magnification images. For the cross-sectional morphologies observation, specimens were embedded in resin and then carefully ground and polished. The grinding process was conducted on SiC emery papers from 320 grit successively up to 4000 grit. After grinding, specimens were polished on a water-free oxide polishing suspension (OPS) containing SiO_2 to remove scratches. Afterwards, specimens were rinsed with ethanol and dried by a stream of cold air. 3D reconstruction for the surface topography without discharge products was conducted via SEM combined with Mex program (Bruker Alicona) for images processing. Depth profiles were obtained to examine the surface roughness and homogeneity.

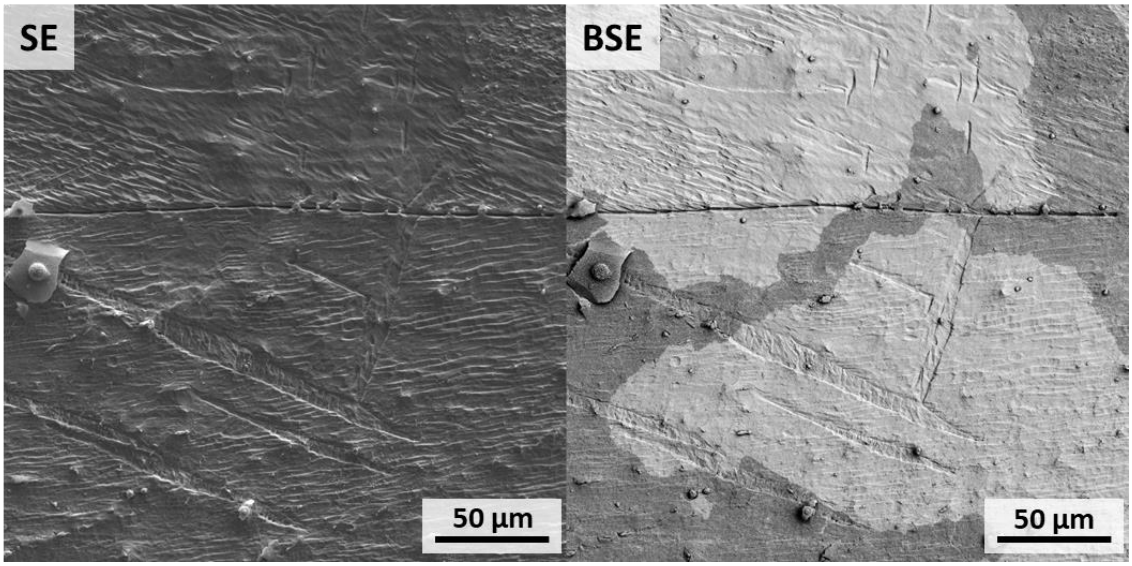

Fig. 4-1. SE and BSE images of HP-Mg after 2 h immersion in 10 mM 3,4-DHB-containing electrolyte.

The HP-Mg electrodes after EIS measurements in 0.05 M NaCl solutions with different pH (in **Section 5.1**) were characterized by scanning electron microscope/ focused ion beam system (SEM/FIB, TESCAN L3) equipped with energy dispersion spectrometer (EDS, OXFORD AZtec Ultim 100). After immersion in testing electrolyte, the samples were rinsed with ethanol,

dried with a stream of cold nitrogen and then immediately stored into a vacuum desiccator. Sample surface was sputtered with Au prior to the characterization by SEM/FIB. The cross-section lamellae for transmission electron microscope (TEM) observation were prepared by FIB *in-situ* lift-out technique. In order to minimize beam damage during ion beam thinning and polishing procedures, a platinum protective layer was deposited by ion beam to the region of interest for TEM observation. The accelerating voltage of FIB ion beam was gradually decreased during the lamellae preparation. The final thicknesses of the cross-section lamellae were approximately 100 nm and they were welded on to a copper grid, as shown in Fig. 4-2. The overview of the lamellae was carried out under scanning transmission electron (STEM) mode in SEM. Elemental maps were also obtained in SEM at a 30 kV accelerating voltage to reduce the possibility of corrosion film degradation during data acquisition.

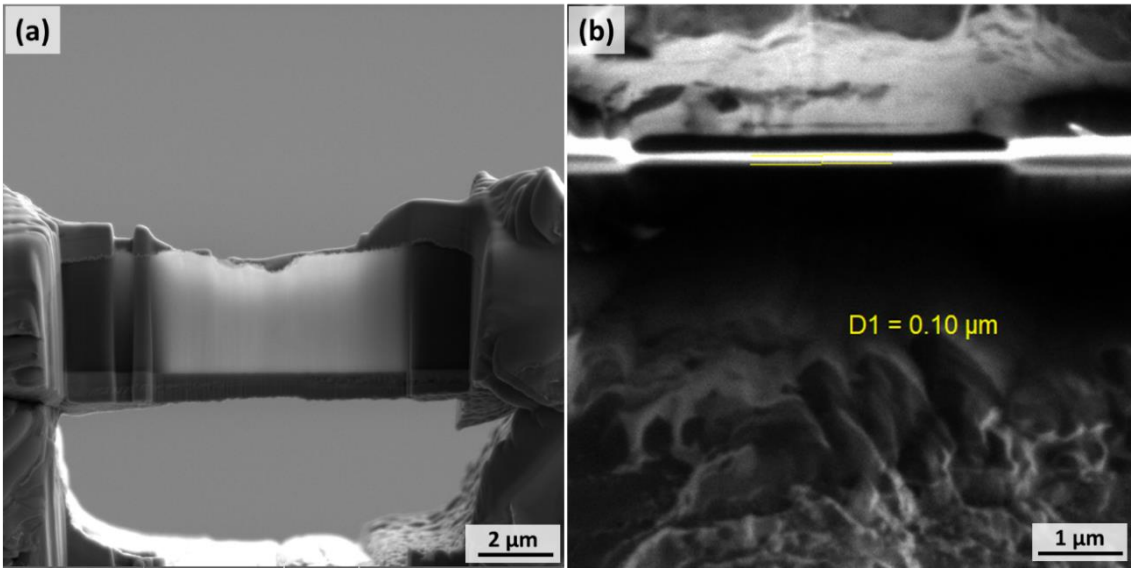

Fig. 4-2. (a) Front view and (b) top-view of cross-sectional lamella prepared by FIB in-situ lift-out technique.

4.2.2 Transmission electron microscope (TEM)

The cross-sectional morphologies and phase composition of HP-Mg electrodes after EIS measurements were characterized by transmission electron microscope (TEM, FEI Titan 80-300 & Thermo Scientific Talos). The cross-section lamellae for TEM were prepared by FIB *in-situ* lift-out technique. The delicate microstructure of surface film/Mg matrix interface was observed in the TEM under STEM mode with 300 kV accelerating voltage. Bright field (BF) and high angle annular dark field (HAADF) images were acquired, as illustrated in Fig. 4-3. The electron diffraction patterns in the selected area were obtained in TEM and compared with the published diffraction patterns for Mg, MgO and $Mg(OH)_2$ to ensure the phase compositions of characterized area. The thicknesses of $Mg(OH)_2$ and MgO layer were measured by ImageJ

software.

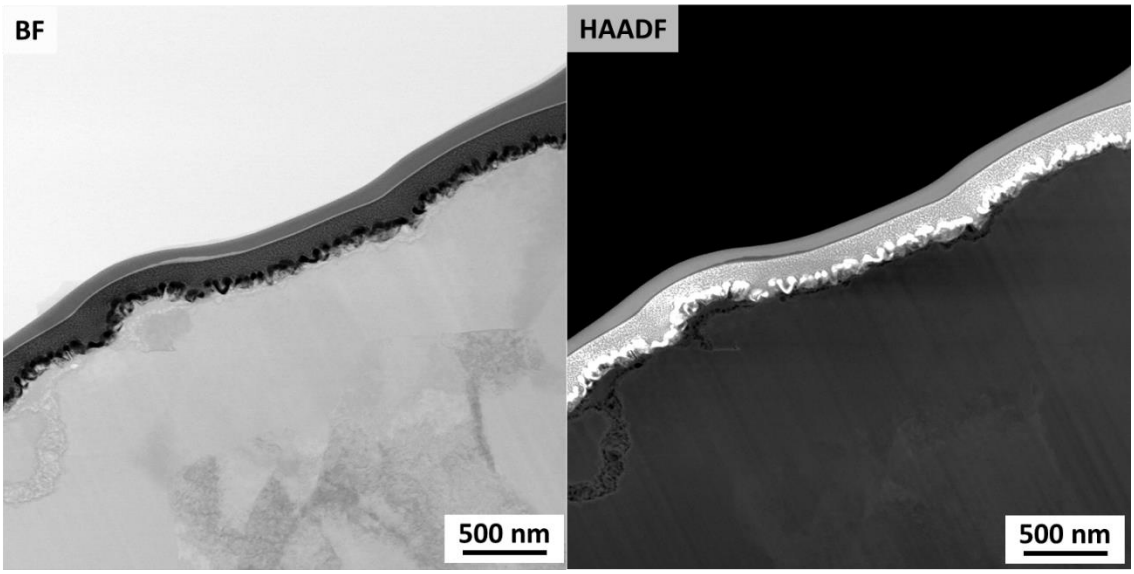

Fig. 4-3. TEM bright field (BF) and HAADF images of surface film formed on HP-Mg in NaCl solution.

4.2.3 Laser confocal scanning microscope (LSM)

Laser scanning microscope (LSM, Zeiss LSM 800) was employed to characterize the HP-Mg electrode surface after Tribo-electrochemical impedance spectroscopy (Tribo-EIS) measurement. Accordingly, the depth profile of scratch left by Tribo-meter was generated, as presented in Fig. 4-4.

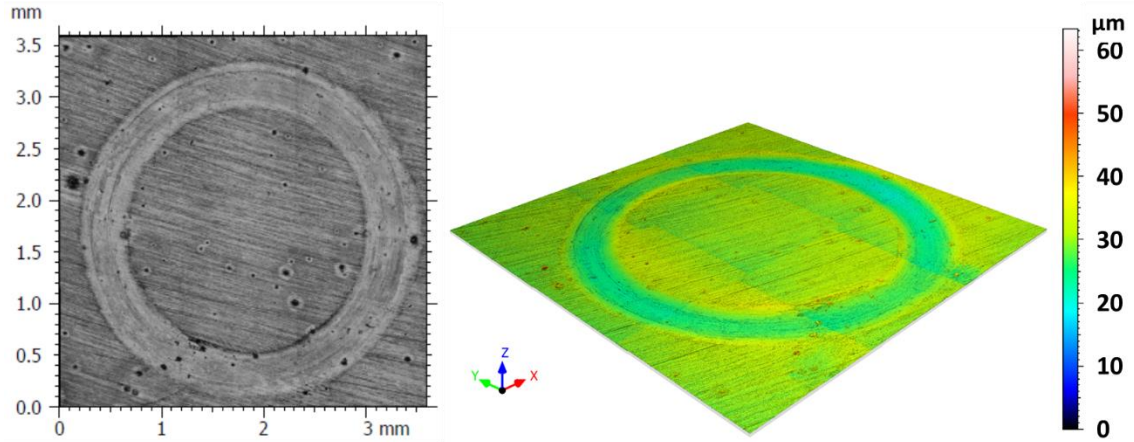

Fig. 4-4. Plane image and 3D topography of scratched Mg surface under LSM.

4.2.4 X-ray diffraction analysis (XRD)

The phase compositions of Mg-0.15Ca anodes after discharged in 3.5 wt.% NaCl and 0.05 M 2,6-DHB-containing NaCl solution were analyzed via X-ray diffraction measurement (XRD, D8 Advance, Brucker AXS) with CuK_α radiation (40 kV, 40 mA). The diffraction angle was

from 15° to 80° with 0.02° step size and the grazing angle was 1°. The dwell time was 1 s for each point.

4.3 Conventional electrochemical measurements

Conventional electrochemical impedance spectroscopy (EIS) and potentiodynamic polarization (PDP) curves were measured by Gamry interface 1000 potentiostat and Reference 600 potentiostat to evaluate the electrochemical properties of all studied Mg-based materials. All measurements were performed in the classic three-electrode system with a Pt counter electrode, a Ag/AgCl reference electrode filled with saturated KCl solution and the Mg-based material as working electrode. All Mg samples, except those used in the EIS measurements after discharge, were ground with SiC emery papers up to 1200 grit before electrochemical measurements. After grinding they were rinsed with ethanol and dried by cold air stream.

4.3.1 Electrochemical impedance spectroscopy (EIS)

Conventional EIS measurements were performed at open circuit potential (OCP) with 10 mV_{rms} perturbation voltage. In **Section 5.1**, HP-Mg-51 electrode with 1 cm^2 exposed surface area was employed as working electrode. EIS measurements were performed at OCP under potentiostatic mode using Gamry Reference 600 potentiostat in order to follow the growth of corrosion product film on HP-Mg in 0.05 M NaCl with pH 3, pH 5.6 and pH 11. The EIS measurement was started from 100 kHz and ended at intermediate frequency (1 Hz) in order to avoid the latent influence on Mg surface caused by possible polarization during low frequency measurement. All the measurements were triplicated to assure data reproducibility and all of the impedance spectra were consistent with the Kramers-Kronig relations.

In **Section 5.3**, Mg-0.04Ca electrode with 2.5 cm^2 exposed surface area was embedded in resin and used as the working electrode. The specimen was connected with copper wire from backside for conducting. The EIS measurements for Mg-0.04Ca electrode were performed after 1 h immersion in 3.5 wt.% NaCl solutions with and without 0.1 M Mg^{2+}-complexing agents (CIT, 2,6-DHB, 3,4-DHB, SAL and 5-sulfoSAL). The tested frequency range was 100 kHz - 0.01 Hz with 10.5 points per decade and all the EIS measurements were repeated three times.

Mg-0.15Ca electrodes with 2.5 cm^2 exposed surface area were prepared by the aforementioned procedure and used as working electrodes in **Section 5.4** and **Section 5.5**. The anode surface conditions during discharge in blank NaCl and 2,6-DHB-containing electrolytes were evaluated by EIS measurements amid discharge interval in **Section 5.4**. The EIS measurements

were carried out at OCP after discharge for different periods (0, 5, 10, 15 and 24 h) in the frequency range from 100 kHz - 0.03 Hz with 9 points per decade. In **Section 5.5**, EIS measurements were also performed at OCP after discharge for a specific period (1, 5 and 24 h) to evaluate the surface condition alteration of Mg-0.15Ca electrode in blank NaCl and $InCl_3$-containing electrolytes. The applied frequency ranged from 100 kHz - 0.1 Hz with 10 points per decade. The setting value of the lowest frequency depends on the testing system and is intend to avoid possible polarization during low frequency EIS measurement.

4.3.2 Potentiodynamic polarization (PDP)

Potentiodynamic polarization curves of Mg-0.15Ca alloy in the NaCl and 2,6-DHB-containing electrolytes were measured by Gamry Interface 1000 potentiostat in the conventional three-electrode system adopting well-ground Mg-0.15Ca alloy with 1 cm^2 exposed surface as the working electrode, Pt wire as the counter electrode and commercial Ag/AgCl electrode as the reference electrode. All the polarization curves were obtained after 1 h immersion in the testing electrolytes by potential scanning from – 400 mV to + 800 mV vs. OCP. The scanning started from the cathodic region to the anodic region with 0.5 mV/s scanning rate.

4.4 Tribo-electrochemical measurements

Tribo-electrochemical measurements were performed by Gamry interface 1010E potentiostat coupled with Tribotechnic pin-on-disc tribometer in a customized cell, as indicated in Fig. 4-5. The pin-on-disc tribometer is mainly composed of a stationary abrasive pin and a rotating disc. The abrasive pin used in this work was a zirconia ball with 6 mm diameter, which was hold by an insulating plastic holder (Fig. 4-5d). The applied load was 5 N for all the tests and there were two different rotation speeds used in the tests, i.e. 2 or 20 rpm. 2 rpm is the slowest rotation speed of the tribometer and 20 rpm was chosen as fast rotation speed to elucidate the impact of rotation speed on the electrochemical measurement. Coiled Pt wire and KCl-saturated Ag/AgCl electrode were used as counter electrode and reference electrode, respectively. Mg samples with various exposed surface areas (0.5, 1.1 and 2 cm^2) were employed as working electrodes. The working electrode was embedded in the groove of the customized cell (Fig. 4-5e). A connection point on the bottom of the cell was used to electrically connect the working electrode with an external brass band. The conductivity of this set-up was checked by multimeter, indicating the resistance is less than 1 ohm. Waterproof adhesive tape with specified size hole stuck on the top of the working electrode and the groove in order to

control the exposed surface area of working electrode and to avoid electrolyte penetration. The water tightness of this set-up was also checked before Tribo-EIS measurement.

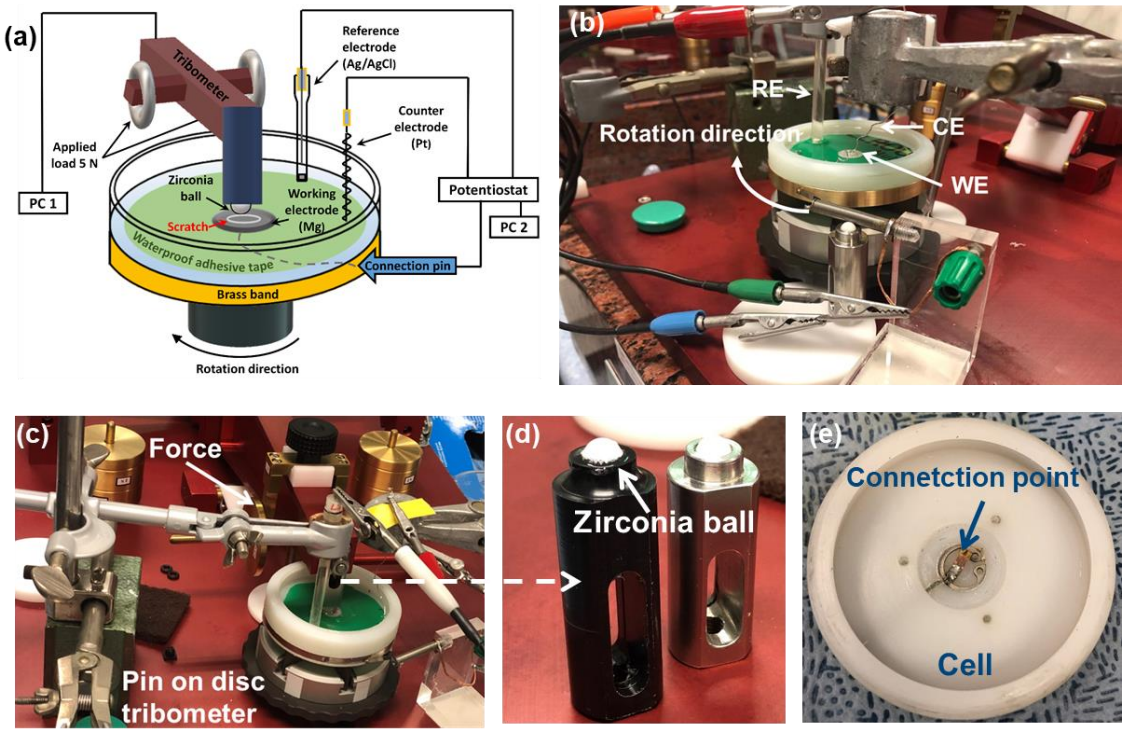

Fig. 4-5. (a) Schematic illustration and (b) real picture of experimental arrangement for Tribo-electrochemical measurement, (c) the pin-on-disc Tribo-meter, (d) the abrasive pin and (e) the electrochemical cell.

4.4.1 Tribo-electrochemical impedance spectroscopy (Tribo-EIS)

All Tribo-EIS measurements were conducted under potentiostatic mode at OCP with 10 mV_{rms} perturbation voltage. All EIS measurements were done during cell rotation and divided into three different stages: (i) the initial stage without abrasion; (ii) the abrasion stage where abrasive pin was scratching Mg surface; (iii) the recovery stage where abrasive pin was removed from the cell after scratching. The EIS measurements without abrasion were started from 100 kHz and ended at 0.01 Hz with 9 points per decade. During EIS measurements without abrasion (i and iii), the abrasive pin did not touch the surface of the working electrode. During the abrasion stage, the working electrode was scratched by the abrasive pin, as illustrated in Fig. 4-5a. The EIS measurements in the abrasion stage (ii) were carried out in the frequency range from 100 kHz to around 0.04 Hz. A circular abraded ring was left on the working electrode surface. All the Tribo-EIS measurements were performed at least three times.

4.4.2 Tribo-potentiodynamic polarization (Tribo-PDP)

Tribo-PDP tests were also performed in the above mentioned experimental arrangement. In order to avoid the influence of electrolyte alkalization and change of electrode surface

condition on the accuracy of PDP tests, anodic and cathodic polarization curves of Mg with 1.1 cm^2 exposed surface area under different states were obtained separately in fresh 0.05 M NaCl solution. All PDP tests were carried out after one hour OCP test to ensure the stabilization of the testing system. The potential scanning with 0.5 mV/s scanning rate was done from − 5 mV (vs. OCP) to + 800 mV (vs. OCP) for anodic branch and from + 5 mV (vs. OCP) to − 2.4 V (vs. Ag/AgCl) for cathodic branch.

4.5 Discharge test

4.5.1 Half-cell discharge test

A Gamry Interface 1000 potentiostat with typical three-electrode arrangement was used to perform the half-cell discharge tests. Mg-0.04Ca and Mg-0.15Ca samples with 2.25 cm^2 exposed surface area were prepared by the same procedure as above mentioned in **Section 4.3**. Half-cell discharge tests were done in a galvanostaic mode with various applied current densities. In **Section 5.3** and **Section 5.4**, working and counter electrodes were placed in two separated beakers connected by a salt bridge (Fig. 4-6). The electrolyte in anode compartment stirred at the 350 rpm during discharge. The two compartments were used in order to avoid influence of rapid pH changes caused by cathodic processes on anode condition during discharge. In order to obtain accurate weight loss, ΔW, Mg-Ca anode samples after discharge were immersed into chromic acid aqueous solution (200 g L^{-1}) for 10 min to remove discharge products and then rinsed with ethanol. Afterwards, the anode mass loss was determined via comparing the sample mass prior to discharge and after removal of discharge products. Utilization efficiency (UE) and specific capacity (SC) of Mg-Ca alloys in different electrolytes were calculated via the following equations [44, 46]:

$$\text{UE}\ (\%) = \frac{W_{theo}}{\Delta W} \times 100\% \tag{4-1}$$

$$\text{SC}\ (\text{Ah g}^{-1}) = \frac{I \times t}{\Delta W} \tag{4-2}$$

Where W_{theo} (g) means the theoretical weight loss of anode and ΔW (g) means the actual weight loss obtained from the mass difference of anode before and after discharge. W_{theo} was calculated via the following equation [44, 46]:

$$W_{theo}(\text{g}) = \frac{I \times t}{F \times \sum(\frac{x_i \times n_i}{m_i})} \tag{4-3}$$

Where I (A) represents the applied current, t (h) represents discharge time, F is the Faraday constant (26.8 Ah mol^{-1}), x_i, n_i, m_i represent the mass fraction, ionic valence and atomic weight of the element, respectively.

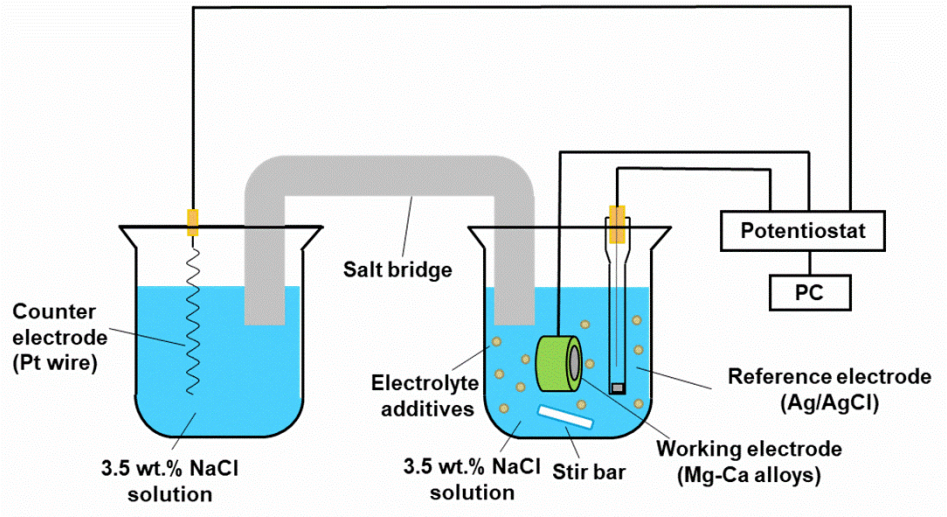

Fig. 4-6. Schematic illustration of experimental arrangement for half-cell discharge test.

4.5.2 Full-cell discharge test

Full cell tests were performed in a lab-made Mg-air cell, which adopted air-breathing cathode with C/MnO_2 fabric with polytetrafluoroethylene (PTFE) gas diffusion layer and Ni mesh (Gaskatel GmbH). The experimental arrangement and air cathode structure are illustrated in Fig. 4-7. Mg-Ca anodes with 2.5 cm^2 surface area worked as anode in **Section 5.3**, **Section 5.4** and **Section 5.5**. The discharge voltage profiles were obtained at various applied current densities (0.5~10 mA cm^{-2}). 3.5 wt. % NaCl solution with and without additives. After discharge, the specific energy of Mg-air batteries were calculated according to the anode mass loss and the equation is expressed as [47]:

$$\text{Specific energy (Wh kg}^{-1}) = \frac{\int_0^t I \times U \times \Delta t}{\Delta W} \quad (4\text{-}4)$$

Where U (V) represents the voltage of discharge, ΔW (kg) is the weight loss of anode after full cell test, I (A) and t (h) represent the applied current and discharge time.

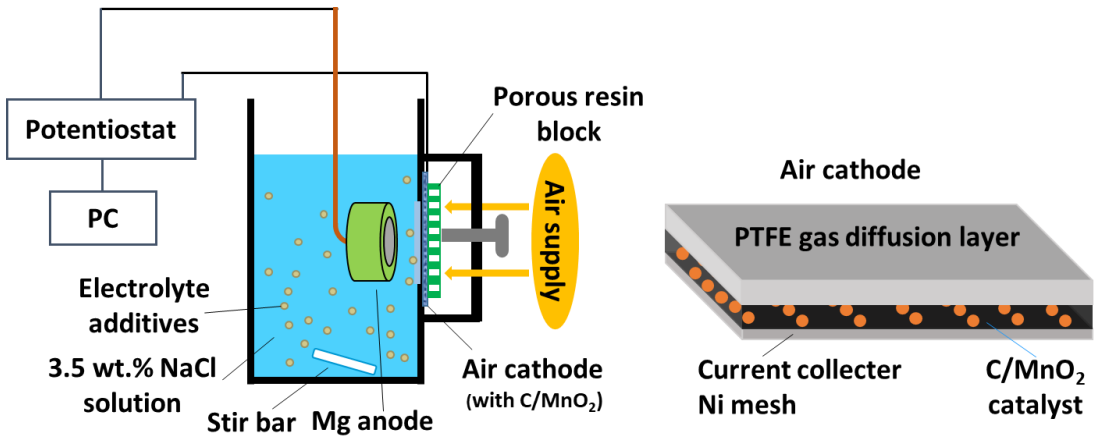

Fig. 4-7. Schematic illustration of experimental arrangement for full-cell discharge test.

In **Section 5.4**, four kinds of Mg-based materials including HP-Mg-24, Mg-0.15Ca, AZ31 and AM50 alloys, were applied as anode materials. The cell voltages of various AMABs in blank NaCl and 0.2 M 2,6-DHB-containg electrolytes were tested at 1, 5 and 10 mA cm^{-2}. The improvements of discharge performance introduced by 2,6-DHB addition were evaluated by the specific energy and power density, which were calculated via Eq. 4-4 and Eq. 4-5, respectively.

$$\text{Power density (mW cm}^{-2}) = \frac{I \times U}{A} \quad (4\text{-}5)$$

Where I (A) and U (V) refer the applied current and cell voltage, respectively. A (cm^2) is the surface area of anode. All the above mentioned measurements were repeated at least twice.

4.6 Hydrogen evolution test (HET)

4.6.1 HET at OCP condition

Hydrogen evolution tests were carried out using eudiometers, as presented in Fig. 4-8. Unlike typical burette-funnel setup, eudiometer is a closed system, thus it excludes the additional intake of O_2, CO_2 and N_2 apart from initially trapped air. The Mg-Ca samples with surface area of 15 cm^2 were tested in 500 mL solution. Before hydrogen evolution test, samples were ground up to 1200 grit emery papers and dried with cold pressed air. The immersion solution was 3.5 wt. % NaCl with and without 0.1 M electrolyte additives. During hydrogen evolution test, the electrolyte was stirred with a constant speed, 350 rpm. The hydrogen was collected during 24 h. All tests were repeated twice, the difference between them was less than 10%.

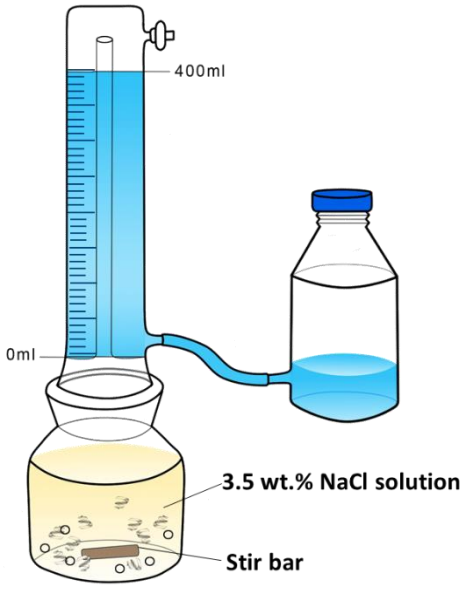

Fig. 4-8. Eudiometer for hydrogen evolution test at OCP.

4.6.2 HET during discharge

Effect of electrolyte additives on the self-discharge behavior of Mg-0.15Ca anode during discharge was investigated by the real-time hydrogen evolution test under galvanostatic polarization. Fig. 4-9 exhibits the experimental set-up for real-time HET during discharge. The traditional inverted burette-funnel setup was applied to collect evolved hydrogen with minimum accuracy of 0.1 mL. A Gamry Interface 1000 potentiostat with the aforementioned three-electrode arrangement was applied to perform an half-cell discharge measurement.

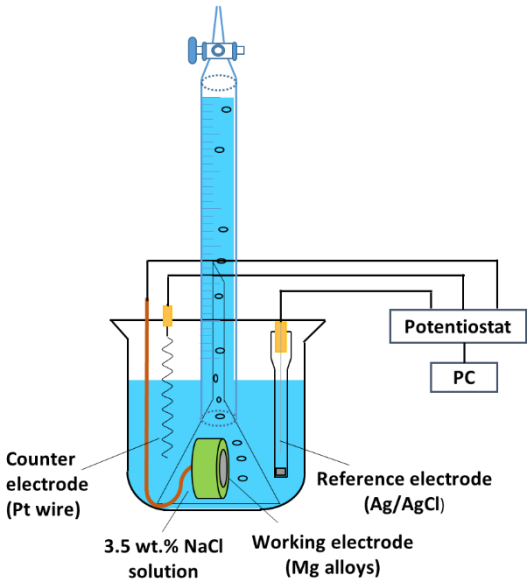

Fig. 4-9. Experimental arrangement for real-time HET during discharge

4.7 Localized measurements

The information about the concentration of the relevant species (pH and dissolved O_2) over the surface of Mg electrode at micro-scale was obtained by scanning ion-selective electrode technique (SIET system Applicable Electronics) and fiber-optic micro-optode (Pyroscience). The experimental set up is described in Fig. 4-10.

In **Section 5.1**, the local pH of HP-Mg-51 immersed in NaCl was detected via a glass-type pH microelectrode with a tip diameter of 10 µm (pH-10, Unisense), with an external Ag/AgCl reference electrode. The pH microelectrode was calibrated daily. The local dissolved O_2 concentration was measured by FireStingO2 fiber-optic O_2 micro-sensor coupled with an O_2 concentration meter (Pyroscience). HP-Mg-51 with approximately 2 mm diameter was embedded in epoxy resin and fixed in a sample holder. Both, the pH microelectrode and O_2 concentration meter, were fixed at 50 µm above the HP-Mg-51 sample by using a custom made dual head stage to simultaneously monitoring the evolution of local pH and dissolved O_2

concentration. The relevant data was acquired by LV4 software (Science Wares) in parallel with PyroOxygenLogger software (Pyroscience).

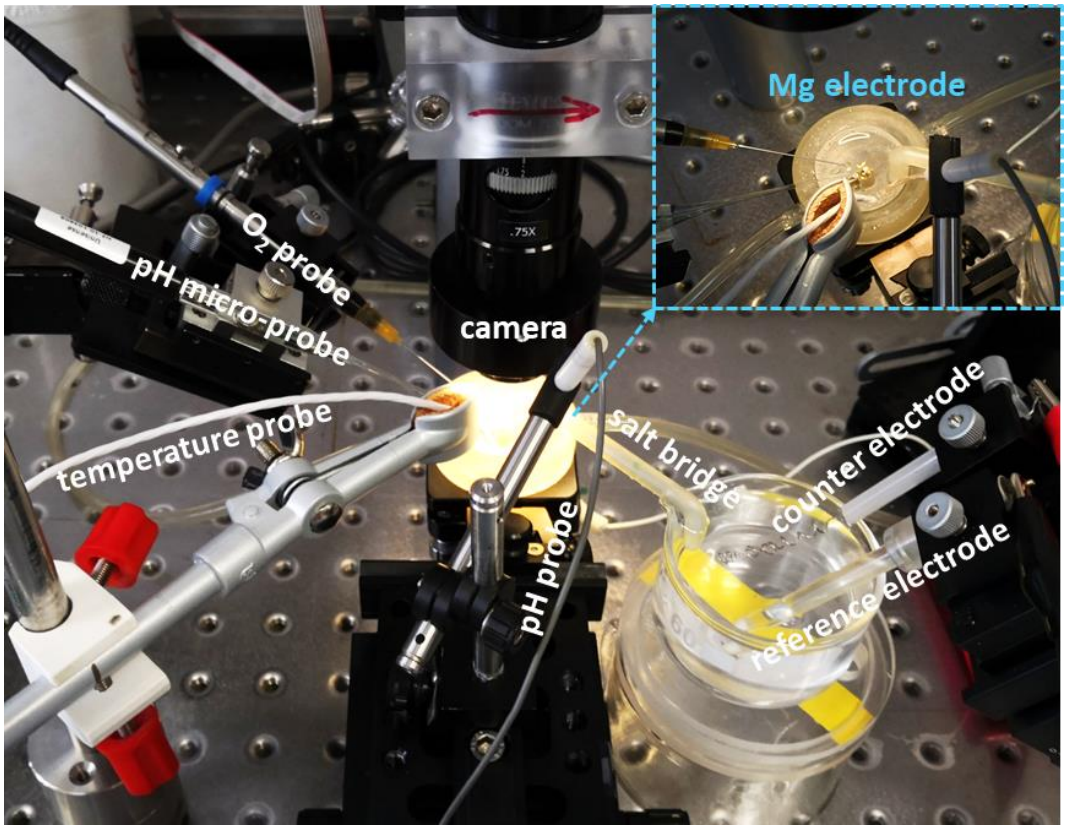

Fig. 4-10. Experimental arrangement for localized measurement of Mg electrodes.

In **Section 5.5**, the local pH of Mg-0.15Ca anode in 3.5 wt. % NaCl with and without $InCl_3$ under 1 mA cm^{-2} galvanostatic polarization was measured via the same pH-10 micrometer. The pH microelectrode was fixed at 20 μm above the Mg-0.15Ca sample with approximately 1 mm diameter in order to record the real-time evolution of local pH during galvanostatic polarization. The applied current density was 1 mA cm^{-2} with the same configuration adopted in half-cell discharge test. The local information for Mg-0.15Ca sample surface was acquired on a sample-centered area (2000 μm × 2000 μm) at 50 μm above it to monitor the distribution of local pH on polarized Mg-0.15Ca surface. All the relevant data was acquired by LV4 software (Science Wares).

5 Results (Published)

The work described in this thesis aims at tailoring electrolyte additives for high-performance Mg-based anode materials in primary AMABs based on the mechanistic understanding of interfacial condition between Mg anode and electrolyte. Hence, the content of this work is composed of two main parts: (i) adopting electrochemical impedance spectroscopy to investigate the surface condition of Mg; (ii) controlling the discharge behavior and surface condition of Mg anode by organic and inorganic electrolyte additive. The research in frame of part (i) focuses on clarifying the physical interpretations of the two time constants with capacitive behavior in Mg impedance spectra. It will facilitate a mechanistic understanding of the effect of selected AMABs electrolyte additives on the interfacial condition of Mg in different electrolytes. Within the frame of part (ii), the investigation aims to address the surface passivation and self-corrosion during discharge via adding organic and inorganic compounds to regulate the interaction between Mg anode and electrolyte. The results are presented in form of four published papers in scientific journals with peer-review process and one submitted paper. The physical interpretation of high frequency time constant in Mg impedance spectra was thoroughly studied in ***paper 1***, proposing that the high frequency time constant originates from the barrier effect of MgO-based surface film. Subsequently, Tribo-EIS measurements were applied to study the origin and interpretations of two capacitive loops (high and middle frequency time constants) in Mg impedance spectra in ***paper 2***. The results further prove that the high frequency time constant should be attribute to the barrier film-relevant behavior and the middle frequency time constant originates from the charge transfer process. Based on the mechanistic study of physical interpretations regarding time constants in Mg impedance spectra in ***paper 1*** and ***paper 2,*** EIS measurements were employed to characterize the *quasi-in-situ* surface condition of Mg anode in additive-containing electrolytes. In ***paper 3***, the influence of five organic additives with varying Mg^{2+} complexing capabilities on the corrosion and discharge performance of novel Mg-Ca anodes based AMABs was investigated. The results indicate that Mg^{2+} complexing agents are capable of inhibiting the precipitation of discharge products film and regulating non-uniform dissolution. The selection of suitable electrolyte additives with different Mg^{2+} complexing ability is dependent on the change of the discharge loads. According to the results presented in ***paper 3***, 2,6-DHB addition is capable of simultaneously improving utilization efficiency and discharge potential of Mg-Ca anode. Hence, the working mechanisms of this organic compound as a versatile electrolyte additive for AMABs was further investigated in ***paper 4***. EIS measurement amid intermittent discharge

and real-time hydrogen evolution test during discharge were applied in this work. The results obtained via these two novel methods lead to a deeper mechanistic understanding of the additive performance and determining the relevant practical conditions. Same methods combined with localized measurements were applied to study the working mechanism of inorganic additive, i.e. $InCl_3$, in AMABs (***paper 5***). The results propose another strategy to improve the discharge performance of AMABs via adding metallic ions with strong hydrolysis effect.

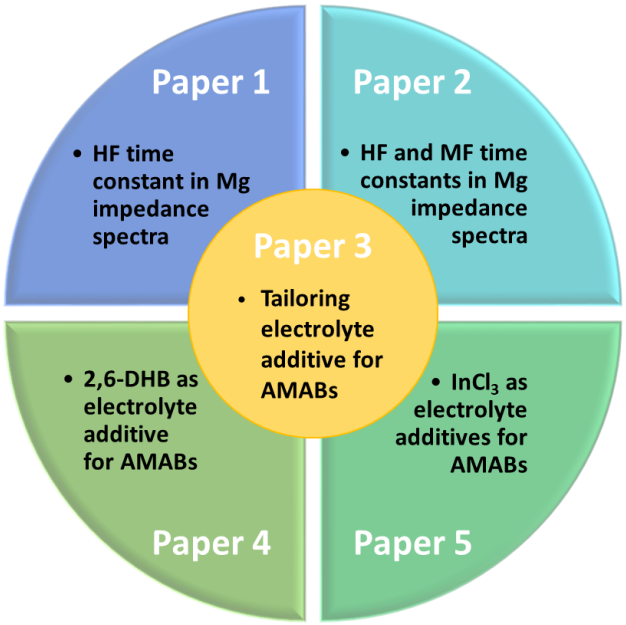

Fig. 5-1. Schematically illustration of the thesis structure.

5.1 Insight into physical interpretation of high frequency time constant in electrochemical impedance spectra of Mg

Paper 1 is published in Corrosion Science, 187 (2021), 109501.

The aim of this work is to clarify the physical interpretation of high frequency time constant in impedance spectra of Mg, which is revealing and beneficial for accurately evaluating interfacial condition and corrosion behavior of Mg-based materials. EIS measurement has been wildly applied to investigate the corrosion properties of Mg and its alloys [48-51]. However, the analysis and interpretation of EIS results for Mg are controversial. These discrepant explanations for the origin of the time constants definitely lead to diverse interpretations for the corrosion behavior of Mg and its alloys. Therefore, it is essential to clarify the physical meaning of different time constants for a better understanding of the information provided by EIS measurement. In this work, the evolution of the high frequency time constant and the surface condition of high purity Mg (HP-Mg) in NaCl solution was studied at three different pH (3, 5.6, and 11) via EIS, TEM and *in-situ* spatially resolved techniques for tracing local concentration of dissolved oxygen and local pH. The results indicate that the most protective film is formed on HP-Mg surface at pH 11, which is also the thinnest film in comparison with that formed at pH 3 and 5.6 according to the cross-sectional images observed by TEM. This experimentally observed tendency is consistent with the calculations based on the HF capacitive loop in the EIS plots, suggesting that the high frequency time constant in impedance spectra of Mg originates from the barrier properties of MgO-based surface film.

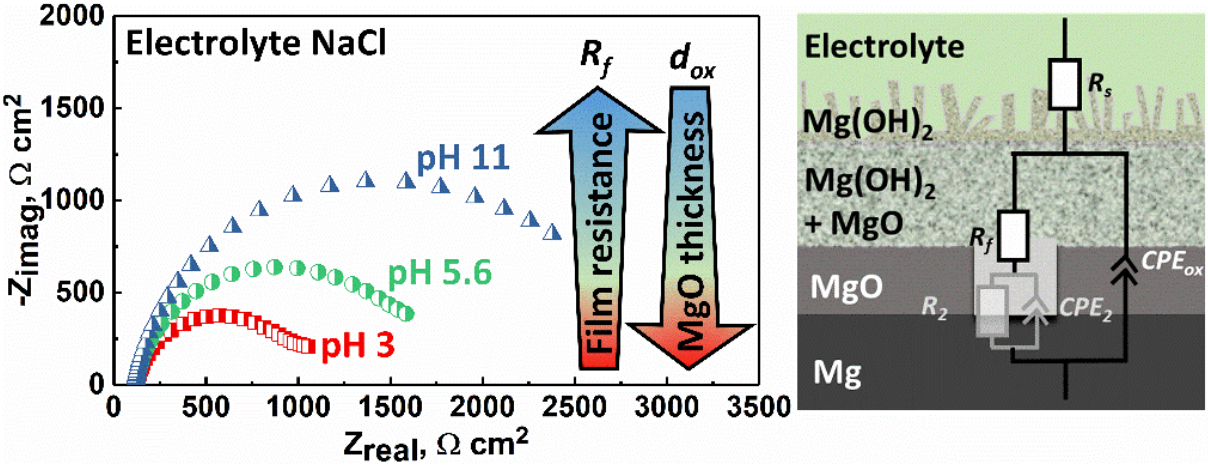

Fig. 5-2. Graphical abstract for **Section 5.1**.

Corrosion Science 187 (2021) 109501

Contents lists available at ScienceDirect

Corrosion Science

journal homepage: www.elsevier.com/locate/corsci

Insight into physical interpretation of high frequency time constant in electrochemical impedance spectra of Mg

Linqian Wang [a,*], Darya Snihirova [a], Min Deng [a], Cheng Wang [a], Bahram Vaghefinazari [a], Gert Wiese [a], Mark Langridge [b], Daniel Höche [a], Sviatlana V. Lamaka [a], Mikhail L. Zheludkevich [a,c]

[a] Institute of Surface Science, Helmholtz-Zentrum Hereon (Hereon), 21502, Geesthacht, Germany
[b] Department of Metal Physics, Helmholtz-Zentrum Hereon (Hereon), 21502, Geesthacht, Germany
[c] Institute of Materials Science, Faculty of Engineering, Kiel University, 24143, Kiel, Germany

ARTICLE INFO

Keywords:
Magnesium
EIS
Corrosion
TEM
Local measurement

ABSTRACT

Electrochemical impedance spectroscopy measurements were performed to study the evolution of surface condition, which related to the high frequency time constant of Mg, in 0.05 M NaCl solution at three different pH. Based on the assumption that the high frequency time constant originates solely from the surface film, the thickness of MgO film was calculated via fitting EIS results. The deduced results were compared with the actual surface condition, characterized by transmission electron microscopy and local measurements. The results verified that the time constant at the high frequency range originates from the barrier properties of the surface film.

1. Introduction

Electrochemical impedance spectroscopy (EIS) is an electrochemical technique, which is carried out by applying small sinusoidal perturbation (potential or current) to measure the response and compute the impedance at each frequency. Therefore, EIS is capable of detecting the minor changes in electrode surface state and correlated electrochemical processes at the electrode/electrolyte interface without changing the surface state. Due to its intrinsic characteristics, EIS is widely applied to study corrosion behavior and mechanism of different bare and coated metals [1–3]. Revealing the corrosion mechanism and enhancing the corrosion resistance of Mg are the subject of intense research during the last decades [4–8]. EIS has been wildly applied to investigate the corrosion properties of Mg and its alloys [9–11], coatings on Mg-based substrate [12–14] and the effect of inhibitors for Mg [15–17].

However, the analysis and interpretation of EIS results for Mg are controversial. The analysis often involves the fitting procedure via equivalent circuit, which is proposed according to the possible electrochemical processes happened on the electrode surface. The corresponding values of electrical parameters for each process can be deduced from fitting procedure. Thus, well-designed equivalent circuit is helpful for the quantitative analysis of EIS results. Nevertheless, there is no agreement on the equivalent circuit for Mg corrosion process. Diverse equivalent circuits are used by different researchers to fit the similar impedance spectra. The common Nyquist plot of bare Mg is normally composed of two capacitive loops and occasionally one inductive loop appearing in the low frequency range as shown in Fig. 1a. For the impedance spectra, which are similar with the one presented in Fig. 1a, some researchers used the equivalent circuit with two in-series connected RC elements as shown in Fig. 1c to fit the spectra [18,19], but other researchers applied the equivalent circuit displayed in Fig. 1d [20,21]. Meanwhile, several works introduce an inductor into the above-mentioned two kinds of equivalent circuits to fit the inductive tail [22–24]. The values obtained from these two circuits may not be significantly different, but they reflect different physical meanings, which leads to different conclusion on studied processes. Hence, attention should be paid when choosing the correct connection mode for circuit elements.

Moreover, the physical interpretations of each electrical circuit element (CPE_1, R_1, CPE_2 and R_2) are also disputed. Table 1 lists the concise interpretations of time constants and corresponding circuit elements at different frequency ranges of Mg impedance spectra. Some researchers suggest that the first capacitive loop, namely the one appearing in the high frequency range, corresponds to the surface film

* Corresponding author at: Institute of Surface Science, Helmholtz-Zentrum Hereon (Hereon), Max-Planck-Str.1, 21502, Geesthacht, Germany.
E-mail address: linqian.wang@hereon.de (L. Wang).

https://doi.org/10.1016/j.corsci.2021.109501
Received 19 February 2021; Received in revised form 23 March 2021; Accepted 24 April 2021
Available online 27 April 2021

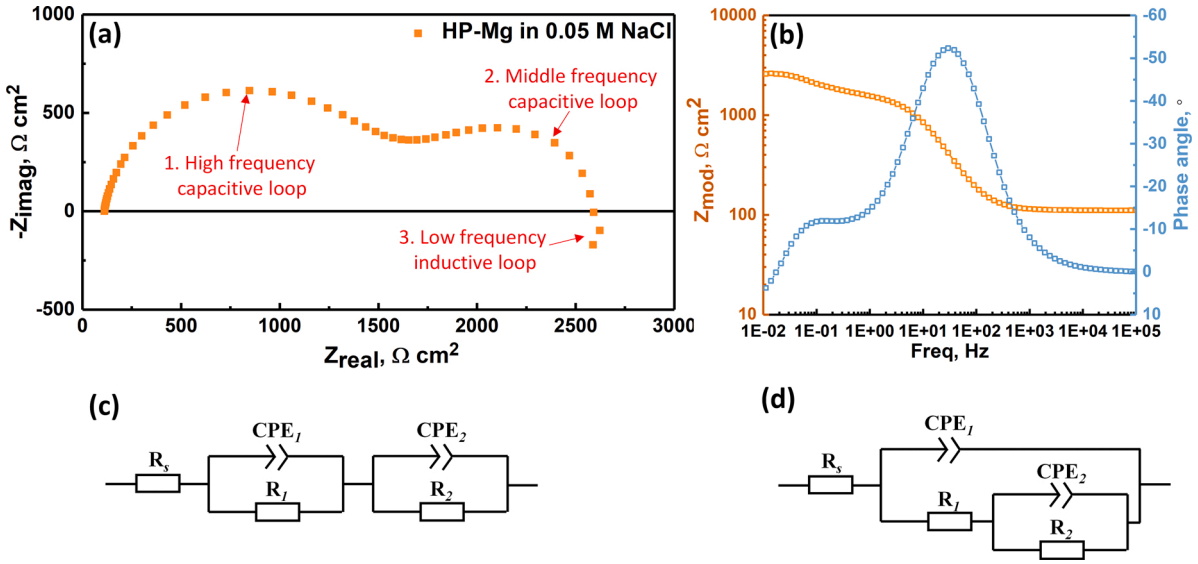

Fig. 1. (a) and (b) Representative Nyquist plot and Bode plot for HP-Mg in 0.05 M NaCl solution; (c) and (d) two kinds of common equivalent circuits for the EIS results of Mg and its alloys.

Table 1
Interpretation of time constants at different frequency range for Mg-based materials.

Ref.	High frequency (capacitive loop)		intermediate frequency (capacitive loop)		Low frequency (inductive loop)
	CPE_1	R_1	CPE_2	R_2	L
[9,25,43]	Surface film capacitance	Charge transfer resistance	Diffusion of electroactive species inside corrosion products		Relaxation of the adsorbed intermediates on Mg surface
[16,18,21,22,24,26,55]	Surface film capacitance	Surface film resistance	Double layer capacitance	Charge transfer resistance	Electrochemical reactions at film/Mg interface [26], Desorption of Mg $(OH)_2$ film [22], Relaxation of the adsorbed intermediates [24]
[11,23,54]	Double layer capacitance	Charge transfer resistance	Surface film capacitance	Surface film resistance	Desorption of corrosion products or nucleation of local corrosion [11,54], Desorption of intermediate [23]
[19,27,56]	Double layer capacitance	Charge transfer resistance	$Mg(OH)_2$ film capacitance	$Mg(OH)_2$ film resistance	Breakdown of partial protective $Mg(OH)_2$ film [27]
[57]	Double layer capacitance	Charge transfer resistance	Product adsorption in the localized corrosion		Collapse of partial protective film due to Mg^+ reaction

capacitance, in parallel with the resistance from the charge transfer process. Here the middle frequency time constant is associated to the mass transport process through the corrosion product film [9,25]. However, some other researchers deem the high frequency time constant to be related to the surface film formed on Mg and its alloy, whilst the charge transfer resistance in parallel with double layer capacitance is the origin of the second time constant in the middle frequency range [21,22,26]. Moreover, there are also many researchers suggesting that the high frequency capacitive loop is double layer capacitance in parallel with charge transfer resistance [11,19,23]. Regarding the inductive loop in the low frequency range, different researchers also hold various views. Some researchers attribute it to the relaxation processes of Mg^+ species on the surface [9,25]. Meanwhile, some researchers assume it might be related to a breakdown of the partially protective $Mg(OH)_2$ film [27,28] or might refer to the occurrence of localized corrosion, such as pitting corrosion [29]. The publication of Shkirskiy and co-workers [30] claims that the inductive loop is due to the higher Mg corrosion rate in low frequency range, which should not be associated to any process related to Mg^+ ion. These discrepant explanations for the origin of the time constants definitely lead to diverse interpretations for the corrosion behavior of Mg and its alloys. Therefore, it is essential to clarify the physical meaning of different time constants for a better understanding of the information provided by EIS measurement. It will be beneficial for accurately evaluating the corrosion behavior of Mg-based materials.

In this work, we thoroughly discuss the physical interpretation of the high frequency time constant of impedance spectra for pure Mg in NaCl solutions, which is revealing for the investigation related to corrosion behavior of Mg and its alloys. We suggest the high frequency (HF) time constant is related to surface film presented on Mg surface, mainly attributed to comparatively dense MgO film. Based on this assumption, 0.05 M NaCl solutions with various initial pH (3, 5.6, and 11) were adopted as testing solutions to introduce different surface conditions of high purity Mg (HP-Mg) in EIS measurements. The influence of various pH on the evolution of HF time constant of HP-Mg was investigated and the results were compared with the surface film morphologies observed via transmission electron microscope (TEM). Local pH, local O_2 concentration and surface conditions of HP-Mg during immersion in NaCl solution with various pH were recorded to monitor the growth of surface film and the corrosion behavior of HP-Mg.

Table 2
Chemical compositions of HP-Mg (ppm).

Materials	Fe	Cu	Si	Mn	Al	Zn	Zr	Ag	Mg
Mg	51	<1	<1	8	50	10	23	0.71	Bal.

2. Experimental

As-Cast HP-Mg was used in this study to avoid the influence of alloying elements on the corrosion and electrochemical behavior. The chemical composition (Table 2) was measured via spark discharge optical emission spectrometry (SD-OES) with spark analyzer vision

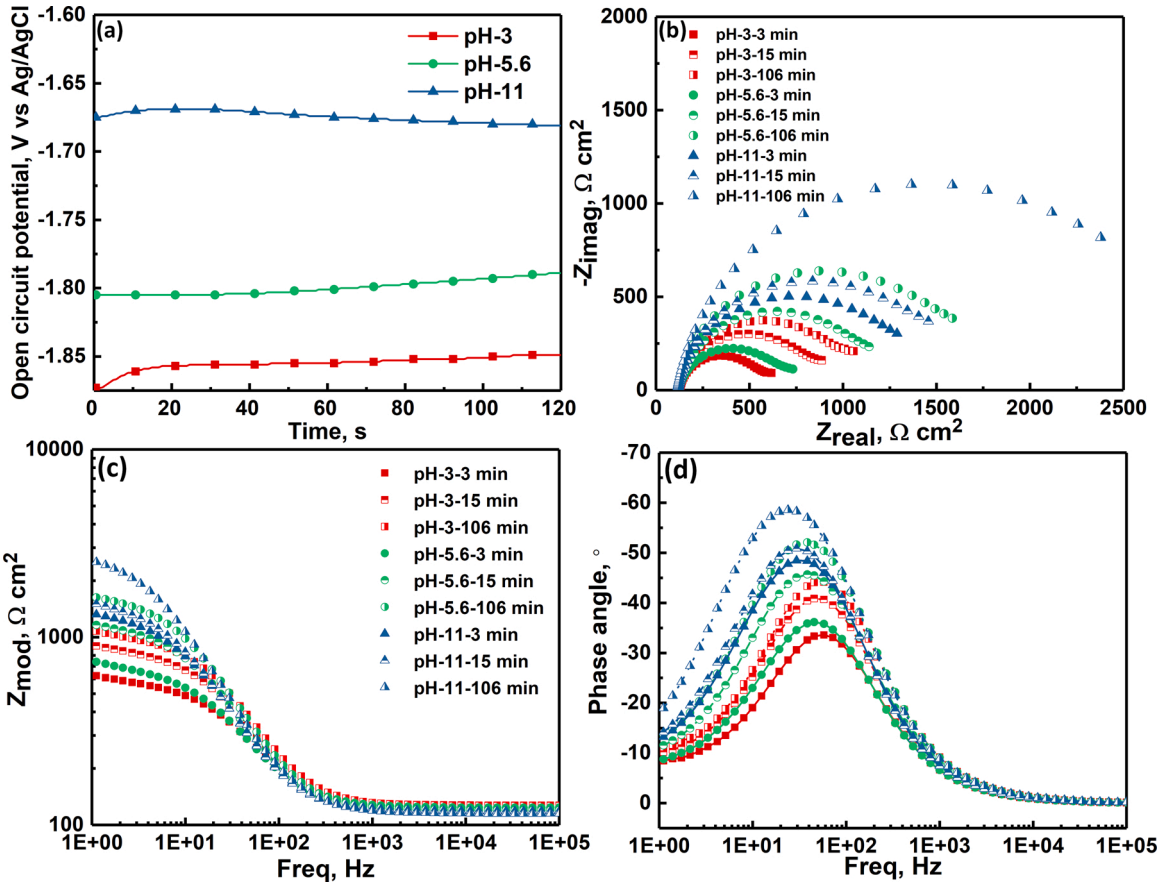

Fig. 2. (a) OCP of HP-Mg in 0.05 M NaCl solution with different initial pH and EIS results of HP-Mg after various immersion time in 0.05 M NaCl of different initial pH: (b) Nyquist plots, (c) modulus value plots, and (d) phase angle plots.

software (SPECTROLAB). The samples were grinded with emery papers up to 1200 grit, rinsed with ethanol, and dried with cold compressed air before each test.

All the electrochemical measurements were carried out in 0.05 M NaCl solution with different initial pH. The initial pH of 0.05 M NaCl without any pH adjustment was 5.6 ± 0.2 (owing to naturally dissolved CO_2 from air), which is denoted as neutral NaCl solution in the following. In order to prevent the influence of compounds that constitute pH buffers, that can interact with Mg^{2+} ions or adsorb on Mg surface, the acidic NaCl solution (pH 3) and the alkaline NaCl solution (pH 11) were prepared by adding 0.1 M HCl and NaOH solution, respectively. The pH adjustment for all testing solutions was conducted by Hanna Metrohm-691 pH meter. The open circuit potential (OCP) and EIS measurements were performed using Gamry Reference 600 potentiostat with three electrodes arrangement. HP-Mg with 1 cm^2 exposed surface area served as a working electrode. Pt coiled wire and KCl-saturated Ag/AgCl electrode were respectively used as counter electrode and reference electrode. The EIS measurements at OCP were conducted under potentiostatic mode and the applied perturbation voltage was 10 mV_{rms}. The EIS measurement was started from 100 kHz and ended at intermediate frequency (1 Hz) in order to avoid the latent influence on Mg surface caused by possible polarization during low frequency measurement. All the measurements were triplicated to assure data reproducibility and all of the impedance spectra were consistent with the Kramers-Kronig transfer relations [31,32]. The corrosion rates of HP-Mg in different pH media were calculated via the weight loss of HP-Mg after 2 h immersion in 3.5 wt. % NaCl solution with different initial pH. Higher concentration of NaCl was adopted to get sufficient weight loss for accurate calculation.

The HP-Mg electrode after EIS measurement was characterized by scanning electron microscope/ focused ion beam system (SEM/FIB, Tescan LYRA3) equipped with energy dispersion spectrometer (EDS, Oxford Aztec Ultim 100) and transmission electron microscope (TEM, FEI Titan 80–300 & Thermo Scientific Talos). After removal from the testing electrolyte, the sample was rinsed with ethanol, dried with a stream of cold nitrogen and then immediately stored into a vacuum desiccator. Sputter coating with gold was performed on the sample surface prior to the characterization by SEM/FIB. The cross-section lamellae for TEM were prepared by FIB in-situ lift-out technique. In order to minimize beam damage during ion beam thinning and polishing procedures, a platinum protective layer was deposited by ion beam to the region of interest for TEM observation. The accelerating voltage of FIB ion beam was gradually decreased during the lamellae preparation. The final thicknesses of the cross-section lamellae were approximately 100 nm and they were welded on to a copper grid. The overview of the lamellae was carried out under scanning transmission electron (STEM) mode in SEM and the delicate microstructure of surface film/Mg interface was observed with the TEM in STEM mode with 300 kV accelerating voltage. Elemental maps for Mg and O were obtained in SEM at a 30 kV accelerating voltage to reduce the possibility of corrosion film degradation during data acquisition. The electron diffraction patterns in the selected area were obtained in TEM and compared with the published diffraction patterns for Mg, MgO and $Mg(OH)_2$ to ensure the phase composition of characterized area. Then, the thicknesses of $Mg(OH)_2$ and MgO layer were measured by ImageJ software.

The local pH was measured via a glass pH microelectrode with a tip diameter of 10 μm (Unisense) with an external Ag/AgCl reference electrode. The local dissolved O_2 concentration was measured by Fire-StingO2 fiber-optic O_2 micro-sensor coupled with an O_2 concentration meter (Pyroscience). HP-Mg with approximately 2 mm diameter was

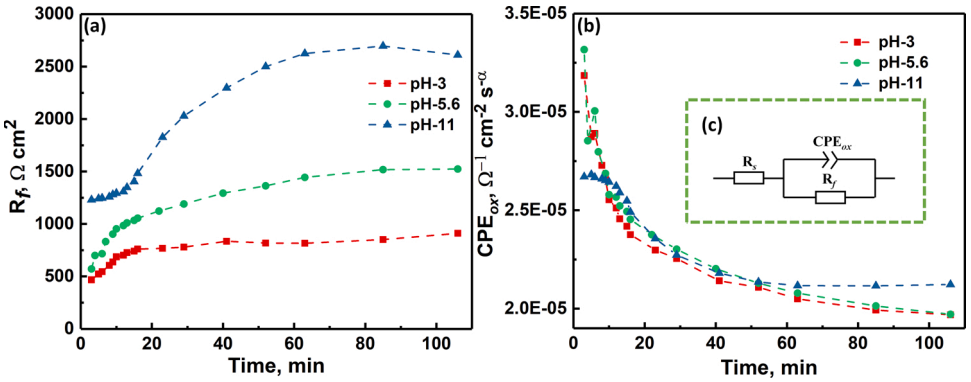

Fig. 3. Fitting results of HP-Mg after various immersion time in 0.05 M NaCl with different initial pH: (a) resistance of surface film, (b) CPE*ox*, and (c) equivalent circuit.

embedded in epoxy resin and fixed in a sample holder. Both, the pH microelectrode and O_2 concentration meter, were fixed at 50 μm above the HP-Mg sample by using a custom made dual head stage to simultaneously monitoring the evolution of local pH and dissolved O_2 concentration. SVET system (Applicable Electronics) was used to position and move the probes, sample and the video camera. The relevant data was acquired by LV4 software (Science Wares) in parallel with PyroOxygenLogger software (Pyroscience).

3. Results and discussion

3.1. Electrochemical impedance measurement

3.1.1. Influence of initial pH on evolution of EIS for HP-Mg

The OCP and EIS plots for HP-Mg in NaCl solution with initial pH of 3, 5.6 and 11 are presented in Fig. 2 and Fig. S1. Fig. 2a illustrates evolution of the OCP of HP-Mg at different pH of NaCl solutions. The OCP in acidic NaCl solution is more negative than that in neutral NaCl solution. Acidic NaCl solution (initial pH 3) was obtained by adding HCl solution, thus the concentration of Cl^- is slightly higher than 0.05 M, which can slightly increase the corrosion rate. Moreover, according to the corrosion rate of HP-Mg in 3.5 wt. % NaCl solution with different initial pH (Table S1), higher amount of H^+ induces faster corrosion, resulting in more negative OCP. The OCP of HP-Mg in alkaline NaCl solution is the most positive among the three tested pH. The initial pH of alkaline NaCl solution is 11. It is above the critical pH of thermodynamically stable $Mg(OH)_2$ formation, which is typically around 10.2–10.5 [33]. Accordingly, the corrosion of HP-Mg in alkaline NaCl solution is slower than that in the neutral solution, leading to relatively positive OCP.

EIS measurements were consecutively performed to monitor the evolution of the HF time constant at the initial stage of immersion. 17 EIS plots were obtained for each testing condition within two hours of immersion. The representative EIS plots of HP-Mg after 3, 15 and 106 min immersion times in NaCl solutions with different pH are normalized and displayed in Fig. 2b–d. Obviously, the increase in immersion time leads to expansion of the HF capacitive loop, which can be attributed to the corrosion of HP-Mg and the following growth of surface film (MgO and $Mg(OH)_2$). As illustrated in Fig. 2c, the |Z| values at lower frequencies on HP-Mg soaked in acidic NaCl solution are less than the corresponding |Z| values in neutral and alkaline NaCl solution. With the increase of immersion time, these |Z| values associated to different initial pH are increasing. The |Z| value in alkaline NaCl solution is the highest, manifesting the surface film formed on HP-Mg in alkaline NaCl solution is the most protective.

The equivalent circuit displayed in Fig. 3c was adopted to fit the measured impedance spectra. The fitted resistance values are depicted in Fig. 3a. During the first 20 min, the surface film resistance in the alkaline NaCl solution grows slowly. After that, the enhancement is accelerated and the resistance achieves the highest value at 85 min. By contrast, the change of surface film resistance for HP-Mg in the neutral and acidic NaCl solution follows a very similar tendency, which differs from that in the alkaline NaCl solution. The growth is rapid in the initial 20 min and then becomes stabilized. The surface film resistance in the acidic NaCl solution is always the lowest during the whole immersion time and that in the alkaline solution is the highest. The CPE_{ox} parameters (Q and α) are also fitted by the equivalent circuit (Fig. 3c) and the CPE_{ox} value (Q) is presented in Fig. 3b, showing a decreasing tendency with the increase of immersion time. The value of CPE_{ox} in acidic and neutral NaCl solution are very close, which are higher than that in alkaline solution during the first 10 min. Nevertheless, the final CPE_{ox} value in alkaline NaCl solution is the highest, indicating the minimum decrease of CPE_{ox} value in alkaline NaCl solution during the whole immersion time.

3.1.2. Influence of initial pH on film thickness calculated from EIS

The surface film formed on HP-Mg in NaCl solution is mainly composed by $Mg(OH)_2$ and MgO [26,34]. The $Mg(OH)_2$ layer does not possess capacitive characteristic due to its porous structure. Thus, if we assume the inner MgO layer acts as an ideal capacitor, the thickness of MgO layer can be deduced from the effective capacitance of time constant by Eq. (1) [9],

$$d_{ox} = \frac{\varepsilon\varepsilon_0}{C_{eff}} \tag{1}$$

Where d_{ox} represents the thickness of MgO layer formed on HP-Mg, ε_0 is the permittivity of vacuum (8.854×10^{-14} F cm^{-1}), ε is the dielectric constant for MgO, which is taken to be 9 [9]. C_{eff} (F cm^{-2}) is the normalized effective capacitance of MgO layer if it acts as a capacitor, which can be extracted from CPE_{ox}. As shown in the equivalent circuit used for fitting (Fig. 3c), the time constant is normally represented as a constant-phase element (CPE) rather than ideal capacitor, because the phase angle is not exactly −90° (Fig. 2d). The overall impedance Z can mathematically be expressed as,

$$Z = R_s + \frac{R_f}{R_f(j\omega)^{\alpha}Q + 1} \tag{2}$$

Where R_s and R_f represent solution resistance and film resistance, Q and α are the CPE_{ox} parameters, ω is angular frequency. Based on Eq. (2), several works have been done to clarify the suitable conversion formula from CPE to effective capacitance C_{eff} [35–37], which are expressed as,

$$C_B = Q^{1/\alpha}\left(\frac{1}{R_s} + \frac{1}{R_f}\right)^{(\alpha-1)/\alpha} \quad \text{(Surface distribution)} \tag{3}$$

$$C_{HM1} = Q(\omega_m'')^{(\alpha-1)} \quad \text{(Normal distribution)} \tag{4}$$

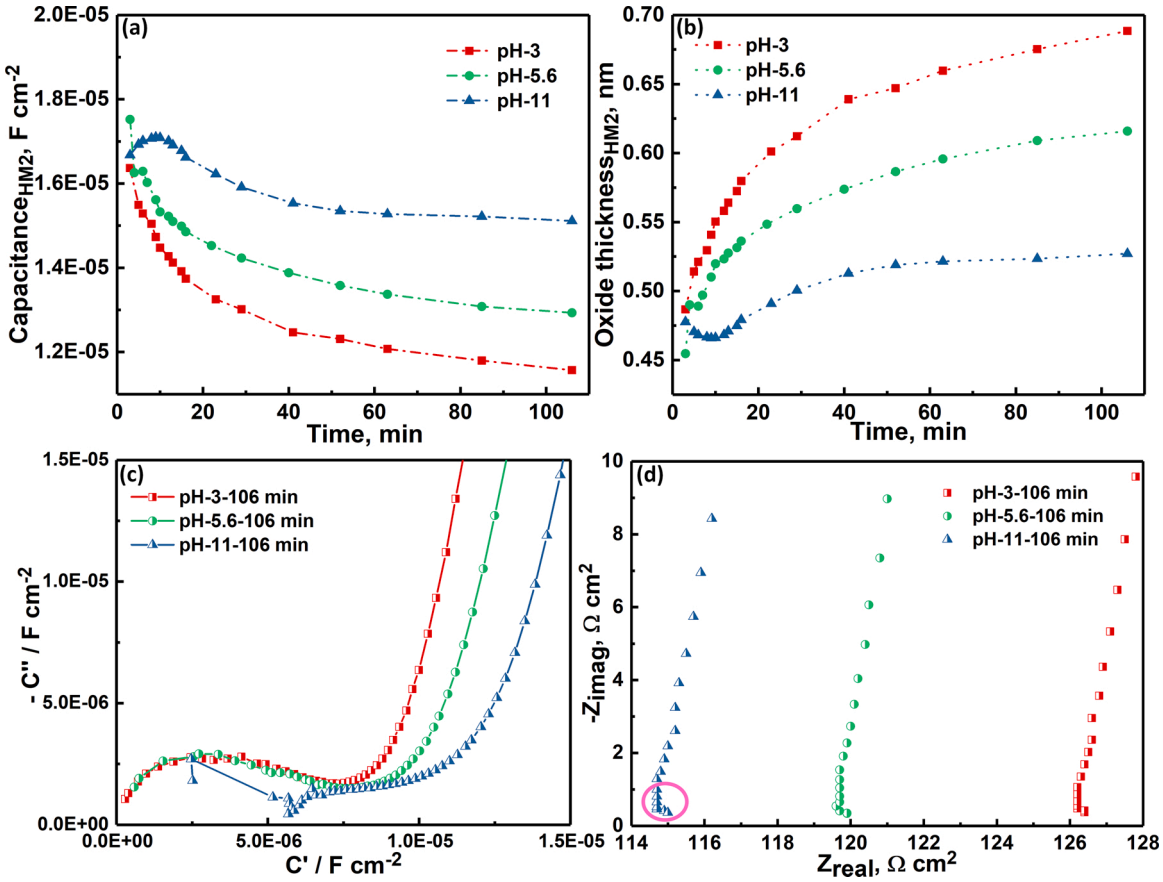

Fig. 4. (a) Effective capacitance and (b) thickness of oxide film on HP-Mg in 0.05 M NaCl with different initial pH, calculated by Eqs. (5) and (1); (c) Cole-Cole plots corresponding to the EIS results of HP-Mg presented in Fig. 2 and (d) magnification of Fig. 2b.

$$C_{HM2} = Q^{1/\alpha} R_f^{(1-\alpha)/\alpha} \text{ (Normal distribution)} \quad (5)$$

Eq. (3) is proposed by Brug et al. [35], where C_B represents the effective capacitance calculated from this equation. Eq. (5) is derived from Eq. (4) and both of them are deduced from the equation proposed by Hsu and Mansfeld [36,37], where ω''_m represents the characteristic angular frequency at which the imaginary part of the impedance reaches maximum and other symbols have the same meaning as aforementioned. The applicable conditions of these equations were thoroughly investigated by Hirschorn et al. [38]. The Brug's equation is adequate for the calculation of time constant with surface distribution, where the total impedance response is represented by the impedance response distributed along the electrode surface. Whereas, the equation and its derivate proposed by Hsu and Mansfeld are suitable for time constant with a normal distribution, which refers to the total impedance represented by the impedance response from different parts of the layer distributed in the direction normal to the electrode. As indicated by Jorcin et al. [39], the capacitance of oxide film formed on AZ91 Mg alloy shows a normal time constant distribution and is independent on the position where the local impedance result obtained. Thus, Eqs. (4) and (5) are more suitable for the calculation of effective capacitances for MgO layer on HP-Mg. The effective capacitance calculated from Eq. (5) is presented in Fig. 4a. The effective capacitances of oxide film decrease with the increase of immersion time except for that in alkaline NaCl solution within the first 10 min. The increase of effective capacitance in the initial period may be due to the progressive conversion of the air-formed film into the surface film formed by corrosion reaction in NaCl solution. In particular, the transition process is more pronounced in alkaline NaCl solution than that in acidic and neutral NaCl solution because the corrosion of Mg is relatively slow and moderate in alkaline environment. The same tendency can also be observed in Fig. S2, which exhibits the effective capacitance calculated via Eqs. (3) and (4). Both of Fig. 4a and Fig. S2 reveal that the final effective capacitance of oxide film is the lowest in acidic solution and the highest in alkaline NaCl solution. The thickness of oxide films is calculated via Eq. (1) and displayed in Fig. 4b. Surprisingly, the oxide film formed on HP-Mg in the acidic NaCl solution is the thickest whilst the surface film resistance (Fig. 3a) and capacitance (Fig. 4a) are the lowest. Moreover, the oxide film thickness calculated by Eqs. (1) and (5) is much less than the reported thickness for oxide film on Mg and Mg alloy [9,40–43]. In the research work of Leleu et al. [43] and Gomes et al. [9], they adopt a special method to extract effective capacitance based on a unique graphical representation of EIS data, Cole-Cole plot or so-called complex-capacitance plot, which was proposed to extract effective capacitance for passive film on passive metal [44,45]. As indicated in the study [44], the extrapolation of the high-frequency data to the real part of C value can be used to calculate the thickness of ZrO_2 film on pure Zr. The calculated results are validated by the thickness value determined via XPS. However, the error on the calculation of the effective capacitance for MgO film (a few nanometers) is big, as referred by Nguyen et al. [46]. Moreover, the dispersion of the initial points in the high-frequency range makes it impossible to extract accurate effective capacitance [43]. This methodology greatly depends on the estimation of electrolyte resistance and the accuracy of the data points in the high-frequency range. Fig. 4c displays the Cole-Cole plots corresponding to the EIS results of HP-Mg presented in Fig. 2. There are several scattered points for the case after 106 min immersion in alkaline NaCl solution, since the initial few points in the high-frequency range of EIS plot is scattered, as shown in Fig. 4d. This phenomenon can also be observed in acidic and neutral NaCl solution, which may also lead to inaccurate estimation of

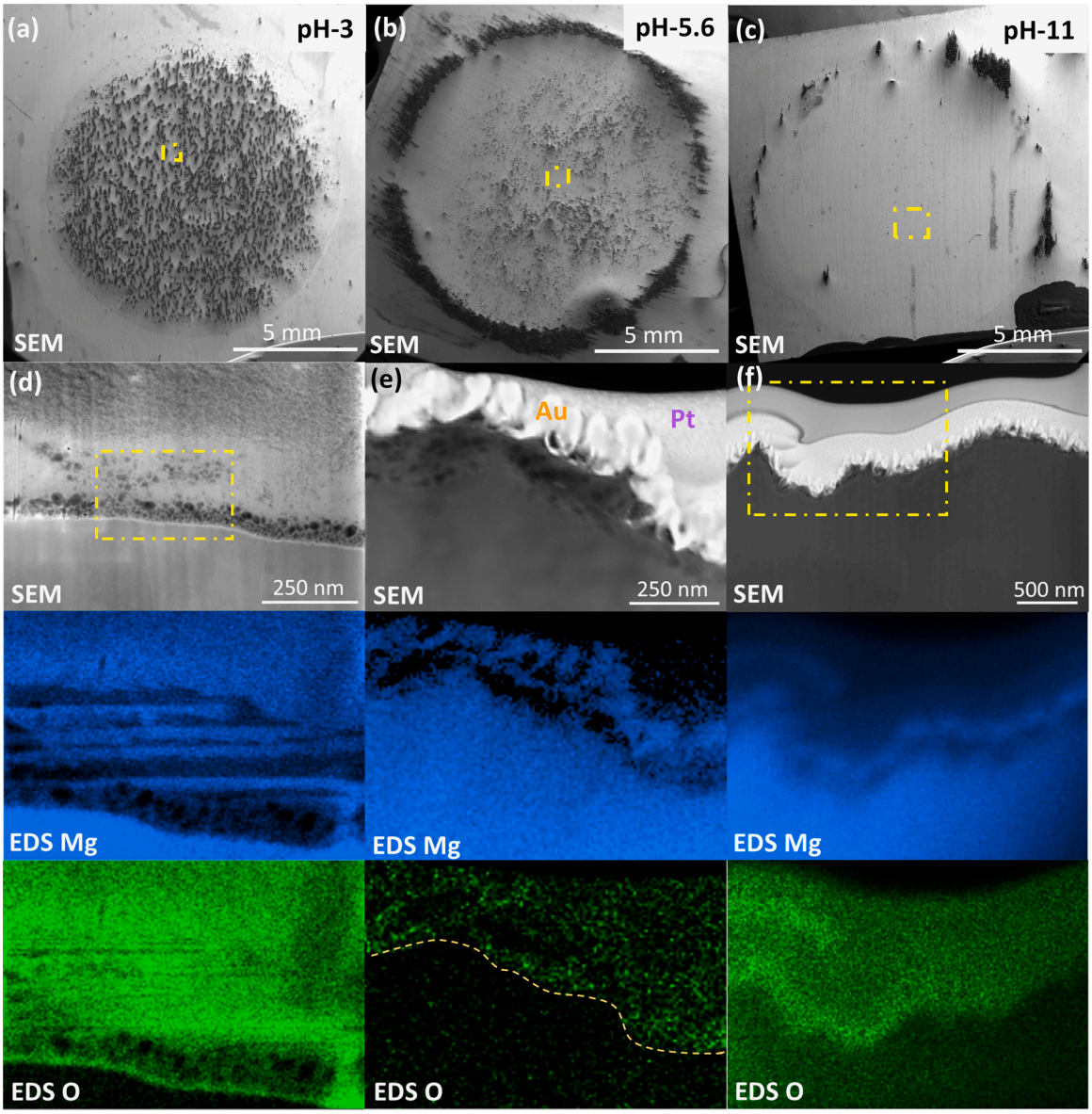

Fig. 5. Secondary electron image of corroded surface for HP-Mg in 0.05 M NaCl solution of (a) initial pH 3, (b) initial pH 5.6 and (c) initial pH 11; Dark field image and EDS mapping results for HP-Mg in 0.05 M NaCl solution of (d) initial pH 3, (e) initial pH 5.6 and (f) initial pH 11. (Corresponding element distribution of Au, C and Pt on the corrosion section of HP-Mg can be found in Fig. S3.)

electrolyte resistance and the choice of high frequency limit of impedance, C_∞, which theoretically can be calculated from the integral formula of the power law model for the HF time constant or determined by extrapolation of the HF time constant presented in Cole-Cole plot [44]. In the study of Leleu et al. [9] and Gomes et al. [43], the points at different frequencies (< 42 kHz and 15 kHz) were adopted to calculate the thickness of MgO film on Mg. However, as shown in Fig. 4c, it is not straightforward to obtain the value of C_∞ via this method for our case. Nevertheless, it is notable that Fig. 4c also indicates the same tendency as shown in Fig. 4a and Fig. S2. The effective capacitance of the MgO film in acidic NaCl solution is the lowest, implying the thickness of the MgO film in acidic NaCl solution is the thickest according to all of these calculation methods. The differences between calculated results and the observed thickness may be explained by the discrepancy between the geometric surface area of working electrode adopted for the calculation (1 cm^2) and the actual surface area of HP-Mg exposed to NaCl solution for a while. Moreover, this calculation is based on the assumption that MgO film can act as ideal capacitor. Nevertheless, the structure of MgO film formed on various Mg and its alloys in different solution environment is not completely the same. Hence, the calculated thickness herein is used merely to show the difference of MgO film on HP-Mg in acidic, neutral and alkaline NaCl solution. More accurate calculation methods for MgO film thickness need further detailed investigation.

3.2. *Surface film morphology in NaCl solution*

The corroded surfaces of HP-Mg in acidic, neutral and alkaline NaCl solution were characterized by SEM as respectively presented in Fig. 5. As displayed in Fig. 5(a–c), the highest amount of black spots left by corrosion process present on the surface of HP-Mg after immersed in acidic NaCl solution indicating the corrosion of HP-Mg in acidic NaCl solution is more severe than that in other two kinds of NaCl solutions. The cross-section lamella of HP-Mg was taken from the marked region via standard lift-out sample preparation procedure and thinning with ion beam. The contrast in the dark field image Fig. 5(d–f) reflects the amount of scattered electron in the specific region, which may be influenced by the mass, the density, the thickness of the sample or even the porosity of the specimen for this case. As shown in Fig. 5d, there is a

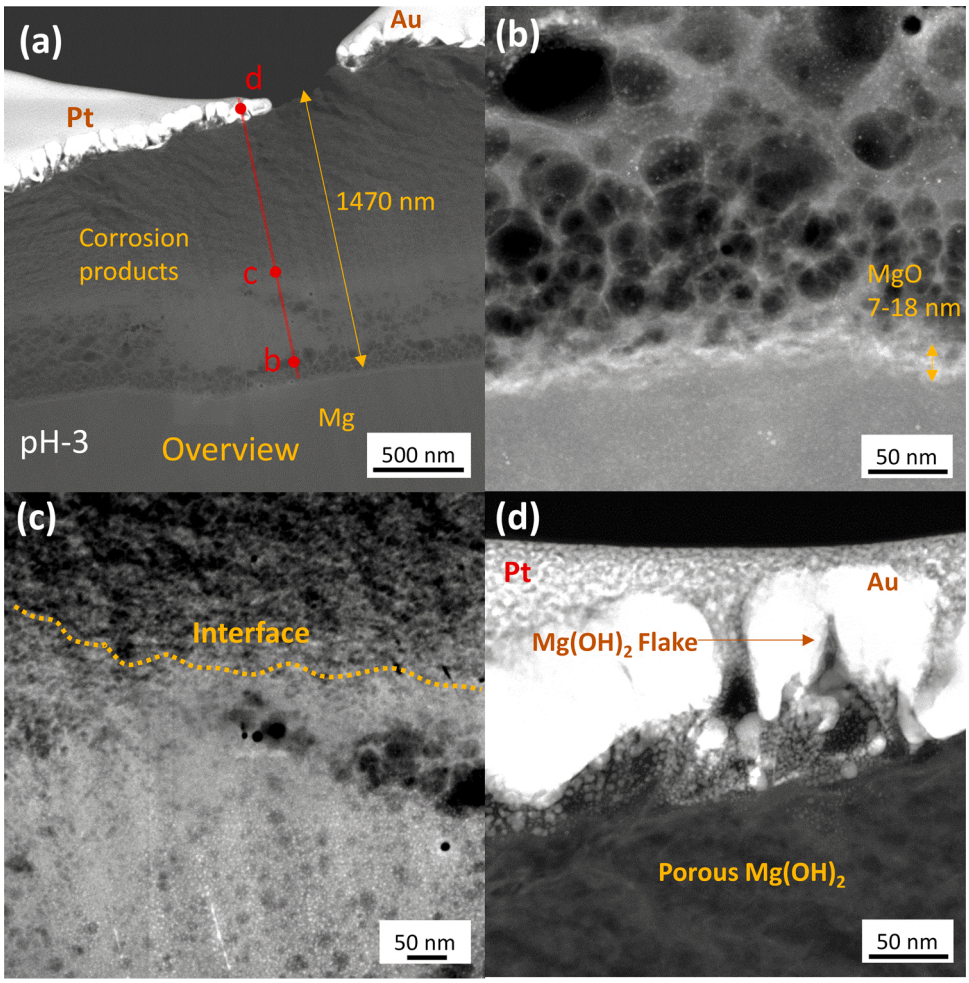

Fig. 6. STEM dark field image on the cross section of HP-Mg after immersion in 0.05 M NaCl pH 3 solution: (a) an overview; (b) the magnified view of point b; (c) the magnified view of point c; and (d) the magnified view of point d.

distinct boundary along the interface between Mg matrix and porous corrosion products when HP-Mg surface was exposed to the acidic NaCl solution. Above the dividing line, the porous layer presents as black holes, where less electron scattering happens. The dividing line is much brighter than the porous layer, suggesting it is a much denser layer. The EDS elemental maps acquired from the region marked in Fig. 5d shows that there is a notable enrichment of O in the interface between Mg matrix and the porous layer. During elemental maps acquisition, there are several lines appearing on the sample, which should be attributed to the degradation of this extremely porous outer layer under medium intensity beam with long time accumulating EDS. Nevertheless, the intensities of Mg and O signal still can be clearly observed. Combining the elemental information and structure information, this inner layer is most likely to be the MgO film which is supported by other techniques in the following results. The elemental information of Au, C and Pt signal was also acquired and used to exclude the possibility that the contrast of the inner layer is caused by the redeposition during FIB thinning procedure, which can be found in Fig. S3a. As represented in Fig. 5e, the surface film formed on the HP-Mg surface in neutral solution is thinner than that formed in acidic NaCl solution and there is also a visible boundary between Mg matrix and the porous layer. On the top of the porous layer, it is supposed to be crystalline $Mg(OH)_2$ flakes covered by sputtered gold according to the EDS elemental maps (Fig. 5e and Fig. S3b). It is mainly composed by Mg, Au, and O. On the top of this $Mg(OH)_2$ flake and sputtered gold layer is the protective Pt layer mixed with C as a consequence of gas deposition system. The enrichment of O signal in the interface between Mg matrix and the porous layer is also observed and there is almost no elemental information found in the porous layer. The surface film formed on HP-Mg surface in alkaline NaCl solution is even thinner than that formed in neutral NaCl solution. The boundary between Mg matrix and the porous layer is almost invisible and needed to be characterized under TEM with higher resolution and magnification.

To acquire more specific microstructure of the surface film formed on HP-Mg, the cross-section lamellae of HP-Mg were analyzed by TEM. Fig. 6 presents the high angle annular dark-field (HAADF) images of the surface film on HP-Mg in acidic NaCl solution. As displayed in Fig. 6a, the surface film of HP-Mg in acidic NaCl solution is relatively thick and the average thickness is 1.5 μm. Along the red line presented in Fig. 6a, several layers with various structures are observed. Fig. 6b displays the microstructure of the region adjacent to Mg matrix. The bottom part is Mg matrix and the top part represents a cellular structure. The bright layer between Mg matrix and the layer with cellular structure is supposed to be the dense MgO layer since it has even stronger contrast than metallic Mg matrix in HAADF image. Nevertheless, the boundary of this layer is ambiguous, which may be the consequence of active corrosion in acidic NaCl solution. Thus, the thickness of this layer can only be roughly estimated as 7−18 nm. Fig. 6c shows a microstructure image of the central region of the surface film. As discussed above, the porous structure in dark field image presents as black hole because fewer scattered electrons are collected from the area. Thus, at least three different structures are distinctly observed in Fig. 6c. The upper region of Fig. 6c displays as more porous structure than the lower region except for the bottom right corner, which shows the same cellular structure as demonstrated in Fig. 6b. Fig. 6d displays the Pt layer and Au layer

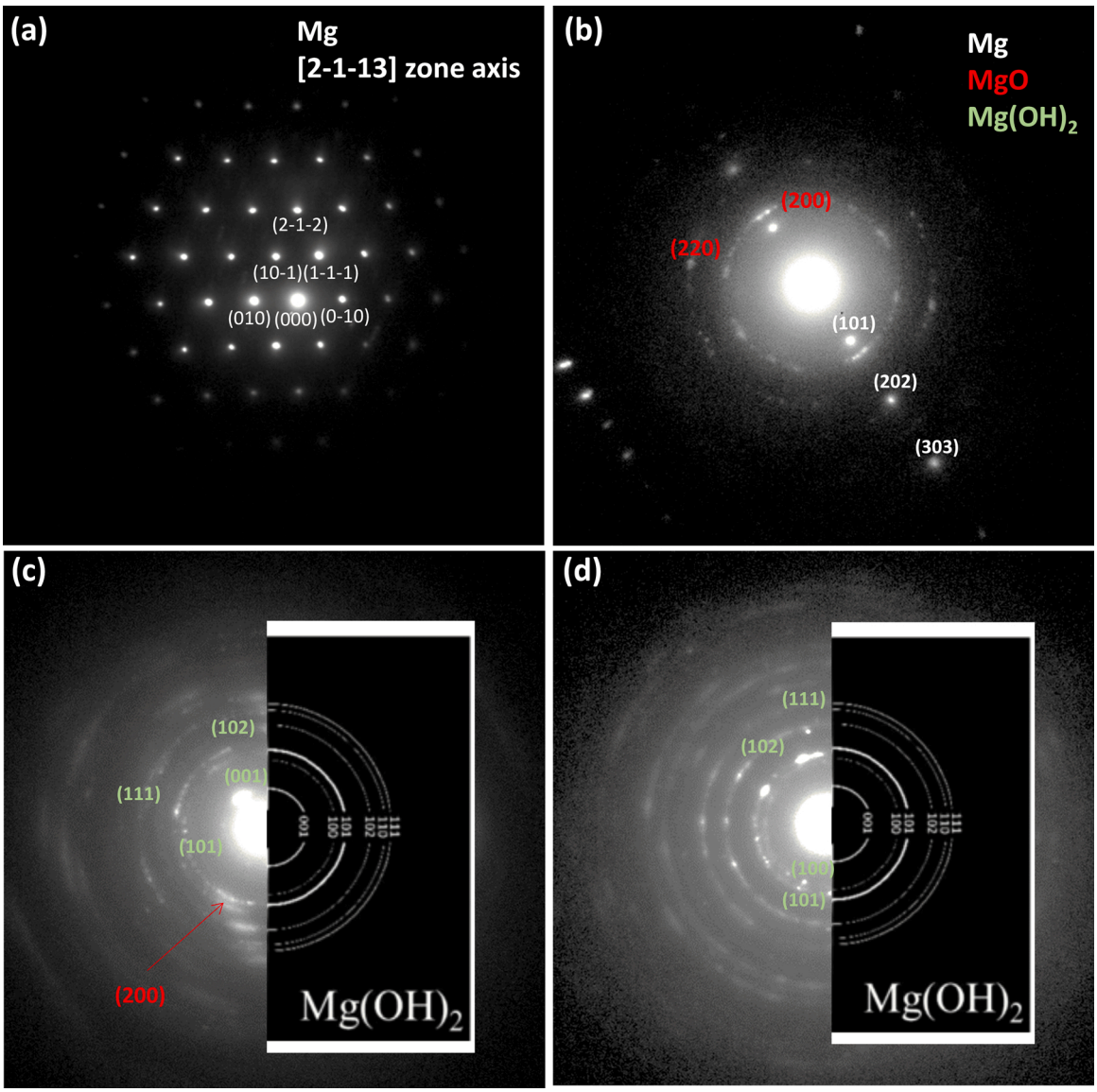

Fig. 7. Diffraction patterns obtained on HP-Mg after immersion in 0.05 M NaCl pH 3 solution from: (a) Mg matrix; (b) the interface between Mg matrix and porous layer; (c) the middle part of the porous layer; and (d) the crystalline $Mg(OH)_2$ flakes. The standard $Mg(OH)_2$ diffraction pattern inserted in the right side of Fig. 7c and 7d are reprinted from reference [49] with permission of Elsevier (Copyright 2015).

artificially deposited on the top of surface film. Crystalline $Mg(OH)_2$ flakes are hidden under the deposited layer. According to its microstructure, the surface film of HP-Mg formed in acidic NaCl solution can be classified as $Mg(OH)_2$ flake layer, a porous layer might be composed by $Mg(OH)_2$, and a relatively dense inner layer might be composed by MgO.

In order to further confirm the composition of the different layers, the electron diffraction patterns for the Mg matrix and specified interfaces were obtained and are presented in Fig. 7. Fig. 7a shows the diffraction patterns of HP-Mg matrix, which is close to the [2-1-13] zone axis. The diffraction patterns shown in Fig. 7b are obtained in the interface between Mg matrix and the porous layer, which is consistent with the MgO (200) and MgO (220) diffraction ring by d-spacing calculation. Meanwhile, the diffraction patterns of Mg are also found in Fig. 7b. The same phenomenon has already been reported in the literature [47,48], which is most likely because the MgO film is too thin. Fig. 7c was obtained from the middle of the porous layer and compared with the standard diffraction rings of $Mg(OH)_2$. Except for the diffraction rings belong to $Mg(OH)_2$, two symmetric diffraction points can be found between with the $Mg(OH)_2$ (101) and $Mg(OH)_2$ (102) diffraction rings, which is from MgO (200) plane. Comparing with the diffraction patterns in Fig. 7c, the diffraction patterns obtained from the top $Mg(OH)_2$ flake (Fig. 7d) does not show any diffraction points belongs to MgO. It is well fitted with the standard diffraction rings of $Mg(OH)_2$ reported in literatures [42,49]. Thus, the corrosion product films formed on HP-Mg in acidic NaCl solution is certainly composed by crystalline $Mg(OH)_2$ flake layer, a porous layer mainly composed by $Mg(OH)_2$, and a thin MgO layer close to Mg matrix, which is coherent with the corrosion products film of Mg reported elsewhere [34,42,50].

Fig. 8 displays the surface film formed on HP-Mg in neutral NaCl solution, which is much thinner and more uneven than that in the acidic NaCl solution. A deep cave left by preferential corrosion was found on the cross-section lamella presented in Fig. 8a. The average thickness of the corrosion products film is around 178 nm and the highest thickness measured in Fig. 8b is 260 nm, which is much thinner than that formed on HP-Mg in acidic NaCl solution. The top layer of the surface film is also made up of $Mg(OH)_2$ flakes. A porous $Mg(OH)_2$ layer is found under Mg $(OH)_2$ flakes. As indicated in Fig. 8c, the thickness of the MgO layer is around 3–6 nm, which is also thinner than that formed in the acidic NaCl solution. Additionally, the boundary of this MgO layer with Mg

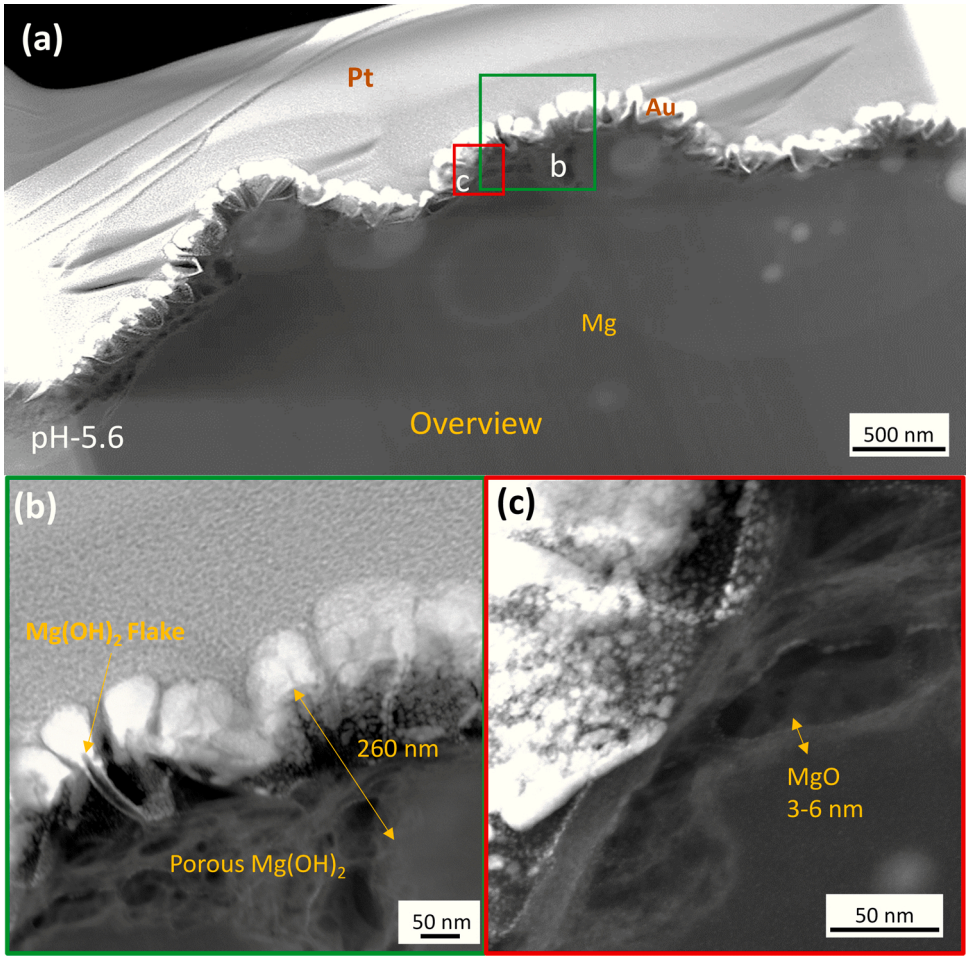

Fig. 8. STEM dark field image on the cross section of HP-Mg after immersion in 0.05 M NaCl pH 5.6: (a) an overview; (b) the magnified view of the marked area in green color; and (c) the magnified view of the marked area in red color.

matrix is more distinct and uniform than that presented in Fig. 6b. Thus, the MgO layer formed in neutral NaCl solution may be more protective than that formed in acidic NaCl solution, leading to higher surface film resistance detected by EIS (Fig. 3a).

Fig. 9a and b show the overview of the surface film of HP-Mg formed in an alkaline NaCl solution. The film is very thin and the boundary between the porous $Mg(OH)_2$ and Mg matrix is fuzzy and indistinct. The average thickness of surface film is around 100 nm. As presented in Fig. 9c, the surface film formed in alkaline NaCl solution is the thinnest among that formed in these NaCl solutions with different pH. The contrast between MgO layer and Mg matrix is weak, which makes the accurate measurement of MgO layer thickness difficult. A rough estimation suggests that the MgO layer formed in alkaline NaCl solution is less than 3 nm thick. Fig. 9d shows that the top layer formed on HP-Mg in alkaline NaCl solution is also crystalline $Mg(OH)_2$ flake.

The morphologies of surface films formed on HP-Mg in NaCl solution of different initial pH manifest that the dense MgO layer formed in acidic NaCl solution is unexpectedly thicker than that in neutral NaCl solution, which agrees with the calculated results obtained by EIS measurement. Besides this, the surface films formed on HP-Mg in different NaCl solutions possess differing characteristics, which likely affect the film resistance estimated from EIS measurements. Although the thickness of the surface film formed on HP-Mg is markedly higher at pH 3 than at pH 11, the film resistance is measurably lower.

3.3. *Local pH and dissolved O_2 concentration*

$Mg(OH)_2$ is supposed to be unstable in acidic solution environment. Thus, it is counterintuitive that the layer formed on the surface of HP-Mg in NaCl solution of pH 3 is even thicker than that in NaCl solution of pH 5.6 and 11. The mentioned pH is the initial bulk pH, which typically does not reflect the real situation at the interface between HP-Mg and electrolyte. To clarify this point, the local pH of the region 50 μm above sample surface was measured by pH-microelectrode. The local concentration of dissolved O_2 in the same region was also measured via fiber-optic micro optode in order to acquire information about the growth of surface film and the corrosion of Mg. Fig. 10 shows the real-time surface condition of HP-Mg during immersion in different NaCl solutions. As displayed in Fig. 10a, there are multiple H_2 bubbles generated on the HP-Mg surface in acidic NaCl solution after 180 s immersion, indicating ongoing Mg corrosion. Similarly, hydrogen evolution is also visible in neutral NaCl solution after 180 s immersion as shown in Fig. 10b, slightly smaller amount of H_2 bubbles. Nevertheless, no visible H_2 bubbles are found on the HP-Mg in alkaline NaCl solution after 180 s immersion (Fig. 10c).

Possible reactions happening in acidic, neutral or alkaline NaCl solutions are listed below.

$$\text{Anodic reaction: } Mg \rightarrow Mg^{2+} + 2e^- \quad (6)$$

$$\text{Cathodic reaction in acidic solution: } 2H^+ + 2e^- \rightarrow H_2 \quad (7)$$

$$O_2 + 4H^+ + 4e^- \rightarrow 2H_2O \quad (8)$$

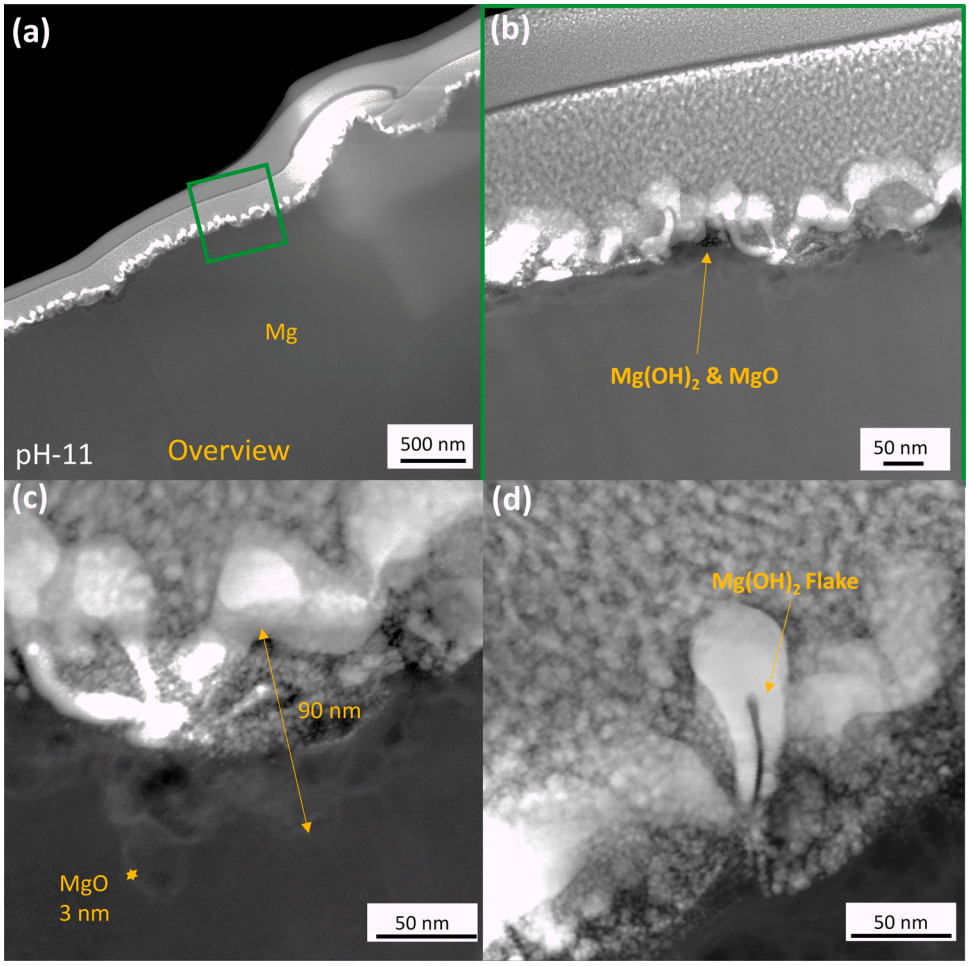

Fig. 9. STEM dark field image on the cross section of HP-Mg after immersion in alkaline 0.05 M NaCl pH 11: (a) an overview; (b) the magnified view of the marked area in green color; (c) the magnified view of (b); and (d) $Mg(OH)_2$ flake formed on the top.

Cathodic reaction in neutral or alkaline solution: $2H_2O + 2e^- \rightarrow H_2 + 2OH^-$ (9)

$$O_2 + 2H_2O + 4e^- \rightarrow 4OH^- \quad (10)$$

The cathodic reaction, like the hydrogen evolution reaction, is always accompanied by the increase of local pH no matter in which kind of solution. The dissolved O_2 is consumed by the cathodic reactions (Eqs. (8) and (10)). Thus, the change of local pH and dissolved O_2 concentration can reflect the intensity of cathodic reaction and corrosion products formation. The local pH and dissolved O_2 concentration of HP-Mg are depicted in Fig. 11.

As shown in Fig. 11a, the first 50 s correspond to the waiting period without electrolyte. In acidic NaCl solution, the local pH increases rapidly from 3 to 10 in 100 s and there is a clear O_2 consumption near the surface (Fig. 11b), indicating that active corrosion of HP-Mg generates favorable conditions for growth of $Mg(OH)_2$ even in NaCl with bulk pH equal to 3. The local pH decreases from 10 to 8 after 300 s, which may correspond to the consumption of OH^- due to crystalline $Mg(OH)_2$ formation or the partial suppression of corrosion activities in the specific location. After that, the local pH is stabilized at around 9, which is a compromise value between the bulk pH 3 and the pH at the corroding interface. Rationally, the local pH closer to Mg surface (probe to sample distance < 50 μm) is expected to be even higher than 9 [51]. Thus, crystalline $Mg(OH)_2$ flakes can be formed at that local pH. The local pH of HP-Mg in neutral NaCl solution also increases sharply from 7 to 11 accompanied by clear reduction of dissolved O_2 concentration. By contrast, the local pH of HP-Mg in NaCl solution with initial pH 11 does not change significantly. The consumption of dissolved O_2 is also slower than that in neutral and acidic NaCl solution. As shown in Fig. 11b, the local concentration of dissolved O_2 is only 2.0 and 1.7 ppm after 180 s immersion in acidic and neutral NaCl solution, respectively, whilst in alkaline NaCl solution it is almost twice of that (3.8 ppm). After 300 s immersion, the local concentration of dissolved O_2 in neutral NaCl solution starts to increase gradually and reaches 4 ppm after 1800s. The corresponding local pH of HP-Mg in neutral NaCl solution starts to decrease after 300 s immersion. By comparison, the O_2 concentration keeps at a relatively low level in acidic NaCl solution. The decrease of local O_2 concentration indicates that the oxygen reduction reaction took place at three initial pH conditions. However, it shows slower kinetics of oxygen consumption in alkaline media than in acidic and neutral media, which may be attributed to the barrier effect of $Mg(OH)_2$ film formed in alkaline environment [52]. The acidic bulk pH promotes HP-Mg corrosion but the alkaline local pH allows the formation of stable $Mg(OH)_2$ on the surface of HP-Mg, leading to the thickest but the least protective surface film. The local pH in alkaline NaCl solution keeps decreasing slowly during 1800s immersion, which is likely the consequence of competition between the influence of dissolved CO_2 and cathodic reaction of HP-Mg on local pH. As represented in Fig. 3a, the resistance of surface film in the alkaline solution shows a plateau in the initial 20 min. There also might be a competition between the film growth and the reaction with dissolved CO_2 [53]. The concentration of dissolved O_2 in alkaline NaCl solution changes slowly and maintains a relatively high value, demonstrating the corrosion as well as the corrosion products formation of HP-Mg in alkaline NaCl solution is slower. As shown in Table. S1, the corrosion rate of HP-Mg in acidic NaCl solution is

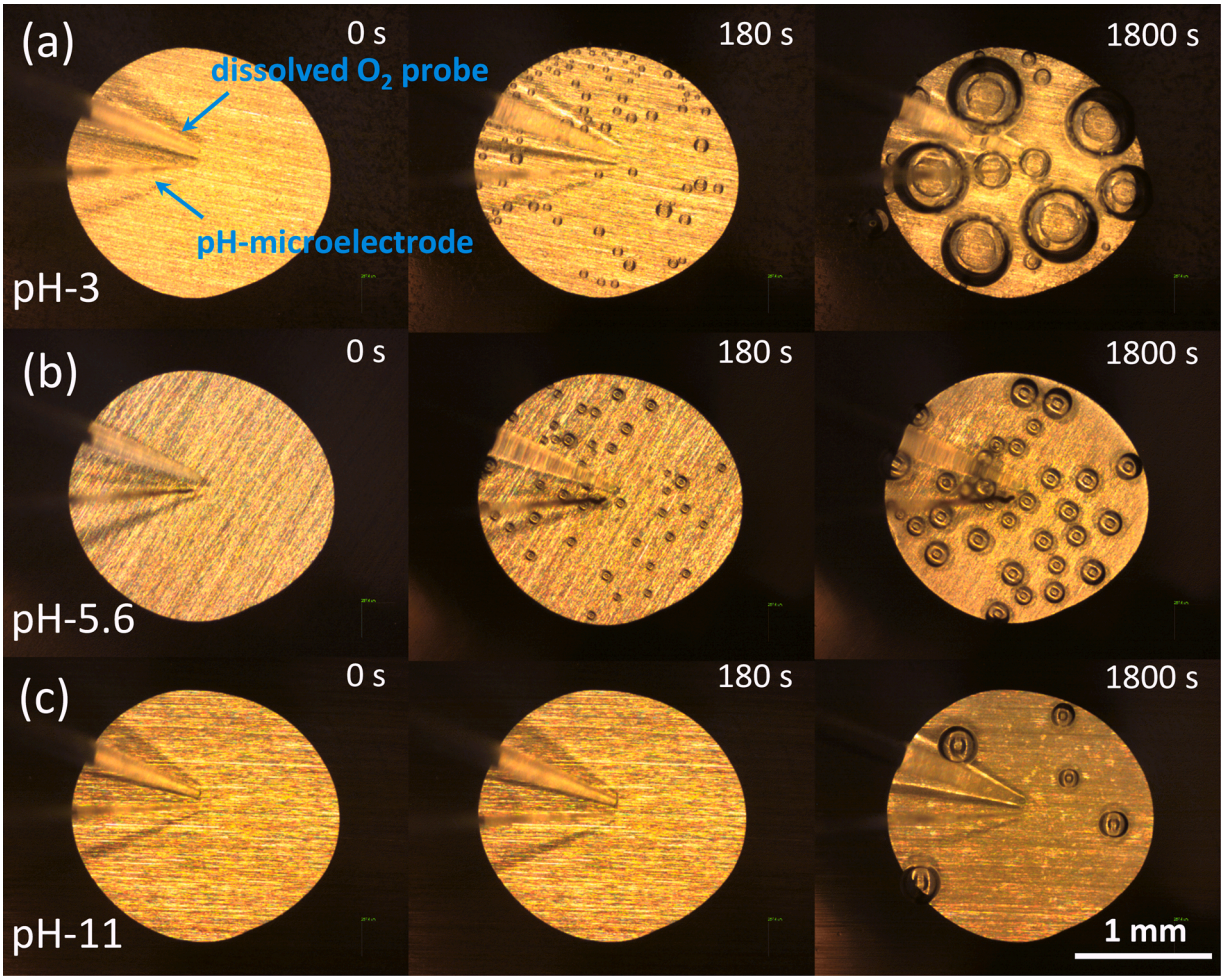

Fig. 10. Surface morphology of HP-Mg during immersion in (a) acidic, (b) neutral, and (c) alkaline NaCl solution. (Two microprobes, pH and O_2 sensitive, are visible in the left central part of each micrograph.)

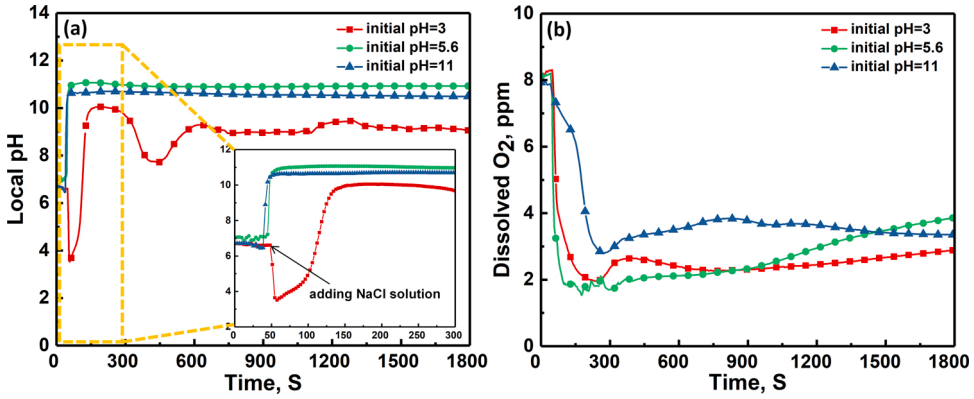

Fig. 11. (a) Local pH and (b) dissolved O_2 concentration over HP-Mg in NaCl solutions of different initial bulk pH. The results were obtained in the region that is 50 μm above sample surface.

0.049 mg cm^{-2} h^{-1}, whilst that in alkaline NaCl is 0.015 mg cm^{-2} h^{-1}. Therefore, more corrosion products (MgO and $Mg(OH)_2$) are expected formed in the acidic solution than in the neutral and alkaline solutions, as demonstrated in Figs. 5–9. The result is in agreement with the calculated MgO thickness based on the assumption that the HF time constant originates from surface film, as indicated in Fig. 4.

3.4. Discussion on the origin of the high frequency time constant

According to the fitting results presented in Fig. 4a, the HF time constant of HP-Mg in acidic NaCl solution exhibits the lowest effective capacitance and should be attributed to the highest film thickness. As clearly illustrated in Figs. 6b and 8 c, the thickness of MgO formed in the acidic NaCl solution is clearly higher than that formed in the neutral solution, being fully consistent with the calculation results shown in

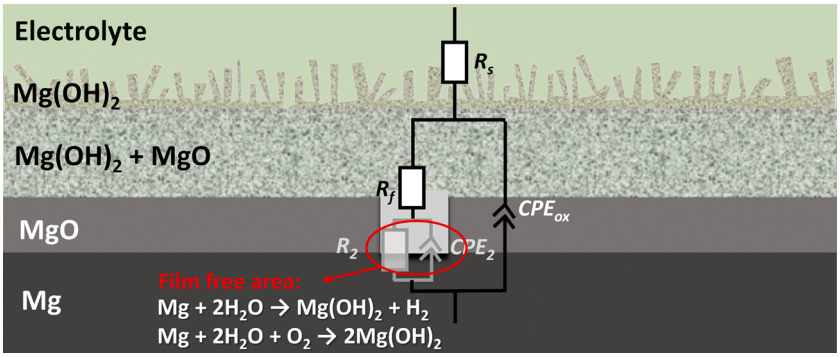

Fig. 12. Schematic illustration of surface film and correlated equivalent circuit elements on HP-Mg in 0.05 M NaCl solution.

Fig. 4b. Therefore, the capacitance of the HF time constant most possibly originates from the oxide film. The continuous MgO film is an insulator, thus implying the resistance of MgO would not be directly reflected as the surface film resistance. However, the surface of Mg is not fully covered by MgO. The resistance of the HF time constant mentioned here is the resistance associated to the MgO film-free area, namely, the defects of MgO film. It depends not only on the structure and thickness of the surface film but also on the fraction of film-free area. The corrosion only happens in the MgO film-free area because the transport of electron is rather improbable through the dielectric MgO film. The corrosion of HP-Mg in acidic NaCl solution is the most active in the circumstance of a thickest oxide film, indicating there should be a largest fraction of defects (or film-free area). In this case, the surface film resistance in acidic NaCl solution is the lowest. Accordingly, the charge transfer resistance in parallel with double layer capacitance is supposed to be represented by the second time constant. Certainly, the confirmation of the physical interpretation for the second time constant needs to be further investigated and will be discussed in our future works. Based on the results presented in this work, the schematic illustration of surface film and correlated equivalent circuit elements concerning HP-Mg in NaCl solution is demonstrated in Fig. 12.

4. Conclusions

In this work, the physical interpretation of high frequency time constant in EIS of Mg immersed in NaCl is thoroughly investigated. The HF time constant is ascribed to the surface film resistance in parallel with the oxide film capacitance. The corresponding equivalent circuit model is proposed.

The surface film on Mg was investigated at different pH of NaCl solutions. EIS confirms the different corrosion activity of Mg in solutions with pH 3, 5.6 and 11. Interestingly, TEM characterization indicates that the surface film formed on Mg in the pH 3 solution is the thickest comparing to that in pH 5.6 and pH 11 solution. This experimentally observed tendency is consistent with the calculations based on the HF capacitive loop in the EIS plots.

Local pH and dissolved oxygen concentration were measured over the surface of corroded Mg in NaCl with three different pH. Local alkalization was observed for all the samples, even for the one with bulk pH 3. Thus, the thickest surface film formed in the acidic solution, confirmed by TEM, is attributed to the high local pH (above 9) and relatively high oxygen consumption in the vicinity of Mg surface.

This work will continue in order to elaborate on the origin of the middle frequency time constant in EIS spectra measured on Mg.

CRediT authorship contribution statement

Linqian Wang: Conceptualization, Investigation, Validation, Writing - original draft, Writing - review & editing. **Darya Snihirova:** Conceptualization, Supervision, Writing - review & editing. **Min Deng:** Conceptualization, Investigation, Writing - review & editing. **Cheng Wang:** Investigation, Writing - review & editing. **Bahram Vaghefinazari:** Conceptualization, Writing - review & editing. **Gert Wiese:** Investigation, Writing - review & editing. **Mark Langridge:** Investigation, Writing - review & editing. **Daniel Höche:** Conceptualization, Supervision, Writing - review & editing. **Sviatlana V. Lamaka:** Conceptualization, Supervision, Writing - review & editing. **Mikhail L. Zheludkevich:** Conceptualization, Supervision, Writing - review & editing.

Declaration of Competing Interest

The authors report no declarations of interest.

Acknowledgements

The authors would like to acknowledge Mrs. Petra Fischer, Mr. Ulrich Burmester, and Mr. Volker Heitmann for the technical support; Prof. Florian Pyczak for the support in TEM characterization; Dr. Xiang Wu for his assistance in TEM analysis. L. Wang, M. Deng and C. Wang are grateful for the award of fellowship from China Scholarship Council (No. 201706370183, No. 201606370031 and No. 201806310128). Additionally, the authors acknowledge SeaMag project funded by ERA-NET cofund MarTERA.

Appendix A. Supplementary data

Supplementary material related to this article can be found, in the online version, at doi:https://doi.org/10.1016/j.corsci.2021.109501.

References

[1] M.E. Orazem, B. Tribollet, Electrochemical Impedance Spectroscopy, John Wiley & Sons, 2017.
[2] R. De Motte, E. Basilico, R. Mingant, J. Kittel, F. Ropital, P. Combrade, S. Necib, V. Deydier, D. Crusset, S. Marcelin, A study by electrochemical impedance spectroscopy and surface analysis of corrosion product layers formed during CO2 corrosion of low alloy steel, Corros. Sci. (2020), 108666.
[3] M.L. Zheludkevich, R. Serra, M.F. Montemor, K.A. Yasakau, I.M.M. Salvado, M.G. S. Ferreira, Nanostructured sol–gel coatings doped with cerium nitrate as pre-treatments for AA2024-T3, Electrochim. Acta 51 (2005) 208–217.
[4] S. Thomas, N.V. Medhekar, G.S. Frankel, N. Birbilis, Corrosion mechanism and hydrogen evolution on Mg, Curr. Opin. Solid State Mater. Sci. 19 (2015) 85–94.
[5] D. Höche, C. Blawert, S.V. Lamaka, N. Scharnagl, C. Mendis, M.L. Zheludkevich, The effect of iron re-deposition on the corrosion of impurity-containing magnesium, Phys. Chem. Chem. Phys. 18 (2016) 1279–1291.
[6] M. Curioni, F. Scenini, T. Monetta, F. Bellucci, Correlation between electrochemical impedance measurements and corrosion rate of magnesium investigated by real-time hydrogen measurement and optical imaging, Electrochim. Acta 166 (2015) 372–384.
[7] S. Fajardo, G.S. Frankel, Effect of impurities on the enhanced catalytic activity for hydrogen evolution in high purity magnesium, Electrochim. Acta 165 (2015) 255–267.
[8] S.V. Lamaka, B. Vaghefinazari, D. Mei, R.P. Petrauskas, D. Höche, M. L. Zheludkevich, Comprehensive screening of Mg corrosion inhibitors, Corros. Sci. 128 (2017) 224–240.

[9] M.P. Gomes, I. Costa, N. Pébère, J.L. Rossi, B. Tribollet, V. Vivier, On the corrosion mechanism of Mg investigated by electrochemical impedance spectroscopy, Electrochim. Acta 306 (2019) 61–70.
[10] X. Liu, J. Xue, S. Liu, Discharge and corrosion behaviors of the α-Mg and β-Li based Mg alloys for Mg-air batteries at different current densities, Mater. Des. 160 (2018) 138–146.
[11] Y. Sun, R. Wang, C. Peng, Z. Cai, Microstructure and corrosion behavior of as-extruded Mg-xLi-3Al-2Zn-0.2Zr alloys (x = 5, 8, 11 wt.%), Corros. Sci. 167 (2020) 108487.
[12] J. Yang, C. Blawert, S.V. Lamaka, D. Snihirova, X. Lu, S. Di, M.L. Zheludkevich, Corrosion protection properties of inhibitor containing hybrid PEO-epoxy coating on magnesium, Corros. Sci. 140 (2018) 99–110.
[13] X. Lu, C. Blawert, Y. Huang, H. Ovri, M.L. Zheludkevich, K.U. Kainer, Plasma electrolytic oxidation coatings on Mg alloy with addition of SiO2 particles, Electrochim. Acta 187 (2016) 20–33.
[14] Y. Chen, X. Lu, S.V. Lamaka, P. Ju, C. Blawert, T. Zhang, F. Wang, M. L. Zheludkevich, Active protection of Mg alloy by composite PEO coating loaded with corrosion inhibitors, Appl. Surf. Sci. 504 (2020), 144462.
[15] N. Dinodi, A.N. Shetty, Alkyl carboxylates as efficient and green inhibitors of magnesium alloy ZE41 corrosion in aqueous salt solution, Corros. Sci. 85 (2014) 411–427.
[16] Y. Li, X. Lu, K. Wu, L. Yang, T. Zhang, F. Wang, Exploration the inhibition mechanism of sodium dodecyl sulfate on Mg alloy, Corros. Sci. 168 (2020), 108559.
[17] M.A. Deyab, Decyl glucoside as a corrosion inhibitor for magnesium–air battery, J. Power Sources 325 (2016) 98–103.
[18] G. Baril, N. Pebere, The corrosion of pure magnesium in aerated and deaerated sodium sulphate solutions, Corros. Sci. 43 (2001) 471–484.
[19] N. Wang, R. Wang, Y. Feng, W. Xiong, J. Zhang, M. Deng, Discharge and corrosion behaviour of Mg-Li-Al-Ce-Y-Zn alloy as the anode for Mg-air battery, Corros. Sci. 112 (2016) 13–24.
[20] L. Wang, D. Snihirova, M. Deng, B. Vaghefinazari, S.V. Lamaka, D. Höche, M. L. Zheludkevich, Tailoring electrolyte additives for controlled Mg-Ca anode activity in aqueous Mg-air batteries, J. Power Sources 460 (2020), 228106.
[21] M. Deng, D. Höche, S.V. Lamaka, D. Snihirova, M.L. Zheludkevich, Mg-Ca binary alloys as anodes for primary Mg-air batteries, J. Power Sources 396 (2018) 109–118.
[22] N. Wang, W. Li, Y. Huang, G. Wu, M. Hu, G. Li, Z. Shi, Wrought Mg-Al-Pb-RE alloy strips as the anodes for Mg-air batteries, J. Power Sources 436 (2019), 226855.
[23] X. Chen, Q. Zou, Q. Le, J. Hou, R. Guo, H. Wang, C. Hu, L. Bao, T. Wang, D. Zhao, F. Yu, A. Atrens, The quasicrystal of Mg–Zn–Y on discharge and electrochemical behaviors as the anode for Mg-air battery, J. Power Sources 451 (2020), 227807.
[24] X. Wang, Z. Chen, J. Ren, H. Kang, E. Guo, J. Li, T. Wang, Corrosion behavior of as-cast Mg–5Sn based alloys with in additions in 3.5 wt% NaCl solution, Corros. Sci. 164 (2020), 108318.
[25] G. Baril, G. Galicia, C. Deslouis, N. Pébère, B. Tribollet, V. Vivier, An impedance investigation of the mechanism of pure magnesium corrosion in sodium sulfate solutions, J. Electrochem. Soc. 154 (2007) C108–C113.
[26] G.-L. Song, K.A. Unocic, The anodic surface film and hydrogen evolution on Mg, Corros. Sci. 98 (2015) 758–765.
[27] H. Xiong, K. Yu, X. Yin, Y. Dai, Y. Yan, H. Zhu, Effects of microstructure on the electrochemical discharge behavior of Mg-6wt%Al-1wt%Sn alloy as anode for Mg-air primary battery, J. Alloys. Compd. 708 (2017) 652–661.
[28] T. Zhang, G. Meng, Y. Shao, Z. Cui, F. Wang, Corrosion of hot extrusion AZ91 magnesium alloy. Part II: Effect of rare earth element neodymium (Nd) on the corrosion behavior of extruded alloy, Corros. Sci. 53 (2011) 2934–2942.
[29] I. Nakatsugawa, R. Martin, E. Knystautas, Improving corrosion resistance of AZ91D magnesium alloy by nitrogen ion implantation, Corrosion 52 (1996) 921–926.
[30] V. Shkirskiy, A.D. King, O. Gharbi, P. Volovitch, J.R. Scully, K. Ogle, N. Birbilis, Revisiting the electrochemical impedance spectroscopy of magnesium with online inductively coupled plasma atomic emission spectroscopy, Chemphyschem 16 (2015) 536–539.
[31] M. Urquidi-Macdonald, S. Real, D.D. Macdonald, Applications of Kramers—kronig transforms in the analysis of electrochemical impedance data—III. Stability and linearity, Electrochimica Acta 35 (1990) 1559–1566.
[32] B. Hirschorn, M.E. Orazem, On the sensitivity of the kramers–Kronig relations to nonlinear effects in impedance measurements, J. Electrochem. Soc. 156 (2009) C345.
[33] R.J. Santucci, M.E. McMahon, J.R. Scully, Utilization of chemical stability diagrams for improved understanding of electrochemical systems: evolution of solution chemistry towards equilibrium, Npj Mater. Degrad. 2 (2018).
[34] S.H. Salleh, S. Thomas, J.A. Yuwono, K. Venkatesan, N. Birbilis, Enhanced hydrogen evolution on Mg (OH)2 covered Mg surfaces, Electrochim. Acta 161 (2015) 144–152.
[35] G. Brug, A. Van Den Eeden, M. Sluyters-Rehbach, J. Sluyters, The analysis of electrode impedances complicated by the presence of a constant phase element, J. Electroanal. Chem. 176 (1984) 275–295.
[36] C. Hsu, F. Mansfeld, Concerning the conversion of the constant phase element parameter Y0 into a capacitance, Corrosion 57 (2001) 747–748.
[37] M.A. Rodríguez, R.M. Carranza, Properties of the passive film on alloy 22 in chloride solutions obtained by electrochemical impedance, J. Electrochem. Soc. 158 (2011) C221–C230.
[38] B. Hirschorn, M.E. Orazem, B. Tribollet, V. Vivier, I. Frateur, M. Musiani, Determination of effective capacitance and film thickness from constant-phase-element parameters, Electrochim. Acta 55 (2010) 6218–6227.
[39] J.-B. Jorcin, M.E. Orazem, N. Pébère, B. Tribollet, CPE analysis by local electrochemical impedance spectroscopy, Electrochim. Acta 51 (2006) 1473–1479.
[40] L.G. Bland, K. Gusieva, J. Scully, Effect of crystallographic orientation on the corrosion of magnesium: comparison of film forming and bare crystal facets using electrochemical impedance and Raman spectroscopy, Electrochim. Acta 227 (2017) 136–151.
[41] S. Feliu, C. Maffiotte, A. Samaniego, J.C. Galván, V. Barranco, Effect of the chemistry and structure of the native oxide surface film on the corrosion properties of commercial AZ31 and AZ61 alloys, Appl. Surf. Sci. 257 (2011) 8558–8568.
[42] M. Taheri, M. Danaie, J. Kish, TEM examination of the film formed on corroding Mg prior to breakdown, J. Electrochem. Soc. 161 (2014) C89–C94.
[43] S. Leleu, B. Rives, J. Bour, N. Causse, N. Pébère, On the stability of the oxides film formed on a magnesium alloy containing rare-earth elements, Electrochim. Acta 290 (2018) 586–594.
[44] M. Benoit, C. Bataillon, B. Gwinner, F. Miserque, M.E. Orazem, C.M. Sánchez-Sánchez, B. Tribollet, V. Vivier, Comparison of different methods for measuring the passive film thickness on metals, Electrochim. Acta 201 (2016) 340–347.
[45] S. Chakri, I. Frateur, M.E. Orazem, E.M.M. Sutter, T.T.M. Tran, B. Tribollet, V. Vivier, Improved EIS analysis of the electrochemical behaviour of carbon steel in alkaline solution, Electrochim. Acta 246 (2017) 924–930.
[46] A.S. Nguyen, N. Causse, M. Musiani, M.E. Orazem, N. Pébère, B. Tribollet, V. Vivier, Determination of water uptake in organic coatings deposited on 2024 aluminium alloy: comparison between impedance measurements and gravimetry, Prog. Org. Coat. 112 (2017) 93–100.
[47] M. Danaie, R.M. Asmussen, P. Jakupi, D.W. Shoesmith, G.A. Botton, The role of aluminum distribution on the local corrosion resistance of the microstructure in a sand-cast AM50 alloy, Corros. Sci. 77 (2013) 151–163.
[48] M. Taheri, R.C. Phillips, J.R. Kish, G.A. Botton, Analysis of the surface film formed on Mg by exposure to water using a FIB cross-section and STEM–EDS, Corros. Sci. 59 (2012) 222–228.
[49] P.-W. Chu, E.A. Marquis, Linking the microstructure of a heat-treated WE43 Mg alloy with its corrosion behavior, Corros. Sci. 101 (2015) 94–104.
[50] M. Taheri, J.R. Kish, N. Birbilis, M. Danaie, E.A. McNally, J.R. McDermid, Towards a physical description for the origin of enhanced catalytic activity of corroding magnesium surfaces, Electrochim. Acta 116 (2014) 396–403.
[51] S.V. Lamaka, J. Gonzalez, D. Mei, F. Feyerabend, R. Willumeit-Römer, M. L. Zheludkevich, Local pH and its evolution near Mg alloy surfaces exposed to simulated body fluids, Adv. Mater. Interfaces 5 (2018), 1800169.
[52] C. Wang, D. Mei, G. Wiese, L. Wang, M. Deng, S.V. Lamaka, M.L. Zheludkevich, High rate oxygen reduction reaction during corrosion of ultra-high-purity magnesium, Npj Mater. Degrad. 4 (2020).
[53] M. Esmaily, J.E. Svensson, S. Fajardo, N. Birbilis, G.S. Frankel, S. Virtanen, R. Arrabal, S. Thomas, L.G. Johansson, Fundamentals and advances in magnesium alloy corrosion, Prog. Mater. Sci. 89 (2017) 92–193.
[54] T. Zheng, Y. Hu, Y. Zhang, S. Yang, F. Pan, Composition optimization and electrochemical properties of Mg-Al-Sn-Mn alloy anode for Mg-air batteries, Mater. Des. 137 (2018) 245–255.
[55] M. Deng, L. Wang, D. Höche, S.V. Lamaka, C. Wang, D. Snihirova, Y. Jin, Y. Zhang, M.L. Zheludkevich, Approaching "stainless magnesium" by Ca micro-alloying, Mater. Horiz. (2020).
[56] Y. Shi, C. Peng, Y. Feng, R. Wang, N. Wang, Enhancement of discharge properties of an extruded Mg-Al-Pb anode for seawater-activated battery by lanthanum addition, J. Alloys. Compd. 721 (2017) 392–404.
[57] S. Yin, W. Duan, W. Liu, L. Wu, J. Yu, Z. Zhao, M. Liu, P. Wang, J. Cui, Z. Zhang, Influence of specific second phases on corrosion behaviors of Mg-Zn-Gd-Zr alloys, Corros. Sci. 166 (2020), 108419.

5.2 Revealing physical interpretation of time constants in electrochemical impedance spectra of Mg via Tribo-EIS measurements

Paper 2 is published in Electrochimica Acta, 404 (2022), 139582.

This work is the follow-up of **Section 5.1** (***paper 1***). The motivation of this work is to elucidate the origin of both high frequency (HF) and middle frequency (MF) capacitive loops in impedance spectra of Mg in NaCl solution via the unique Tribo-EIS measurement. The intrinsic surface film formed on Mg in NaCl solution was intentionally abraded by the Tribo-meter resulting in the following changes reflected on HF and MF ranges of impedance spectra. The abrasion leads to the decrease of the total impedance of affected Mg surface, but the influence of abrasion on the HF time constant is less significant than that of the MF time constant. The effect of scratch on the integral surface film resistance and the charge transfer resistance of Mg was quantitatively analyzed, verifying the high frequency time constant originates from the barrier properties of the MgO-based surface film and the middle frequency time constant stems from the charge transfer process.

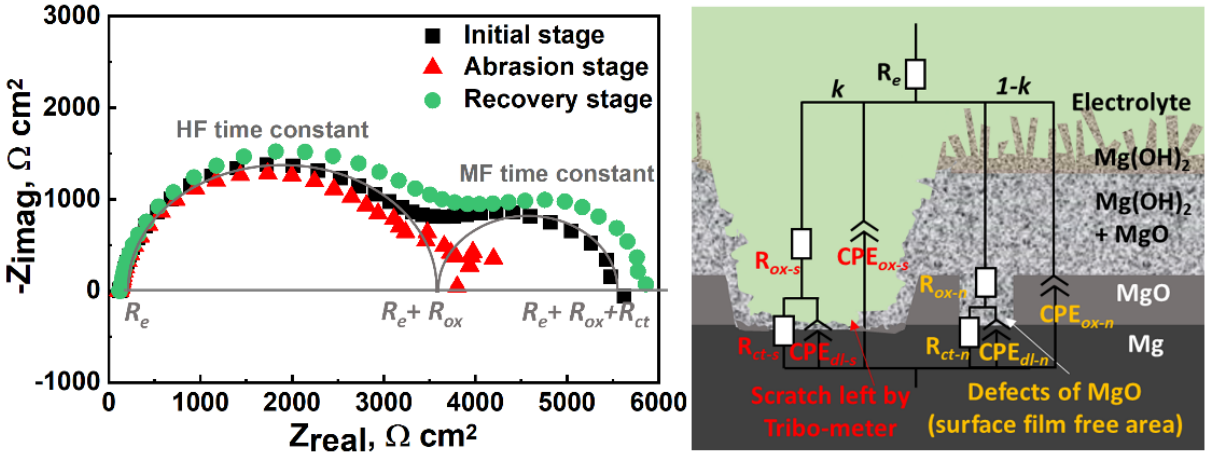

Fig. 5-3. Graphical abstract for **Section 5.2**.

Electrochimica Acta 404 (2022) 139582

Contents lists available at ScienceDirect

Electrochimica Acta

journal homepage: www.elsevier.com/locate/electacta

Revealing physical interpretation of time constants in electrochemical impedance spectra of Mg via Tribo-EIS measurements

Linqian Wang[a,*], Darya Snihirova[a], Min Deng[a], Bahram Vaghefinazari[a], Daniel Höche[a], Sviatlana V. Lamaka[a], Mikhail L. Zheludkevich[a,b]

[a] Institute of Surface Science, Helmholtz-Zentrum Hereon, Geesthacht 21502, Germany
[b] Institute of Materials Science, Faculty of Engineering, Kiel University, Kiel 24143, Germany

ARTICLE INFO

Article history:
Received 10 September 2021
Revised 1 November 2021
Accepted 11 November 2021
Available online 12 November 2021

Keywords:
Magnesium
Electrochemical impedance spectroscopy
Tribo-electrochemistry
Corrosion

ABSTRACT

Tribo-electrochemical impedance spectroscopy (Tribo-EIS) measurements of pure Mg were performed to identify the origin of two time constants during standard EIS measurements in NaCl solution. The influence of abrasion introduced by tribometer on EIS spectra was investigated under different rotation speeds. Further quantitative analyses of abrasion on Mg with different surface areas were performed. The resistances associated to the two time constants on the abraded surface were deduced from the fitted results, verifying that the high frequency time constant originates from the barrier properties of the MgO-based surface film and the middle frequency time constant stems from the charge transfer process.

1. Introduction

Electrochemical impedance spectroscopy (EIS) measurement possesses several merits to investigate the corrosion behavior of metals and coatings [1–3], due to low disturbance to the tested sample, high sensitivity for electrochemical reaction detection, and capability for diffusion-limited reactions identification. In recent years, a number of research works have focused on revealing the corrosion mechanism of Mg via EIS measurement [4–9]. However, researchers have not reached an agreement on the origin of time constants and relevant interpretation of Mg impedance spectra. When there are two capacitive loops and one inductive loop in the whole frequency range for bare Mg in simple media, such as NaCl solution, several researchers attribute the high frequency capacitive loop (HF time constant) to the surface film formed on Mg. Accordingly, the middle frequency capacitive loop (MF time constant) is explained as the resistance from charge transfer process in parallel with double layer capacitance [10–12]. Nevertheless, some researchers hold an opposite view [13–15]. They believe that the HF time constant is associated with the electrical double layer and the MF time constant is related to the surface film. There are also some other opinions regarding the assignment of relaxation processes on corroded Mg surface [5,16], which are briefly summarized in our previous work [17]. The multifarious interpretations concerning the origin of time constants that appear in different frequency ranges may cause the misleading explanations for Mg corrosion behavior. Hence, it is very important to reveal the physical interpretations of each time constant in impedance spectra of Mg-based materials for a better understanding of respective corrosion mechanisms. Our previous work investigated the origin of the HF time constant, which was attributed to the barrier effect of thin surface film that always presents at the metal surface even at acidic conditions. However, the physical interpretation for the MF time constant is still not clear. The conventional electrochemical techniques usually reflect the generalized electrochemical information on the surface of the sample. Therefore, it is hard to distinguish the single electrochemical process and identify the origin of the HF and MF time constants on Mg EIS spectra.

Except for conventional EIS measurement, many other electrochemical test methods have been used to study the corrosion behavior and interfacial condition of metallic materials, such as scanning vibrating electrode technique (SVET) [18–20], scanning electrochemical microscopy (SECM) [9,21,22], and modified EIS measurements [23–25], etc. Tribo-electrochemical technique is one of the unique electrochemical test techniques that adopts traditional electrochemical measurement set-up to acquire the electrochemical response of the surface undergoing mechanical abrasion from tribometer [26–29]. This technique is similar to the scratched electrode technique, which generates a bare surface by removing the passive film on the testing materials and measures the associated electrochemical response, such as transient current, transient potential, or impedance evolution [23,30,31]. These electrochemi-

* Corresponding author.
E-mail address: linqian.wang@hereon.de (L. Wang).

https://doi.org/10.1016/j.electacta.2021.139582
0013-4686/

cal responses throw light on the recovery process happening on the scratched surface and contribute to a better understanding of metal dissolution on film-free area, reconstruction of double layer and recovery of surface film. Thus, tribo-electrochemical technique and scratched electrode technique have been used in the mechanistic study of corrosion behavior for various passive metallic materials [32–36]. Recently, the scratched electrode technique was also adopted to study the corrosion mechanism of pure Mg and Mg-Li alloys [37,38]. Through detecting the current transient under polarization or the dissolution rates of different alloying elements, the dissolution and re-passivation processes that happen on the scratched Mg surface can be *in-situ* characterized. This information may also be useful to distinguish the origin of the different time constants on Mg impedance spectra since it may follow the dynamic reconstruction process of double layer and surface film. During tribo-electrochemical tests, the applied force and the speed at the contact point can be precisely controlled to create bare metal surface. Hence, comparing to the normal scratched electrode technique, the tribo-electrochemical technique gives more possibilities to identify the origin of the time constants on Mg impedance spectra. Based on the results presented in our previous work, we conclude that the HF time constant is related to the surface film formed on Mg. Accordingly, the origin of the MF time constant is most likely related to the charge transfer process and respective double layer structure formed at the interface. As demonstrated in previous literature [17,39,40], the surface film formed on pure Mg in NaCl is composed of an outer $Mg(OH)_2$ flakes (brucite) layer, a $Mg(OH)_2$ and MgO mixed layer and a dense inner MgO layer. The dielectric constant of MgO is around 9 [5] and the band gap for a pure bulk MgO is about 7.8 eV [41,42], indicating that MgO can be considered as an insulator and, thus, the electron transition process can rarely happen in the region covered by integrated MgO film. Rather, corrosion reaction with charge transfer process can only happen in the defects of MgO film, which is also termed as film-free area on Mg surface [5,6]. By performing Tribo-EIS measurement on Mg, the ratio of film-free area could be artificially tailored and the influence of the reconstruction of surface film and double layer on the evolution of time constants can be investigated.

Thus, in this work, Tribo-EIS measurements were performed on pure Mg in 0.05 M NaCl solution to elucidate the physical interpretations of two time constants in Mg impedance spectra. The intrinsic surface film on Mg was intentionally damaged using a tribometer with the following changes reflected on high and middle frequencies of impedance spectra. The influence of rotation speed and abrasion on the evolution of time constants of Mg electrodes with various surface areas was investigated. The effect of scratch on the integral surface film resistance and the charge transfer resistance of Mg was quantitatively analyzed. The corrosion and repassivation behavior on the scratched surface of Mg in diluted NaCl solution was discussed.

2. Experimental

2.1. Materials

As-cast high purity Mg with 99.98% Mg; 51 ppm Fe; 50 ppm Al; 23 ppm Zr; 10 ppm Zn; 8 ppm Zn; and less than 1 ppm Si, Cu, and Ag was used in this work. The chemical composition was determined by spark discharge-optical emission spectrometry (SD-OES). Before every electrochemical test, the Mg sample was well ground by emery papers from 320 to 1200 grit. 0.05 M NaCl solution was adopted as the testing electrolyte for electrochemical tests, which was prepared by 99.5% NaCl from Carl Roth, CAS No. 7647–14–5, with deionized water. The pH of NaCl solution was measurement by Metrohm-691 pH meter.

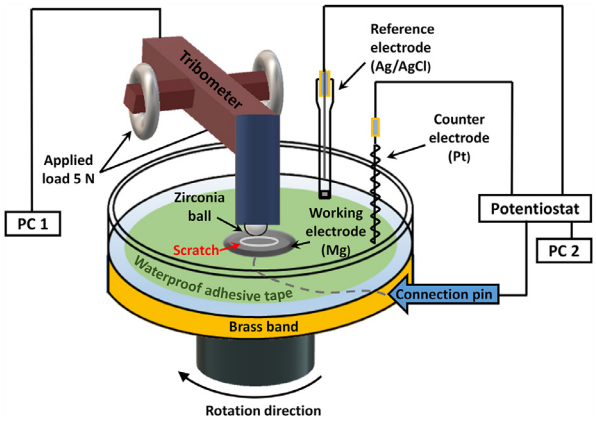

Fig. 1. Schematic illustration of experimental arrangement for Tribo-EIS measurement.

2.2. Tribo-electrochemical tests

All electrochemical measurements were performed by Gamry interface 1010E potentiostat coupled with tribotechnic Pin-on-Disk tribometer in a customized cell as schematically indicated in Fig. 1 and optical photograph Fig. S1. The pin-on-disk tribometer is mainly composed of a stationary abrasive pin and a rotating disk. The abrasive pin used in this work was a zirconia ball with 6 mm diameter, which was held by an insulating plastic holder. The applied load was 5 N for all the tests and there were two different rotation speeds used in the tests, i.e. 2 or 20 rpm. 2 rpm is the slowest rotation speed of the tribometer and 20 rpm is chosen as a fast rotation speed to elucidate the impact of rotation speed on the electrochemical measurement. Coiled Pt wire and KCl-saturated Ag/AgCl electrode were used as counter electrode and reference electrode, respectively. Mg samples with various exposed surface areas (0.5, 1.1 and 2 cm^2) were employed as working electrodes. The working electrode was embedded in the groove of the customized cell (Fig. S1c). A connection point on the bottom of the cell was used to electrically connect the working electrode with an external brass brand. The conductivity of this set-up was checked by multimeter, indicating that the resistance of this set-up is less than 1 ohm. Green waterproof adhesive tape with a hole of specified size was stuck on the top of the working electrode and the groove in order to control the exposed surface area of working electrode and to avoid electrolyte penetration. The water resistance of this set-up was also checked before Tribo-EIS measurement. All Tribo-EIS measurements were conducted under potentiostatic mode at open circuit potential (OCP) with 10 mV_{rms} perturbation voltage. All EIS measurements were done during cell rotation and divided into three different stages: (i) the initial stage without damage; (ii) the abrasion stage where abrasive pin was scratching Mg surface; (iii) the recovery stage where abrasive pin was removed from the cell after scratching. The EIS measurements without abrasion were started from 100 kHz and ended at 0.01 Hz with 9 points per decade. During EIS measurements without abrasion (i and iii), the abrasive pin did not touch the surface of the working electrode. During the abrasion stage, the working electrode was scratched by the abrasive pin as illustrated in Fig. 1. The EIS measurements in the abrasion stage (ii) were carried out in the frequency range from 100 kHz to around 0.04 Hz. A circular abraded ring was left on the working electrode surface. All the Tribo-EIS measurements were performed at least three times. After Tribo-EIS measurement, the electrode surface was characterized by laser scanning microscope (LSM, Zeiss LSM 800) and scanning electron microscope (SEM, TESCAN VEGA 3).

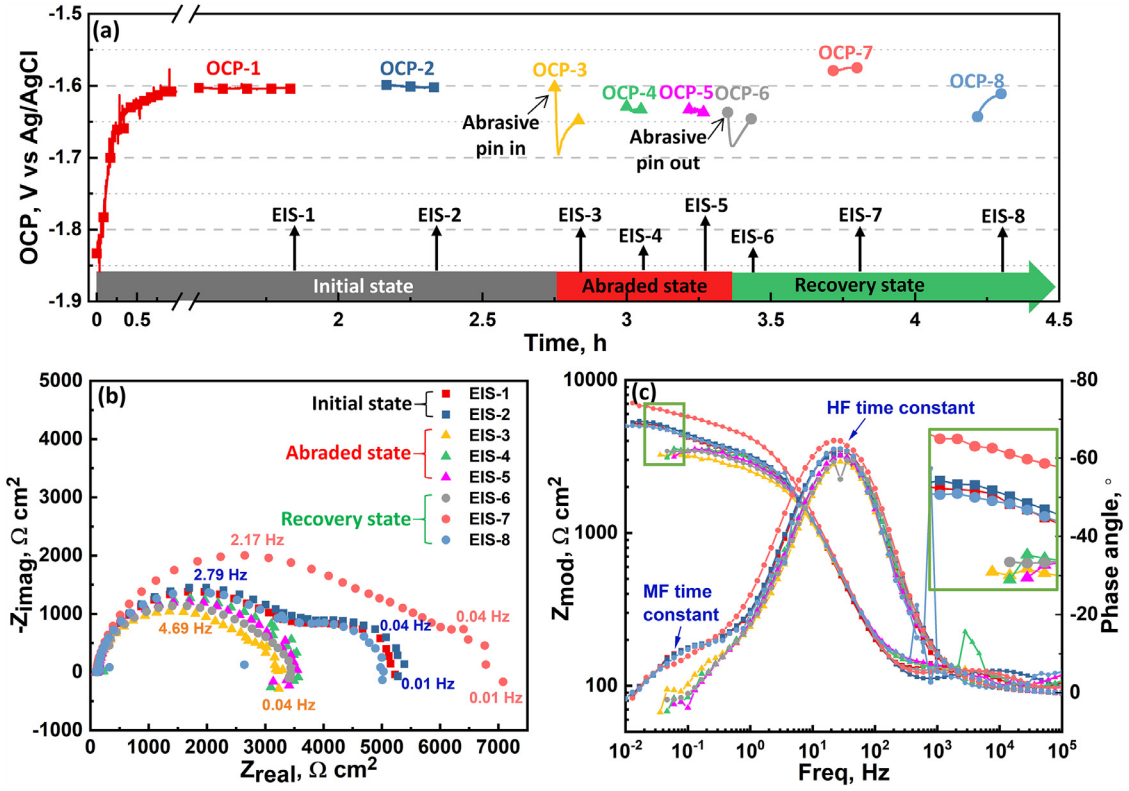

Fig. 2. (a) OCP of Mg in 0.05 M NaCl solution at different states; (b) Nyquist plots; and (c) Bode plots of Mg in 0.05 M NaCl solution (rotation rate: 2 rpm).

Potentiodynamic polarization tests were also performed in the above mentioned experimental arrangement. In order to avoid the influence of electrolyte alkalization and change of electrode surface condition on the accuracy of potentiodynamic polarization tests, anodic and cathodic polarization curves of Mg with 1.1 cm^2 exposed surface area under different states were obtained separately in fresh 0.05 M NaCl solution. All potentiodynamic polarization tests were carried out after 1 h OCP test to ensure the stabilization of the testing system. The potential scanning for anodic polarization curves was from − 5 mV (vs. OCP) to + 800 mV (vs. OCP) and that for cathodic polarization curves is from + 5 mV (vs. OCP) to − 2.4 V (vs. Ag/AgCl) with a 0.5 mV/s scanning rate.

3. Results and discussion

3.1. Tribo-electrochemical test for Mg

In comparison with the fast rotation speed adopting in other literature [9,43], a low rotation speed of 2 rpm is applied in order to diminish the impact of rotation caused stirring on the electrochemical measurements and to make the obtained results comparable with that obtained in the steady state measurements. The results of electrochemical measurements performed under 2 rpm rotation are presented in Fig. 2. As depicted in Fig. 2a, the OCPs of Mg in NaCl solution before, during and after abrasion reflect the general surface condition of Mg under different states. The timeline for the measurements is also illustrated in Fig. 2a. The initial state corresponds to the first and second consecutive OCP and EIS tests without any interference of abrasive pin. As shown in Fig. 2a, the OCP of Mg at the initial state shifts positively with the increase of time during the initial one hour because of the corrosion reaction and the accumulation of corrosion products on the Mg surface. The first EIS measurement is performed after the testing condition is stabilized and the OCP of Mg reaches a stable value of −1.6 V (vs. Ag/AgCl). The change of OCP is less than 1 mV per min. After the first EIS measurement, the OCP of Mg still remains at −1.6 V (Fig. 2a), indicating a sufficient stability of the testing system for EIS measurement with 2 rpm rotation. As presented in Fig. 2b, the Nyquist plots of two EIS measurements in the initial stage are similar and are composed of two well-defined capacitive loops. The total impedance increases slightly with time.

When the abrasive pin is put inside the cell and the abrasion on Mg electrode starts, the OCP decreases sharply from −1.6 V to −1.7 V and then increases back to −1.65 V (Fig. 2a). Consequently, the HF capacitive loop (EIS-3) slightly shrinks but the MF capacitive loop becomes less evident. The overall impedance modulus value decreases in comparison to that of Mg at the initial state (EIS 1–2) and there is no distinct time constant in the middle frequency range as indicated by Fig. 2c. The decrease of impedance is expected under the abrasion state, since the abrasive pin continuously scratches the surface film formed on Mg and creates a fresh film-free area for a certain time. Nevertheless, it is more noteworthy that the responses of the two time constants to the abrasion are different. At the initial state, the dimensions of two capacitive loops appearing in different frequency ranges are comparable. However, the MF capacitive loop during abrasion is almost invisible, while the HF capacitive loop only slightly shrinks. With the increase of abrasion time, the OCP of Mg nearly stabilizes at −1.64 V (OCP 4–5), indicating that the surface is under a quasi-steady state. Correspondingly, the Nyquist plots at the abrasion state are also presented in a similar way as a stretched semi-circle with approximately equal impedance values.

When the abrasive pin is removed from the cell, the OCP also decreases, which may be related to the change of local condition on the Mg surface. For instance, the fast corrosion in the scratched region leads to the rapid increase of local pH and the movement of abrasive pin incidentally disturbs the local environment. Consequently, the OCP drops and then shifts to a more positive value.

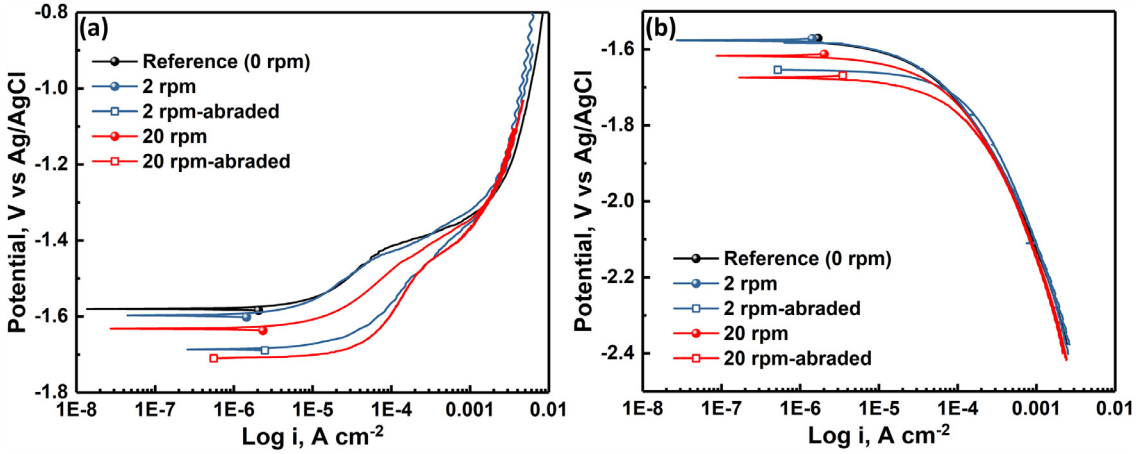

Fig. 3. Polarization curves of Mg obtained in 0.05 M NaCl solution at different states with various rotation rates.

As indicated in Fig. 2b, the first EIS result at the recovery state (EIS-6) shows a similar impedance value and shape to that at the abrasion state (EIS 3–5). However, the second EIS result at the recovery state (EIS-7) represents as an expanded semi-circle and the modulus value is even higher than that at the initial state, which demonstrates a transition process from the abrasion state to the recovery state. Meanwhile, the corresponding OCP is the most positive, i.e. −1.58 V. This exceptional spectrum may be caused by the above mentioned disturbance introduced by the lift out procedure of the abrasive pin and the following transportation process of OH^- happened during this transition process. After that, the Nyquist plot of EIS-8 is almost identical with that at the initial state, which is also composed of two well-defined capacitive loops and the impedance modulus value is comparable with that at the initial state, manifesting that the abraded surface of Mg has recovered and the newly formed surface film on the scratched region possesses similar property as the intrinsic film on the unscratched area. After all the EIS measurements, the bulk pH of the NaCl solution increases from 5.6 to 7.7.

3.1.1. Influence of rotation speeds

As mentioned above, 2 rpm rotation is adopted to eliminate the influence of stirring caused by rotation on the electrochemical measurements. Nevertheless, several research works have investigated the influence of rotation speeds on the corrosion behavior of Mg-based materials, indicating that faster rotation speeds induce higher corrosion rates because faster rotation speeds decrease the amount of precipitated corrosion products [43,44]. In order to clarify the influence of rotation speeds on the tribo-electrochemical measurements, the potentiodynamic polarization tests and EIS measurements of Mg in 0.05 M NaCl solution under different rotation speeds were performed.

As shown in Fig. 3, the corrosion potential of Mg is more negative when the rotation is accelerated. The corrosion potential tested with 20 rpm rotation speed is −1.63 V, whilst that tested without rotation is −1.58 V. The corrosion potential difference between the reference test (0 rpm) and the test with 2 rpm rotation is only 17 mV and the measured anodic branches are almost overlapped, indicating that 2 rpm rotation speed would not introduce significant influence on the dissolution behavior of Mg. Therefore, the EIS measurement conducted under 2 rpm rotation can be considered similar to the test done without rotation. As shown in Fig. 3a, the anodic branch of Mg significantly shifts towards the position with higher current density when the rotation speed increases to 20 rpm. The anodic current density of Mg at −1.5 V (vs. Ag/AgCl) is 26.5 μA cm^{-2} when the rotation speed is 2 rpm in comparison to 75.4 μA cm^{-2} with 20 rpm, indicating that the kinetics of anodic reaction tends to be faster with a higher rotation speed. Abrasion during polarization test further increases the anodic current density of Mg and the corrosion potential of Mg under abrasion is more negative than that without abrasion. Moreover, the rotation induces stronger impact on unscratched Mg surface than on the surface under abrasion. Nevertheless, different rotation speeds and abrasion do not have significant influence on the cathodic branch (Fig. 3b).

Fig. 4a displays the OCP of Mg in NaCl solution under different states with 20 rpm rotation. Comparing to the OCP of Mg shown in Fig. 2a, higher rotation speed shifts the OCP of Mg at different states to a more negative potential, which is consistent with the results presented in Fig. 3. At the initial state, faster rotation promotes the dissolution of Mg, which may be attributed to the acceleration of mass transport process in the electrochemical cell. The re-passivated area of the scratched surface is reduced amid abrasion at a higher rotation speed. Thus, the OCP of Mg at the abrasion state (OCP 4–5) with 20 rpm rotation also stabilizes at a more negative potential (−1.74 $V_{Ag/AgCl}$) than that with 2 rpm rotation (−1.64 $V_{Ag/AgCl}$). With a faster rotation speed, the OCP of Mg at the recovery state also differs from that under a slower rotation speed. As illustrated in Fig. 4a, the OCP of Mg (OCP-6) only shows a small fall after the abrasive pin is removed from the cell and then sharply increases to a more positive value than the final OCP at the recovery state (OCP-8). Nevertheless, the OCP of Mg at the recovery state (OCP 6–8) is always more negative than that measured at the initial state (OCP-2).

Fig. 4b and c show the EIS results of Mg in NaCl solution under different states with 20 rpm rotation. According to the Nyquist plots presented in Fig. 4b, the acceleration of rotation speed leads to the shrinkage of both capacitive loops at high and middle frequency ranges in comparison to the spectra presented in Fig. 2b, but the two well-defined capacitive loops are visible at the initial and full recovery stages for both rotation speeds. However, the Nyquist plots of Mg at the abrasion state with 20 rpm rotation are different from those with 2 rpm rotation. When the rotation speed is 20 rpm, the shrinkage of the HF capacitive loop is more significant than that with 2 rpm rotation and the MF capacitive loop does not disappear completely. In order to obtain the full spectra of the MF time constant, the total abrasion duration in Tribo-EIS measurements with 20 rpm rotation is slightly longer than that with 2 rpm rotation (0.75 h vs. 0.6 h). As presented in Fig. 4c, the MF time constant at the abrasion state can be readily observed. Nevertheless, the reduction of the MF time constant is still more significant than that of the HF time constant. Besides, the recov-

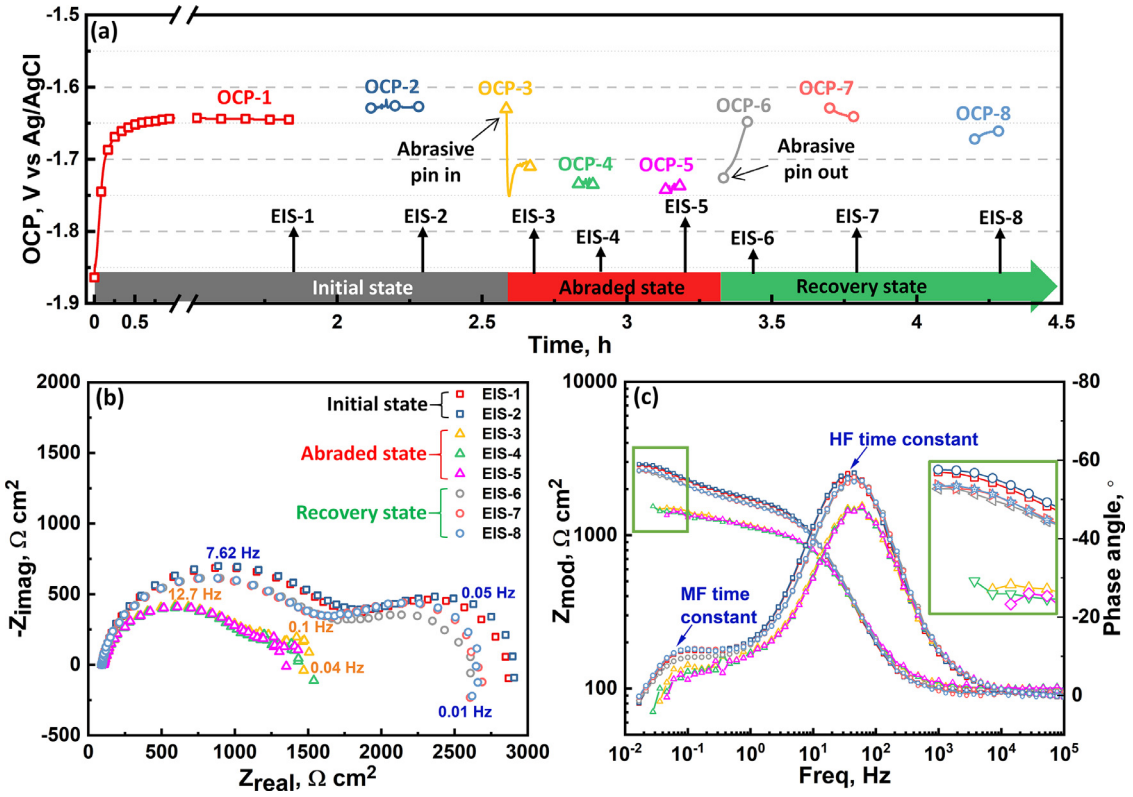

Fig. 4. (a) OCP of Mg in 0.05 M NaCl solution at different states; (b) Nyquist plots; and (c) Bode plots of Mg in 0.05 M NaCl solution (rotation rate: 20 rpm).

ery process of Mg with 20 rpm rotation is also different from that with 2 rpm rotation. The first EIS result at the recovery state (EIS-6) with 20 rpm rotation has already presented as two capacitive loops with slightly lower impedance value than that at the initial state (EIS-1), indicating that faster rotation speed also accelerates the recovery process of the abraded surface. Moreover, the transition process from the abrasion state to the recovery state, as indicated by EIS-7 in Fig. 2b, is not observed in Fig. 4b. Therefore, it is rational to deem that the transition process observed in Fig. 2b is possibly related to some transport limitations happening on the abraded surface, such as the transport of $OH^-$and Mg^{2+} from the abraded area to the unscratched area.

3.1.2. Influence of exposed electrode surface area

As presented in Figs. 2 and 4, the influence of intentionally increased film-free area on the HF and MF time constants of Mg in EIS measurement is not equal. As recently demonstrated, the HF time constant is related to the barrier effect of the surface film [17]. The MF time constant then is most probably related to the double layer capacitance and relative charge transfer process happening on the film-free area where electrochemical reaction occurs [6,17,45]. Thus, by fixing the scratched area and changing the area of surface covered with film, it is possible to clarify the origin of both time constants. For this purpose, the OCP and impedance spectra of Mg electrodes with three different exposed surface areas were tested. The abraded surface area is always kept the same but the ratio of abraded surface area to the unscratched surface area varies (Fig. 5c). The applied rotation speed is 2 rpm. The representative OCP of Mg with various exposed surface areas (0.5, 1.1 and 2.0 cm^2) at different states are displayed in Fig. 5a and b. The rest of the information is provided in Fig. S2.

As shown in Fig. 5a, the OCPs of Mg electrodes with various surface areas before abrasion are almost the same. During abrasion, the OCP of Mg decreases sharply and there is a strong correlation between the exposed surface area and the OCP value at the abrasion state (OCP-3). The tendency is the same for the OCP of Mg at the initial stage of recovery (OCP-6) in Fig. 5b. With higher exposed surface area, the OCP of Mg at the abrasion state (OCP-3) and at the initial stage of recovery (OCP-6) is more positive. The alteration of OCP between the two different surface states is less, because the ratio of abraded to exposed surface area is less. Thus, the impact introduced by abrasion is less. Nevertheless, the final OCP of Mg (OCP-8) does not depend on the exposed surface area and shows the similar value with that at the initial state (OCP-2). The surface conditions at the final stage of recovery are relatively stable and comparable between samples with different surface areas.

The representative EIS spectra of Mg with various exposed surface areas are presented in Fig. 6. The rest of EIS spectra for Mg with 0.5 and 2.0 cm^2 exposed surface areas also can be found in Fig. S2. All the EIS results are normalized by the total exposed surface area. As shown in Fig. 6a, the Nyquist plots and modulus values on Mg samples with various exposed surface areas at the initial stage are similar to each other. The HF time constants (EIS-3) shrink during abrasion for all the samples. The reduction shows a strong correlation with the exposed surface area. The HF capacitive loop of Mg-0.5 cm^2 strongly shrinks during abrasion, but the HF capacitive loop of Mg-2 cm^2 amid abrasion almost overlaps with that at initial stage. Meanwhile, the abrasion makes the shape of the MF time constant dispersed for all Mg samples, and no well-defined time constant can be observed in the frequency range between 1 Hz to 0.03 Hz (Fig. 6b). After removing the abrasive pin from the Mg electrode surface, the HF capacitive loop of Mg-0.5 cm^2 (EIS-8) is slightly smaller than that of the initial state, and the MF capacitive loop is still not distinct. Nevertheless, the Nyquist plots of Mg electrodes with 1.1 and 2.0 cm^2 exposed surface areas are composed of two explicit capacitive loops. Additionally, the total impedance of Mg-2.0 cm^2 at the recovery stage

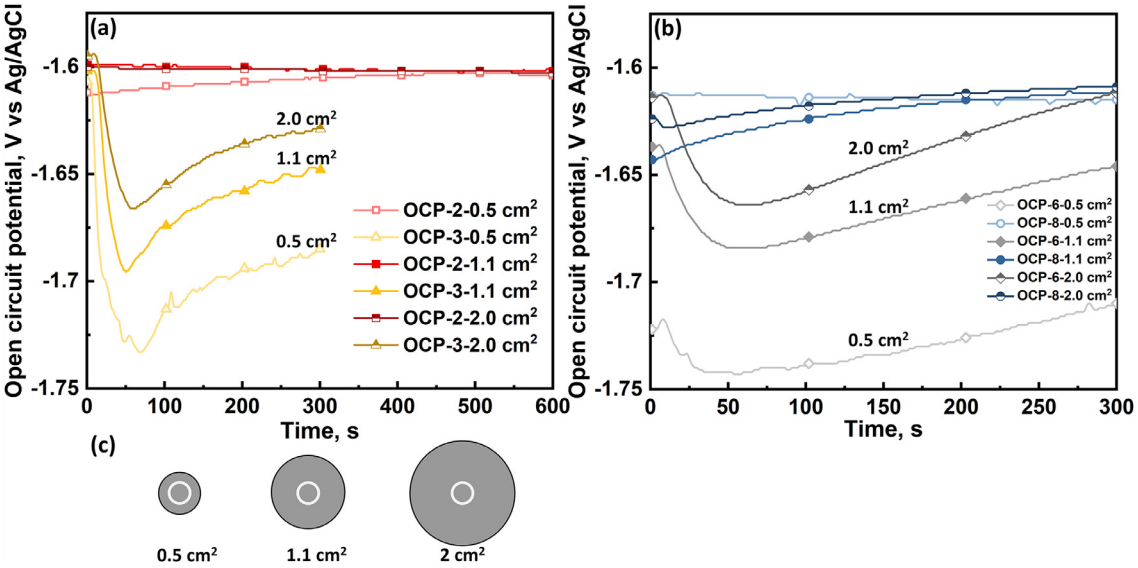

Fig. 5. OCP of Mg with various exposed surface areas in 0.05 M NaCl solution at (a) initial and abrasion states, (b) at recovery state, and (c) illustration of abraded surface (rotation rate: 2 rpm).

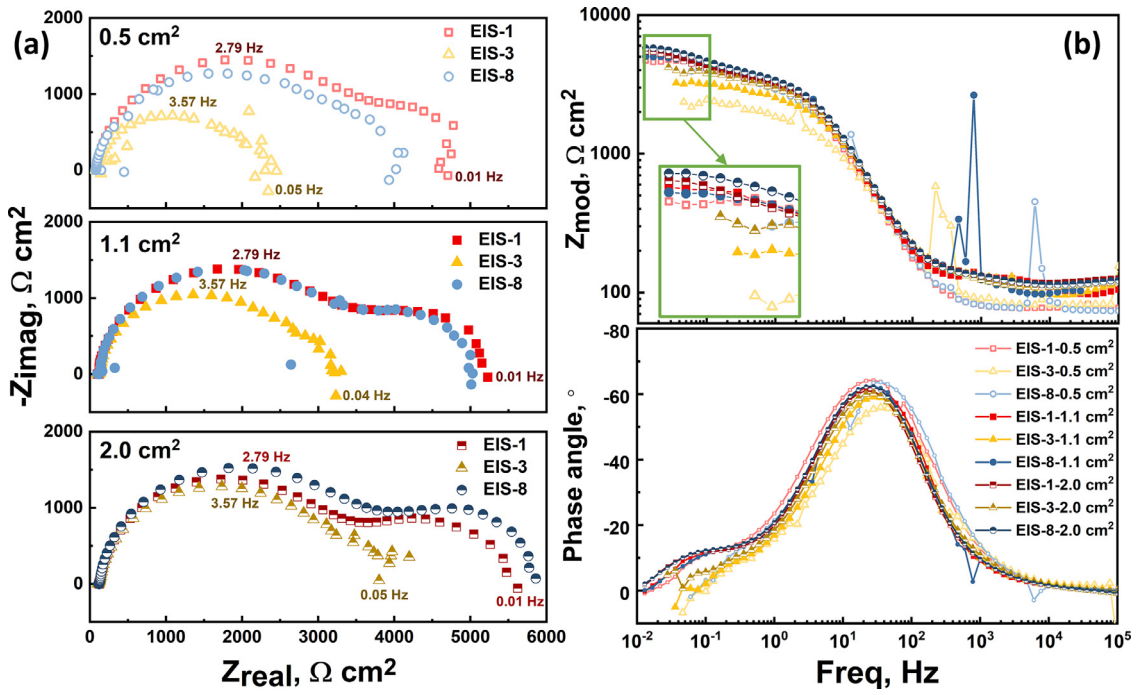

Fig. 6. (a) Nyquist plots and (b) Bode plots of Mg with various exposed surface areas in 0.05 M NaCl solution at different stages (rotation rate: 2 rpm).

(EIS-8) is the highest and it is even higher than that at the initial stage.

3.2. Discussion on the origin of time constants

In order to quantitatively analyze the influence of abrasion on the two time constants respectively, the EIS results of Mg with various exposed surface areas need to be fitted. Fig. 7a and b present the representative Nyquist and Bode plots of pure Mg in 0.05 M NaCl solution, respectively. The plots are obtained from Mg with 2.0 cm^2 exposed surface areas under 2 rpm rotation (EIS-2). As indicate by Fig. 7a, the Mg Nyquist plot mainly consists of HF and MF capacitive loops, which are represented as HF and MF time constants in the Bode plot. The resistances of electrolyte, HF time constant, and MF time constant can be fitted via adopting the equivalent circuit illustrated in Fig. 7c. The values obtained from Fig. 7c are referred to as fitted values.

The average fitted results and standard deviations of three parallel tests for each state are presented in Fig. 8 and Tables. S1–S4. The resistances of the HF time constants R_{HF} of Mg with various exposed surface areas follow a similar evolution tendency (Fig. 8a). When the rotation rate is the same (2 rpm), the R_{HF} at the initial states obtained from different samples are close to each other (EIS 1–2), which encounters a sharp decrease when the abrasion starts (EIS-3). The reduction of R_{HF} is less for Mg with larger exposed surface area. It is worth noting that the R_{HF} of Mg-2.0 cm^2 firstly decreases and then increases significantly during abrasion, with R_{HF} of EIS-4 being higher than that at the initial states (EIS-

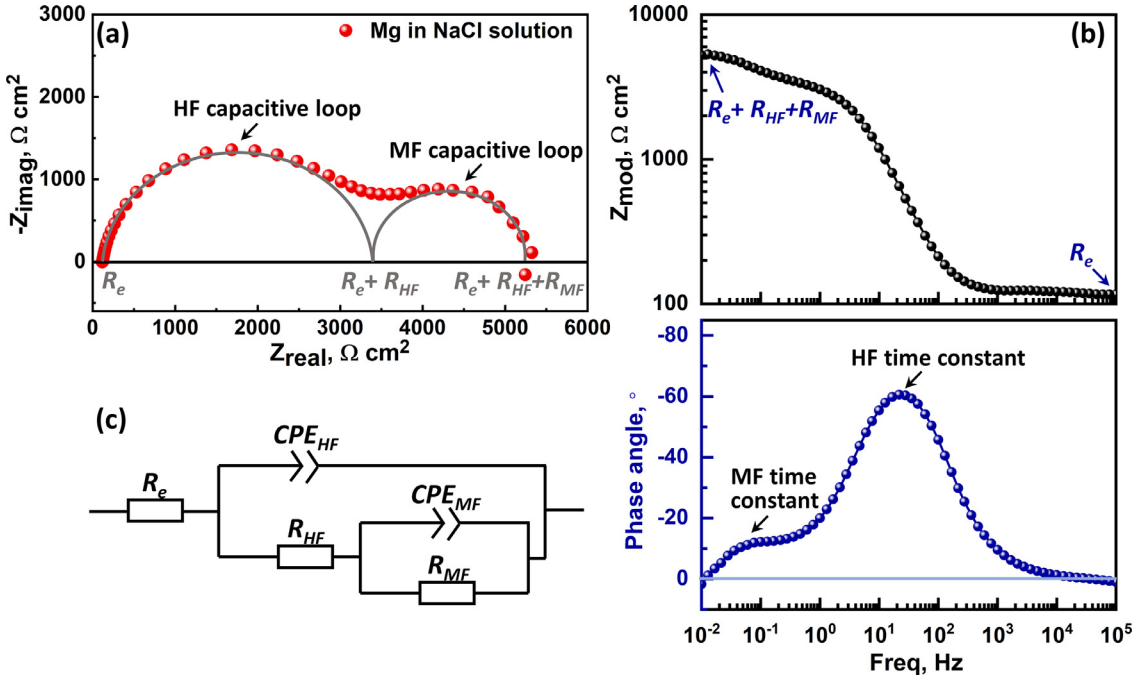

Fig. 7. (a) Nyquist plot, (b) Bode plot of Mg in 0.05 M NaCl solution, and (c) equivalent circuit used for fitting.

1 and EIS-2). With higher unscratched surface area, the increase of R_{HF} is more pronounced. Nevertheless, when the rotation speed is 20 rpm, the R_{HF} at the abrasion states (EIS 3–5) maintains a relatively stable and low value in comparison with that obtained with 2 rpm rotation. The abrasion also causes a significant loss of R_{MF} of all tested Mg samples with different exposed surface areas. However, the loss of R_{MF} does not show strong correlation with exposed surface area. During abrasion, regardless of the exposed surface area and rotation rate, no significant change is observed. In the recovery stage, the R_{MF} of Mg-0.5 cm^2 keeps increasing. Nevertheless, the R_{MF} values of Mg with higher exposed surface areas (1.1 and 2.0 cm^2) firstly increase and then decrease to a value close to the initial value in EIS-1. As above mentioned, EIS-7 is obtained at an unstable transition stage from abrasion state to recovered state. The deviation of parallel experimental results for this state is also more significant than other results because of the instability of this state. Faster rotation makes the transition becomes shorter. The R_{MF} at the recovery state obtained with 20 rpm rotation increases and then stables at the value similar to the initial value.

As shown in Fig. 7c, the constant phase element (CPE) is adopted for the fitting procedure rather than capacitor, because the phase angles of time constants in Mg impedance spectra vary and are less than −90°. CPE parameters include the CPE value and the exponent, which are referred to as CPE and α in this work. Fig. 8c and d present the fitted CPE values of high frequency time constant CPE_{HF} and middle frequency time constant CPE_{MF} of Mg in NaCl solution. Even though there are large standard deviations of the fitted CPE values, all CPE_{HF} increase when the abrasion starts (EIS-3), which may relate to the decrease of oxide film thickness. The CPE_{MF} of Mg-1.1 cm^2 with 20 rpm rotation also increases in EIS-3. Nevertheless, all CPE_{MF} of Mg with 2 rpm rotation decrease after abrasion starts. CPE values at different states may be not directly comparable due to the different exponent α (Tables S1–S4), especially for CPE_{MF}. There are several methods with variant application limits that are capable of extracting effective capacitance C_{eff} from CPE parameters [46–49]. As discussed in previous works [17,24], the equation proposed by Hsu and Mansfeld [47] is well-suited for the CPE-to-C_{eff} conversion of Mg time constants due to the normal distribution characteristic. This refers to the time constants distribution along the direction perpendicular to the Mg surface rather than the direction horizontal to the Mg surface. However, the distribution of time constants for the scratched Mg surface is more complex than that under steady state condition, which is neither a purely normal distribution nor a surface distribution. Hence, the conversion of CPE to effective capacitance is not performed in this work.

In order to analyze the influence of abrasion quantitatively, a factor k is introduced, which is defined as the ratio between abraded and total surface area (Eq. (1)),

$$k = \frac{S_A}{S_{WE}} \tag{1}$$

Where S_A is the abraded surface area and S_{WE} represents the total exposed surface area of the working electrode. The surface morphology of Mg-1.1 cm^2 after abrasion is illustrated in Fig. 9a and b. As shown in Fig. 9b, the maximum depth of the scratch is around 5–8 μm, which is around hundred times less than the width of the scratch presented in Fig. 9a. Thus, the depth of scratch was not considered in the calculation of the abraded surface area. According to Fig. 9a, the abraded surface area is calculated to be 4.2 mm^2. The calculated ratios for different samples, k, are presented in Fig. 9c. A higher k value means a higher weighting factor of the abraded area. Thus, the impact of scratch and the reduction of impedance should be more significant, which is consistent with the results presented in Fig. 8a. In order to clarify the correlation between the ratio k and the change of two time constants caused by abrasion, the difference of resistance before and after abrasion ($R_{EIS\text{-}2}$ and $R_{EIS\text{-}3}$), ΔR, is calculated by Eq. (2) and also presented in Fig. 9c.

$$\Delta R = R_{EIS-2} - R_{EIS-3} \tag{2}$$

As presented in Fig. 9c, ΔR_{HF} shows a positive correlation with k. Nevertheless, there is no clear relationship between ΔR_{MF} and k. The reduction of film resistance most likely shows a positive correlation with k, since k is inversely proportional to the surface film coverage. Thus, ΔR_{HF} is most likely to be the reduction of the sur-

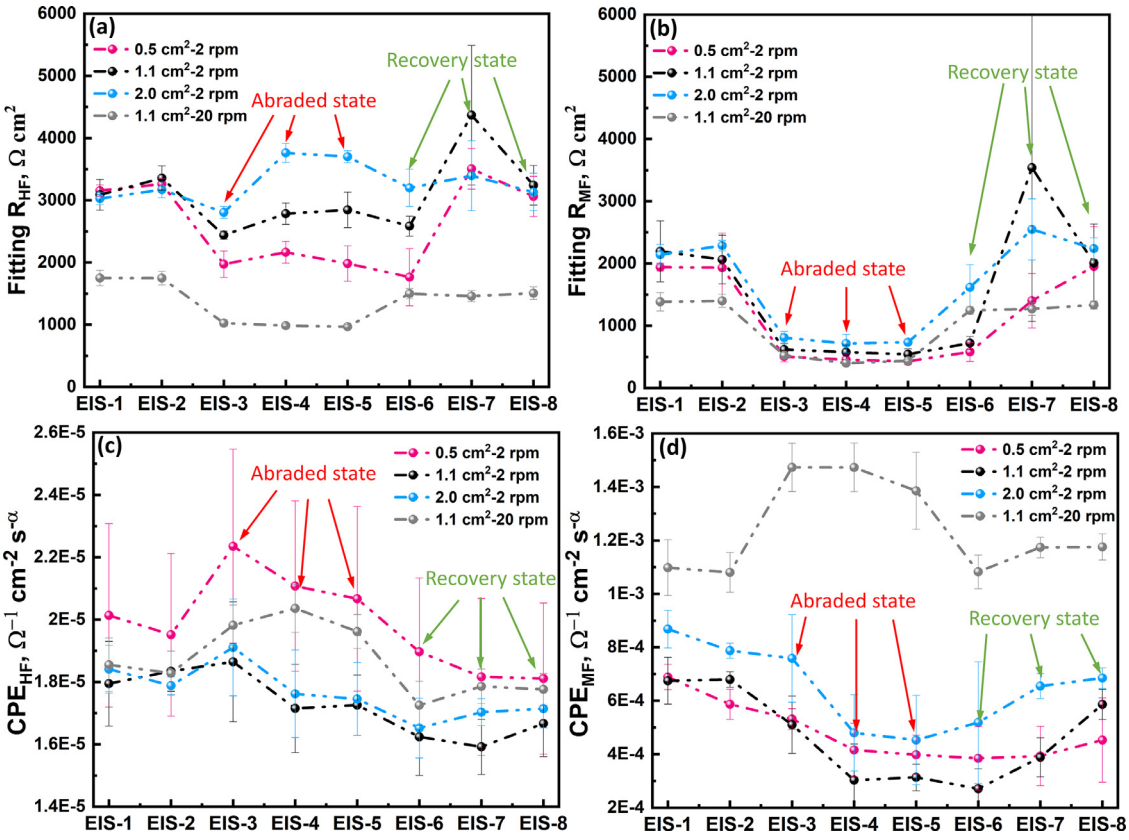

Fig. 8. (a) Fitted resistance and (c) fitted CPE parameter of HF time constant R_{HF}; (b) fitted resistance and (d) fitted CPE parameter of MF time constant R_{MF} of Mg in 0.05 M NaCl solution with various exposed surface areas. (Fitted by equivalent circuit presented in Fig. 7c).

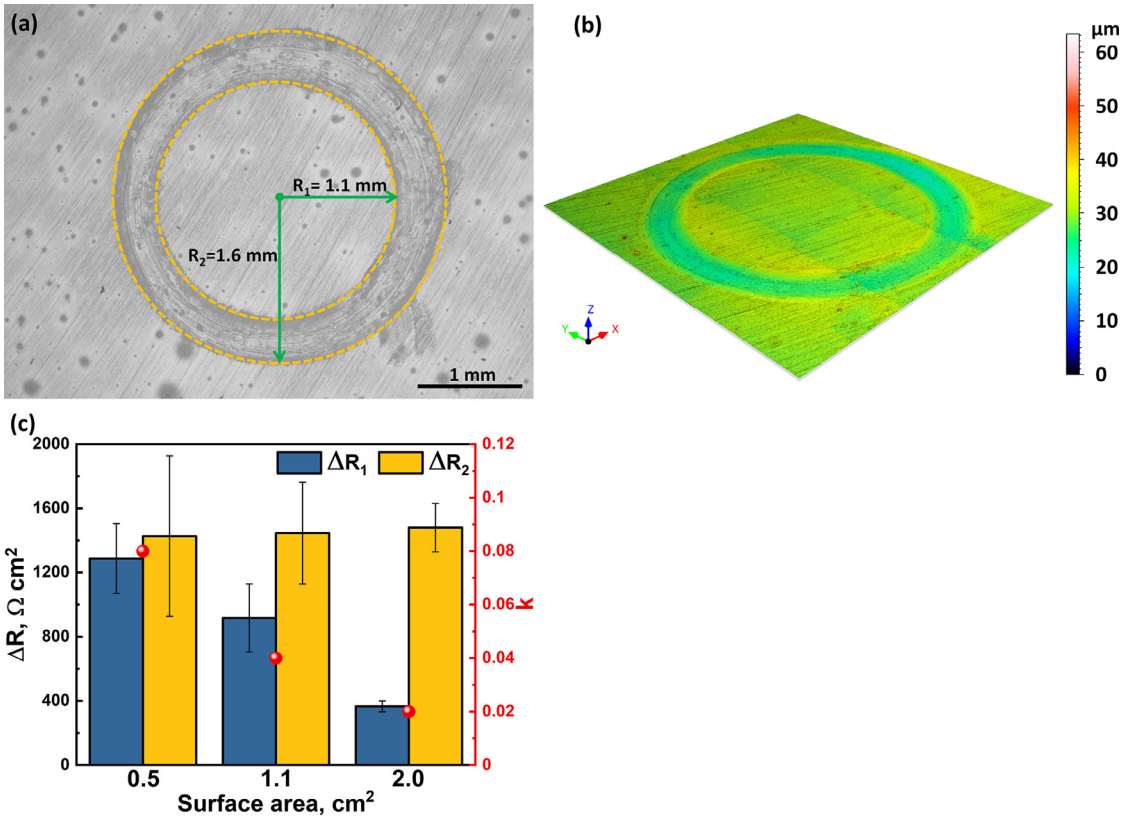

Fig. 9. (a) Actual surface morphology of scratched Mg under SEM ; (b) 3D topography of scratched Mg under LSM; (c) reduction of resistance caused by abrasion and ratio of scratched surface area for Mg with different exposed surface areas (rotation rate: 2 rpm).

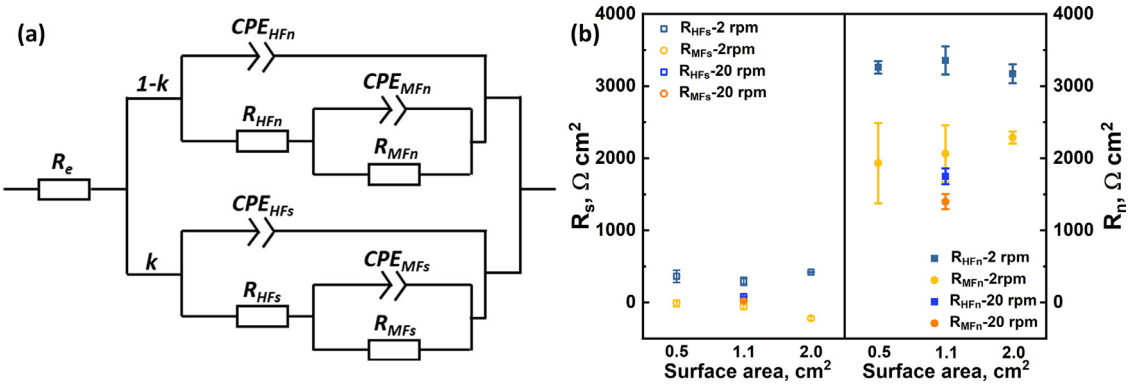

Fig. 10. (a) Equivalent circuit of abraded surface and (b) calculated results of abraded Mg in 0.05 M NaCl solution with various exposed surface areas.

face film resistance, rather than ΔR_{MF}. The difference in CPE values of Mg with various exposed surface areas before and after abrasion are neither calculated nor compared since the standard deviations of CPE values are large and the exponents α for different states are not the same.

To further verify the origin of the two time constants, the influence of scratched surface is estimated for R_{HF} and R_{MF}. Accordingly, the equivalent circuit presented in Fig. 7c is updated and illustrated in Fig. 10a. This equivalent circuit (Fig. 10a) is designed to separate the contribution from the surface of the scratch and the surface of the unscratched electrode, where k and (1- k) are adopted to define the impact of each contribution. This model is used to explain the way to calculated R_{HFs} and R_{MFs}, and is not used in the fitting procedure via software. As shown in Fig. 10a, R_{HFs} and CPE_{HFs} represent the resistance and capacitance of high frequency time constant in the scratch. R_{MFs} and CPE_{MFs} are the resistance and capacitance of middle frequency time constant in the scratch, respectively. R_{HFn}, R_{MFn}, CPE_{HFn}, and CPE_{MFn} represent the corresponding elements for the unscratched surface. R_e is the electrolyte resistance. At the initial stage, the scratched surface area is 0 and k is also equal to 0. In this case, the total resistance in the direct current mode (without the contribution from imaginary component), R_{total}, is the sum of R_e, R_{HFn}, and R_{MFn}. At the abrasion stage, R_{total} depends on the ratio of abraded surface area, k. The total resistance of the whole system, R_{total}, can be expressed as [50],

$$R_{total} = R_e + \frac{1}{\frac{(1-k)}{R_{HFn}+R_{MFn}} + \frac{k}{R_{HFs}+R_{MFs}}} \tag{3}$$

Theoretically, R_{total} is equal to the value of Z_{real} when Z_{imag} is equal to 0, which can be obtained from the Nyquist plot, as illustrated in Fig. 7a. Besides, the diameter of the HF capacitive loop in Nyquist plot is equal to the total resistance of the HF time constant, R_{HF}, which can be obtained by fitting procedure and also can be calculated by the following equation,

$$\frac{1}{R_{HF}} = \frac{1-k}{R_{HFn}} + \frac{k}{R_{HFs}} \tag{4}$$

If we assume the unscratched surface film possesses the same properties as the surface film at the initial stage, then the R_{HFn} should be equal to the fitted R_{HF}', estimated from EIS-2 via the equivalent circuit in Fig. 7c. The R_{HF}'' is the total fitted resistance of the HF time constant at the abraded state, which is estimated from EIS-3 via the same circuit (Fig. 7c). Thus, Eq. (4) can be transformed to the following equation,

$$\frac{1}{R_{HF}''} = \frac{1-k}{R_{HF}'} + \frac{k}{R_{HFs}} \tag{5}$$

Thus, R_{HFs} can be expressed as following,

$$R_{HFs} = \frac{k}{\frac{1}{R_{HF}''} - \frac{1-k}{R_{HF}'}} \tag{6}$$

R_{MFs} can be expressed from Eq. (3) by:

$$R_{MFs} = \frac{k}{\frac{1}{R_{total}-R_e} - \frac{1-k}{R_{HFn}+R_{MFn}}} - R_{HFs} \tag{7}$$

Where R_{MFn} is equal to the fitted R_{MF}' of MF time constant in EIS-2 via the equivalent circuit from Fig. 7c. By combining Eqs. (6) and (7), R_{MFs} is expressed as:

$$R_{MFs} = \frac{k}{\frac{1}{R_{total}-R_e} - \frac{1-k}{R_{HF}'+R_{MF}'}} - \frac{k}{\frac{1}{R_{HF}''} - \frac{1-k}{R_{HF}'}} \tag{8}$$

The R_{HFs} and R_{MFs} of abraded Mg with different exposed surface areas under rotation with different speeds are calculated by Eqs. (6) and (8), which are referred to as calculated values and presented in Tables S5 and S6. The average values and deviations calculated from three parallel testes are illustrated in Fig. 10b. As shown in Fig. 10b, the calculated R_{HFs} and R_{MFs} are much less than R_{HFn} and R_{MFn}, indicating that the surface film and corrosion resistance on the abraded surface are much less than those on the surface covered by natural film. The calculated R_{HFs} for Mg with different surface areas under 2 rpm rotation are very close to each other. 20 rpm rotation leads to the decrease of both R_{HFs} and R_{HFn}. The calculated R_{MFs} for Mg with different surface areas are very close to zero or even negative values. Neither the resistance of surface film nor the resistance of charge transfer process is expected to be negative. The unexpected results appear probably because the actual value of R_{MFs} is very small and some inevitable errors are introduced in the process of obtaining $R_{HF}'(R_{HFn})$, R_{HF}'', $R_{MF}'(R_{MFn})$, and R_{total}-R_e values, such as the fitting error introduced by scattering of MF time constant and the estimation of scratched surface area.

As mentioned above, the native surface film of Mg formed in NaCl solution is composed of $Mg(OH)_2$ and MgO [17,39,40]. During abrasion, the abrasive pin mechanically removes the natural surface film and exposes bare Mg to the electrolyte for a certain amount of time. Fig. 11 illustrates the surface film of Mg during abrasion. As shown in Fig. 11, a part of the native surface film ($Mg(OH)_2$/MgO) is removed by the abrasive pin and more active sites for corrosion reaction are exposed in the scratch, and, thus, the surface film resistance and the charge transfer resistance in the scratch should be much less than those of the unscratched surface, which is consistent with the calculated results presented in Fig. 10b. The film resistance is related to the film intrinsic properties, integrity, presence of natural defects and induced damage, if any. When the abraded surface area does not change, but the exposed surface area of working electrode increases, the unscratched

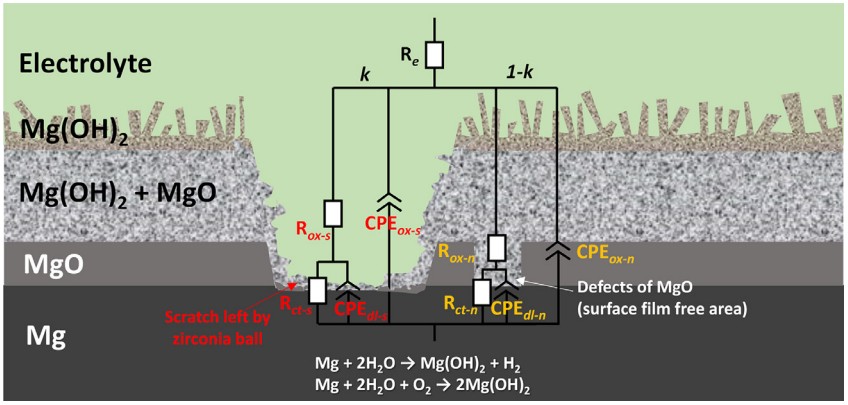

Fig. 11. Schematic illustration of surface film of abraded Mg in NaCl solution (cross section).

area increases, and, thus, the reduction of overall film resistance should be less and proportional to the weighting factor of the abraded area, k. As shown in Fig. 9c, ΔR_{HF} shows a positive correlation with k, elucidating that most likely the origin of the high frequency time constant is related to the surface film. Besides, with the same rotation rate, the film resistance in the scratch should possess a similar value in spite of the different exposed area of the Mg electrode because the properties of the film formed on the scratched region of Mg with different exposed areas with the same rotation rate should be close to each other. It is consistent with the calculated value of R_{HFs} as presented in Fig. 10b. Moreover, a faster rotation rate will reduce the re-passivated area during abrasion, resulting in the decrease of surface film resistance in the scratch. This is also compliant with the results of R_{HFs} in Fig. 10b. Furthermore, the fast re-passivation procedure of surface film ensures that the resistance of surface film in the scratch should never be zero. The values of R_{MFs} are calculated to be close to zero or even negative. Hence, the surface film resistance in the scratch should be R_{HFs} instead of R_{MFs}.

The charge transfer resistance, referred to in this work, reflects the kinetics of Mg corrosion reaction and, theoretically, should not be directly influenced by this kind of mechanical abrasion. Mg under anodic polarization is known to be a nearly ideally non-polarizable electrode with very small charge transfer resistance [51–54], which is consistent with the calculated R_{MFs}. However, as mentioned above, corrosion reaction can only happen in the film-free area enabling electrolyte access. Thus, the overall charge transfer resistance of Mg obtained by EIS measurement is also related to the ratio of film-free area to the entire exposed surface. The film-free area in native film of Mg is supposed to count for a very small area of the total exposed surface. According to the research of Gomes and co-authors [5], the proportion of film-free area is calculated as 0.003 of the total area of the natural surface film formed on Mg in Na_2SO_4 solution after 10 h under 1000 rpm rotation. The proportion of film-free area in our case is certainly different from their case due to the disparity of material, electrolyte and testing parameters. If we assume the ratio of film-free area in the native film of Mg under our testing condition is also 0.003, the total film-free area was in natural surface film varies from 0.15 to 0.6 mm^2 taking into account different exposed surface areas of 0.5~2.0 cm^2. During abrasion, the surface area of scratch is around 4.2 mm^2, which is 7~28 times larger than the native film-free area. The corrosion reaction would preferentially happen in the abraded region and the corrosion rate of Mg is greatly accelerated. The significantly increased film-free area created by abrasion certainly leads to remarkable reduction of the overall charge transfer resistance on entire exposed Mg surface, which is consistent with the evolution of the second time constant. Besides, during abrasion, the charge transfer resistance of Mg with different exposed surface areas should possess a similar value since it is mainly determined by the film-free area in the scratch and the created scratch is the same for all samples. Therefore, after abrasion, the reduction of overall charge transfer resistance is alike concerning the different exposed surface areas and does not show any correlation with the k value. This further demonstrates that the charge transfer process is represented by the MF time constant in the EIS of Mg concluded from the results presented in Figs. 6–10. Meanwhile, no well-defined time constant related to charge transfer process is expected to be observed in Mg EIS spectra under the abrasion state, because the impact of scratch on the charge transfer process is much larger than that of the intrinsic defects of MgO. The latter one can be considered as a state of dynamic equilibrium but the former one is always varying and is influenced by the abrasion, the reconstruction of double layer, and the reconstruction of surface film. Hence, the origin of the second time constant should be attributed to the charge transfer process. Based on the above discussion, the equivalent circuit with clear physical interpretations of time constants appearing in abraded Mg EIS spectra is proposed and presented in Fig. 11.

4. Conclusions

In this work, the origin and physical interpretations of time constants appearing in the high and middle frequency range of Mg EIS spectra in 0.05 M NaCl were studied by tribo-electrochemical technique. The results indicate that the abrasion introduced by tribometer, dramatically increases film-free sites for Mg corrosion reaction. Abrasion leads to the decrease of the total impedance of affected Mg surface, but the influence of abrasion on the high frequency time constant is less significant than that of the middle frequency time constant. The resistance reduction of the high frequency time constant is associated with the ratio of the abraded surface area to the total exposed surface area of Mg, which is consistent with the expectation for the change of surface film resistance caused by abrasion. The quantitative analysis further proves that the high frequency time constant stems from the surface film. The values of extracted film resistance in the scratch of Mg were comparable, even if the exposed area of the electrode was varied from 0.5 cm^2 to 2 cm^2. This is due to the similar properties of the surface film in the scratch. The middle frequency time constant is attributed to the double layer capacitance in parallel with the charge transfer resistance, which possesses extremely small value in the scratch. This shows the non-polarizable feature of Mg.

CRediT authorship contribution statement

Linqian Wang: Conceptualization, Investigation, Validation, Writing – original draft, Writing – review & editing. **Darya Snihirova:** Conceptualization, Supervision, Writing – review & editing. **Min Deng:** Conceptualization, Investigation, Writing – review & editing. **Bahram Vaghefinazari:** Conceptualization, Writing – review & editing. **Daniel Höche:** Conceptualization, Supervision, Writing – review & editing. **Sviatlana V. Lamaka:** Conceptualization, Supervision, Writing – review & editing. **Mikhail L. Zheludkevich:** Conceptualization, Supervision, Writing – review & editing.

Declaration of Competing Interest

The authors declare that they have no known competing financial interests or personal relationships that could have appeared to influence the work reported in this paper.

Credit authorship contribution statement

Linqian Wang: Conceptualization, Investigation, Validation, Writing – original draft, Writing – review & editing. **Darya Snihirova:** Conceptualization, Supervision, Writing – review & editing. **Min Deng:** Conceptualization, Investigation, Writing – review & editing. **Bahram Vaghefinazari:** Conceptualization, Writing – review & editing. **Daniel Höche:** Conceptualization, Supervision, Writing – review & editing. **Sviatlana V. Lamaka:** Conceptualization, Supervision, Writing – review & editing. **Mikhail L. Zheludkevich:** Conceptualization, Supervision, Writing – review & editing.

Acknowledgments

The authors would like to acknowledge Mr. Ulrich Burmester for the technical support; Mr. Volker Heitmann and Ms. Ting Wu for their help in microstructure characterization via laser scanning microscope; Linqian Wang and Min Deng are grateful for the award of fellowship from China Scholarship Council (No. 201706370183 and No. 201606370031). Additionally, the authors acknowledge SeaMag project funded by ERA-NET cofund MarTERA.

Supplementary materials

Supplementary material associated with this article can be found, in the online version, at doi:10.1016/j.electacta.2021.139582.

References

[1] M. Benoit, C. Bataillon, B. Gwinner, F. Miserque, M.E. Orazem, C.M. Sánchez-Sánchez, B. Tribollet, V. Vivier, Comparison of different methods for measuring the passive film thickness on metals, Electrochim. Acta 201 (2016) 340–347.
[2] R. De Motte, E. Basilico, R. Mingant, J. Kittel, F. Ropital, P. Combrade, S. Necib, V. Deydier, D. Crusset, S. Marcelin, A study by electrochemical impedance spectroscopy and surface analysis of corrosion product layers formed during CO_2 corrosion of low alloy steel, Corros. Sci. 172 (2020) 108666.
[3] M.L. Zheludkevich, R. Serra, M.F. Montemor, K.A. Yasakau, I.M.M. Salvado, M.G.S. Ferreira, Nanostructured sol-gel coatings doped with cerium nitrate as pre-treatments for AA2024-T3, Electrochim. Acta 51 (2005) 208–217.
[4] M. Curioni, L. Salamone, F. Scenini, M. Santamaria, M. Di Natale, A mathematical description accounting for the superfluous hydrogen evolution and the inductive behaviour observed during electrochemical measurements on magnesium, Electrochim. Acta 274 (2018) 343–352.
[5] M.P. Gomes, I. Costa, N. Pébère, J.L. Rossi, B. Tribollet, V. Vivier, On the corrosion mechanism of Mg investigated by electrochemical impedance spectroscopy, Electrochim. Acta 306 (2019) 61–70.
[6] G.L. Song, K.A. Unocic, The anodic surface film and hydrogen evolution on Mg, Corros. Sci. 98 (2015) 758–765.
[7] L.G. Bland, K. Gusieva, J. Scully, Effect of crystallographic orientation on the corrosion of magnesium: comparison of film forming and bare crystal facets using electrochemical impedance and Raman spectroscopy, Electrochim. Acta 227 (2017) 136–151.
[8] V. Shkirskiy, A.D. King, O. Gharbi, P. Volovitch, J.R. Scully, K. Ogle, N. Birbilis, Revisiting the electrochemical impedance spectroscopy of magnesium with online inductively coupled plasma atomic emission spectroscopy, Chemphyschem 16 (2015) 536–539.
[9] G. Baril, G. Galicia, C. Deslouis, N. Pébère, B. Tribollet, V. Vivier, An impedance investigation of the mechanism of pure magnesium corrosion in sodium sulfate solutions, J. Electrochem. Soc. 154 (2007) C108–C113.
[10] X. Wang, Z. Chen, J. Ren, H. Kang, E. Guo, J. Li, T. Wang, Corrosion behavior of as-cast Mg-5Sn based alloys with In additions in 3.5wt% NaCl solution, Corros. Sci. 164 (2020) 108318.
[11] Y. Li, X. Lu, K. Wu, L. Yang, T. Zhang, F. Wang, Exploration the inhibition mechanism of sodium dodecyl sulfate on Mg alloy, Corros. Sci. 168 (2020) 108559.
[12] Y. Jin, C. Blawert, F. Feyerabend, J. Bohlen, M.S. Campos, S. Gavras, B. Wiese, D. Mei, M. Deng, H. Yang, R. Willumeit-Römer, Time-sequential corrosion behaviour observation of micro-alloyed Mg-0.5Zn-0.2Ca alloy via a quasi-in situ approach, Corros. Sci. 158 (2019) 108096.
[13] Y. Sun, R. Wang, C. Peng, Z. Cai, Microstructure and corrosion behavior of as-extruded Mg-xLi-3Al-2Zn-0.2Zr alloys (x = 5, 8, 11 wt.%), Corros. Sci. 167 (2020) 108487.
[14] Y. Shi, C. Peng, Y. Feng, R. Wang, N. Wang, Enhancement of discharge properties of an extruded Mg-Al-Pb anode for seawater-activated battery by lanthanum addition, J. Alloys Compd. 721 (2017) 392–404.
[15] X. Chen, Q. Zou, Q. Le, J. Hou, R. Guo, H. Wang, C. Hu, L. Bao, T. Wang, D. Zhao, F. Yu, A. Atrens, The quasicrystal of Mg-Zn-Y on discharge and electrochemical behaviors as the anode for Mg-air battery, J. Power Sources 451 (2020) 227807.
[16] S. Yin, W. Duan, W. Liu, L. Wu, J. Yu, Z. Zhao, M. Liu, P. Wang, J. Cui, Z. Zhang, Influence of specific second phases on corrosion behaviors of Mg-Zn-Gd-Zr alloys, Corros. Sci. 166 (2020) 108419.
[17] L. Wang, D. Snihirova, M. Deng, C. Wang, B. Vaghefinazari, G. Wiese, M. Langridge, D. Höche, S.V. Lamaka, M.L. Zheludkevich, Insight into physical interpretation of high frequency time constant in electrochemical impedance spectra of Mg, Corros. Sci. 187 (2021) 109501.
[18] S. Fajardo, C.F. Glover, G. Williams, G.S. Frankel, The source of anodic hydrogen evolution on ultra high purity magnesium, Electrochim. Acta 212 (2016) 510–521.
[19] O.V. Karavai, A.C. Bastos, M.L. Zheludkevich, M.G. Taryba, S.V. Lamaka, M.G.S. Ferreira, Localized electrochemical study of corrosion inhibition in microdefects on coated AZ31 magnesium alloy, Electrochim. Acta 55 (2010) 5401–5406.
[20] G. Williams, N. Birbilis, H.N. McMurray, The source of hydrogen evolved from a magnesium anode, Electrochem. Commun. 36 (2013) 1–5.
[21] S.H. Salleh, S. Thomas, J.A. Yuwono, K. Venkatesan, N. Birbilis, Enhanced hydrogen evolution on Mg $(OH)_2$ covered Mg surfaces, Electrochim. Acta 161 (2015) 144–152.
[22] S.S. Jamali, S.E. Moulton, D.E. Tallman, M. Forsyth, J. Weber, G.G. Wallace, Evaluating the corrosion behaviour of magnesium alloy in simulated biological fluid by using SECM to detect hydrogen evolution, Electrochim. Acta 152 (2015) 294–301.
[23] T. Balusamy, T. Nishimura, Localized electrochemical impedance spectroscopy observation on scratched epoxy coated carbon steel in saturated $Ca(OH)_2$ with various chloride concentration, J. Anal. Bioanal. Tech. 7 (2016) 328.
[24] J.B. Jorcin, M.E. Orazem, N. Pébère, B. Tribollet, CPE analysis by local electrochemical impedance spectroscopy, Electrochim. Acta 51 (2006) 1473–1479.
[25] J. Wysocka, S. Krakowiak, J. Ryl, Evaluation of citric acid corrosion inhibition efficiency and passivation kinetics for aluminium alloys in alkaline media by means of dynamic impedance monitoring, Electrochim. Acta 258 (2017) 1463–1475.
[26] M. Keddam, P. Ponthiaux, V. Vivier, Tribo-electrochemical impedance: a new technique for mechanistic study in tribocorrosion, Electrochim. Acta 124 (2014) 3–8.
[27] S. Barril, S. Mischler, D. Landolt, Triboelectrochemical investigation of the friction and wear behaviour of TiN coatings in a neutral solution, Tribol. Int. 34 (2001) 599–608.
[28] M. Azzi, J.A. Szpunar, Tribo-electrochemical technique for studying tribocorrosion behavior of biomaterials, Biomol. Eng. 24 (2007) 443–446.
[29] M. Keddam, F. Liao, P. Ponthiaux, V. Vivier, New advances in triboelectrochemistry: from steady state to impedance of abraded stainless steel in acidic medium, J. Solid State Electrochem. 19 (2015) 2591–2599.
[30] G. Burstein, D. Davies, The electrochemical behavior of scratched iron surfaces in aqueous solutions, J. Electrochem. Soc. 128 (1981) 33–39.
[31] G.S. Frankel, Repassivation transients measured with thin film breaking electrodes, J. Electrochem. Soc. 138 (1991) 643.
[32] P. Bastek, R. Newman, R. Kelly, Measurement of passive film effects on scratched electrode behavior, J. Electrochem. Soc. 140 (1993) 1884.
[33] C.J. Park, Repassivation kinetics of zirconium alloys investigated by a scratching electrode technique, Met. Mater. Int. 14 (2008) 71–75.
[34] G. Burstein, R. Newman, Anodic behaviour of scratched silver electrodes in alkaline solution, Electrochim. Acta 25 (1980) 1009–1013.
[35] S. Barril, N. Debaud, S. Mischler, D. Landolt, A tribo-electrochemical apparatus for in vitro investigation of fretting–corrosion of metallic implant materials, Wear 252 (2002) 744–754.
[36] T.M. Manhabosco, S.M. Tamborim, C.B. dos Santos, I.L. Müller, Tribological, electrochemical and tribo-electrochemical characterization of bare and nitrided Ti6Al4V in simulated body fluid solution, Corros. Sci. 53 (2011) 1786–1793.

[37] A.D. Gabbardo, G.S. Frankel, Hydrogen evolution on bare Mg surfaces using the scratched electrode technique, Corros. Sci. 164 (2020) 108321.
[38] Y. Yan, P. Zhou, O. Gharbi, Z. Zeng, X. Chen, P. Volovitch, K. Ogle, N. Birbilis, Investigating ion release using inline ICP during in situ scratch testing of an Mg-Li(-Al-Y-Zr) alloy, Electrochem. Commun. 99 (2019) 46–50.
[39] M. Taheri, M. Danaie, J. Kish, TEM examination of the film formed on corroding Mg prior to breakdown, J. Electrochem. Soc. 161 (2014) C89–C94.
[40] M. Taheri, J.R. Kish, N. Birbilis, M. Danaie, E.A. McNally, J.R. McDermid, Towards a physical description for the origin of enhanced catalytic activity of corroding magnesium surfaces, Electrochim. Acta 116 (2014) 396–403.
[41] D. Roessler, W. Walker, Electronic spectrum and ultraviolet optical properties of crystalline MgO, Phys. Rev. 159 (1967) 733.
[42] R. Whited, C.J. Flaten, W. Walker, Exciton thermoreflectance of MgO and CaO, Solid State Commun. 13 (1973) 1903–1905.
[43] I. Marco, O. Van der Biest, Polarization measurements from a rotating disc electrode for characterization of magnesium corrosion, Corros. Sci. 102 (2016) 384–393.
[44] A. Younes, S. Omanovic, Effect of electrolyte flow on the corrosion behavior of magnesium alloy AZ31B, Corrosion 75 (2019) 973–981.
[45] R.Q. Hou, F. Zhang, P.L. Jiang, S.G. Dong, J.S. Pan, C.J. Lin, Corrosion inhibition of pre-formed mussel adhesive protein (Mefp-1) film to magnesium alloy, Corros. Sci. 164 (2020) 108309.
[46] G. Brug, A. Van Den Eeden, M. Sluyters-Rehbach, J. Sluyters, The analysis of electrode impedances complicated by the presence of a constant phase element, J. Electroanal. Chem. 176 (1984) 275–295.
[47] C. Hsu, F. Mansfeld, Concerning the conversion of the constant phase element parameter Y_0 into a capacitance, Corrosion 57 (2001) 747–748.
[48] M.A. Rodríguez, R.M. Carranza, Properties of the passive film on alloy 22 in chloride solutions obtained by electrochemical impedance, J. Electrochem. Soc. 158 (2011) C221–C230.
[49] S. Chakri, I. Frateur, M.E. Orazem, E.M.M. Sutter, T.T.M. Tran, B. Tribollet, V. Vivier, Improved EIS analysis of the electrochemical behaviour of carbon steel in alkaline solution, Electrochim. Acta 246 (2017) 924–930.
[50] M.E. Orazem, B. Tribollet, Electrochemical Impedance Spectroscopy, John Wiley & Sons2017.
[51] A.D. King, N. Birbilis, J.R. Scully, Accurate electrochemical measurement of magnesium corrosion rates; a combined impedance, mass-loss and hydrogen collection study, Electrochim. Acta 121 (2014) 394–406.
[52] Y. Yang, F. Scenini, M. Curioni, A study on magnesium corrosion by real-time imaging and electrochemical methods: relationship between local processes and hydrogen evolution, Electrochim. Acta 198 (2016) 174–184.
[53] S. Fajardo, G. Frankel, Gravimetric method for hydrogen evolution measurements on dissolving magnesium, J. Electrochem. Soc. 162 (2015) C693.
[54] S. Fajardo, F.R. García-Galvan, V. Barranco, J.C. Galvan, S.F. Batlle, A critical review of the application of electrochemical techniques for studying corrosion of mg and mg alloys: opportunities and challenges, Magnes. Alloys Sel. Issue (2018).

5.3 Tailoring electrolyte additives for controlled Mg-Ca anode activity in aqueous Mg-air batteries

Paper 3 is published in Journal of Power Sources, 460 (2020), 228106.

The emphasis of the work is to enhance the discharge performance of primary AMAB with newly developed Mg-0.04Ca anode by tailoring the electrolyte additives. In this paper, we proposed to use Mg^{2+} complexing agents as electrolyte additives and investigated the effect of selected electrolyte additives (CIT, SAL, 5-SulfoSAL, 2,6-DHB and 3,4-DHB) on the corrosion behavior and discharge performance of Mg-Ca anode. The results indicated that Mg^{2+} complexing agents overall have positive effect on the discharge performance of Mg-Ca based MAB, attributed to their capability of hindering the precipitation of discharge products and reducing the efficiency loss caused by chunk effect. Nevertheless, different additives should be used for different discharge loads to obtain optimal effect because strong complexing agents (like 3,4-DHB) cause significant loss of UE at low current densities but moderate complexing agents (like SAL) are not sufficient to hinder the formation of precipitates at high current densities.

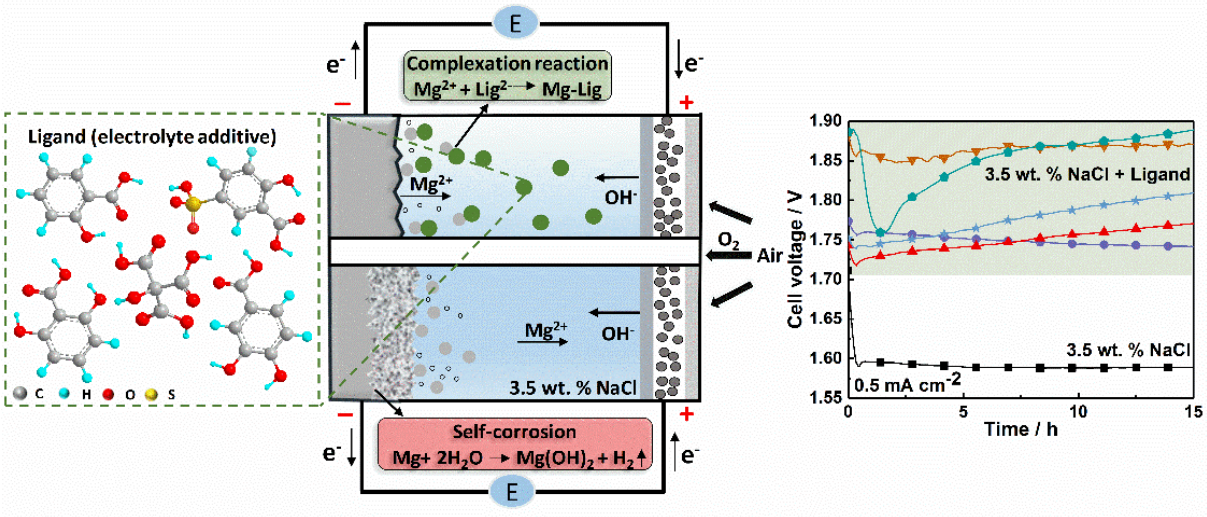

Fig. 5-4. Graphical abstract for **Section 5.3**.

Journal of Power Sources 460 (2020) 228106

Contents lists available at ScienceDirect

Journal of Power Sources

journal homepage: www.elsevier.com/locate/jpowsour

Tailoring electrolyte additives for controlled Mg-Ca anode activity in aqueous Mg-air batteries

Linqian Wang [a,*], Darya Snihirova [a], Min Deng [a], Bahram Vaghefinazari [a], Sviatlana V. Lamaka [a], Daniel Höche [a], Mikhail L. Zheludkevich [a,b]

[a] MagIC—Magnesium Innovation Center, Helmholtz-Zentrum Geesthacht (HZG), 21502, Geesthacht, Germany
[b] Institute of Materials Science, Kiel University, 24143, Kiel, Germany

HIGHLIGHTS

- Mg^{2+} complexing agent was used as electrolyte additive for aqueous Mg-air battery.
- Discharge properties depend on the stability of the complex formed with Mg^{2+}.
- Coverage of $Mg(OH)_2$ was hindered and Chunk effect was reduced.
- High specific energy density of 3007 Wh kg^{-1} and voltage of 1.86 V was achieved.

GRAPHICAL ABSTRACT

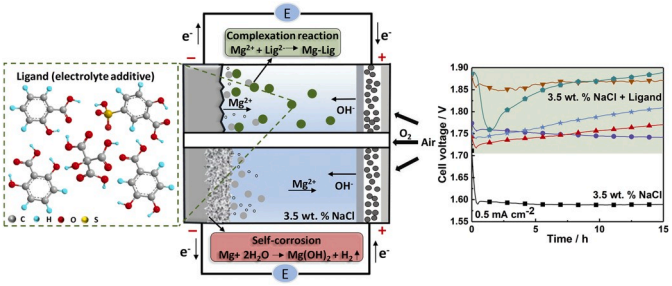

ARTICLE INFO

Keywords:
Aqueous primary Mg-air battery
Electrolyte additives
Mg^{2+} complexing agent
Discharge performance
Chunk effect

ABSTRACT

Aqueous primary Mg-air batteries exhibit many merits as potential energy storage and conversion devices. In this work, the discharge performance of water based Mg-air batteries with advanced Mg-Ca anode was boosted by adding Mg^{2+} complexing agents into the electrolyte. The effect of electrolyte additives on the corrosion behavior and discharge properties of micro-alloyed Mg-Ca anode was investigated via hydrogen evolution test and half-cell discharge test. Electrochemical impedance spectroscopy (EIS) was performed to evaluate the effect of different electrolyte additives on the discharge activity of Mg-Ca anode. Basic characteristics of aqueous Mg-air battery in selected additive solution were tested and compared to pure NaCl solution. The results show that the addition of dedicated Mg^{2+} complexing agents can efficiently increase the discharge voltage and specific energy of respective Mg-air batteries. At 0.5 mA cm^{-2}, the discharge voltage reaches 1.86 V with regard to the cell containing 0.1 M 5-Sulfosalicylate, which is 270 mV higher than the discharge voltage in bulk 3.5 wt % NaCl. The highest specific energy for the tested system is above 3.0 kWh kg^{-1} in NaCl solution with 0.1 M citrate at 1 mA cm^{-2} discharge current density.

1. Introduction

Aqueous primary Mg-air batteries can be adopted as attractive electrochemical energy storage and conversion devices because of superior discharge performance, safety, low cost, and environmental amiability [1–3]. Mg-air batteries consume oxygen from the air and the

* Corresponding author. Helmholtz-Zentrum Geesthacht, Max-Planck-Str. 1, 21502, Geesthacht, Germany.
E-mail address: Linqian.Wang@hzg.de (L. Wang).

https://doi.org/10.1016/j.jpowsour.2020.228106
Received 21 January 2020; Received in revised form 4 March 2020; Accepted 24 March 2020
Available online 5 April 2020

electrolyte as cathodic reactant, which is environmentally friendly and beneficial for the weight reduction of battery system, increasing the specific energy. Besides, water based Mg-air batteries can be artificially recharged through displacing anode material, which makes them as promising candidates for portable devices, remote devices, marine applications and military technologies [4].

As anode material, Mg exhibits highly negative standard electrode potential (−2.37 V vs SHE) and high volumetric capacity, which is even higher than that of Li (3833 mA h cm^{-3} for Mg vs. 2046 mA h cm^{-3} for Li) [1,5–7]. However, during the discharge process, Mg anode materials suffer from serious self-corrosion, like micro-galvanic corrosion provoked by impurities or second phases, and chunk effect caused by the detachment of metallic particles from the anode surface as well as the accelerated corrosion due to negative difference effect [8,9]. These side reactions significantly decrease the anode utilization efficiency and consequently reduce the battery capacity. Meanwhile, Mg anode surface is typically covered by discharge products, such as $Mg(OH)_2$ and MgO, which hinder the contact of the reactive surface with the electrolyte, and thus, decrease the discharge voltage [10]. Therefore, the actual discharge performance of Mg anode shifts far away from the theoretical value, adversely affecting the working voltage and practical specific energy of Mg-air batteries.

The possible technical solutions to diminish the difference between the theoretical and practical discharge performance of the studied Mg-air batteries are the modification of the anode and the optimization of the electrolyte composition. Numerous published works have focused on increasing the discharge performance of Mg-air batteries by looking for suitable Mg anode materials, which possess high discharge activities and low corrosion rates [10–14]. Aiming at improving the discharge performance of Mg anode materials, a lot of researchers put emphasis on alloying Mg with various metallic elements, such as, Al, Zn, Li, Mn, Ga, Pb, Hg, rare earth, etc. [15–21]. These metallic elements are in favor of the inhibition of the parasitic side reactions and the improvement of discharge potential due to activation or their own electronegativity. Meanwhile, the addition of alloying elements improves the deformability of Mg alloy, which is also an important issue considering their practical application in Mg-air batteries [22–26]. However, some alloying elements are toxic, not economically relevant and demonstrate a low efficiency in enhancing the discharge performance. Recently, Deng et al. [27] proposed a newly developed Mg-Ca binary alloy as the anode material for Mg-air battery. Ca is an environmentally friendly and cost-effective alloying element. Upon addition of minor amount of Ca, the anode material gains higher discharge voltage and increased specific energy. Beside of alloy composition optimization, improving the microstructure of Mg anode materials by adopting deformation methods (such as extrusion and rolling) and heat treatments (such as normalizing, solid solution annealing and aging) also attracts attention of many researchers [28–31].

In addition to the modification of anode materials, the introduction of additives into electrolyte can also effectively improve the discharge performance of Mg-air batteries. One way to improve Mg-air battery performance is using corrosion inhibitors of Mg as electrolyte additives to obtain higher utilization efficiency [32–34]. However, the addition of traditional corrosion inhibitors normally does not improve the discharge voltage or makes it even worse. Recently, research work of Höche et al. [35,36] showed that the self-corrosion of Mg could be decreased through hindering the re-deposition of iron. The utilization efficiency of commercially pure Mg (220 ppm Fe) doubled while the battery voltage of Mg-air battery increased by adopting salicylate as electrolyte additive at 0.5 mA cm^{-2}. Nevertheless, the utilization efficiency of commercially pure Mg in NaCl solution with salicylate is 27.2%. Some researchers also try to adopt surfactants with long chain as electrolyte additives [37,38]. By the physical adsorption mechanism of surfactant, the corrosion rate of Mg anode would be decreased. According to the research work of Deyab [38], decyl glucoside as electrolyte additive can increase the utilization efficiency of pure Mg anode as well as improve its operating voltage. Whereas, this paper puts emphasis on the corrosion efficiency of decyl glucoside and dose not clarify the reason for the improvement of operating voltage.

This work aims to enhance the discharge performance of (Mg-Ca)-air battery by tailoring the electrolyte additives. New and earlier selected Mg^{2+} complexing agents [39,40] are studied as potential candidates due to their ability to form soluble Mg-complexes and hinder the formation of $Mg(OH)_2$. The effect of selected Mg^{2+} complexing agents on the corrosion behavior of Mg-Ca anode and the discharge performance of respective (Mg-Ca)-air battery is systematically investigated, which contributes to a better understanding of the working mechanism of Mg^{2+} complexing agents in aqueous Mg-air batteries.

2. Materials and methods

2.1. Materials and electrolytes

According to the research work of Deng et al. [27], with the increase of Ca content, the discharge performance of Mg-Ca becomes worse. The results of composition optimization indicate that Mg-0.1 wt % Ca has the best discharge performance. However, the discharge performance of minor alloying Mg-Ca alloy (Ca content is less than 0.1 wt %) has not been tested. Thus, Mg-0.04 wt % Ca, which is denoted as Mg-Ca in the following, was prepared by the same procedure represented in the aforementioned work [27] and adopted as anode material for this work. The chemical composition of Mg-Ca alloy was analyzed via atomic absorption spectroscopy (AAS) and spark optical emission spectrometry (SOES), which is summarized in Table 1 and indicates low impurity contents (Fe, Cu and Ni).

The electrolyte used in this work was 3.5 wt % NaCl solution with and without 0.1 M additives. The blank NaCl solution as background electrolyte was prepared by adopting 99% NaCl from Fisher Chemical and deionized water. The following chemicals from Sigma-Aldrich were used as electrolyte additives without further purification: citric acid (CIT); salicylic acid (SAL); 2,6-dihydroxybenzoic acid (2,6-DHB); 5-sulfosalicylic acid (5-sulfoSAL) and 3,4-dihydroxybenzoic acid (3,4-DHB). The pH of all prepared solutions was adjusted to 7.0 ± 0.3 by adding NaOH, monitored by Metrohm-691 pH meter.

2.2. Hydrogen evolution test

Hydrogen evolution tests were carried out using eudiometers. Unlike typical buret-funnel setup, eudiometer is a closed system, thus it excludes the additional intake of O_2, CO_2 and N_2 apart from initially trapped air. The Mg-Ca samples with surface area of 15 cm^2 were tested in 500 ml solution. Before hydrogen evolution test, samples were ground up to 1200 grit emery papers and dried with cold pressed air. The immersion solution was 3.5 wt % NaCl with and without 0.1 M electrolyte additives. During hydrogen evolution test, the electrolyte was stirred with a constant speed, 350 ± 100 rpm. The hydrogen was collected during 24 h. All tests were repeated at twice, the difference between these two tests is less than 10%.

2.3. Electrochemical measurement

Electrochemical impedance spectroscopy (EIS) measurements at OCP were performed using Gamry Reference 600 potentiostat with conventional three electrodes arrangement. Pt coiled wire worked as counter electrode, saturated Ag/AgCl electrode worked as reference electrode and Mg-Ca coupon was employed as working electrode. The surface area of working electrode was 2.5 cm^2, and before EIS measurements, Mg-Ca surface was prepared by the same procedure as the sample for hydrogen evolution test. The sample was immersed into the electrolyte for 1 h prior the test to achieve stable surface state and stable open circuit potential (OCP). The tested electrode surface must be at a steady state throughout the time required for EIS measurement to ensure

Table 1
Chemical composition of Mg-Ca alloy (wt. %).

Materials	Ca	Mn	Si	Zn	Al	Fe	Cu	Ni	Mg
Mg-Ca	0.041	0.019	0.0086	0.0038	<0.010	0.0021	0.0012	0.0010	Bal.

the accuracy of results. The applied perturbation voltage was 10 mV_{rms} and frequency range was 100 kHz - 0.01 Hz with 10.5 points per decade. All the EIS measurements were repeated three times.

2.4. Half-cell discharge test

A Gamry Interface 1000 potentiostat with typical three-electrode arrangement was used to perform the half-cell discharge tests. The sample for the half-cell test is the same as the sample for EIS test, which has the same surface area and the same preparation procedure. Half-cell discharge tests were done in a galvanostaic mode with applied current densities of 1 mA cm^{-2}, 5 mA cm^{-2}, and 10 mA cm^{-2}. Working and counter electrodes were placed in two separated beakers connected by a salt bridge (Fig. 1). The two compartments were used in order to avoid influence of rapid pH changes caused by cathodic processes on anode discharge. During discharge, the electrolyte stirred at the same speed used in hydrogen evolution test. After half-cell discharge test, the surface of the remaining Mg-Ca anode was cleaned by aqueous solution of chromic acid to remove the discharge products and calculate the weight loss. The surface morphologies of Mg-Ca were characterized by scanning electron microscope (SEM; Tescan Vega 3) equipped with energy dispersion spectrometer (EDS; iXRF system). Utilization efficiencies of Mg-Ca alloy in different additive solutions were calculated via the following equation [41,42]:

$$Utilization\ efficiency\ (\%) = \frac{W_{theo}}{\Delta W} \times 100\% \quad (1)$$

Where W_{theo} (g) means the theoretical weight loss of anode and ΔW (g) means the actual weight loss obtained from the mass difference of anode before and after discharge. W_{theo} was calculated via the following equation [41,42]:

$$W_{theo} = \frac{I \times t}{F \times \sum\left(\frac{x_i \times n_i}{m_i}\right)} \quad (2)$$

where I (A) represents the applied current, t (h) represents discharge time, F is the Faraday constant (26.8 Ah mol^{-1}), x_i, n_i, m_i represent the mass fraction, ionic valence and atomic weight of the element, respectively.

2.5. Mg-air battery full cell test

Mg-air battery full cell tests were performed in 3.5 wt % NaCl solution with and without additives. Mg-Ca alloy with 2.5 cm^2 surface area worked as anode and Carbon/MnO_2 fabric with PTFE gas diffusion layer and Ni mesh (Kynol Europa GmbH) worked as cathode. The discharge voltage was tested at various applied current densities 0.5 mA cm^{-2}, 1 mA cm^{-2}, 5 mA cm^{-2}, and 10 mA cm^{-2}. After discharge, the specific energy of Mg-air battery based on Mg anode was calculated via the following equation [43]:

$$Specific\ energy\ (Wh\ \ kg^{-1}) = \frac{\int_0^t I \times U \times \Delta t}{\Delta W} \quad (3)$$

where U (V) represents the voltage of discharge, ΔW (kg) is the weight loss of anode after full cell test, I (A) and t (h) represent the same meaning as previously mentioned.

3. Results and discussion

3.1. Hydrogen evolution test

The corrosion of metallic Mg in neutral aqueous solution is accompanied by hydrogen evolution. Eq. (4) represents the global reaction of Mg corrosion, where 1 mol corroded Mg produces 1 mol hydrogen [2,44]. Hydrogen evolution test can directly reflect the difference of the corrosion rate of Mg-Ca in different electrolytes. However, this only holds true, if oxygen reduction reaction, as secondary cathodic reaction during Mg corrosion, is negligible. Although it was recently shown that oxygen is significantly consumed at the surface of corroding Mg [45], it is still not clear what is the ratio between HER and ORR when considering cathodic process as a whole. It is assumed that the contribution of ORR to the total cathodic process is minimal in the confined volume of eudiometers used in current work.

$$Mg + 2H_2O \rightarrow Mg(OH)_2 + H_2\uparrow \quad (4)$$

Fig. 2a represents the volume of evolved hydrogen during 24 h test. Several additives with different abilities to form complexes with Mg^{2+} were tested. The lowest hydrogen volume, thus the lowest corrosion

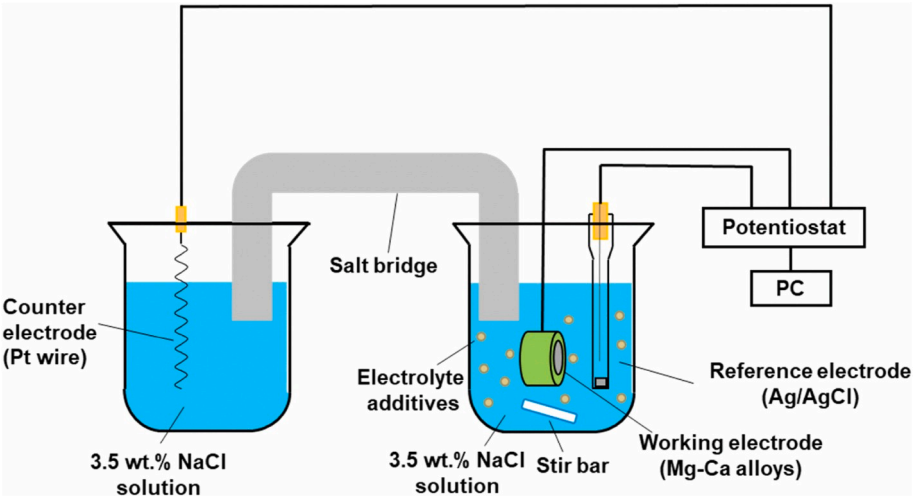

Fig. 1. Schematic of discharge test performed in half-cell arrangement.

rate, was detected for Mg-Ca in blank 3.5 wt % NaCl solution, which demonstrates good corrosion resistance. All selected additives accelerated the dissolution of Mg-Ca in NaCl solution at different extent. The different hydrogen evolution rates can be correlated to the stability constants of Mg^{2+} complexes, which are listed in Table 2 except for 2,6-DHB. The information about stability constant of complexes formed by 2,6-DHB with Mg^{2+} was not found in literature. It should be noted that the main idea behind choice of additives was their ability to keep anode surface clean during discharge, namely, their ability to produce soluble complexes with Mg^{2+} of mild stability. Hence, the generation of Mg $(OH)_2$ is retarded and the IR drop caused by $Mg(OH)_2$ is diminished during discharge. However, it might also increase the corrosion rate of Mg-Ca without load or with low current load, especially if an additive forms highly stable complexes with Mg^{2+} and the stability constant is high.

Hydra-Medusa software was adopted here to simulate the possible chemical equilibria in order to estimate the in-situ surface condition of Mg-Ca alloy after 24 h hydrogen evolution test in the presence and absence of selected additives. The estimated concentration of Mg(II) ions in different additive solution was calculated from the result of hydrogen evolution test: 1.16 mM for blank NaCl solution, 4.20 mM for NaCl solution with 0.1 M CIT and 90.18 mM for NaCl solution with 0.1 M 3,4-DHB. The difference in the initial concentration of Mg(II) ions will influence the critical pH for the generation of $Mg(OH)_2$, namely, the generation of precipitates. The results of Hydra-Medusa simulation are plotted in Fig. 2.

Fig. 2b shows the formation of insoluble $Mg(OH)_2$ in blank NaCl solution takes place at pH 10.4. The final pH of blank NaCl solution after 24 h hydrogen evolution test is 10.7, which is above 10.4, and insoluble corrosion products start to precipitate on Mg-Ca alloy surface at this pH, like Fig. 2e shows. When 0.1 M CIT as Mg^{2+} complexing agent is introduced to NaCl solution (Fig. 2c), the precipitation of $Mg(OH)_2$ is delayed from pH 10.4 to pH 10.8 even the total amount of Mg(II) ions generated by the dissolution of Mg-Ca is higher than in blank NaCl solution. From Fig. 2c, soluble Mg-ligand complexes form and exist in a wide pH range at least from pH 5 to 14. Hence, even the total amount of Mg(II) ions is higher, the free Mg^{2+} in the solution is even less than in blank NaCl solution. Between the pH ranges from 7 to 10.8, soluble complexes form and the dissolution of Mg-Ca is accelerated. However, after 24 h hydrogen evolution test, the final pH of this solution is 11.4, which exceeds the critical pH. The formed precipitates changed the color of Mg-Ca alloy surface, as shown in Fig. 2e. According to Fig. 2a, a large amount of Mg-Ca was dissolved into NaCl solution with 0.1 M 3,4-DHB. Thus, the total amount of Mg(II) ions in NaCl solution with 0.1 M 3,4-

Table 2
Stability constants of Mg^{2+} complexes produced by selected electrolyte additives and equilibrium constants of selected additives after 24 h hydrogen evolution tests [46–48].

Complexing agent	Stability constants		pH after 24 h of hydrogen evolution test (initial pH 7)
	$logKMg^{2+}$	Ref.	
NaCl reference	-	-	10.7
CIT	ML/M.L 3.45 MHL/M.HL 1.81 MH2L/M. H2L 0.7	[48]	11.4
SAL	ML/M.L 4.7	[46]	11.2
2,6-DHB	n/a	-	11.2
5-sulfoSAL	ML/M.L 5.1 MHL/M.HL 0.73	[48]	11.0
3,4-DHB	ML/M.L 5.67 ML2/M.L2 9.84	[47]	9.5

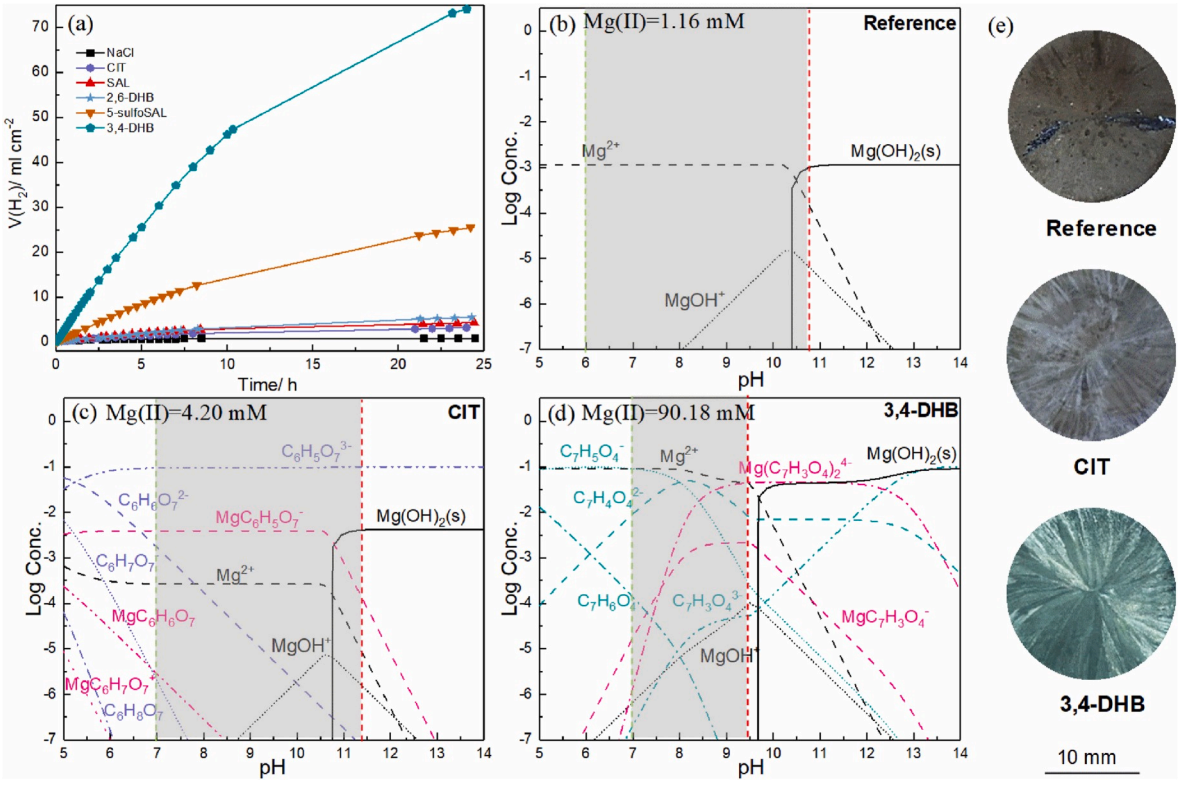

Fig. 2. (a) Hydrogen evolution curves of Mg-Ca in 3.5 wt % NaCl solution with and without additives and thermodynamic calculation of the equilibrium composition of relevant species in (b) blank 3.5 wt % NaCl; and the same electrolyte with 0.1 M (c) CIT; and (d) 3,4-DHB. The green and red lines present the initial pH and the final pH after 24 h hydrogen evolution test. The optical images of samples after 24 h hydrogen evolution test are shown in (e). (For interpretation of the references to color in this figure legend, the reader is referred to the Web version of this article.)

DHB is almost hundred times higher than that for blank NaCl solution. Even 3,4-DHB possesses the strongest complexation ability among selected additives, the concentration of free Mg^{2+} in NaCl solution with 0.1 M 3,4-DHB is still higher than that in blank NaCl solution (Fig. 2d). Hence, the critical pH in NaCl solution with 0.1 M 3,4-DHB is 9.7, which is lower than the critical pH in blank NaCl solution. As Fig. 2d shows, Mg complexes with 3,4-DHB ($Mg(C_7H_3O_4)_2^{4-}$ and $MgC_7H_3O_4^-$) exist and are stable at high pH, especially for $Mg(C_7H_3O_4)_2^{4-}$. After 24 h hydrogen evolution test, the final pH of NaCl solution with 3,4-DHB is 9.5, which does not exceed the critical pH for the generation of stable precipitates. This is in line with the experimentally observed surface of Mg-Ca alloy in NaCl solution with 3,4-DHB, which is macroscopically clean with metallic luster and without the coverage of $Mg(OH)_2$ (Fig. 2e). When 3,4-DHB is adopted as electrolyte additives for Mg-air battery, it might hinder the precipitation of discharge products and increase the anode activity during discharge.

As Table 2 shows, the final pH of tested electrolyte containing CIT, SAL, 5-sulfoSAL and 2,6-DHB is higher than the final pH of blank NaCl solution, because OH^- generated during hydrogen evolution reaction (HER, Eq. (4)) is barely consumed for formation of $Mg(OH)_2$. However, the final pH of NaCl solution with 3,4-DHB is lower than 10.7. 3,4-DHB has the strongest complexation ability with Mg^{2+} among selected additives and the amount of hydrogen evolved within 24 h test is the highest. Therefore, the amount of OH^- released into the electrolyte should be even higher than in other additive solutions. From Table 2 and Fig. 2d, the bulk pH of NaCl solution with 3,4-DHB increased to 9.5 after 24 h hydrogen evolution test and the complexation reaction between Mg^{2+} and 3,4-DHB can be written as Eq. (5) and Eq. (6) [49,50].

$$Mg^{2+} + (C_7H_5O_4)^- \rightarrow MgC_7H_3O_4^- + 2H^+ \quad (5)$$

$$MgC_7H_3O_4^- + (C_7H_5O_4)^- \rightarrow Mg(C_7H_3O_4)_2^{4-} + 2H^+ \quad (6)$$

Most of the OH^- generated during HER (Eq. (4)) is consumed to neutralize the H^+ generated by complexation reaction (Eq. (5) and Eq. (6)). Therefore, the final pH of electrolyte containing 3,4-DHB is the lowest and the formation of $Mg(OH)_2$ in this electrolyte is more difficult than in other electrolytes.

3.2. Impedance measurement

The effect of selected additives on the self-corrosion behavior of Mg-Ca was also determined by electrochemical impedance spectroscopy (EIS). The Nyquist plot of Mg-Ca anode in different electrolytes (Fig. 3a and b) revealed two capacitive loops. The high frequency one relates to the natural oxide layer presented on the surface of Mg-Ca and the middle frequency one relates to the charge transfer process [27,51]. In presence of additives, two capacitive loops at high and middle frequencies were followed by a low frequency inductive loop. The origin of the inductive loop presented on EIS spectra of Mg alloys is generally subject of discussion. It has been attributed to non-stationarity during measurements [52,53]. The origin of the inductive like behavior at low frequencies requires detailed investigation, which is out of the scope of this work.

In order to quantitatively evaluate the effect of additives on the behavior of Mg-Ca alloy, the EIS spectra were fitted with the equivalent

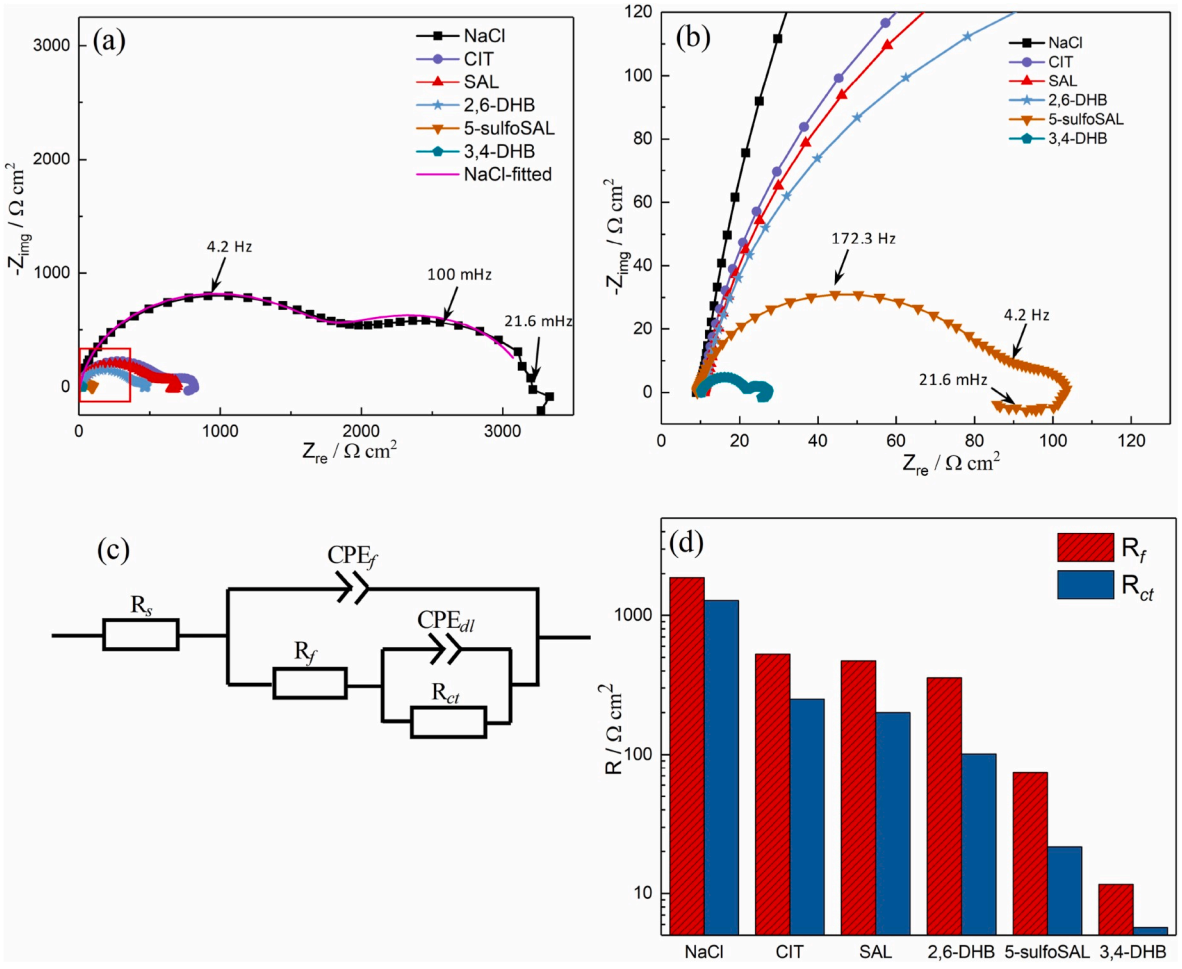

Fig. 3. EIS results of Mg-Ca in 3.5 wt % NaCl solution with and without different additives: (a) Nyquist plots; (b) and magnification of the high frequency part of (a); (c) Equivalent circuit; (d) Film resistance and charge transfer resistance (log scale).

circuit shown in Fig. 3c. The inductive loop was not considered in fitting process, hence the EIS results were fitted to different low frequency limits, like 0.02 Hz for NaCl and 0.2 Hz for 5-sulfoSAL. In this circuit, R_s means the internal resistance of the electrolyte. R_f and CPE_f are the resistance and capacitance of the oxide film respectively. R_{ct} represents the resistance due to charge transfer and CPE_{dl} is the electric double layer capacitance. The fitting results are presented in Fig. 3d. With the presence of additives in 3.5 wt % NaCl solution, both the R_f and the R_{ct}

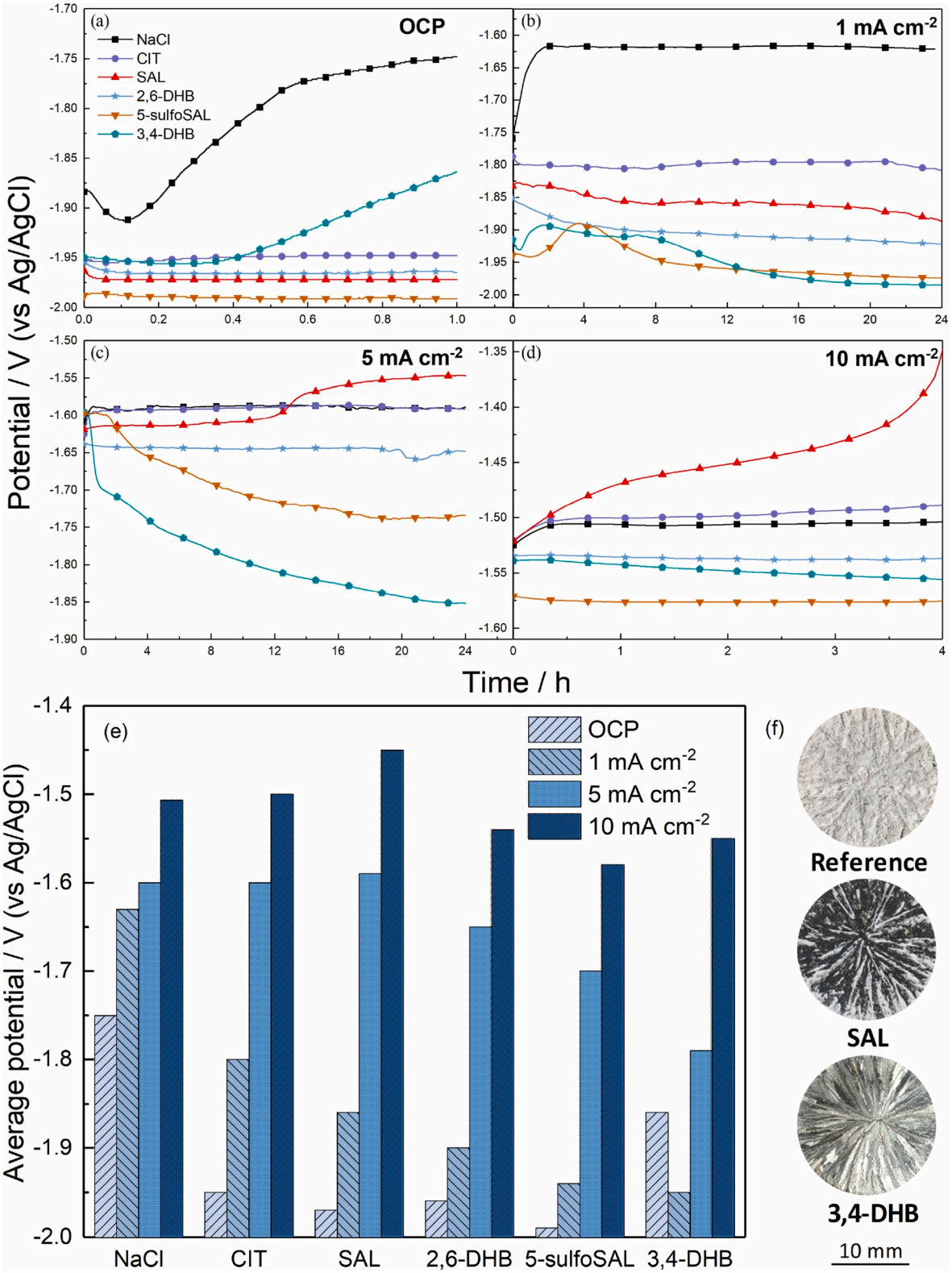

Fig. 4. Discharge curves of Mg-Ca in 3.5 wt % NaCl solution with and without different additives at current density: (a) open circuit; (b) 1; (c) 5; (d) 10 mA cm^{-2}; (e) average discharge potential of Mg-Ca at different current densities; and (f) macro-morphologies of Mg-Ca after 24 h discharge test at 5 mA cm^{-2} in different electrolytes.

decreased in the following order: 3.5 wt % NaCl > CIT > SAL > 2,6-DHB > 5-sulfoSAL > 3,4-DHB. This order directly corresponds to the ranking of the additives during the hydrogen evolution test. In blank NaCl solution, Mg-Ca alloys released the least amount of H_2 while in presence of 3,4-DHB the amount of released H_2 was the highest. It is noticed that, with the addition of 5-sulfoSAL and 3,4-DHB, the calculated values of R_f and R_{ct} were much lower than the R_f and R_{ct} in blank 3.5 wt % NaCl solution, as presented in Fig. 3d. In the electrolytes with these two kinds of additives, the dissolution rates of Mg-Ca were much faster than in other electrolytes. Low R_{ct} indicates the low corrosion resistance and high dissolution rate. It is apparent that the presence of additives increased the dissolution rate. Low R_{ct} also reflects better discharge activity of Mg-Ca in electrolyte with selected additives. Notably, the presence of additives decreased the overall impedance. This is probably due to their ability to form soluble complexes with Mg^{2+}, which stimulates the dissolution kinetic via near surface interaction. A correlation shows: the higher is stability constant of the involved complex the faster Mg gets dissolved. These results are in a good agreement with the hydrogen evolution tests.

3.3. OCP and half-cell discharge test

Fig. 4 indicates the half-cell discharge performance of Mg-Ca alloys in presence of different electrolyte additives. Once the selected substances were added to the blank NaCl solution, the OCP of Mg-Ca decreased (Fig. 4a). The OCP of the anode in presence of 5-sulfoSAL reached −1.98 V (vs Ag/AgCl), which was 200 mV lower than that in blank NaCl solution. During 1 h test, the OCP of Mg-Ca in 3,4-DHB kept changing because the reaction on anode surface was too intense to achieve the stable state. Mg-Ca at 1 mA cm^{-2} revealed more negative discharge potential with 2,6-DHB, 3,4-DHB and 5-sulfoSAL additives in comparison with blank NaCl. The discharge potential of Mg-Ca in CIT and SAL solution was also more negative than the reference. Whereas the discharge current density is 5 mA cm^{-2}, the discharge potential of Mg-Ca became more positive with less or no differences in potential between blank NaCl and NaCl solution with CIT. In NaCl solution with SAL, the initial discharge potential of Mg-Ca was more negative than that in the blank NaCl solution. However, after 14 h, the discharge potential of Mg-Ca in NaCl solution with SAL increased sharply and the final discharge potential was even higher than the reference. Strong Mg^{2+} complexing agents, like 5-sulfoSAL and 3,4-DHB, maintained a relatively negative discharge potential with a decreasing tendency even after 24 h discharge. The discharge potential of Mg-Ca with 2,6-DHB was 50 mV lower than the reference and relatively stable along 24 h test. At 10 mA cm^{-2}, the discharge potential of Mg-Ca in NaCl solution with SAL increased rapidly to positive direction after 4 h discharge. In NaCl solution with CIT, the discharge potential of Mg-Ca was also more positive than in blank NaCl solution. Nevertheless, with the addition of 5-sulfoSAL, 2,6-DHB and 3,4-DHB the discharge potential of the anode was still more negative than the reference.

The discharge potential of anodes in half-cell can be expressed as:

$$E_{anode} = E_{ocp} - \eta_{ct} - \eta_{diff} - IR \quad (7)$$

where E_{ocp} represents the open circuit potential, η_{ct} means the potential drop related to charge transfer process, η_{diff} is the potential drop due to discharge products (e.g. transport aspect), I and R represents the applied current and the resistance of electrolyte between metal surface of working anode and the reference electrode [1,27,54]. According to this equation, the improvement of discharge potential of an anode can be achieved by more negative open circuit potential and minimization of potential drop caused by discharge products. The average value of open circuit potential of Mg-Ca in different electrolytes in the last 10 min of the test is presented in Fig. 4e, because the open circuit potential of Mg-Ca in the last 10 min is more stable than at the beginning of the test. The average discharge potentials of Mg-Ca at different current densities during 24 h discharge are also calculated and presented in Fig. 4e. Obviously, all selected electrolyte additives led to more negative OCP values of the tested anode material. As shown in Fig. 4e, all electrolyte additives efficiently made the average discharge potential of Mg-Ca anode more negative when the applied current density was 1 mA cm^{-2}. At 5 and 10 mA cm^{-2}, the average discharge potential of Mg-Ca in electrolyte containing moderate additives, like CIT and SAL, was similar to that in blank NaCl solution. In electrolyte containing 2,6-DHB, 5-sulfoSAL and 3,4-DHB, the average discharge potential of Mg-Ca was always more negative than the average discharge potential of Mg-Ca in blank NaCl solution. As the optical images in Fig. 4f show, the surface of Mg-Ca in blank NaCl solution was fully covered by discharge products after half-cell discharge test. With the presence of moderate additive SAL, the deposition of discharge products was not inhibited, while in electrolyte containing 3,4-DHB, the surface was clean and without any discharge products.

The deposition of discharge products was further evaluated by SEM of the samples after discharge test. Fig. 5 presents the surface morphology of Mg-Ca after 24 h discharge in blank NaCl solution, in NaCl solution with SAL and in NaCl solution with 3,4-DHB at dry condition. The surface of Mg-Ca in blank NaCl solution was completely covered by discharge products. At 1 mA cm^{-2} (Fig. 5a), the layer was thick with some big cracks. After discharged at higher current density, the discharge products became denser without large cracks (Fig. 5b). In presence of SAL, at 1 mA cm^{-2}, the anode surface was clean without discharge products. However, discharge products fully covered the anode surface at 5 mA cm^{-2}. In presence of 3,4-DHB, which has the strongest ability to form soluble complex with Mg^{2+}, the formation of discharge products film was not observed at both current densities. From the surface morphologies of Mg-Ca anode after discharge (Fig. 5), it is possible to conclude that selected electrolyte additives retarded the formation of discharge products to different degrees, contributing to less overpotential during discharge test at small current density. For discharge tests at large current density, the dissolution of anode material is faster. The electrolyte additives should have stronger complexation ability and faster kinetics to hinder the formation of discharge products. For SAL and CIT, which have relatively weak complexation ability with Mg^{2+}, both of them could not prevent the formation of discharge products at 5 and 10 mA cm^{-2}. Hence, the discharge potential of the anode in these two additive solutions either shows no apparent difference to the reference test or becomes even more positive than the reference test. 3,4-DHB decreases the OCP of Mg-Ca as it possesses the strongest ability to form soluble complex with Mg^{2+}, which means the overpotential caused by discharge products is the lowest. Hence, the average discharge potentials of the anode in NaCl solution with 3,4-DHB were always 40-320 mV more negative than that in blank NaCl solution.

3.4. Utilization efficiency

Utilization efficiency of an anode is an essential technical factor to be considered when evaluating the discharge performance of anode materials in different electrolytes. The utilization efficiencies of Mg-Ca in different electrolytes are presented in Table 3. In comparison with Mg-Al-Zn, Mg-Al-Pb, Mg-Al-In, Mg-Al-Sn [12,17,30,55–57], Mg-Ca alloy with low Ca content shows relatively high utilization efficiency when acts as anode material, 58.2% and 55.6%, respectively at 5 and 10 mA cm^{-2} [27]. Nevertheless, the utilization efficiency of Mg-Ca can be additionally improved by adopting electrolyte additives. The influence of selected electrolyte additives on the utilization efficiency of Mg-Ca depends on the complexation ability and applied current density as listed in the Table 3. At 1 mA cm^{-2}, Mg-Ca showed highest utilization efficiency in NaCl solution with CIT. It reached 64.7%, 12% higher than the utilization efficiency of Mg-Ca in blank NaCl solution. The addition of other complexing agents at the same applied current density decreased the utilization efficiency of Mg-Ca due to the fast consumption of anode supported by complexing of Mg^{2+}. At 5 mA cm^{-2}, the Mg-Ca in

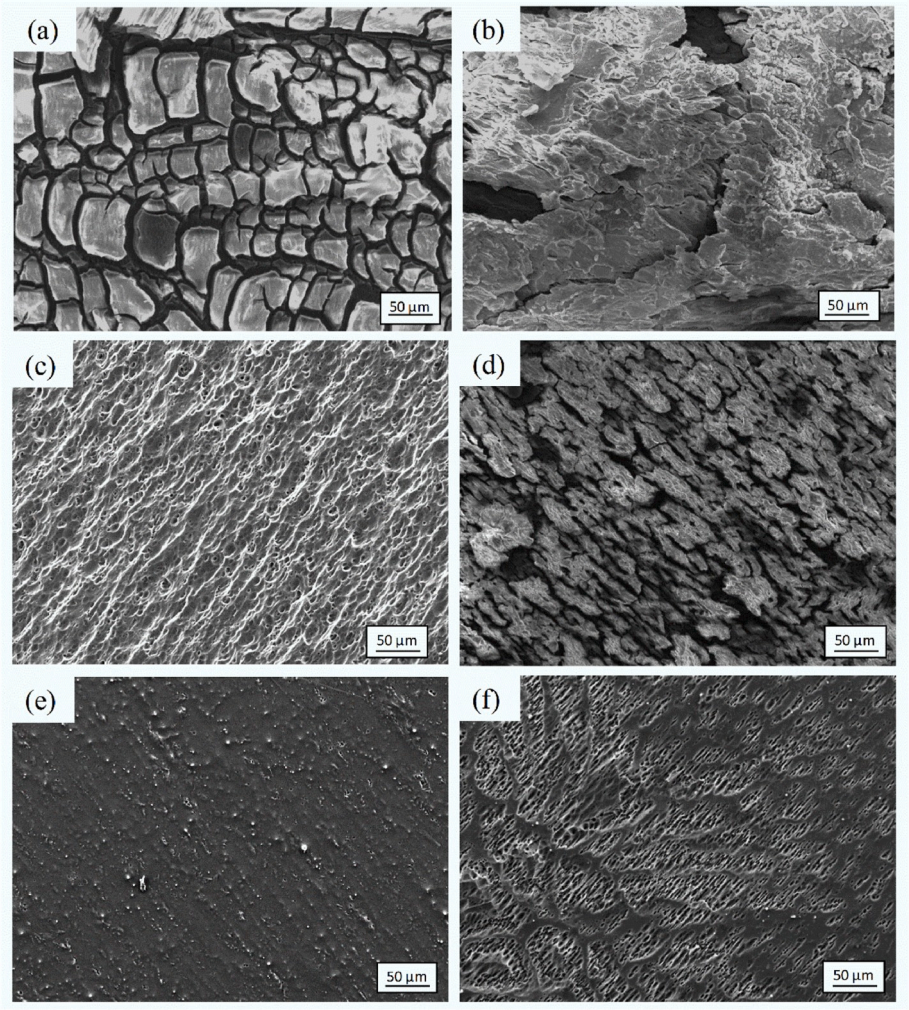

Fig. 5. Surface morphologies of Mg-Ca after 24 h discharge in 3.5 wt % NaCl (a) without additive at 1 and (b) 5 mA cm^{-2}; (c) with SAL at 1 and (d) 5 mA cm^{-2}; (e) with 3,4-DHB at 1 and (f) 5 mA cm^{-2} measured via SEM on dried but uncleaned anode.

Table 3
Utilization efficiency (in %) of Mg-Ca in 3.5 wt % NaCl solution with and without different electrolyte additives at current densities 1, 5 and 10 mA cm^{-2}.

Current density	3.5 wt % NaCl	CIT	SAL	2,6-DHB	5-sulfoSAL	3,4-DHB
1 mA cm^{-2}	53.0 ± 0.1	64.7 ± 2.7	46.3 ± 4.5	37.8 ± 0.5	24.6 ± 5.2	9.0 ± 0.6
5 mA cm^{-2}	60.0 ± 2.2	60.5 ± 2.8	62.9 ± 2.2	65.0 ± 1.5	56.1 ± 1.4	35.6 ± 2.1
10 mA cm^{-2}	59.7 ± 3.2	56.5 ± 1.0	58.8 ± 3.8	67.2 ± 0.7	61.7 ± 3.5	62.3 ± 0.2

blank NaCl solution revealed 60.0% utilization efficiency. With the addition of 2,6-DHB and SAL, the utilization efficiencies were further improved to 65.0% and 62.9% respectively. The highest utilization efficiency 67.2% at 10 mA cm^{-2} was achieved for 2,6-DHB. In the case of 5-sulfoSAL and 3,4-DHB, which have strong ability to form complex with Mg^{2+}, the utilization efficiencies of Mg-Ca increased with the increase of current density. In these two additive solutions, the utilization efficiencies of Mg-Ca at 10 mA cm^{-2} reached 61.7% and 62.3%, respectively.

According to Eq. (1), utilization efficiency shows the difference between the actual weight loss and the calculated theoretical value. The actual weight loss consists of the theoretical weight loss, the weight loss due to self-corrosion and the weight loss due to chunk effect [20,58,59]. The chunk effect specifically refers to the weight loss caused by the detachment of metallic particles from the anode surface [60,61]. The theoretical weight loss of anode material follows Faraday's law. The difference of utilization efficiency of Mg-Ca in general in presence of different additives is caused by the various contribution from self-corrosion and the chunk effect. As shown in Fig. 2a, Mg-Ca had a very low hydrogen evolution rate in blank NaCl solution, therefore high corrosion resistance. With the addition of selected Mg^{2+} complexing agents, the corrosion resistance decreased due to faster Mg dissolution. However, as shown in Table 3, the highest utilization efficiency was achieved by adding different Mg^{2+} complexing agents. One of the reasons could be the ability of all selected additives to decrease the chunk effect. Fig. 6 presents the SEM (BSE) images of the cross section of Mg-Ca after 24 h discharge tests at 5 mA cm^{-2} in different electrolytes. The anode suffered from chunk effect in blank NaCl solution. As shown in Fig. 6a, the surface of tested Mg-Ca was covered by discharge products. In several locations, undissolved Mg-Ca matrix was completely surrounded by discharge products and lost contact with the bulk anode matrix (Fig. 6a) and did not contribute to the measured electric current. Besides, inside the bulk anode matrix, some (tortuous) channels were formed during discharge. This may cause the metal spalling and formation of undissolved metallic chunks. During discharge, those undissolved metallic chunks were trapped by discharge products or released into the electrolyte. This leads to weight loss of anode without any contribution to the discharge current. In turn, this massively causes the

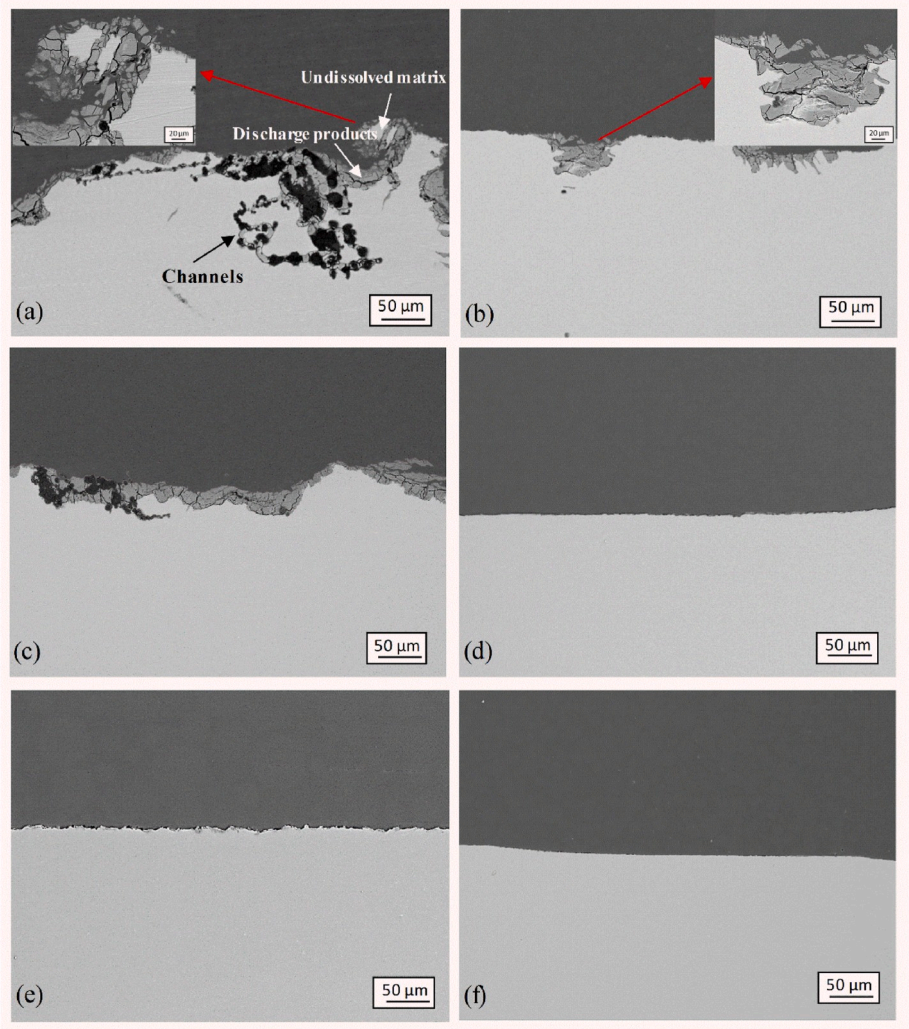

Fig. 6. Cross-section SEM images (BSE mode) of Mg-Ca after 24 h discharge at 5 mA cm^{-2} in (a) 3.5 wt % NaCl and the same electrolyte with 0.1 M (b) CIT; (c) SAL; (d) 5-sulfoSAL; (e) 2,6-DHB; (f) 3,4-DHB.

decrease of utilization efficiency [60,62]. As shown in Fig. 6b, only part of the Mg-Ca surface accumulated discharge products and only few metallic particles were entrapped by discharge products. Moreover, except for in NaCl solution with CIT, no apparent chunk effect was found in NaCl solution with other selected additives. In NaCl solution with SAL, the thin layer of corrosion product was formed on the surface of the anode but entrapped metallic particles were not detected (Fig. 6c). In NaCl solution with 5-sulfoSAL, 2,6-DHB and 3,4-DHB, Mg-Ca anode surfaces were completely clean with no evidence of chunk effect. The weight loss caused by chunk effect in these three additive solutions was negligible. According to Fig. 2a, among these additives, Mg-Ca shows the lowest corrosion rate in NaCl solution with 2,6-DHB, which exhibits the moderate Mg^{2+} complexation ability. Thus, 2,6-DHB would not greatly additionally dissolve anode material during discharge comparing to 5-sulfoSAL and 3,4-DHB. Therefore, Mg-Ca in NaCl solution with 2,6-DHB shows the highest utilization efficiency at 5 mA cm^{-2}.

3.5. Mg-air full battery discharge test

In order to clarify the effect of selected electrolyte additives on the discharge performance of aqueous (Mg-Ca)-air battery, full-cell discharge tests were done in a lab-made Mg-air battery setup. The discharge curves of (Mg-Ca)-air batteries in various electrolytes at defined current densities are presented in Fig. 7. All the selected additives greatly increased the output voltage of the cell. In NaCl solution with 5-sulfoSAL, (Mg-Ca)-air battery exhibited the highest and quite stable discharge voltage at 0.5 and 1 mA cm^{-2}, which is ~1.86 and 1.82 V, respectively, compared to ~1.60 and 1.55 V in the blank NaCl solution. At 5 mA cm^{-2}, the addition of Mg^{2+} complexing agents kept the battery voltage higher than that of Mg-air battery in blank NaCl solution. The highest voltage value, ~1.58 V, was obtained in NaCl solution with 3,4-DHB. As the applied current density was 10 mA cm^{-2}, SAL and CIT additives could not efficiently hinder the formation of discharge products, and therefore, the Mg-air batteries failed. However, in NaCl solution with 2,6-DHB, 3,4-DHB and 5-sulfoSAL, which have relatively high complexation ability with Mg^{2+}, the battery voltages were still enhanced, by 70–110 mV, compared to the reference.

The specific energy of (Mg-Ca)-air batteries in different electrolytes at various current densities is shown in Fig. 8. At lower discharge currents, higher specific energy was achieved by adding CIT and SAL. Both of them have relatively weak complexation ability with Mg^{2+}. The lower current density indicates lower rate of Mg^{2+} produced by discharge process. Those complexing agents with mild complexation ability can retard the formation of discharge product film and maintain high discharge voltage without additional dissolution of Mg based anode. Hence, the highest specific energy was achieved by adding CIT at 1 mA cm^{-2}. It reached 3007 Wh kg^{-1}, which was 880 Wh kg^{-1} higher than the specific energy of (Mg-Ca)-air battery in blank NaCl solution at 1 mA cm^{-2}. Compared with literatures [13,27,36,63–65], it is much higher than the specific energy of Mg-air battery based on different Mg alloys

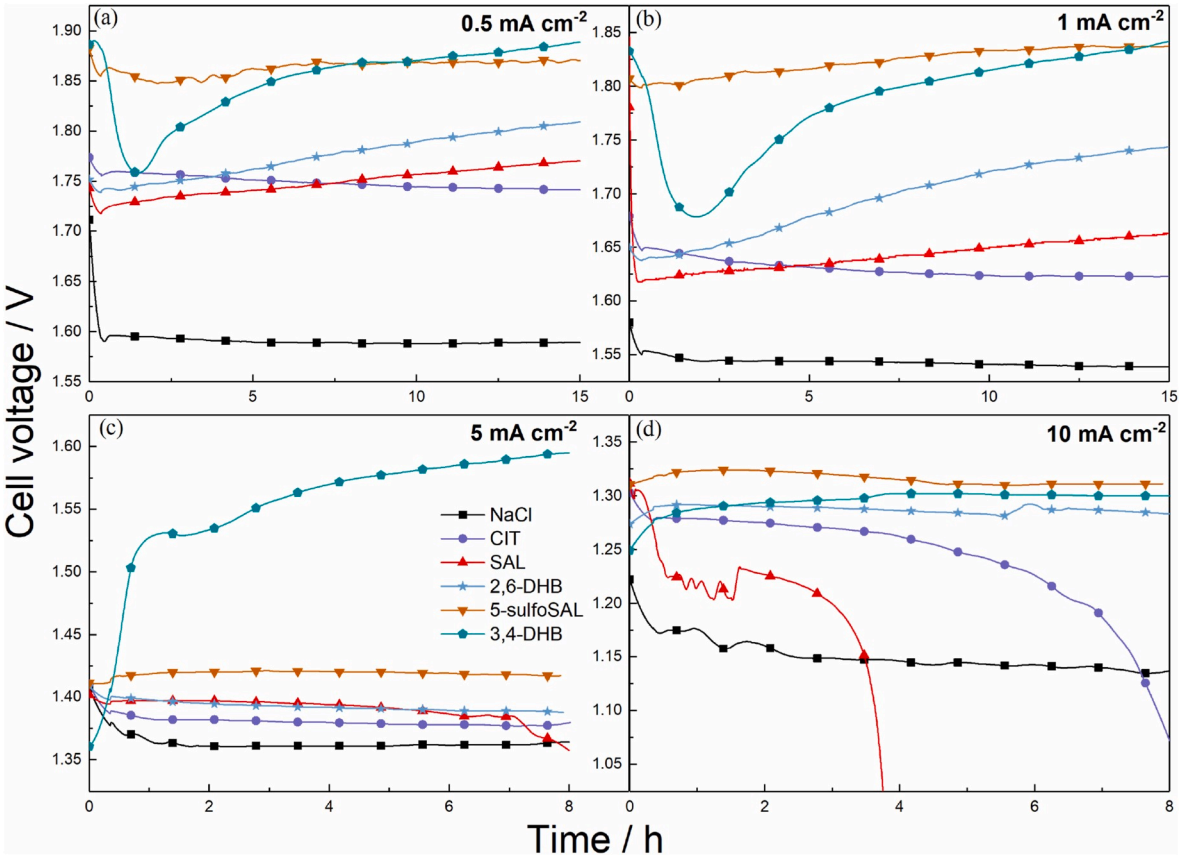

Fig. 7. Discharge performance of (Mg-Ca)-air battery in 3.5 wt % NaCl solution with and without additives at various current densities: (a) 0.5; (b) 1; (c) 5 and (d) 10 mA cm^{-2}.

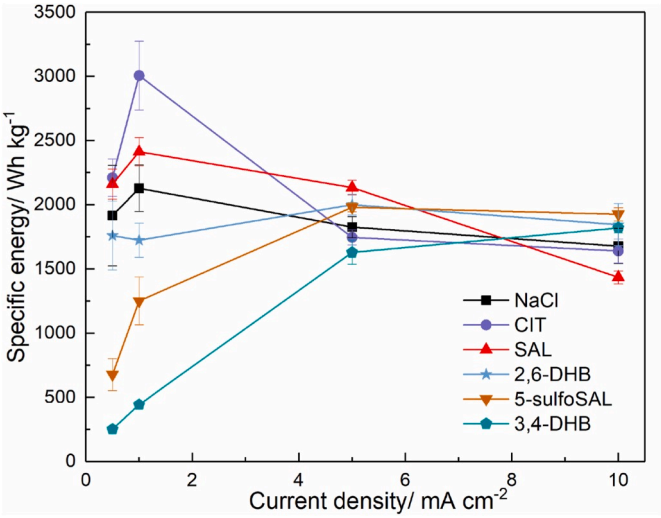

Fig. 8. Specific energy of (Mg-Ca)-air battery in 3.5 wt % NaCl solution with and without additives at various current densities.

anodes in different aqueous electrolytes, although the different experimental environment and cathode materials might cause deviations. The specific energy of (Mg-Ca)-air battery in moderate additive solution decreased with the increase of current density. At relatively high current density, a higher rate of Mg^{2+} generated and released into the electrolyte. In this case complexing agents with strong ability of forming complex with Mg^{2+}, like 2,6-DHB, 3,4-DHB and 5-sulfoSAL, keep the anode surface clean, maintaining a relatively high cell voltage. At the same time, they do not greatly dissolve the additional anode materials because a large amount of Mg^{2+} exists in the electrolyte. Therefore, (Mg-Ca)-air batteries containing 2,6-DHB, 3,4-DHB and 5-sulfoSAL had relatively high specific energy at 10 mA cm^{-2}. The effect of selected electrolyte additives depends on the applied current density and the complexation ability with Mg^{2+}.

4. Conclusions

In this work, Mg^{2+} complexing agents were used as electrolyte additives for aqueous Mg-air battery. The effect of the electrolyte additives on the corrosion behavior and discharge performance of Mg-Ca was investigated.

(1) Additives that form soluble complexes with Mg^{2+} overall have positive effect on the discharge performance of (Mg-Ca)-air battery. According to their complexation ability with Mg^{2+}, different additives should be used for different discharge loads to obtain optimal effect.
(2) Stability constants of soluble complexes with Mg^{2+} is an important aspect enhancing anode activity. (Mg-Ca)-air battery at lower discharge current exhibits ideal performance by using additives with moderate stability constant, such as CIT and SAL. At higher discharge loads, better performance is achieved when using the additives with strong complexation ability, such as 3,4-DHB and 5-sulfoSAL. The peak specific energy appears at 1 mA cm^{-2} in NaCl with CIT and reaches 3007 Wh kg^{-1}. At 10 mA cm^{-2}, the specific energy of Mg-Ca in NaCl solution with 5-sulfoSAL is the highest, achieving 1925 Wh kg^{-1}.
(3) The selected additives hinder the formation of discharge products on the anode surface and provide more active area for discharge

according to their different complexation ability with Mg^{2+}, resulting in more negative OCP and less potential drop caused by discharge products. In half-cell discharge test, the average discharge potential of Mg-Ca in NaCl with 0.1 M 3,4-DHB reaches −1.95 V at 1 mA cm^{-2}, which is 320 mV more negative than that in blank NaCl solution. In full-cell discharge test, the highest cell voltage of (Mg-Ca)-air battery is achieved by the usage of 5-sulfoSAL at 0.5 mA cm^{-2}, 1.86 V, which is 270 mV higher than the reference.

(4) At low current density, the addition of strong complexing agent (like 3,4-DHB) causes significant loss of utilization efficiency. However, the utilization efficiency of Mg-Ca is improved by using moderate Mg^{2+} complexing agents at relatively high current density. The highest utilization efficiency was shown for 2,6-DHB (65% at 5 mA cm^{-2} and 67.2% at 10 mA cm^{-2}), because the addition of 2,6-DHB makes the dissolution of Mg-Ca more uniform, eliminating the weight loss caused by chunk effect which is significant in pure NaCl solution.

Declaration of competing interest

The authors declare that they have no known competing financial interests or personal relationships that could have appeared to influence the work reported in this paper.

CRediT authorship contribution statement

Linqian Wang: Methodology, Investigation, Validation, Writing - original draft, Writing - review & editing. **Darya Snihirova:** Conceptualization, Supervision, Writing - review & editing, Funding acquisition, Project administration. **Min Deng:** Methodology, Resources, Writing - review & editing. **Bahram Vaghefinazari:** Methodology, Writing - review & editing. **Sviatlana V. Lamaka:** Conceptualization, Supervision, Writing - review & editing. **Daniel Höche:** Conceptualization, Supervision, Writing - review & editing. **Mikhail L. Zheludkevich:** Conceptualization, Supervision, Writing - review & editing.

Acknowledgements

The authors would like to acknowledge the technical support from Mr. Ulrich Burmester, Mr. Volker Heitmann and Mr. Gert Wiese. L. Wang and M. Deng are grateful for the award of fellowship from China Scholarship Council (No. 201706370183 and No. 201606370031). Dr. D. Snihirova would like to acknowledge Alexander von Humboldt foundation for financial support via postdoctoral grant. Additionally, the authors acknowledge SeaMag project funded by ERA-NET cofund MarTERA.

References

[1] D. Linden, T.B. Reddy, Handbook of Batteries, McGraw-Hill, New York, 2002.
[2] T. Zhang, Z. Tao, J. Chen, Mater. Horiz. 1 (2014) 196–206, https://doi.org/10.1039/c3mh00059a.
[3] M. Fichtner, B.J. Ingram, E. Sheridan, R. Mohtadi, C. Battaglia, Z. Zhao-Karger, P. Canepa, R. Dominko, D. Hoeche, M. Weil, Magnesium Batteries: Research and Applications, Royal Society of Chemistry, 2019.
[4] F. Cheng, J. Chen, Chem. Soc. Rev. 41 (2012) 2172–2192, https://doi.org/10.1039/c1cs15228a.
[5] D. Cao, L. Wu, Y. Sun, G. Wang, Y. Lv, J. Power Sources 177 (2008) 624–630, https://doi.org/10.1016/j.jpowsour.2007.11.037.
[6] R. Mohtadi, F. Mizuno, Beilstein J. Nanotechnol. 5 (2014) 1291–1311, https://doi.org/10.3762/bjnano.5.143.
[7] H.D. Yoo, I. Shterenberg, Y. Gofer, G. Gershinsky, N. Pour, D. Aurbach, Energy Environ. Sci. 6 (2013) 2265, https://doi.org/10.1039/c3ee40871j.
[8] M. Esmaily, J.E. Svensson, S. Fajardo, N. Birbilis, G.S. Frankel, S. Virtanen, R. Arrabal, S. Thomas, L.G. Johansson, Prog. Mater. Sci. 89 (2017) 92–193, https://doi.org/10.1016/j.pmatsci.2017.04.011.
[9] S. Fajardo, G.S. Frankel, Electrochim. Acta 165 (2015) 255–267, https://doi.org/10.1016/j.electacta.2015.03.021.
[10] M. Yuasa, X. Huang, K. Suzuki, M. Mabuchi, Y. Chino, J. Power Sources 297 (2015) 449–456, https://doi.org/10.1016/j.jpowsour.2015.08.042.
[11] L. Wen, K. Yu, H. Xiong, Y. Dai, S. Yang, X. Qiao, F. Teng, S. Fan, Electrochim. Acta 194 (2016) 40–51, https://doi.org/10.1016/j.electacta.2016.02.088.
[12] H. Xiong, K. Yu, X. Yin, Y. Dai, Y. Yan, H. Zhu, J. Alloys Compd. 708 (2017) 652–661, https://doi.org/10.1016/j.jallcom.2016.12.172.
[13] X. Liu, J. Xue, P. Zhang, Z. Wang, J. Power Sources 414 (2019) 174–182, https://doi.org/10.1016/j.jpowsour.2018.12.092.
[14] T. Zheng, Y. Hu, Y. Zhang, S. Yang, F. Pan, Mater. Des. 137 (2018) 245–255, https://doi.org/10.1016/j.matdes.2017.10.031.
[15] Y. Feng, R. Wang, K. Yu, C. Peng, J. Zhang, C. Zhang, J. Alloys Compd. 473 (2009) 215–219, https://doi.org/10.1016/j.jallcom.2008.05.054.
[16] N. Wang, R. Wang, Y. Feng, W. Xiong, J. Zhang, M. Deng, Corrosion Sci. 112 (2016) 13–24, https://doi.org/10.1016/j.corsci.2016.07.002.
[17] N. Wang, R. Wang, C. Peng, B. Peng, Y. Feng, C. Hu, Electrochim. Acta 149 (2014) 193–205, https://doi.org/10.1016/j.electacta.2014.10.053.
[18] G. Huang, Y. Zhao, Y. Wang, H. Zhang, F. Pan, Mater. Lett. 113 (2013) 46–49, https://doi.org/10.1016/j.matlet.2013.09.041.
[19] Y. Lv, Y. Xu, D. Cao, J. Power Sources 196 (2011) 8809–8814, https://doi.org/10.1016/j.jpowsour.2011.06.001.
[20] L. Wang, R. Wang, Y. Feng, M. Deng, N. Wang, J. Electrochem. Soc. 164 (2017) A438–A446, https://doi.org/10.1149/2.1211702jes.
[21] Y. Feng, W. Xiong, J. Zhang, R. Wang, N. Wang, J. Mater. Chem. 4 (2016) 8658–8668, https://doi.org/10.1039/c6ta02574a.
[22] K.K. Alaneme, E.A. Okotete, Journal of Magnesium and Alloys 5 (2017) 460–475, https://doi.org/10.1016/j.jma.2017.11.001.
[23] S. Yagi, A. Sengoku, K. Kubota, E. Matsubara, Corrosion Sci. 57 (2012) 74–80, https://doi.org/10.1016/j.corsci.2011.12.032.
[24] J.W. Seong, W.J. Kim, Corrosion Sci. 98 (2015) 372–381, https://doi.org/10.1016/j.corsci.2015.05.068.
[25] S.-M. Baek, H.J. Kim, H.Y. Jeong, S.-D. Sohn, H.-J. Shin, K.-J. Choi, K.-S. Lee, J. G. Lee, C.D. Yim, B.S. You, H.-Y. Ha, S.S. Park, Corrosion Sci. 112 (2016) 44–53, https://doi.org/10.1016/j.corsci.2016.07.011.
[26] S.-H. Kim, J.U. Lee, Y.J. Kim, B.G. Moon, B.S. You, H.S. Kim, S.H. Park, Mater. Sci. Eng. 703 (2017) 1–8, https://doi.org/10.1016/j.msea.2017.07.048.
[27] M. Deng, D. Höche, S.V. Lamaka, D. Snihirova, M.L. Zheludkevich, J. Power Sources 396 (2018) 109–118, https://doi.org/10.1016/j.jpowsour.2018.05.090.
[28] N. Wang, R. Wang, C. Peng, Y. Feng, B. Chen, Corrosion Sci. 64 (2012) 17–27, https://doi.org/10.1016/j.corsci.2012.06.024.
[29] L. Wang, R. Wang, Y. Feng, M. Deng, N. Wang, JOM (J. Occup. Med.) 69 (2017) 2467–2470, https://doi.org/10.1007/s11837-017-2276-z.
[30] N. Wang, R. Wang, C. Peng, Y. Feng, Corrosion Sci. 81 (2014) 85–95, https://doi.org/10.1016/j.corsci.2013.12.005.
[31] N. Wang, Y. Mu, Q. Li, Z. Shi, RSC Adv. 7 (2017) 53226–53235, https://doi.org/10.1039/c7ra10652a.
[32] F.W. Richey, B.D. McCloskey, A.C. Luntz, J. Electrochem. Soc. 163 (2016) A958–A963.
[33] Y. Zhao, G. Huang, C. Zhang, C. Peng, F. Pan, Mater. Chem. Phys. 218 (2018) 256–261, https://doi.org/10.1016/j.matchemphys.2018.07.037.
[34] M. Mayilvel Dinesh, K. Saminathan, M. Selvam, S.R. Srither, V. Rajendran, K.V.I. S. Kaler, J. Power Sources 276 (2015) 32–38, https://doi.org/10.1016/j.jpowsour.2014.11.079.
[35] D. Höche, C. Blawert, S.V. Lamaka, N. Scharnagl, C. Mendis, M.L. Zheludkevich, Phys. Chem. Chem. Phys. 18 (2016) 1279–1291, https://doi.org/10.1039/c5cp05577f.
[36] D. Höche, S.V. Lamaka, B. Vaghefinazari, T. Braun, R.P. Petrauskas, M. Fichtner, M.L. Zheludkevich, Sci. Rep. 8 (2018) 7578, https://doi.org/10.1038/s41598-018-25789-8.
[37] Y. Li, J. Ma, G. Wang, F. Ren, Y. Zhu, Y. Song, J. Electrochem. Soc. 165 (2018) A1713–A1717, https://doi.org/10.1149/2.0581809jes.
[38] M.A. Deyab, J. Power Sources 325 (2016) 98–103, https://doi.org/10.1016/j.jpowsour.2016.06.006.
[39] S.V. Lamaka, B. Vaghefinazari, D. Mei, R.P. Petrauskas, D. Höche, M. L. Zheludkevich, Corrosion Sci. 128 (2017) 224–240, https://doi.org/10.1016/j.corsci.2017.07.011.
[40] D. Höche, S. Lamaka, M. Zheludkevich, EU patent EP3291361 A (2016) 1.
[41] M.C. Lin, C.Y. Tsai, J.Y. Uan, Corrosion Sci. 51 (2009) 2463–2472, https://doi.org/10.1016/j.corsci.2009.06.036.
[42] D. Cao, L. Wu, G. Wang, Y. Lv, J. Power Sources 183 (2008) 799–804, https://doi.org/10.1016/j.jpowsour.2008.06.005.
[43] L. Fan, H. Lu, J. Power Sources 284 (2015) 409–415, https://doi.org/10.1016/j.jpowsour.2015.03.063.
[44] G. Song, Adv. Eng. Mater. 7 (2005) 563–586, https://doi.org/10.1002/adem.200500013.
[45] E.L. Silva, S.V. Lamaka, D. Mei, M.L. Zheludkevich, Chemistry 7 (2018) 664–668, https://doi.org/10.1002/open.201800076.
[46] J.A. Dean, Lange's Handbook of Chemistry, McGraw-Hill, Inc., New york; London, 1999.
[47] A.E. Martell, R.M. Smith, Critical Stability Constants, Springer, 1974.
[48] R.M. Smith, A.E. Martell, Critical Stability Constants, second supplement, Springer, 1989.
[49] Y. Murakami, K. Nakamura, M. Tokunaga, Bull. Chem. Soc. Jpn. 36 (1963) 669–675, https://doi.org/10.1246/bcsj.36.669.
[50] V. Athavale, L. Prabhu, D. Vartak, J. Inorg. Nucl. Chem. 28 (1966) 1237–1249, https://doi.org/10.1016/0022-1902(66)80450-5.
[51] P. Jiang, C. Blawert, R. Hou, N. Scharnagl, J. Bohlen, M.L. Zheludkevich, J. Alloys Compd. 783 (2019) 179–192, https://doi.org/10.1016/j.jallcom.2018.12.296.

[52] V. Shkirskiy, A.D. King, O. Gharbi, P. Volovitch, J.R. Scully, K. Ogle, N. Birbilis, ChemPhysChem 16 (2015) 536–539, https://doi.org/10.1002/cphc.201402666.
[53] R. Pinto, M.G.S. Ferreira, M.J. Carmezim, M.F. Montemor, Electrochim. Acta 56 (2011) 1535–1545, https://doi.org/10.1016/j.electacta.2010.09.081.
[54] C. Daniel, J.O. Besenhard, Handbook of Battery Materials, John Wiley & Sons, 2012.
[55] X. Li, H. Lu, S. Yuan, J. Bai, J. Wang, Y. Cao, Q. Hong, J. Electrochem. Soc. 164 (2017) A3131–A3137, https://doi.org/10.1149/2.0971713jes.
[56] M. Deng, R.-c. Wang, Y. Feng, N.-g. Wang, L.-q. Wang, Trans. Nonferrous Metals Soc. China 26 (2016) 2144–2151, https://doi.org/10.1016/s1003-6326(16)64330-3.
[57] J. Li, K. Wan, Q. Jiang, H. Sun, Y. Li, B. Hou, L. Zhu, M. Liu, Metals 6 (2016) 65, https://doi.org/10.3390/met6030065.
[58] D. Cao, X. Cao, G. Wang, L. Wu, Z. Li, J. Solid State Electrochem. 14 (2009) 851–855, https://doi.org/10.1007/s10008-009-0865-7.
[59] Y. Shi, C. Peng, Y. Feng, R. Wang, N. Wang, J. Alloys Compd. 721 (2017) 392–404, https://doi.org/10.1016/j.jallcom.2017.05.267.
[60] G. Marsh, E. Schaschl, J. Electrochem. Soc. 107 (1960) 960–965, https://doi.org/10.1149/1.2427579.
[61] M. Andrei, F. Di Gabriele, P. Bonora, D. Scantlebury, Mater. Corros. 54 (2003) 5–11, https://doi.org/10.1002/maco.200390010.
[62] M. Deng, L. Wang, D. Höche, S.V. Lamaka, D. Snihirova, B. Vaghefinazari, M. L. Zheludkevich, J. Power Sources 441 (2019), 227201, https://doi.org/10.1016/j.jpowsour.2019.227201.
[63] X. Liu, S. Liu, J. Xue, J. Power Sources 396 (2018) 667–674, https://doi.org/10.1016/j.jpowsour.2018.06.085.
[64] X. Liu, J. Xue, D. Zhang, J. Alloys Compd. (2019), https://doi.org/10.1016/j.jallcom.2019.07.151.
[65] S. Yuan, H. Lu, Z. Sun, L. Fan, X. Zhu, W. Zhang, J. Electrochem. Soc. 163 (2016) A1181–A1187, https://doi.org/10.1149/2.0371607jes.

5.4 Enhancement of discharge performance for aqueous Mg-air batteries in 2,6-dihydroxybenzoate-containing electrolyte

Paper 4 is published to Chemical Engineering Journal, 429 (2022), 132369.

This work is the follow-up of **Section 5.3** (***paper 3***). The results in ***paper 3*** demonstrate that 2,6-DHB yielded not only the highest UE via the suppression of the chunk effect on Mg-0.04Ca but also a considerable improvement for the discharge potential among a range of organic electrolyte additives. Previous results showed that 2,6-DHB is able to simultaneously improve the UE and discharge potential of Mg-Ca anode. Further improvement is possible by exploring the effect of concentration of this additive. Additionally, the performance of 2,6-DHB towards other anode materials was evaluated. Therefore, this work is dedicated to finding out main mechanisms and common features responsible for improved performance on various anode materials, namely HP-Mg, Mg-0.15Ca, AZ31 and AM50 Mg anodes. EIS measurements amid intermittent discharge and real-time hydrogen evolution measurements during discharge were applied to clarify the effective mechanisms of 2,6-DHB. The results reveal that sufficient amount of 2,6-DHB simultaneously improves the discharge activity and inhibits self-discharge of Mg-0.15Ca anode, leading to negative average potential and high anodic UE. Combining with its effect on the alleviation of chunk effect, 2,6-DHB efficiently improves the discharge performance of AMABs with different Mg anodes.

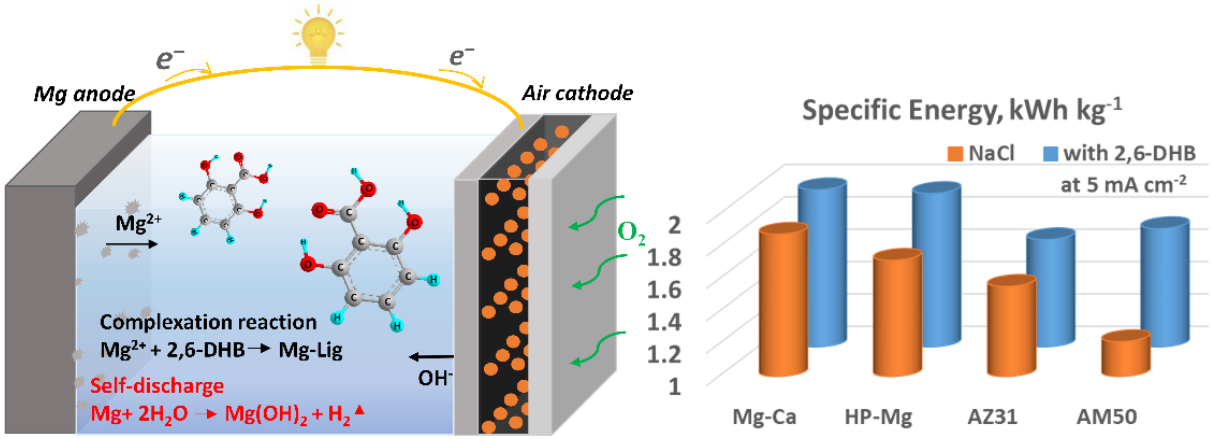

Fig. 5-5. Graphical abstract for **Section 5.4**.

Chemical Engineering Journal 429 (2022) 132369

Contents lists available at ScienceDirect

Chemical Engineering Journal

journal homepage: www.elsevier.com/locate/cej

Enhancement of discharge performance for aqueous Mg-air batteries in 2,6-dihydroxybenzoate-containing electrolyte

Linqian Wang [a,*], Darya Snihirova [a], Min Deng [a], Bahram Vaghefinazari [a], Daniel Höche [a], Sviatlana V. Lamaka [a], Mikhail L. Zheludkevich [a,b]

[a] Institute of Surface Science, Helmholtz-Zentrum Hereon (Hereon), 21502 Geesthacht, Germany
[b] Institute of Materials Science, Faculty of Engineering, Kiel University, 24143 Kiel, Germany

ARTICLE INFO

Keywords:
Primary Mg-air battery
Electrolyte additives
Self-discharge
EIS measurement

ABSTRACT

In this work, 2,6-dihydroxytbenzoate (2,6-DHB) is evaluated as an efficient electrolyte additive for aqueous Mg-air batteries based on diverse metallic Mg anodes. EIS measurements amid intermittent discharge and real-time hydrogen evolution measurements during discharge were applied to clarify the effective mechanism. The dependence of working mechanism on 2,6-DHB concentration was investigated for a newly developed Mg-0.15Ca anode. The results reveal that sufficient amount of 2,6-DHB simultaneously improves the discharge activity and inhibits the self-discharge of Mg-0.15Ca anode, leading to negative average potential and high anodic utilization efficiency. Accordingly, 0.2 M 2,6-DHB is determined as the most suitable electrolyte concentration and applied during Mg-air battery tests based on diverse commercial Mg anodes (pure Mg, Mg-0.15Ca, AZ31 and AM50). The results demonstrate that 2,6-DHB efficiently improves the discharge performance of Mg-air batteries with different Mg anodes.

1. Introduction

In past decades, metal-air batteries have been investigated intensively due to superior theoretical discharge performance [1–5]. The theoretical specific energy of metal-air batteries based on different metallic anodes varies from 1.3 to 13.0 kWh kg^{-1} (excluding the molar loss of O_2), which is 3 to 30 times higher than that of Li-ion batteries [6,7]. Aqueous Mg-air batteries as desirable energy storage options attracted much attention among existing metal-air battery systems. The advantages of these batteries include the high security owing to aqueous electrolyte, cost-effectiveness due to abundant resources from earth crust and environmental amiability [8–10]. The mechanically rechargeable feature and long shelf life of aqueous Mg-air battery systems contribute to its potential as a reliable energy supply for marine devices and as a reserve power source for hospitals, schools, etc. [11–13]. Nevertheless, the sluggish electrode reaction kinetics and severe self-discharge of Mg anode amid discharge reduce the practical performance of aqueous Mg-air batteries. Numerous endeavors have been made to boost the practical discharge performance of aqueous Mg-air batteries from diverse aspects, but most of the previous studies focused on the novel Mg anode development rather than the modification of electrolyte [14–23].

As one of the key components for aqueous Mg-air batteries, electrolyte is decisive for the actual reactions and practical performance of the system. The ideal electrolyte for aqueous Mg-air batteries should possess high conductivity and have an inhibiting effect against parasitic reactions. It should promote the Mg anode discharge activity and contribute to enhanced discharge performance from aspects of utilization efficiency and cell voltage. Nevertheless, only a limited numbers of published works have covered this criteria and mainly have focused on the improvement of utilization efficiency by adopting Mg corrosion inhibitors or surfactants [24–28]. For instance, Dinesh et al. [25] used graphene as electrolyte additive to prolong the operating life of Mg-air battery but the cell voltage was slightly decreased. Similarly, Zhao et al. reported the addition of phosphate and vanadate improved the anodic efficiency of AZ31 anode, which however, imparted negligible enhancement to the cell voltage [26]. The above studies adopted electrolyte additives based on their ability of adsorbing on Mg anode surface or forming a protective surface film. This concept is somehow contradictory to the requirement of improving discharge activity and cell voltage of Mg-air batteries. More recent studies attempted to boost the battery performance from both aspects [15,18,29–33]. The study of

* Corresponding author.
E-mail address: linqian.wang@hereon.de (L. Wang).

https://doi.org/10.1016/j.cej.2021.132369
Received 8 April 2021; Received in revised form 17 July 2021; Accepted 5 September 2021
Available online 10 September 2021

Höche et al. [15] suggested a novel strategy of adopting organic additives, which were able to coordinate with iron impurities and thereby improve the anodic utilization efficiency by hindering the redepostion of metallic Fe from $Fe^{2+/3+}$ ions on the Mg anode surface. Meanwhile, the organic additives also formed soluble coordination compounds with Mg^{2+} and therefore decreased the IR drop related to insoluble products formed during discharge. However, among the selected additives, only salicylate and Tiron were capable of simultaneously improving the utilization efficiency and discharge voltage of commercial purity Mg (220 ppm Fe) under certain applied current densities. Most of the selected additives can only show the improvement from one aspect, either discharge voltage or utilization efficiency. Snihirova et al. [30] proposed the strategy to adopt mixture of salicylate and nitrate to improve the discharge performance of commercial purity Mg (178 ppm Fe) via their synergistic effect. Nevertheless, these studies were carried out on the specified Mg anode materials with relatively high content of iron, which are not informative for predicting its efficacy for other Mg anode materials with lower content of impurities. So far, most studies concerning the development of novel electrolyte additives for aqueous Mg-air batteries have only targeted on the performance improvemen for merely one kind of Mg-based anodes. Nevertheless, it would be highly beneficial if one sole additive, which is working based on the intrinstic properties of Mg, posesses the capability of boosting the properties of diverse commercial Mg anodes..

According to our previous research [31], 2,6-DHB yielded not only the highest utilization efficiency via the suppression of the chunk effect on Mg-0.04 wt% Ca but also a considerable improvement for the discharge potential among a range of organic electrolyte additives. The improvement on the mentioned anode also suggested that 2,6-DHB may be effective for other Mg anodes. If 2,6-DHB is universally effective for aqueous Mg-air batteries based on diversity of Mg anodes, it should be helpful to accelerate the commercialization of this energy system. Although 2,6-DHB was previously reported as a potential additive [31], which suppresses the chunk effect on specific anode material, the range of conditions as well as range of substrates at which the additive can perform was not addressed there. It is unclear if the results can be transferable to other conditions and systems important for potential applications. Hence, further investigation into revealing the working mechanism of 2,6-DHB is still needed, which may be indicative for the discovery of other novel electrolyte additives and novel Mg-air battery systems.

Therefore, the current work was dedicated to find out main mechanisms of of 2,6-DHB as an electrolyte additve and its common features responsible for improved performance on aqueous Mg-air batteries based on various anode materials. Moreover the range of conditions (concentration) at which the effect can be observed was also investigated. The anode surface condition evaluation during discharge was investigated by electrochemical impedance measurements amid intermittent discharge to determine the effect of 2,6-DHB at different concentrations on the discharge potential. Meanwhile, real-time hydrogen evolution measurements during discharge were performed to clarify the influence of varied 2,6-DHB additions on the self-discharge behavior of Mg anode. Hence, the working mechanism of 2,6-DHB was thoroughly discussed and the applied parameter for optimum discharge performance was proposed.

2. Experimental details

2.1. Materials and electrolyte

Mg-0.15 wt% Ca with distinguish corrosion resistance was adopted as one of the anode materials in this work, which was prepared via the conventional casting processes. The detailed fabrication processes was reported in the previous work from our group [34]. Except for Mg-0.15Ca alloy, commercially available AZ31, AM50 Mg alloy and high purity Mg (HP-Mg) were also applied as anode materials. The composition of anode materials were analyzed via atomic absorption spectroscopy (AAS) and spark optical emission spectrometry (SOES). The results are displayed in Table 1.

3.5 wt% NaCl solution was utilized and denoted as reference electrolyte for all the electrochemical tests appearing in this work. 2,6-dihydroxybenzoic acid with various concentrations (0.05, 0.1, 0.2, and 0.3 M) were added into NaCl solution as electrolyte additives. All the electrolytes with 2,6-dihydroxybenzoic acid were neutralized by NaOH to pH 7.0 ± 0.1. Hence, 2,6-dihydroxybenzoic acid was fully neutralized into sodium 2,6-dihydroxybenzoate, which is denoted as 2,6-DHB. All the electrolytes were prepared with deionized water.

2.2. Electrochemical measurement

Potentiodynamic polarization curves of Mg-0.15Ca alloy in the above-mentioned electrolytes were measured by Gamry Interface 1000 potentiostat in conventional three electrodes system adopting well-ground Mg-0.15Ca alloy with 1 cm^2 exposed surface as the working electrode, Pt wire as the counter electrode and commercial Ag/AgCl electrode as the reference electrode. All the polarization curves were obtained after 1 h immersion in the testing electrolytes by potential scanning from – 400 mV to + 800 mV vs. open circuit potential (OCP). The scanning started from cathodic region to anodic region with 0.5 mV/s scanning rate.

The half-cell discharge tests were performed in the same configuration used in our previous work [31]. The Mg-0.15Ca anode with 2.25 cm^2 exposed surface area and Ag/AgCl reference electrode were separated from Pt counter electrode via a salt bridge. The duration of the tests was 24 h with 5 mA cm^{-2} discharge current density. The electrolyte was stirred at 350 rpm during the test. After discharge tests, the weight loss of the anode in the discharging process, ΔW, was obtained after removal of surface precipitates and applied for the calculation of the anodic utilization efficiencies (UE) in different electrolytes via the following equations ,

$$\mathrm{UE} = \frac{W_{theo}}{\Delta W} \times 100\% \quad (1)$$

$$W_{theo} = \frac{I \times t \times M}{F \times n} \quad (2)$$

Theoretical weight loss W_{theo} in Eq. (1) is calculated according to the equation as presented in Eq. (2), where I and t represent the applied current and discharge duration. M is the atomic mass of anode material. F and n represent the Faraday constant and the ionic valence of anode material, respectively.

The anode surface condition during discharge was evaluated by electrochemical impedance spectroscopy (EIS) measurements. The EIS measurements were done at OCP after discharge for different periods (0, 5, 10, 15 and 24 h), hereafter referred as intermittent discharge test. The measurements were carried out in the frequency range from 100 kHz to 0.03 Hz with 9 points per decade. The applied perturbation voltage was 10 mV_{rms}.

Real-time hydrogen evolution rate of Mg-0.15Ca in 2,6-DHB-containing NaCl solution during discharge was evaluated via a modified experimental set-up based on the one used in the published work of Deng et al. [35]. Briefly, a burette-funnel set-up was adopted to collect the evolved hydrogen from anode. In order to keep the similar testing environment, the counter electrode was also placed into a separate beaker, which was connected to the beaker with gas collecting set-up, anode and reference electrode via a salt bridge.

Full cell tests were performed in a lab-assembled Mg-air battery, which adopted air-breathing cathode with MnO_2 catalyzer (Gaskatel GmbH) and modified electrolyte (330 mL) with optimized concentration of 2,6-DHB. Four kinds of Mg-based materials, including high purity Mg, Mg-0.15Ca, AZ31 and AM50 alloy, were applied as anode materials. The cell voltage of Mg-air battery was tested at 1, 5 and 10 mA cm^{-2}. The

Table 1
Chemical compositions of metallic Mg anode materials (wt. %).

Materials	Ca	Al	Fe	Ni	Cu	Mn	Si	Zn	Mg
Mg-0.15Ca	0.15	0.0021	0.0014	0.0002	0.0002	0.016	0.0056	0.002	Bal.
HP-Mg	0.0016	0.0030	0.0024	0.0003	0.0004	0.025	0.0093	0.0018	Bal.
AZ31	0.0011	2.97	0.0011	0.0007	0.0019	0.358	0.0309	0.732	Bal.
AM50	0.0011	4.85	0.0002	0.0005	0.0017	0.430	0.0637	0.0418	Bal.

improvements of discharge performance introduced by 2,6-DHB addition were evaluated by the specific energy and power density, which were calculated by the following equations.

$$\text{Specific energy} = \frac{\int_0^t I \times U \times \Delta t}{\Delta W} \quad (3)$$

$$\text{Power density} = \frac{I \times U}{A} \quad (4)$$

Where U and A refer to the cell voltage and the surface area of anode, respectively. The above mentioned characters represent the same meanings as introduced. All the above mentioned measurements were repeated.

2.3. Surface analysis

The surface morphologies of Mg-0.15Ca, HP-Mg, AZ31 and AM50 anodes after 24 h discharge were characterized by optical microscope and scanning electron microscope (SEM, Tescan Vega 3). The phase composition of surface layer was analyzed via X-ray diffraction measurement (XRD, D8 Advance, Brucker AXS) with CuK_α radiation (40 kV, 40 mA). The diffraction angle was from 15° to 80° with 0.02° step size and the grazing angle was 1°. The dwell time is 1 s for each point.

3. Results and discussion

3.1. Potentiodynamic polarization curves

The polarization curves of Mg-0.15Ca in reference electrolyte and electrolytes with various 2,6-DHB concentrations are displayed in Fig. 1. As shown in Fig. 1a, the addition of 2,6-DHB shifts the corrosion potential, namely the OCP of Mg-0.15Ca, to a more negative value. With the increase of 2,6-DHB concentration, the OCP of Mg-0.15Ca slightly decreases. The shift of OCP is mainly attributed to the accelerated anodic reaction kinetics. Adding 2,6-DHB significantly increases the anodic current density of Mg-0.15Ca, indicating that discharge activity for Mg-0.15Ca in 2,6-DHB-containing electrolyte might be increased. Moreover, the increase of 2,6-DHB concentration makes greater impact on the anodic branch of Mg-0.15Ca, as presented in magnified Fig. 1b. Nevertheless, only a minor difference can be observed between the cathodic branches corresponding to different 2,6-DHB concentrations. The molecular structure of 2,6-DHB acid is illustrated in Fig. 1b. As the hydroxyl derivative of salicylic acid, 2,6-dihydroxybenzoic acid, contains one more hydroxyl group *ortho* to the carboxyl group, which supplies one more potential binding site and is an effective ligand for metal cations, such as Al^{3+}, $Fe^{2+/3+}$, Cu^{2+} et al. [36–40]. As reported in our previous work [31], 2,6-DHB acid is also capable of forming soluble complexes with Mg^{2+}, which disturbs formation of insoluble products on the anode and promotes the anodic dissolution of Mg. Besides, the symmetric intramolecular hydrogen bonds of 2,6-DHB acid, which are formed between carboxyl group and hydroxyl groups make the deprotonation process of 2,6-DHB acid on the hydroxyl groups more difficult than other isomers [41], such as 3,4-DHB, which demonstrated a pH buffering effect in our previous work [31]. The disassociation constant for the first ionization and the second ionization of 2,6-DHB, pKa_1 and pKa_2, are 1.2 and 12.57, and that for 3,4-DHB are 4.32 and 8.83, respectively [42]. The carboxylate proton has already dissociated when the pH of 2,6-DHB-containing electrolyte was adjusted to pH 7. Hence, 2,6-DHB does not possess strong pH buffering capability as 3,4-DHB. More negative OCP and faster anodic reaction kinetics of Mg-0.15Ca in 2,6-DHB-containing electrolyte both indicate that its discharge activity and potential should be improved in such circumstance.

3.2. Half-cell discharge performance

The half-cell discharge curves of Mg-0.15Ca in different electrolytes are presented in Fig. 2a. The discharge potential of Mg-0.15Ca in reference electrolyte stabilizes at −1.56 $V_{Ag/AgCl}$ after fluctuations during the initial 2 h discharge. The initial discharge potential of Mg-0.15Ca in 0.05 M 2,6-DHB-containing electrolyte shifts to a more negative value of −1.62 V and then starts to gradually increase with the increase of discharging time. After 20 h discharge, the final discharge potential keeps relatively stable at −1.54 V. The discharge curve of Mg-0.15Ca in 0.1 M 2,6-DHB-containing electrolyte is stable amid the whole measurement and is always more negative than that in reference electrolyte. 2,6-DHB addition in high concentrations (0.2 M and 0.3 M) also leads to more negative discharge potential in comparison to that in reference electrolyte. In particularly, the discharge potential of Mg-0.15Ca in

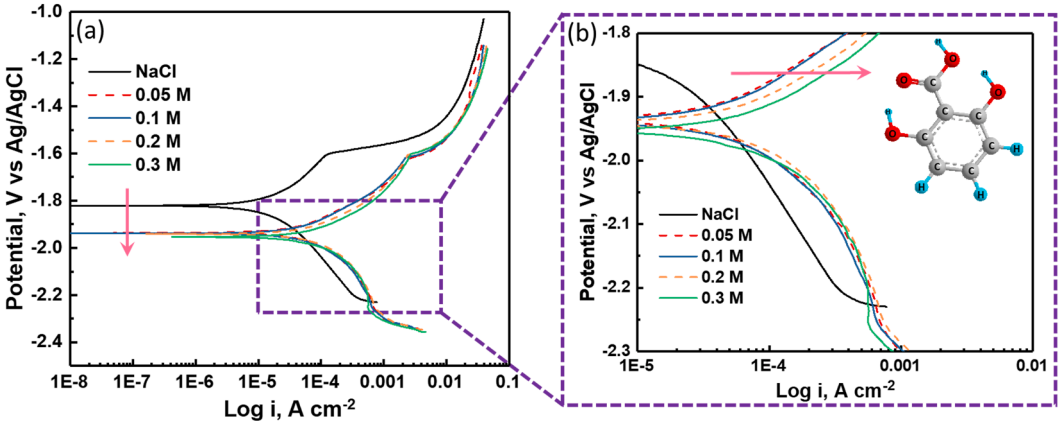

Fig. 1. Potentiodynamic polarization curves of Mg-0.15Ca in reference electrolyte and electrolytes with 2,6-DHB of various concentrations.

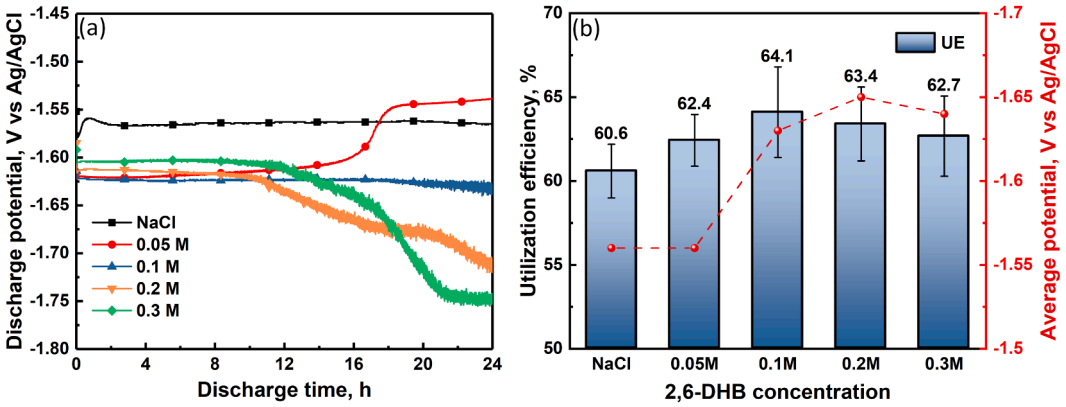

Fig. 2. Half-cell discharge performance of Mg-0.15Ca in reference electrolyte and electrolytes with various concentrations of 2,6-DHB: (a) discharge curves and (b) utilization efficiency and average potential of Mg-0.15Ca. (Applied current density: 5 mA cm^{-2}).

electrolytes with high concentrations 2,6-DHB gradually shifts to more negative value after 12 h discharge. The possible reason might be related to the changes of the surface area. Fig. 2b exhibits the anodic utilization efficiencies and average potential of anodes in different electrolytes. The addition of 2,6-DHB, regardless of concentration, enhances the anodic utilization efficiency. Among them, the anodic utilization efficiency in 0.1 M 2,6-DHB-containing electrolyte is the highest. The anodic utilization efficiency yielded by the addition of 0.2 M 2,6-DHB is similar with that in 0.1 M 2,6-DHB-containing electrolyte. Meanwhile, with the addition of 0.2 M 2,6-DHB, Mg-0.15Ca anode exhibits the best average discharge potential. It should be noted that higher concentration 2,6-DHB, i.e. 0.3 M, does not further improve the discharge potential but inversely causes the loss of utilization efficiency. Based on the above presented results and discussion, 0.2 M is proposed to be the optimum concentration of 2,6-DHB as an electrolyte additive.

The surface conditions of anode after discharge in different electrolytes are presented in Fig. 3 and the macro surface morphologies are presented in the insets in the bottom left corner. In reference electrolyte and the electrolyte with 0.05 M 2,6-DHB, the surface of Mg-0.15Ca is completely covered by discharge products. The discharge products in reference electrolyte are gray and porous (Fig. 3a), whereas that in electrolyte with 0.05 M 2,6-DHB are greenish, exhibiting an inner layer and an outer layer (Fig. 3b). The structure of the inner layer (Fig. 3c) shows a large number of cracks, which may be the natural structure of this layer but also could be the consequence of dehydration during sample preparation and microstructure analysis. Under the same preparation and analysis conditions, the outer layer is significantly denser than the inner layer. The phase composition of discharge products film in reference electrolyte and electrolyte with 0.05 M 2,6-DHB are exhibited in Fig. 3h. The grazing angle for XRD measurement was 1°, which ensures that the information was mainly obtained from the top layer of the specimens. The sample discharged in reference electrolyte possesses a distinct peak for metallic Mg. On the contrary, the peak for metallic Mg is absent for the sample discharged in NaCl with 0.05 M 2,6-DHB and an additional peak appears in the range between 20° to 25°, which is not well fitted to any peak that can be found in the database. The accurate characterization for the composition of precipitation is out of the scope for this work. The relevant results presented in Fig. 3 have already demonstrated that the addition of 0.05 M 2,6-DHB changes the structure and composition of discharge products of Mg-0.15Ca. Fig. 3e-g depict the anode surface morphologies after 24 h discharge in 0.1, 0.2 and 0.3 M 2,6-DHB-containing electrolytes, respectively, which are clean without any visible discharge products.

The cross sections of Mg-0.15Ca after discharge in 2,6-DHB-containing electrolytes indicate that the addition of high concentration 2,6-DHB seems to increase the anode surface roughness (Fig. 4). Consequently, it may increases the electrochemically active surface area of Mg-0.15Ca anode, which may influence the tested discharge potential. The half-

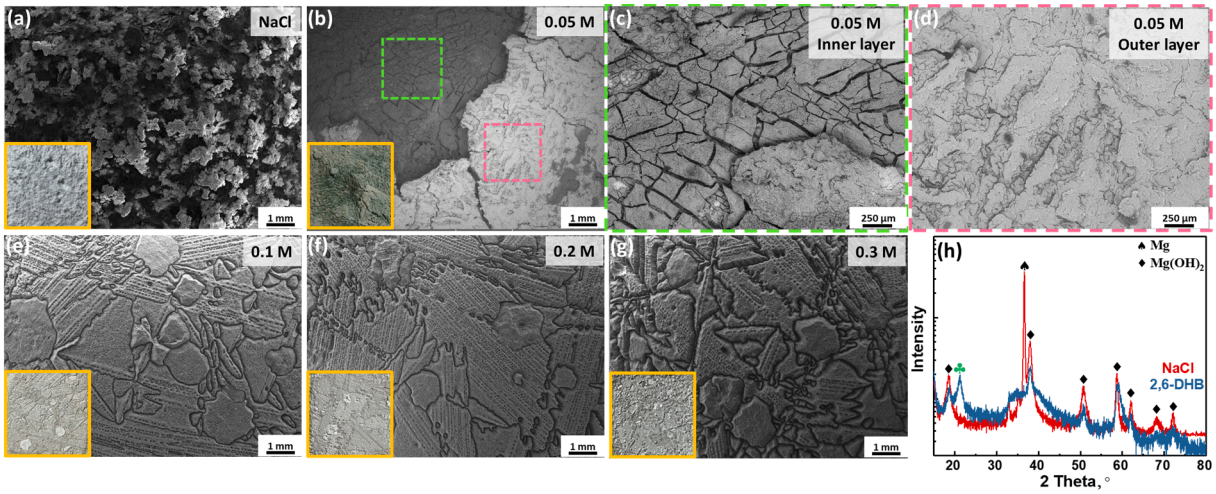

Fig. 3. Surface of Mg-0.15Ca anode after 24 h discharge at 5 mA cm^{-2}: (a) in reference electrolyte; (b-d) in electrolyte with 0.05 M 2,6-DHB; (e) with 0.1 M 2,6-DHB; (f) with 0.2 M 2,6-DHB; (g) with 0.3 M 2,6-DHB and (h) XRD diffraction patterns of Mg-0.15Ca anode in reference electrolyte and in electrolyte with 0.05 M 2,6-DHB. (Corresponding macro-surface morphologies of Mg-0.15Ca anode with 1.5 × 1.5 cm dimension after discharge are presented in the left lower corners of each figure).

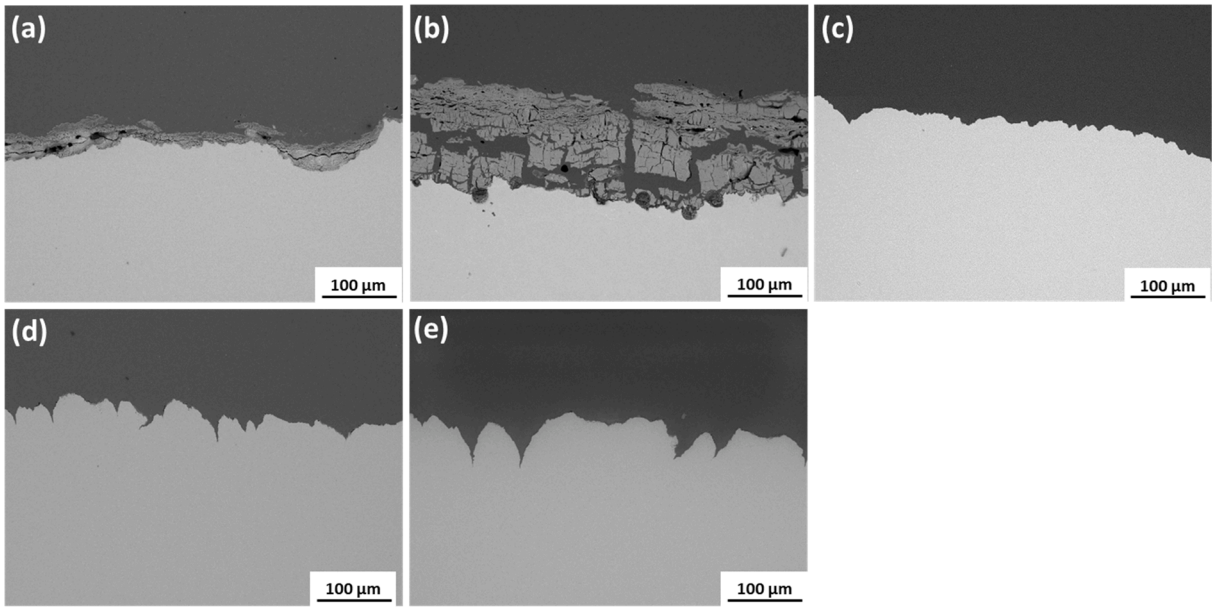

Fig. 4. Cross sections of Mg-0.15Ca anodes after 24 h discharge at 5 mA cm^{-2}: (a) in reference electrolyte, and in electrolytes with (b) 0.05 M; (c) 0.1 M; (d) 0.2 M; (e) 0.3 M 2,6-DHB.

cell discharge test was done in galvanostatic mode, and thus, the increase of electrochemically active surface area will decrease the effective applied anodic current density. Lower current density will give rise to more negative discharge potential of Mg anode [31]. Therefore, the negatively shifting discharge potential in 0.2 and 0.3 M 2,6-DHB-containing electrolytes amid later discharge period might be related to the change of electrochemically active surface area. Nevertheless, certainly, it is not the only reason for the improvement of discharge potential in 2,6-DHB-containing electrolytes.

3.3. Electrochemical impedance measurements amid intermittent discharge tests

In order to reveal the working mechanism of 2,6-DHB addition on the discharge performance of Mg anode, the evolution of anode surface condition during discharge was evaluated by EIS measurements amid intermittent discharge tests. Moreover, the OCP of anode before and after discharge tests were recorded for comparison. Additions of 0.2 M and 0.3 M 2,6-DHB impart similar improvement to the discharge properties of Mg-0.15Ca anode, thus, 0.2 M is chosen as the highest concentration applied in the intermittent discharge test. Fig. 5a presents the intermittent discharge curves of Mg-0.15Ca in different electrolytes, indicating very similar discharge behavior to that presented in Fig. 2a. The peak on the discharge curve corresponds to the moment, when OCP and EIS were measured. After each interval, the discharge potential drops back in few seconds, manifesting EIS measurements during each interval were done at stable surface condition, which was not greatly changed during EIS measurements. Fig. 5b shows the OCP of Mg-0.15Ca for varied periods in different electrolytes. Note that the OCP measurement only lasts for 60 s in order to maintain a surface condition close to that during discharge. The addition of 2,6-DHB with higher concentration shifts the OCP of Mg-0.15Ca to a more negative value. After 5 h discharge, the OCP of Mg-0.15Ca in reference electrolyte is stabilized at −1.73 V. The OCP of Mg-0.15Ca in 0.05 M 2,6-DHB-containing electrolyte after 15 h discharge jumps from −1.93 V (after 10 h discharge) to −1.72 V and the corresponding discharge potential (Fig. 5a) shifts from −1.60 V to −1.52 V. After 24 h discharge, the OCP of Mg-0.15Ca in 0.05 M 2,6-DHB-containing electrolyte drops slightly back to −1.77 V, which is almost similar to that in reference electrolyte. The OCP of Mg-0.15Ca in electrolyte with 0.1 M 2,6-DHB amid 24 h discharge keeps steady at −1.98 V, while that in 0.2 M 2,6-DHB decreases from −1.97 V to −1.99 V.

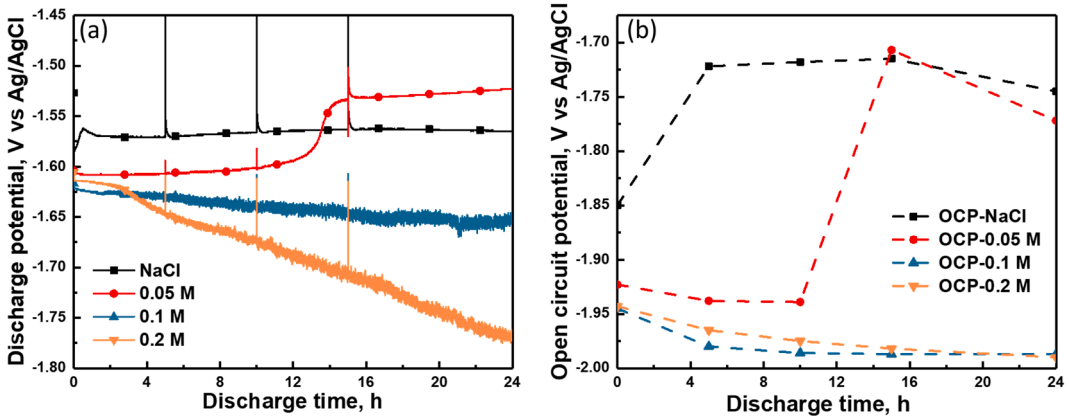

Fig. 5. (a) Intermittent discharge curves and (b) OCP of Mg-0.15Ca in reference electrolyte and electrolytes with various concentrations 2,6-DHB.

The Nyquist plots of Mg-0.15Ca are illustrated in Fig. 6. The Nyquist plot of Mg-0.15Ca in reference electrolyte before discharge is composed of two well-defined capacitive loops and the diameters are much less than that of after discharge. Conversely, the capacitive loops of Mg-0.15Ca in 0.1 M and 0.2 M 2,6-DHB-containing electrolytes shrink within the 24 h discharge process. The addition of 0.1 M or 0.2 M 2,6-DHB reduces the impedance of Mg-0.15Ca anode due to its ability to retard the formation of discharge products, as shown in Fig. 3e and Fig. 3f. In 0.05 M 2,6-DHB-containing electrolyte, the capacitive loops of Mg-0.15Ca firstly shrink and then expand after 15 h discharge. Eventually, after 24 h discharge, they become even larger than that in reference electrolyte. Meanwhile, as shown in Fig. 6b, the high frequency part of Nyquist plot shifts to higher value during the 24 h discharge in 0.05 M 2,6-DHB-containing electrolyte. Normally, the real component value of this part represents the solution resistance between the working electrode and reference electrode, that is to say, the solution resistance increases amid the 24 h discharge in 0.05 M 2,6-DHB-containing electrolyte. However, during discharge, the solution resistance is theoretically stable if the distance between the working electrode and reference electrode is fixed, or slightly decreases due to the increase of ion concentration. For instance, the initial solution resistance of 0.2 M 2,6-DHB-containing electrolyte is slightly less than that of blank NaCl solution because of higher ion concentration. The pronounced increase of solution resistance in 0.05 M 2,6-DHB-containing electrolyte should be attributed to the formation of outer layer of discharge products as presented in Fig. 3d. This layer is denser and more protective than the porous $Mg(OH)_2$ film formed in reference electrolyte. Thus, the increase of this part after discharge in reference electrolyte is less noticeable. Moreover, a small loop emerges in the high frequency part of Mg-0.15Ca after discharge in 0.05 M 2,6-DHB-containing electrolyte for 15 h, which is possibly related to the inner layer of discharge products formed in this modified electrolyte.

Eq. (5) is the formula for qualitative analysis of anode discharge potential, which is expressed as,

$$-E_{anode} = |E_{ocp}| - \eta_{ct} - \eta_{mt} - IR \tag{5}$$

Where E_{ocp} is the OCP of anode versus reference electrode, η_{ct} and η_{mt} refer to the potential drop because of charge transfer process and mass transport process through discharge products, respectively. I represents the applied current and R is the electrolyte resistance [43–45]. As illustrated in Fig. 5b, the representing OCP of anode at defined discharge times is changing during the whole discharge process, thus the OCP obtained before discharge is not representative for discharge potential prediction. For instance, Mg-0.15Ca in electrolyte with 0.05 M 2,6-DHB possesses more negative OCP than that in reference electrolyte. Nevertheless, with the accumulation of discharge products, the OCP becomes more positive and simultaneously,η_{ct} and η_{mt} increase, resulting in the potential jump after 12 h discharge as shown in Fig. 5a. In contrast, in the electrolyte with 0.2 M 2,6-DHB, the anode efficiently maintains negative OCP amid the whole 24 h discharge and exhibits relatively small IR value. Moreover, smaller impedance value indicates higher anodic dissolution activity and less film barrier property, portending less

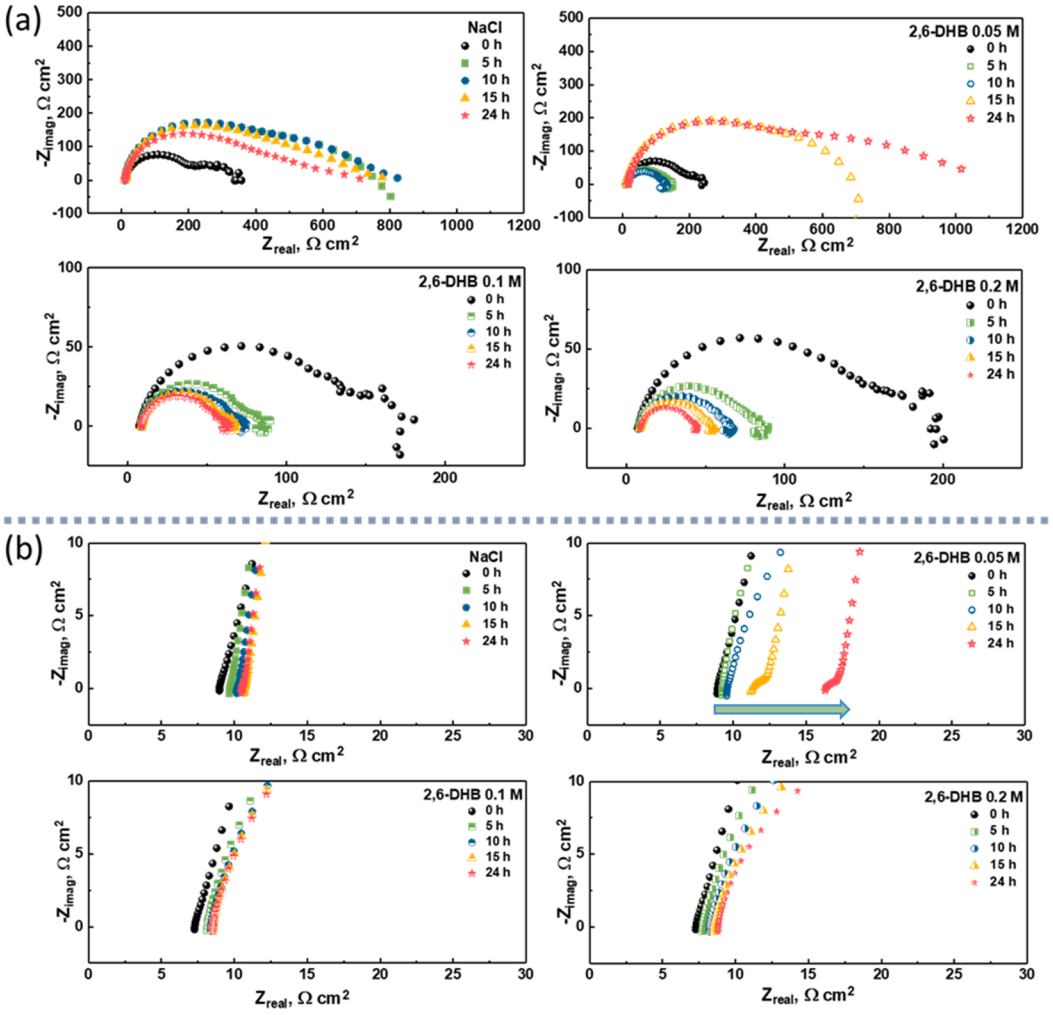

Fig. 6. (a) Nyquist plots and (b) magnified Nyquist plots of Mg-0.15Ca in reference electrolyte and electrolytes with various concentrations 2,6-DHB.

potential drop due to charge transfer and mass transport process. Therefore, Mg-0.15Ca anode always maintains high discharge activity and more negative discharge potential in electrolytes containing 2,6-DHB of high concentrations.

3.4. Real-time hydrogen evolution measurement during discharge

Anomalous hydrogen evolution of Mg during anodic polarization is recongized as negative difference effect. A considerable amount of literature has been published and discussed the important characteristic of Mg [46–50]. Mg-0.15Ca anode undergoes anodic polarization during the whole discharge test. Hence, the negative difference effect plays an important role to the anode utilization efficiency. As presented in Eq. (6), the total weight loss during discharge test is composed of three main components, including the theoretical weight loss (W_{theo}), the weight loss caused by chunk effect ($W_{chunk\ effect}$) and the weight loss caused by self-discharge of anode substrate ($W_{self\text{-}discharge}$). As shown in Eq. (2), for the fixed anode material, W_{theo} is only determined by the applied current and discharge time. Our previous research has thoroughly discussed the impact of $W_{chunk\ effect}$ and $W_{self\text{-}discharge}$ on the anodic utilization efficiency, indicating both aspects affect the practical utilization efficiency decisively [35]. $W_{self\text{-}discharge}$ primarily refers to the weight loss caused by the hydrogen evolution reaction from anode during discharge, as the parasitic reaction of discharge.

$$\Delta W = W_{theo} + W_{chunk\ effect} + W_{self-discharge} \quad (6)$$

The hydrogen evolution of Mg-0.15Ca discharged in different electrolytes is depicted in Fig. 7. Within the initial 5 h, the hydrogen evolution under anodic polarization in the electrolyte with 0.05 M 2,6-DHB is the slowest and with the increase of 2,6-DHB concentration the evolved hydrogen amount slightly increases, which is still less than that in reference electrolyte. The inhibited hydrogen evolution rate by 2,6-DHB addition continues to the end of 24 h discharge. It is noteworthy that the hydrogen evolution rate in 0.05 M 2,6-DHB-containing electrolyte amid later discharging period becomes similar with that in reference electrolyte, as exhibited in Fig. 7a. It may be related to the formation of surface discharge products film with double layer structure, which would not be discussed in-depth in this work since it is relevant to the mechanism of NDE effect on Mg, which has been intensively discussed in the last decade but is still controversial [51–55]. What is noticeable is that the addition of 2,6-DHB depresses the hydrogen evolution of Mg-0.15Ca under anodic polarization. In particularly, Mg-0.15Ca in electrolyte with 0.1 M 2,6-DHB shows the slowest hydrogen evolution and consequently the least weight loss related to self-discharge, being consistent with the result presented in Fig. 2b. Utilization efficiency manifests the discrepancy between the theoretical weight loss and the actual weight loss. The addition of 2,6-DHB reduces the weight loss caused by self-discharge, resulting in the enhancement of utilization efficiency. Meanwhile, no visible evidence for severe chunk effect can be observed from the anode cross section in different electrolytes (Fig. 4). Therefore, the main improvement of anodic utilization efficiency is due to the inhibition effect of 2,6-DHB on self-discharge rate of Mg-0.15Ca and the impact of chunk effect is less pronounced than that of self-discharge, as indicated by our results. Moreover, the working mechanism of 2,6-DHB is mainly based on the intrinsic properties of Mg. Hence, it may also be capable of boosting the discharge performance of other Mg-based anode materials.

3.5. Full cell discharge test

Based on the above discussion, 0.2 M is proposed to be the optimum concentration of 2,6-DHB as an electrolyte additive working for Mg-Ca anode. Nevertheless, as a candidate for commercial electrolyte additive, 2,6-DHB should not only be effective to boost Mg-Ca anode based Mg-air battery performance, but should also be able to improve the battery performance based on commercial Mg anodes, which mainly refer to pure Mg, AZ series and AM series Mg alloys as suggested in literature [56–60]. Thus, except for Mg-0.15Ca, commercially available high purity Mg (HP-Mg), AZ31 and AM50 Mg alloys were adopted as representative Mg anode materials to fully evaluate the potential of 2,6-DHB. The full cell discharge performance of lab-assembled Mg-air batteries based on the above mentioned four kinds of anodes was tested in reference electrolyte and 0.2 M 2,6-DHB-containing electrolyte. In order to provide sufficient amount of 2,6-DHB, the volume of the electrolyte applied in this work was 330 mL. For practical applications, the design of flow battery [61] or the Mg-air battery with electrolyte circulation system [62] would be promising cell arrangements.

The full cell discharge curves are illustrated in Fig. 8. In reference electrolyte, Mg-0.15Ca alloy and HP-Mg based Mg-air batteries always exhibit higher cell voltage than that of AM50 and AZ31 alloy based Mg-air batteries. Under 1 and 5 mA cm^{-2} curent densities, the cell voltage of AM50 based Mg-air battery is higher than that based on AZ31. However, the cell voltage of AM50 based battery decreases rapidly after 8 h discharge at 10 mA cm^{-2}. As presented in Fig. 8a, the addition of 2,6-DHB improves the cell voltage of all Mg-air batteries, especially for HP-Mg and Mg-0.15Ca alloy based batteries. The cell voltage of Mg-0.15Ca based Mg-air battery is enhanced from 1.52 V to 1.75 V (at 1 mA cm^{-2}) and the improvement for HP-Mg based battery is around 140 mV (Fig. 8a). With the increase of applied current density, the improvement of cell voltage introduced by 2,6-DHB addition becomes

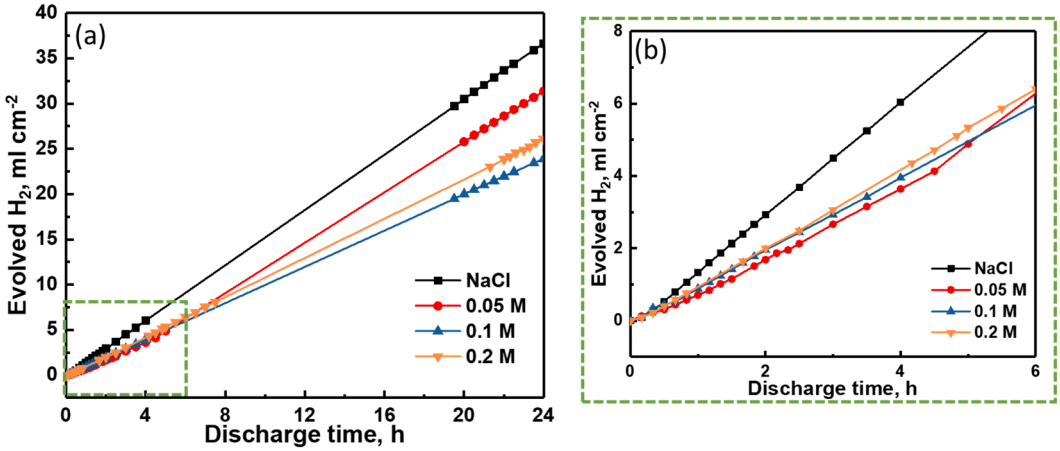

Fig. 7. Real-time hydrogen evolution curves of Mg-0.15Ca during discharge in reference electrolyte and electrolytes with different concentrations of 2,6-DHB: (a) 24 h and (b) initial 6 h. (Applied current density: 5 mA cm^{-2}).

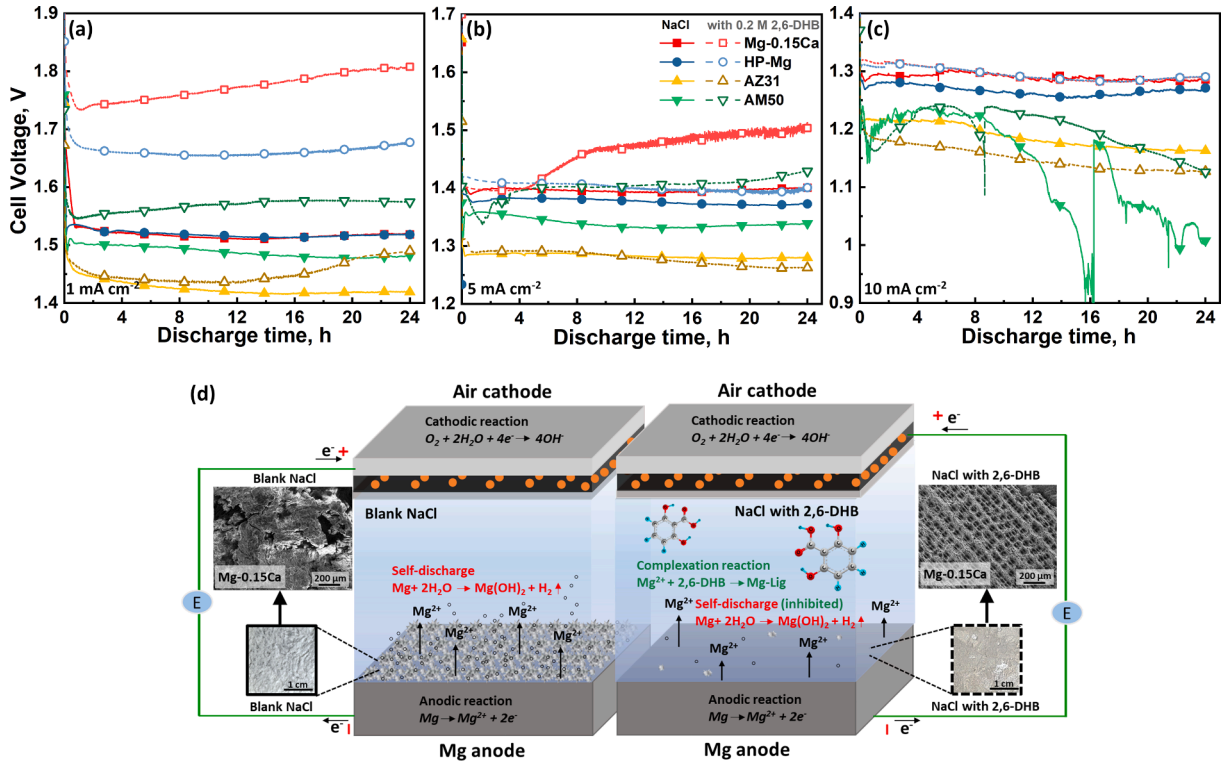

Fig. 8. Full cell discharge curves of Mg-air batteries based on different anodes under various applied current densities (a) 1 mA cm^{-2}, (b) 5 mA cm^{-2}, (c) 10 mA cm^{-2}, and (d) schematic illustration of 2,6-DHB working mechanism in aqueous Mg-air battery.

less significant, especially for AZ31 based battery. The cell voltage of AZ31 based battery in 2,6-DHB-containing electrolyte is slightly lower than that in blank NaCl solution at 10 mA cm^{-2} (Fig. 8c).

As illustrated in Fig. 8d, the working mechanism of 2,6-DHB for the enhancement of cell voltage is mainly related with its ability to bind Mg^{2+}, which hinders the anode surface blockage by alleviating discharge products precipitation and consequently decreases related potential drop. However, the discharge products formed on AZ31 contain not only $MgO/Mg(OH)_2$, but also relatively compact $Al_2O_3/Al(OH)_3$ or $ZnO/Zn(OH)_2$ [63–67], which is the reason why AZ31 possesses good corrosion resistance and lowest discharge cell voltage in NaCl solution. Introducing 2,6-DHB into NaCl solution can not

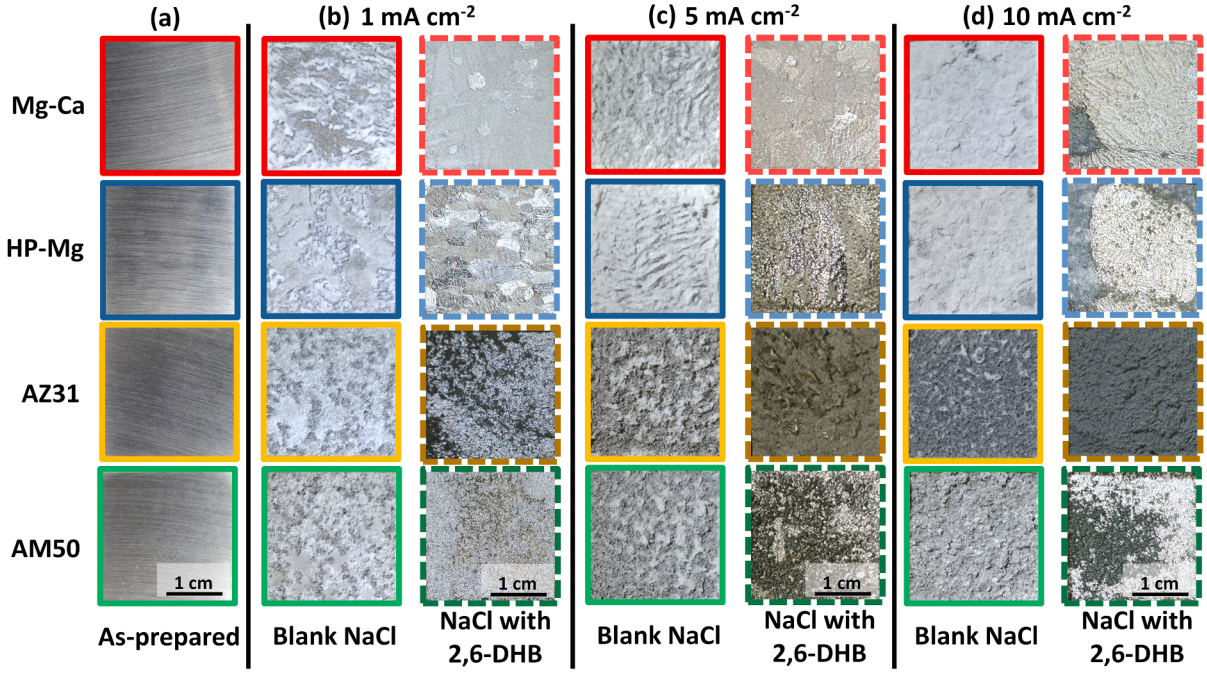

Fig. 9. Surface morphologies of Mg-based anodes before and after discharge in reference electrolyte and electrolyte with 0.2 M 2,6-DHB: (a) as prepared, (b) 1 mA cm^{-2}, (c) 5 mA cm^{-2}, and (d) 10 mA cm^{-2}.

completely impede the precipitation of discharge products on AZ31 anode. As shown in Fig. 9c and 9d, the surfaces of AZ31 electrodes after 24 h discharge (5 and 10 mA cm^{-2}) in 2,6-DHB containing electrolyte are completely covered by discharge products in green. AM50 alloy also contains Al element, but the cell voltages of AM50 based Mg-air battery under 1 and 5 mA cm^{-2} are greatly enhanced via adding 2,6-DHB, from 1.35 V to 1.42 V (at 5 mA cm^{-2}, in Fig. 8b). Possibly due to the absence of Zn-containing compounds in dishcarge precipitates, the addition of 2,6-DHB is still able to hinder the full coverage of AM50 by discharge products. As exhibited in Fig. 9b and 9c, some parts of AM50 anodes

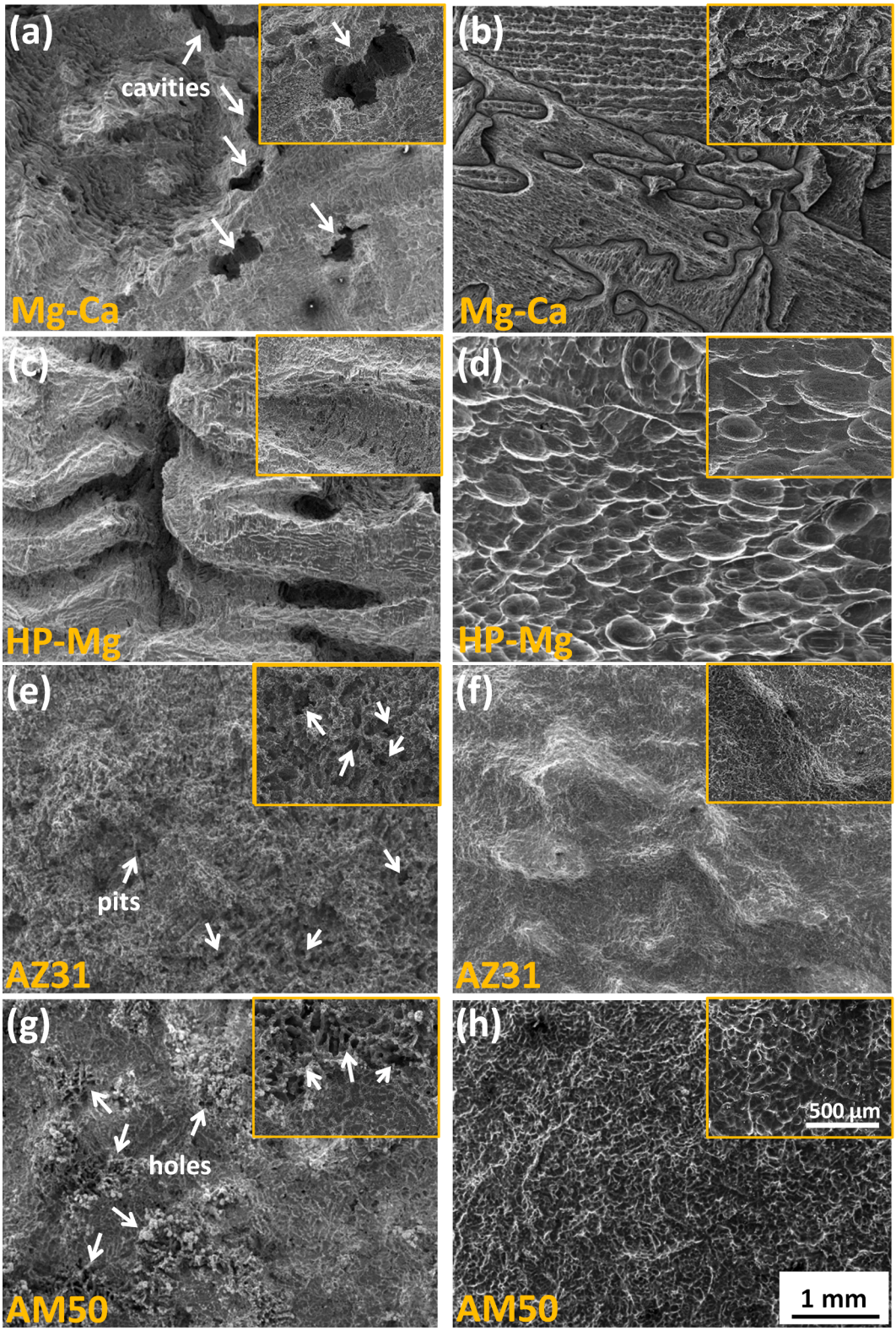

Fig. 10. Surface morphologies of different Mg anodes after 24 h discharge under 5 mA cm^{-2} and discharge products removal: (a, c, e, g) different Mg anodes in reference electrolyte; (b, d, f, h) different Mg anodes in electrolyte with 0.2 M 2,6-DHB.

after 24 h discharge in 2,6-DHB-containing electrolyte still exhibit metallic luster, whilst the surfaces of Mg-0.15Ca and HP-Mg anodes are completely clean without any coverage of grayish discharge products. Correspondingly, the cell voltages of Mg-0.15Ca and HP-Mg based Mg-air battery are improved by the addition of 2,6-DHB.

According to the results obatined via real-time hydrogen evolution tests (Fig. 7), the addition of 2,6-DHB is capable of inhibiting the self-discharge of Mg-0.15Ca and improving the anodic utilization efficiency. Fig. 10 displays the surface morphologies of Mg anodes after discharging at 5 mA cm^{-2} for 24 h and removing dischrage products, indicating the addition of 2,6-DHB is able to induce more uniform dissolution of Mg anodes. As shown in Fig. 10a, several cavities are left on the surface of Mg-0.15Ca after 24 h discharge in reference electrolyte. Similarily, HP-Mg anode in blank NaCl solution suffers from non-uniform dissolution during 24 h discharge (Fig. 10c). The surfaces of AZ31 and AM50 anodes in reference electrolyte seems more even than that of HP-Mg anode. Nevertheless, the magnified view of AM50 surface shows a large amount of holes, which are left by localized dissolution and detachment of second phases (Fig. 10g). The magnified view of AZ31 surface in Fig. 10e also illustrates that there are several pits and holes left by localized dissolution. All the anodes without exception possess more even morphologies during discharge in the electrolyte with 2,6-DHB as compared to that of referenece electrolyte. As illustrated in Fig. 10d, the surface of HP-Mg in 2,6-DHB-containing electrolyte is relatively uniform without any deep grooves and posesses a fish scale like structure. Fig. 10f and Fig. 10*h* demonstrate that the addition of 2,6-DHB is conducive to reduce the localized dissolution of AZ31 and AM50 anodes.

Fig. 11 presents the specific energy and power density of Mg-air batteries based on diverse Mg-based anodes in reference electrolyte and electrolyte with 0.2 M 2,6-DHB. The specific energy of Mg-air batteries is calculated via Eq. (3), which is based on the weight loss of anode materials. As shown in Fig, 11, the improvement of 0.2 M 2,6-DHB addition at 1 mA cm^{-2} is only represented by the increase of power density of the battery. For Mg-0.15Ca, AZ31 and AM50 based Mg-air batteries, the addition of 0.2 M 2,6-DHB at 1 mA cm^{-2} greatly acclearates the dissolution of Mg-based anodes, because the complexing ability of 2,6-DHB exceeds the amount of Mg^{2+} generated by the anodic reaction at 1 mA cm^{-2}. Our previous work also reported this phenomenen and suggested to adopt moderate Mg^{2+} complexing agents, such as sodium citrate and sodium salicylate, under 1 mA cm^{-2} [31]. As exhibited in Fig. 11a, the addition of 0.2 M 2,6-DHB improves the specific energy of all the tested Mg-air batteries under 5 and 10 mA cm^{-2}, especially for AM50 based battery. In reference electrolyte, the specific energy of AM50 based Mg-air battery under various current densities is always the lowest. Nevertheless, the specific energy of AM50 based Mg-air battery in 0.2 M 2,6-DHB-containing electrolyte is even higher than that based on AZ31 anode, 1737 vs. 1663 Wh kg^{-1} for 5 mA cm^{-2} discharge and 1850 vs. 1640 Wh kg^{-1} for 10 mA cm^{-2} discharge. The enhancement of specific energy caused by 2,6-DHB addition is the highest for AM50 based Mg-air battery. From one aspect, the addition of 2,6-DHB significantly increases the cell voltage of AM50 anode as shown in Fig. 8, which also greatly increases the power density of AM50 based Mg-air battery. From another aspect, it decreases the localised dissolution of AM50 during discharge as presented in Fig. 10*h*, which is beneficial to reduction of the extra weight loss induced by chunk effect. As demonstrated by Deng et al. [35], chunk effect led to high efficiency loss of around 35% to AM50 anode at 5 mA cm^{-2}. HP-Mg based Mg-air battery also exhibits a significant enhancement of specific energy, which is partly attributed to uniform dissolution promoted by the addition of 2,6-DHB. Besides, similar to Mg-Ca anode, the self-corrosion of HP-Mg may also be inhibited by the addition of 2,6-DHB. The reduction of localized dissolution on AZ31 anode as shown in Fig. 10e and Fig. 10f also contributes to the improvement of specific energy for AZ31 based battery under relatively high current densities (5 mA cm^{-2}), even though its power density decreases slightly. Mg-0.15Ca anode does not suffer from severe localized corrosion in comparison to HP-Mg, AM50 and AZ31 anode. Hence, the improvement for specific energy induced by 0.2 M 2,6-DHB addition is less significant than other tested systems. Nevertheless, the combination of Mg-0.15Ca anode and 2,6-DHB-containing electrolyte exhibits the best specific energy (2027 Wh kg^{-1}) and the highest energy density (12.95 mW cm^{-2}) among all studied Mg-air batteries in the present work. Therefore, discharge performance of aqueous Mg-air battery is not decided by single component of the system, but relies on the interactions of each component and operating conditions.

4. Conclusions

The present study exhibits the potential of 2,6-dihydroxybenzoate (2,6-DHB) as a verstaile electrolyte additive for aqueous Mg-air batteries. The influence of the applied concentration and the working mechanism of 2,6-DHB was explored on novel Mg-0.15Ca anode. The results suggest that the addition of 2,6-DHB of adequte concentrations is capable of simultaneously improving the discharge potential and utilization efficiency of Mg-0.15Ca anode. Low concentration of 2,6-DHB, such as 0.05 M, is not able to impede the precipitation of discharge products on Mg-0.15Ca anode, leading to the formation of dense products film and large voltage drop. By contrast, with addition of sufficient 2,6-DHB, e.g. 0.1 M, precipitation of discharge products is efficiently hindered and, thus, voltage drop is diminished. The best average discharge potential is obtained for 0.2 M 2,6-DHB, at −1.65 V vs Ag/AgCl. More concentrated 2,6-DHB (0.3 M) does not further improve the discharge potental but leads to the decrease of utilization efficiency. The inhibition effect of 2,6-DHB addition on the self-discharge of Mg anode is verified for the first time, which is justified by real-time hydrogen evolution tests during discharge and results in increased utilization efficiencies of Mg-0.15Ca in the electrolytes with 2,6-DHB. Considering

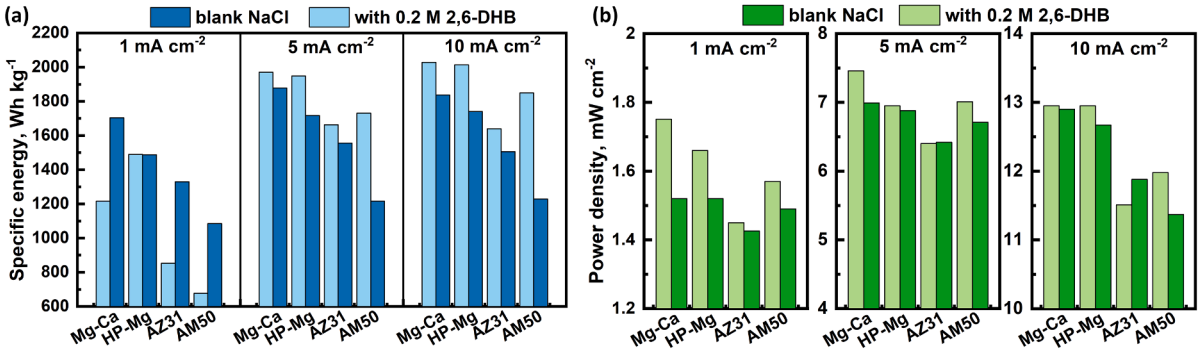

Fig. 11. (a) Specific energy and (b) power densities of Mg-air battery based on different anodes in reference electrolyte and electrolyte with 0.2 M 2,6-DHB.

the improved discharge potential and utilization efficiency, 0.2 M is set as the optimal concentration for 2,6-DHB for 5 mA cm^{-2} discharge condition. Full-cell tests manifest that 0.2 M 2,6-DHB-containing electrolyte successfully improves the discharge performance of Mg-air batteries with diverse Mg anodes, including pure Mg and commercial Mg alloy anodes. Under low current densities (e.g. 1 mA cm^{-2}), the additive improves the battery performance in terms of cell voltage and power dnesity, while for high current densities (e.g. 10 mA cm^{-2}) the enhancement of the specific energy is significant. Comparing to that in reference electrolyte (3.5% NaCl) at 10 mA cm^{-2}, the specific energy of Mg-air batteries employing AZ31, HP-Mg, and AM50 anodes in 2,6-DHB-containing electrolyte has increased by 8% (reaching 1640 Wh kg^{-1}), 15.6% (2013 Wh kg^{-1}), and 50.5% (1850 Wh kg^{-1}), respectively. The highest specific energy is achieved in Mg-0.15Ca based Mg-air battery with 2,6-DHB electroylte, as 2027 Wh kg^{-1}.

Declaration of Competing Interest

The authors declare that they have no known competing financial interests or personal relationships that could have appeared to influence the work reported in this paper.

Acknowledgements

The authors would like to acknowledge Mr. Ulrich Burmester and Mr. Volker Heitmann for the technical support. L. Wang and M. Deng are grateful for the award of fellowship from China Scholarship Council (No. 201706370183 and No. 201606370031). Additionally, the authors acknowledge SeaMag project funded by ERA-NET cofund MarTERA.

References

[1] Q. Liu, Z. Pan, E. Wang, L. An, G. Sun, Aqueous metal-air batteries: Fundamentals and applications, Energy Storage Materials 27 (2020) 478–505.
[2] J. Pan, Y.Y. Xu, H. Yang, Z. Dong, H. Liu, B.Y. Xia, Advanced Architectures and Relatives of Air Electrodes in Zn-Air Batteries, Advanced Science 5 (2018) 1700691.
[3] Y. Sun, X. Liu, Y. Jiang, J. Li, J. Ding, W. Hu, C. Zhong, Recent advances and challenges in divalent and multivalent metal electrodes for metal–air batteries, Journal of Materials Chemistry A 7 (31) (2019) 18183–18208.
[4] L. Grande, E. Paillard, J. Hassoun, J.B. Park, Y.J. Lee, Y.K. Sun, S. Passerini, B. Scrosati, The lithium/air battery: still an emerging system or a practical reality? Advanced Materials 27 (2015) 784–800.
[5] M.a. Jingling, W. Jiuba, Z. Hongxi, L.i. Quanan, Electrochemical performances of Al–0.5Mg–0.1Sn–0.02In alloy in different solutions for Al–air battery, Journal of Power Sources 293 (2015) 592–598.
[6] T. Zhang, Z. Tao, J. Chen, Magnesium–air batteries: from principle to application, Materials Horizons 1 (2) (2014) 196–206.
[7] Y. Li, J. Lu, Metal-Air Batteries: Will They Be the Future Electrochemical Energy Storage Device of Choice? ACS Energy Letters 2 (2017) 1370–1377.
[8] N. Wang, W. Li, Y. Huang, G. Wu, M. Hu, G. Li, Z. Shi, Wrought Mg-Al-Pb-RE alloy strips as the anodes for Mg-air batteries, Journal of Power Sources 436 (2019), 226855.
[9] X. Chen, Q. Zou, Q. Le, J. Hou, R. Guo, H. Wang, C. Hu, L. Bao, T. Wang, D. Zhao, F. Yu, A. Atrens, The quasicrystal of Mg–Zn–Y on discharge and electrochemical behaviors as the anode for Mg-air battery, Journal of Power Sources 451 (2020), 227807.
[10] X. Liu, J. Xue, P. Zhang, Z. Wang, Effects of the combinative Ca, Sm and La additions on the electrochemical behaviors and discharge performance of the as-extruded AZ91 anodes for Mg-air batteries, Journal of Power Sources 414 (2019) 174–182.
[11] J. Yu, B.-Q. Li, C.-X. Zhao, Q. Zhang, Seawater electrolyte-based metal–air batteries: from strategies to applications, Energy & Environmental Science 13 (10) (2020) 3253–3268.
[12] N. Wang, R. Wang, Y. Feng, W. Xiong, J. Zhang, M. Deng, Discharge and corrosion behaviour of Mg-Li-Al-Ce-Y-Zn alloy as the anode for Mg-air battery, Corrosion Science 112 (2016) 13–24.
[13] M. Deng, D. Höche, D. Snihirova, L. Wang, B. Vaghefinazari, S.V. Lamaka, M. L. Zheludkevich, Aqueous Mg Batteries, Magnesium Batteries (2019) 275–308.
[14] M. Deng, L. Wang, D. Höche, S.V. Lamaka, P. Jiang, D. Snihirova, N. Scharnagl, M. L. Zheludkevich, Ca/In micro alloying as a novel strategy to simultaneously enhance power and energy density of primary Mg-air batteries from anode aspect, Journal of Power Sources 472 (2020), 228528.
[15] D. Höche, S.V. Lamaka, B. Vaghefinazari, T. Braun, R.P. Petrauskas, M. Fichtner, M.L. Zheludkevich, Performance boost for primary magnesium cells using iron complexing agents as electrolyte additives, Scientific Reports 8 (2018) 7578.
[16] X. Zhao, L. Wang, X. Chen, W. Wang, H.L. Xin, X. Du, J. Yang, Ultrafine SmMn2O5-δ electrocatalysts with modest oxygen deficiency for highly-efficient pH-neutral magnesium-air batteries, Journal of Power Sources 449 (2020), 227482.
[17] C. Shu, E. Wang, L. Jiang, G. Sun, High performance cathode based on carbon fiber felt for magnesium-air fuel cells, International Journal of Hydrogen Energy 38 (14) (2013) 5885–5893.
[18] B. Vaghefinazari, D. Höche, S.V. Lamaka, D. Snihirova, M.L. Zheludkevich, Tailoring the Mg-air primary battery performance using strong complexing agents as electrolyte additives, Journal of Power Sources 453 (2020), 227880.
[19] M. Deng, L. Wang, D. Höche, S.V. Lamaka, D. Snihirova, P. Jiang, M. L. Zheludkevich, Corrosion and discharge properties of Ca/Ge micro-alloyed Mg anodes for primary aqueous Mg batteries, Corrosion Science 177 (2020), 108958.
[20] B. Xiao, G.-L. Song, D. Zheng, F. Cao, A corrosion resistant die-cast Mg-9Al-1Zn anode with superior discharge performance for Mg-air battery, Materials & Design 194 (2020), 108931.
[21] C. Cheng, S. Li, Y.i. Xia, L. Ma, C. Nie, C. Roth, A. Thomas, R. Haag, Atomic Fe-Nx Coupled Open-Mesoporous Carbon Nanofibers for Efficient and Bioadaptable Oxygen Electrode in Mg-Air Batteries, Advanced Materials 30 (40) (2018) 1802669, https://doi.org/10.1002/adma.v30.4010.1002/adma.201802669.
[22] X. Liu, S. Liu, J. Xue, Discharge performance of the magnesium anodes with different phase constitutions for Mg-air batteries, Journal of Power Sources 396 (2018) 667–674.
[23] L. Wang, R. Wang, Y. Feng, M. Deng, N. Wang, Effect of Al and Pb contents on the corrosion electrochemical properties and activation of Mg-Al-Pb alloy anode, Journal of the Electrochemical Society 164 (2) (2017) A438–A446.
[24] Y. Li, J. Ma, G. Wang, F. Ren, Y. Zhu, Y. Song, Investigation of sodium phosphate and sodium dodecylbenzenesulfonate as electrolyte additives for AZ91 magnesium-air battery, Journal of the Electrochemical Society 165 (9) (2018) A1713–A1717.
[25] M. Mayilvel Dinesh, K. Saminathan, M. Selvam, S.R. Srither, V. Rajendran, K.V.I. S. Kaler, Water soluble graphene as electrolyte additive in magnesium-air battery system, Journal of Power Sources 276 (2015) 32–38.
[26] Y. Zhao, G. Huang, C. Zhang, C. Peng, F. Pan, Effect of phosphate and vanadate as electrolyte additives on the performance of Mg-air batteries, Materials Chemistry and Physics 218 (2018) 256–261.
[27] J. Ma, G. Wang, Y. Li, W. Li, F. Ren, Influence of Sodium Silicate/Sodium Alginate Additives on Discharge Performance of Mg–Air Battery Based on AZ61 Alloy, Journal of Materials Engineering and Performance 27 (5) (2018) 2247–2254.
[28] Y.-C. Zhao, G.-S. Huang, G.-L. Gong, T.-Z. Han, D.-B. Xia, F.-S. Pan, Improving the Intermittent Discharge Performance of Mg–Air Battery by Using Oxyanion Corrosion Inhibitor as Electrolyte Additive, Acta Metallurgica Sinica (English Letters) 29 (11) (2016) 1019–1024.
[29] M.A. Deyab, Decyl glucoside as a corrosion inhibitor for magnesium–air battery, Journal of Power Sources 325 (2016) 98–103.
[30] D. Snihirova, L. Wang, S.V. Lamaka, C. Wang, M. Deng, B. Vaghefinazari, D. Hoche, M.L. Zheludkevich, Synergistic Mixture of Electrolyte Additives: A Route to a High-Efficiency Mg-Air Battery, Journal of Physical Chemistry Letters (2020) 8790–8798.
[31] L. Wang, D. Snihirova, M. Deng, B. Vaghefinazari, S.V. Lamaka, D. Höche, M. L. Zheludkevich, Tailoring electrolyte additives for controlled Mg-Ca anode activity in aqueous Mg-air batteries, Journal of Power Sources 460 (2020), 228106.
[32] F.W. Richey, B.D. McCloskey, A.C. Luntz, Mg anode corrosion in aqueous electrolytes and implications for Mg-Air batteries, Journal of the Electrochemical Society 163 (6) (2016) A958–A963.
[33] L. Wang, D. Snihirova, M. Deng, C. Wang, D. Höche, S.V. Lamaka, M. L. Zheludkevich, Indium chloride as an electrolyte additive for primary aqueous Mg batteries, Electrochimica Acta 373 (2021), 137916.
[34] M. Deng, L. Wang, D. Höche, S.V. Lamaka, C. Wang, D. Snihirova, Y. Jin, Y. Zhang, M.L. Zheludkevich, Approaching "stainless magnesium" by Ca micro-alloying, Materials Horizons 8 (2) (2021) 589–596.
[35] M. Deng, L. Wang, D. Höche, S.V. Lamaka, D. Snihirova, B. Vaghefinazari, M. L. Zheludkevich, Clarifying the decisive factors for utilization efficiency of Mg anodes for primary aqueous batteries, Journal of Power Sources 441 (2019), 227201.
[36] M.S. Aksoy, U. Özer, Potentiometric and spectroscopic studies with chromium (III) complexes of hydroxysalicylic acid derivatives in aqueous solution, Turkish Journal of Chemistry 27 (2003) 667–674.
[37] T. Kiss, K. Atkári, M. Jezowska-bojczuk, P. Decock, COMPLEXES OF Al(III) WITH HYDROXYAROMATIC LIGANDS, Journal of Coordination Chemistry 29 (1-2) (1993) 81–96.
[38] T. Kiss, H. Kozlowski, G. Micera, L.S. Erre, Cupric ion binding by dihydroxybenzoic acids, Polyhedron 8 (5) (1989) 647–651.
[39] C. Gerard, R. Njomgang, J.-C. Pierrard, J. Rimbault, R. Hugel, Modelling of the interactions of metal cations with soil organic matter. II: Thermodynamic stability of iron (III) and manganese (II) complexes with three dihydroxybenzoic acids, Journal of chemical research. Synopses (Print) (1987) 294–295.
[40] L.H.J. Lajunen, A. Kostama, M. Karvo, G. Olofsson, V.B. Sokolov, V.P. Spiridonov, T.G. Strand, THE COMPLEX EQUILIBRIA BETWEEN BE2+ IONS AND 4-OR 6-HYDROXYSALICYLIC ACID IN 0.5 M NACLO4 MEDIUM, Acta Chemica Scandinavica 33a (1979) 681–685.
[41] L. Lajunen, R. Portanova, J. Piispanen, M. Tolazzi, Critical evaluation of stability constants for alpha-hydroxycarboxylic acid complexes with protons and metal ions and the accompanying enthalpy changesPart I: Aromatic ortho-hydroxycarboxylic acids (Technical Report), Pure and Applied Chemistry 69 (1997) 329–382.
[42] A.E. Martell, R.M. Smith, Critical Stability Constants 5, Springer, First Supplement, 1982.
[43] D. Linden, T.B. Reddy, Handbook of Batteries, McGraw-Hill, New York, 2002.

[44] C. Daniel, J.O. Besenhard, Handbook of battery materials, John Wiley & Sons, 2012.
[45] M. Deng, D. Höche, S.V. Lamaka, D. Snihirova, M.L. Zheludkevich, Mg-Ca binary alloys as anodes for primary Mg-air batteries, Journal of Power Sources 396 (2018) 109–118.
[46] S. Fajardo, C.F. Glover, G. Williams, G.S. Frankel, The Source of Anodic Hydrogen Evolution on Ultra High Purity Magnesium, Electrochimica Acta 212 (2016) 510–521.
[47] J. Huang, G.-L. Song, A. Atrens, M. Dargusch, What activates the Mg surface—A comparison of Mg dissolution mechanisms, Journal of Materials Science & Technology 57 (2020) 204–220.
[48] T. Würger, C. Feiler, G.B. Vonbun-Feldbauer, M.L. Zheludkevich, R.H. Meißner, A first-principles analysis of the charge transfer in magnesium corrosion, Scientific Reports 10 (1) (2020), https://doi.org/10.1038/s41598-020-71694-4.
[49] M. Esmaily, J.E. Svensson, S. Fajardo, N. Birbilis, G.S. Frankel, S. Virtanen, R. Arrabal, S. Thomas, L.G. Johansson, Fundamentals and advances in magnesium alloy corrosion, Progress in Materials Science 89 (2017) 92–193.
[50] G.L. Song, A. Atrens, Corrosion mechanisms of magnesium alloys, Advanced engineering materials 1 (1) (1999) 11–33.
[51] D. Höche, C. Blawert, S.V. Lamaka, N. Scharnagl, C. Mendis, M.L. Zheludkevich, The effect of iron re-deposition on the corrosion of impurity-containing magnesium, Physical Chemistry Chemical Physics 18 (2) (2016) 1279–1291.
[52] S.H. Salleh, S. Thomas, J.A. Yuwono, K. Venkatesan, N. Birbilis, Enhanced hydrogen evolution on Mg (OH)2 covered Mg surfaces, Electrochimica Acta 161 (2015) 144–152.
[53] J. Chen, J. Dong, J. Wang, E. Han, W. Ke, Effect of magnesium hydride on the corrosion behavior of an AZ91 magnesium alloy in sodium chloride solution, Corrosion Science 50 (12) (2008) 3610–3614.
[54] G.-L. Song, K.A. Unocic, The anodic surface film and hydrogen evolution on Mg, Corrosion Science 98 (2015) 758–765.
[55] Z. Shi, F. Cao, G.-L. Song, A. Atrens, Low apparent valence of Mg during corrosion, Corrosion Science 88 (2014) 434–443.
[56] J. Li, K. Wan, Q. Jiang, H. Sun, Y. Li, B. Hou, L. Zhu, M. Liu, Corrosion and Discharge Behaviors of Mg-Al-Zn and Mg-Al-Zn-In Alloys as Anode Materials, Metals 6 (2016) 65.
[57] M. Yuasa, X. Huang, K. Suzuki, M. Mabuchi, Y. Chino, Discharge properties of Mg–Al–Mn–Ca and Mg–Al–Mn alloys as anode materials for primary magnesium–air batteries, Journal of Power Sources 297 (2015) 449–456.
[58] Y. Ma, N. Li, D. Li, M. Zhang, X. Huang, Performance of Mg–14Li–1Al–0.1Ce as anode for Mg-air battery, Journal of Power Sources 196 (4) (2011) 2346–2350.
[59] N. Wang, R. Wang, C. Peng, B. Peng, Y. Feng, C. Hu, Discharge behaviour of Mg-Al-Pb and Mg-Al-Pb-In alloys as anodes for Mg-air battery, Electrochimica Acta 149 (2014) 193–205.
[60] X. Li, H. Lu, S. Yuan, J. Bai, J. Wang, Y. Cao, Q. Hong, Performance of Mg–9Al–1In alloy as anodes for Mg-air batteries in 3.5 wt% NaCl solutions, Journal of the Electrochemical Society 164 (13) (2017) A3131–A3137.
[61] H. Wen, Z. Liu, J. Qiao, R. Chen, R. Zhao, J. Wu, G. Qiao, J. Yang, High energy efficiency and high power density aluminum-air flow battery, International Journal of Energy Research 44 (9) (2020) 7568–7579.
[62] L. Zhang, J. Park, K. Jang, S. Seo, J. Park, W. Kwon, D. Kim, S. Defilla, W. Chu, A study on the electrolyte circulation effect of Mg-air battery, E3S Web of Conferences 233 (2021) 01043.
[63] J.H. Nordlien, K. NişancioGu, S. Ono, N. Masuko, Morphology and structure of oxide films formed on MgAl alloys by exposure to air and water, Journal of the Electrochemical Society 143 (1996) 2564.
[64] L. Wang, T. Shinohara, B.-P. Zhang, XPS study of the surface chemistry on AZ31 and AZ91 magnesium alloys in dilute NaCl solution, Applied Surface Science 256 (20) (2010) 5807–5812.
[65] K.A. Unocic, H.H. Elsentriecy, M.P. Brady, H.M. Meyer, G.L. Song, M. Fayek, R. A. Meisner, B. Davis, Transmission electron microscopy study of aqueous film formation and evolution on magnesium alloys, Journal of the Electrochemical Society 161 (6) (2014) C302–C311.
[66] P. Jiang, C. Blawert, R. Hou, N. Scharnagl, J. Bohlen, M.L. Zheludkevich, Microstructural influence on corrosion behavior of MgZnGe alloy in NaCl solution, Journal of Alloys and Compounds 783 (2019) 179–192.
[67] P. Jiang, C. Blawert, N. Scharnagl, J. Bohlen, M.L. Zheludkevich, Mechanistic understanding of the corrosion behavior of Mg4Zn0.2Sn alloys: From the perspective view of microstructure, Corrosion Science 174 (2020), 108863.

5.5 Indium chloride as an electrolyte additive for primary aqueous Mg batteries

Paper 5 is published in Electrochimica Acta, 373 (2021), 137916.

Indium has been widely studied as an alloying element for Al anodes and Mg anodes [52-55]. Newly developed Mg-Ca-In anode exhibits not only superior discharge voltage but also excellent anodic efficiency [19]. Nevertheless, the possibility of using $InCl_3$ as an electrolyte additive for aqueous Mg batteries and the working mechanism has not been systematically investigated. Hence, $InCl_3$ as an electrolyte additive for primary aqueous Mg batteries was evaluated in this work in terms of its effect on discharge potential, self-discharge rate and UE of a newly developed Mg-0.15Ca anode. The addition of In^{3+} is capable of retarding electrolyte alkalization during discharge due to its hydrolysis reactions, which leads to better discharge activity and less film-relevant potential drop. Local measurement reveals that 1 mM $InCl_3$ addition only shows pH buffering effect for the bulk environment. Thus, 1 mM $InCl_3$ addition imparts less improvement for discharge activity of Mg-0.15Ca anode than 10 mM $InCl_3$ addition, but the addition of 1 mM $InCl_3$ significantly reduces the self-discharge rate of Mg-0.15Ca under anodic polarization and thus improves the anodic UE. Moreover, the addition of $InCl_3$ homogenizes the anode dissolution, reducing anodic UE loss caused by chunk effect. Therefore, cell voltage and specific energy of AMAB are enhanced by the addition of $InCl_3$.

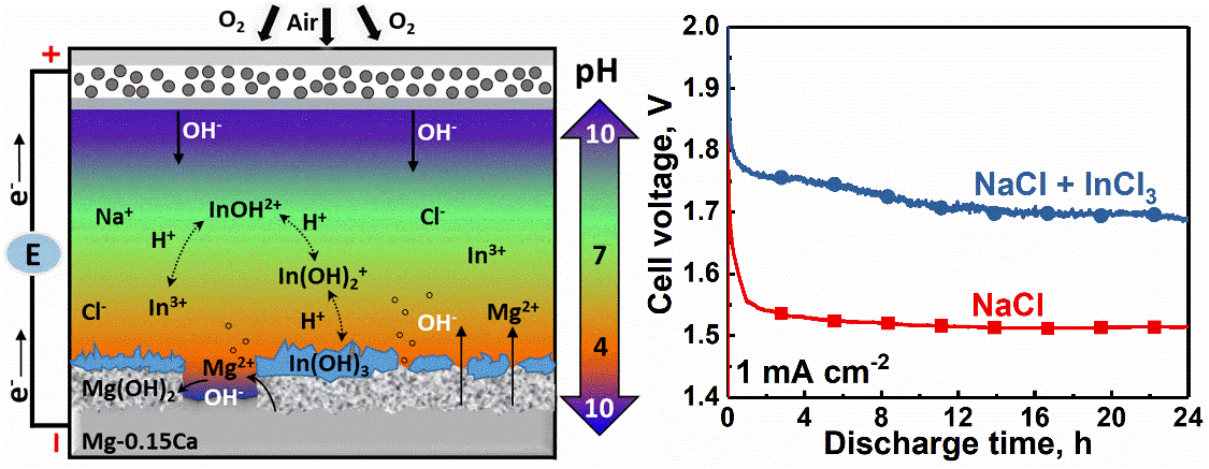

Fig. 5-6. Graphical abstract for **Section 5.5**.

Electrochimica Acta 373 (2021) 137916

Contents lists available at ScienceDirect

Electrochimica Acta

journal homepage: www.elsevier.com/locate/electacta

Indium chloride as an electrolyte additive for primary aqueous Mg batteries

Linqian Wang[a,*], Darya Snihirova[a], Min Deng[a], Cheng Wang[a], Daniel Höche[a], Sviatlana V. Lamaka[a], Mikhail L. Zheludkevich[a,b]

[a] Institute of Surface Science, Helmholtz-Zentrum Geesthacht (HZG), Max-Planck-Str. 1, 21502, Postal address: Helmholtz, Geesthacht 21502, Germany
[b] Institute of Materials Science, Faculty of Engineering, Kiel University, Kiel 24143, Germany

ARTICLE INFO

Article history:
Received 21 December 2020
Revised 18 January 2021
Accepted 1 February 2021
Available online 5 February 2021

Keywords:
Primary aqueous Mg batteries
Electrolyte additive
Local pH measurement
Self-corrosion

ABSTRACT

Indium chloride ($InCl_3$) as an electrolyte additive for primary aqueous Mg batteries is evaluated in this work in terms of its effect on discharge potential, self-corrosion rate and utilization efficiency of a newly developed Mg-0.15Ca anode. $InCl_3$ addition to aqueous electrolyte leads to a more negative discharge potential but the enhancement weakens along with the consumption of In^{3+} to form $In(OH)_3$ precipitates during the discharge process. Utilization efficiency of the anode is increased by adding $InCl_3$ due to uniform anodic dissolution and suppressed self-corrosion with reduced chunk effect. Mg-air battery test results indicate that 10 mM $InCl_3$ as electrolyte additive significantly enhances the cell voltage of aqueous Mg-air battery to 1.74 V and the specific energy based on anode weight loss to 2.26 kWh/ kg at 1 mA cm^{-2}.

1. Introduction

Metallic Mg possesses attractive electrochemical characteristics as an electrode material for energy storage, like the acknowledged highly negative redox potential (– 2.37 V_{SHE}) and high volumetric capacity (3832 mA h cm^{-3}) [1-3]. Owing to the huge potential as power sources for marine equipment and as standby emergency energy suppliers for schools, hospitals, etc., aqueous Mg batteries have been the subjects of intense research in recent years [4-14]. Meanwhile, some new applications of aqueous Mg batteries have been proposed and evaluated lately, such as acting as the power supply for transient implantable devices [15], electronic contact lenses [16] and urine purifying [17]. The practical performance of aqueous Mg batteries still leaves much to be desired due to two major issues, i.e. large overvoltage caused by sluggish anodic and cathodic reaction kinetics and fast self-corrosion of Mg anodes in aqueous electrolytes. In this context, many approaches from diverse aspects aiming of performance boost regarding Mg-based batteries have been proposed, including anodes design [4-6, 18-20], electrolyte modification [21-27] and cathode catalysts optimization [28-30]. Among these approaches, electrolyte modification has attracted much attention in recent years. Some improvements have been achieved by electrolytes modification in terms of introducing diverse chemical reagents into the electrolytes. Generally, the conventional electrolyte additives for aqueous Mg batteries are required with capability of inhibiting the corrosion of Mg to enhance the anodic utilization efficiency and, thus, the capacity and energy density of the battery. As reported by Deyab [24], the adoption of 2.5 mM decyl glucoside, which is a kind of corrosion inhibitor of Mg, improved the utilization efficiency of pure Mg in concentrated NaCl electrolyte, from 36.9% to 86.2% at 5 mA cm^{-2}. Ma and co-workers found the addition of sodium phosphate and sodium dodecylbenzenesulfonate enhances the anodic efficiency of AZ91 anode in 3.5 wt.% NaCl solution from 44.1% to 48.7% with ~1.1 V discharge voltage at 20 mA cm^{-2} current density [31]. Both decyl glucoside and sodium dodecylbenzenesulfonate are surfactant, which are capable of adsorbing on Mg anode to act as inhibitors. Thus, the utilization efficiency of Mg anode can be improved. Lately, Höche and co-workers [22] proposed a novel idea for selecting electrolyte additives for aqueous Mg batteries, which mainly focuses on Fe^{2+}/Fe^{3+} complexing agents that are able to prevent the re-deposition of Fe, which is typical corrosion inducing impurity in Mg. The self-corrosion rate of Mg anode was reduced due to the retardation of Fe re-deposition [32-34]. Meanwhile, battery voltage is improved since the selected chemical agents are capable of forming complexes with Mg^{2+} and, thus, the film-relevant overvoltage is reduced. Vaghefinazari et al. [26] and Wang et al. [27] both reported great enhancement of battery voltage for aqueous Mg-air system with commercially pure Mg and Mg-Ca anodes

* Corresponding author.
E-mail address: Linqian.Wang@hzg.de (L. Wang).

https://doi.org/10.1016/j.electacta.2021.137916
0013-4686/

by Mg^{2+} complexing agents, e.g. Tiron, NTA, 5-sulfosalicylate and 3,4-dihydroxybenzoate. For instance, the voltage of Mg-air battery was 1.86 V in 5-sulfosalicylate-containing electrolyte in comparison to 1.59 V in blank NaCl solution at 0.5 mA cm^{-2} current density [27]. Nevertheless, some of them may also introduce the loss of anodic utilization efficiency under specific current density. The addition of 3,4-dihydroxybenzoate into 3.5 wt.% NaCl electrolyte at 1 mA cm^{-2} current density tremendously decreases the utilization efficiency of Mg-0.04 wt.% Ca anode from 53% to 9%, but it increases the utilization efficiency of the same anode from 59.7% to 62.3% under 10 mA cm^{-2} current density. Thus, these issues could be solved by parameter optimization (additive concentration and initial pH) and battery design. Nevertheless, searching for new high-quality additives based on different working mechanism still requires more efforts [35].

Indium (In) alloying is a successful way for activating Al-based aqueous batteries because In^{3+} can re-deposit onto Al anode surface [36-39]. The influence of In as an alloying element on the discharge performance of Mg anodes (particularly Mg-Al-based) has thereby been investigated in recent years [19, 40-43], demonstrating a degree of enhancements on discharge voltage but rare improvements regarding the anode utilization efficiency. Newly developed Mg-Ca-In anode exhibits not only superior discharge voltage but also excellent anodic efficiency, 80.2% [44]. The activation of Mg anodes induced by In alloying was proposed to be resulted from In^{3+} re-deposition on the anode surface by the following replacement reaction [41].

$$3Mg + 2In^{3+} = 3Mg^{2+} + 2In \quad (1)$$

The In^{3+} ions produced by Mg-In alloy dissolution re-deposited back to the anode surface, leading to a less-protective surface film and faster dissolution of anode substrate due to formation of micro-galvanic corrosion couples. This research sparked the idea in our group that the existence of In^{3+} ions in the electrolyte could be the key point for the improvement of anode discharge performance. Recently, Gore et al. [45] investigated the anodic activation of a high purity Mg in diluted NaCl solution (0.1 M) with the presence of In^{3+}. As reported, 1 mM $InCl_3$ addition accelerated anodic dissolution but did not change the cathodic kinetics of Mg under polarization. Hence, the authors recommended that $InCl_3$ is a potential additive to develop aqueous Mg batteries with high performance. In that work, more emphasis was put on the effect of $InCl_3$ on the anodic and cathodic kinetics of Mg by performing potentiodynamic polarization tests and few discharge tests have been done to evaluate the improvement of Mg battery introduced by $InCl_3$ addition. Moreover, the working mechanism of $InCl_3$ as cathodic reaction inhibitor via the formation of $In(OH)_3$ has been proposed.

In this work, we thoroughly evaluate the possibility of using $InCl_3$ as an electrolyte additive for aqueous Mg batteries. The anode material adopted herein is a newly developed binary Mg-0.15Ca alloy with high performance previously proposed by our group [4, 8, 46]. The effect of $InCl_3$ on discharge potential, self-corrosion rate and utilization efficiency of Mg-0.15Ca anode in 3.5 wt.% NaCl solution is investigated. The working mechanism of $InCl_3$ as electrolyte additives is thoroughly discussed. Accordingly, the concentration of $InCl_3$ is optimized and then the Mg-air battery performance is evaluated in the electrolyte with optimum concentration of $InCl_3$.

2. Experimental section

2.1. Materials and electrolyte

A binary Mg-0.15Ca (wt.%) alloy was produced by direct chill casting and used as the anode material. Pure Mg (99.96 wt.%) and pure Ca (99.9 wt.%) were melted under protection of Ar/SF_6 gas in a steel crucible at 760 °C. The melts were then poured into a 700 °C preheated steel mold coated with boron nitride. Immediately, the mold was then immersed into a flowing water bath with a descending speed of 15 cm min^{-1} for solidification. The actual composition of the prepared alloy is shown in Table 1. The contents of Fe, Ni and Cu impurities were controlled below the traditional accepted tolerance limits [47].

3.5 wt.% NaCl solution with unbuffered pH 5.6 ± 0.1 was used as the background electrolyte. $InCl_3$ as electrolyte additive was introduced into the background solution with concentration of 1, 5 and 10 mM. The $InCl_3$-containing electrolytes were unbuffered showing pH of 4.4 ± 0.1, 4.1 ± 0.1 and 3.9 ± 0.1 corresponding to 1, 5 and 10 mM, respectively. All the electrolytes were prepared by chemical reagents purchased from Sigma-Aldrich and deionized water.

2.2. Half-cell discharge test

Discharge testing in half-cell was carried out in a three-electrode cell composed of a KCl-saturated Ag/AgCl reference electrode, a Pt counter electrode and the Mg-0.15Ca working electrode with 15 × 15 mm exposed surface area. Discharge potential of the Mg-0.15Ca anode in the electrolyte with and without $InCl_3$ at a constant current density (1 mA cm^{-2}) was recorded by Gamry Interface 1000 potentiostat. After half-cell discharge testing, utilization efficiency and discharge capacity were calculated based on the mass loss of the anode amid the complete discharge period via the following equations,

$$\text{Utilization efficiency} = \frac{m_{dis}}{\Delta m} \times 100\% \quad (2)$$

$$m_{dis} = \frac{I \times t \times M}{F \times n} \quad (3)$$

$$\text{Specific capacity} = \frac{I \times t}{\Delta m} \quad (4)$$

Where m_{dis} and Δm represent the Faradaic mass loss of anode due to applied discharge current I and the actual mass loss respectively, t is the discharge time and F represents the Faraday constant (26.8 Ah mol^{-1}). M and n are the atomic mass and the ionic valence for Mg. In order to obtain accurate mass loss, anode samples after discharge were immersed into chromic acid aqueous solution (200 g l^{-1}) for 10 min to remove discharge products and then rinsed with ethanol. Afterwards, the anode mass loss was determined via comparing the sample mass prior to discharge and after removal of discharge products.

2.3. Electrochemical impedance spectroscopy (EIS)

EIS measurements at open circuit potential (OCP) after discharge for a specific period (1, 5 and 24 h) were also performed by Gamry Interface 1000 potentiostat to evaluate the surface condition alteration of the anode. The applied frequency ranged from 10^5–10^{-1} Hz, while a perturbation voltage of 10 mV rms was used.

2.4. Hydrogen evolution test under polarization

Effect of $InCl_3$ on the self-corrosion of Mg-0.15Ca anode during discharge was investigated by the real-time hydrogen evolution test under galvanostatic polarization. Evolved hydrogen gas from Mg-0.15 Ca sample under 1 mA cm^{-2} constant current density was collected with a common eudiometer-like set-up previously used in published work [9]. Briefly, the working electrode was also the Mg-0.15Ca sample with 15 × 15 mm exposed surface area. Volume of the produced H_2 was easily recorded from an inverted burette with minimum scale of 0.1 ml.

Table 1
Chemical composition of the produced Mg-0.15Ca alloy anode (wt.%).

	Ca	Fe	Ni	Cu	Si	Al	Zn	Mg
Mg-0.15Ca	0.15	0.0014	0.0002	0.0002	0.0056	0.0021	0.0020	Bal.

2.5. Surface analysis

The anode surface and cross-sectional morphologies after discharge were characterized by a scanning electron microscope (SEM, TESCAN VEGA 3). Elemental mapping was carried out for selected regions via SEM under backscattered-electron (BSE) mode at 15 kV. Additionally, the morphology anode surface after removal of discharge products was observed under secondary electron (SE) mode in SEM. 3D reconstruction for the surface topography without discharge products was conducted via SEM combined with Mex program (Bruker Alicona) for images processing. Depth profiles were obtained to examine the surface roughness and homogeneity.

2.6. Local pH measurement

The local pH of Mg-0.15Ca anode in 3.5 wt.% NaCl with and without $InCl_3$ under 1 mA cm^{-2} galvanostatic polarization was measured via a glass-type pH microelectrode with a tip diameter of 10 μm (pH-10, Unisense), which was calibrated daily. The pH microelectrode was fixed at 20 μm above the Mg-0.15Ca sample with approximately 1 mm diameter in order to record the real-time evolution of local pH during galvanostatic polarization. The applied current density was 1 mA cm^{-2} with the same configuration adopted in half-cell discharge test. The local information for Mg-0.15Ca sample surface was acquired on a sample-centered area (2000 μm $\times$ 2000 μm) at 50 μm above it to demonstrate the distribution of local pH on polarized Mg-0.15Ca surface. All the relevant data was acquired by LV4 software (Science Wares). A commercial SVET-SIET system (Applicable Electronics) is employed for the positioning and movement of the pH microelectrode.

2.7. Mg-air battery test

At last, the viability of $InCl_3$ as an electrolyte additive for aqueous Mg batteries was evaluated in a lab-made Mg-air cell. A commercially available air cathode with MnO_2/C catalyst (Gaskatel GmbH) was used as cathode. The working surface was square of 15 $\times$ 15 mm for the Mg-0.15Ca anode, while round with 18 mm diameter for the cathode. The anode-to-cathode distance was kept the same for all discharge tests. Discharge curves of the battery in electrolytes with and without $InCl_3$ additive were recorded by IVIUM OctoStat at constant current densities. Specific energy of Mg-air batteries were calculated according to the anode mass loss and the equation is expressed as,

$$\text{Specific energy} = \frac{\int_0^t I \times U \times \Delta t}{\Delta m} \quad (5)$$

Where I, t and Δm are the same meaning as above mentioned. U represents the cell voltage.

3. Results and discussion

3.1. Half-cell discharge performance

In order to evaluate the influence of various concentrations of $InCl_3$ on the discharge performance of the Mg-0.15Ca alloy, half-cell discharge tests were performed. Fig. 1a shows the discharge curves of the Mg-0.15Ca anode in NaCl electrolyte with and without $InCl_3$. In blank NaCl electrolyte, the discharge potential is relatively stable (– 1.61 $V_{Ag/AgCl}$) during the whole discharge period following a positive shift at the initial 0.5 h stage. By contrast, in the electrolyte with 1 mM and 5 mM $InCl_3$, a short-term move of the potential towards more negative value appears at the beginning, after which the potential starts to shift positively. Subsequently, the potential remains relatively stable after around 2 h and 14 h in the solution with 1 mM and 5 mM $InCl_3$, respectively, and the steady potential (– 1.63 $V_{Ag/AgCl}$) has no large difference with that in blank NaCl solution. Differently, the addition of 10 mM $InCl_3$ enables the anode to maintain a significantly more negative potential (– 1.76 $V_{Ag/AgCl}$) during the whole 24 h discharging process. The results indicate that addition of $InCl_3$ is able to improve the discharge potential of the Mg-0.15Ca anode, but the enhancement effect may weaken along with the continuous discharging. Higher concentration of $InCl_3$ not only imparts greater improvement on discharge potential but also slows down the weakening of the enhancement effect induced by $InCl_3$ additive. It is noteworthy that the bulk pH of blank NaCl solution increases from 5.6 $\pm$ 0.1 to 10.4 $\pm$ 0.1 amid 24 h discharge test whereas the final bulk pH of $InCl_3$-containing electrolytes remains below 5. This suggests that $InCl_3$ has strong pH buffering effect for the electrolyte alkalization amid discharge. Nevertheless, Mg-0.15Ca anode in $InCl_3$-containing electrolytes with similar final pH presented distinct discharge behavior, which will be discussed in the following section. Fig. 1b illustrates the utilization efficiency of the Mg-0.15Ca anode as well as the capacity after discharge at 1 mA cm^{-2} for 24 h in NaCl electrolyte with and without $InCl_3$. Addition of 1 and 5 mM $InCl_3$ increases the utilization efficiency and capacity of the Mg-0.15Ca anode, while addition of 10 mM $InCl_3$ does not impart any negative effect on the utilization efficiency. Nevertheless, Mg-0.15Ca in NaCl with 10 mM $InCl_3$ presents the most negative potential. Thus, the best comprehensive discharge performance of Mg-0.15Ca anode is achieved by addition of 10 mM $InCl_3$.

3.2. Evolution of anode surface state in $InCl_3$-containing electrolytes

The change of discharge potential often correlates to the alteration of surface state of the anode. Thus, EIS measurements were performed on the anode after different discharge periods to check the alteration of the anode surface condition by the discharge, as presented in Fig. 2. Obviously, with increasing discharge time the low frequency impedance of the anode in blank NaCl solution decreases (Fig. 2a). Seemingly, the lower impedance may imply that the thin surface film at the interface becomes less protective with increasing discharge time. Additionally, the increase of actual surface area due to anode dissolution also contributes to the lowering of impedance. Besides, an indication of the changes in actual surface area may serve the slight decrease in the discharge potential for NaCl at the end of the discharge test (shown in Fig. 1a). On the contrary, as illustrated in Fig. 2c, the impedance of the anode after discharge in solution with 5 mM $InCl_3$ shows an enhancing tendency with increasing discharge time. The increased impedance is most likely caused by the progressive formation of a surface film on the anode, which leads to positive shift of potential as shown in Fig. 1a. Nevertheless, the impedances of Mg-0.15Ca in NaCl solution with 5 mM $InCl_3$ are always lower than that in blank NaCl. Thus, the surface film formed in the electrolyte with 5 mM $InCl_3$ is less protective than that formed in blank NaCl and induces less surface film-relevant overvoltage, resulting in a more negative discharge potential especially in the initial 10 h.

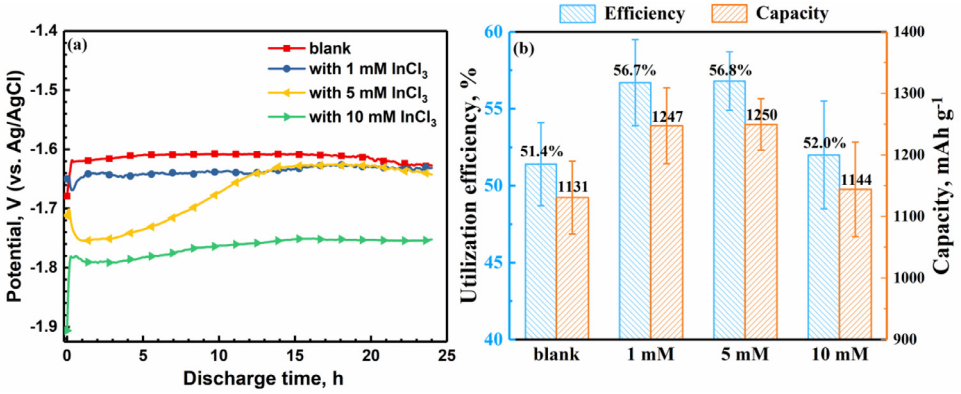

Fig. 1. Half-cell discharge performance of Mg-0.15Ca anode at 1 mA cm^{-2} in 3.5 wt.% NaCl with and without $InCl_3$: (a) discharge curves and (b) utilization efficiency and discharge capacity of Mg-0.15Ca.

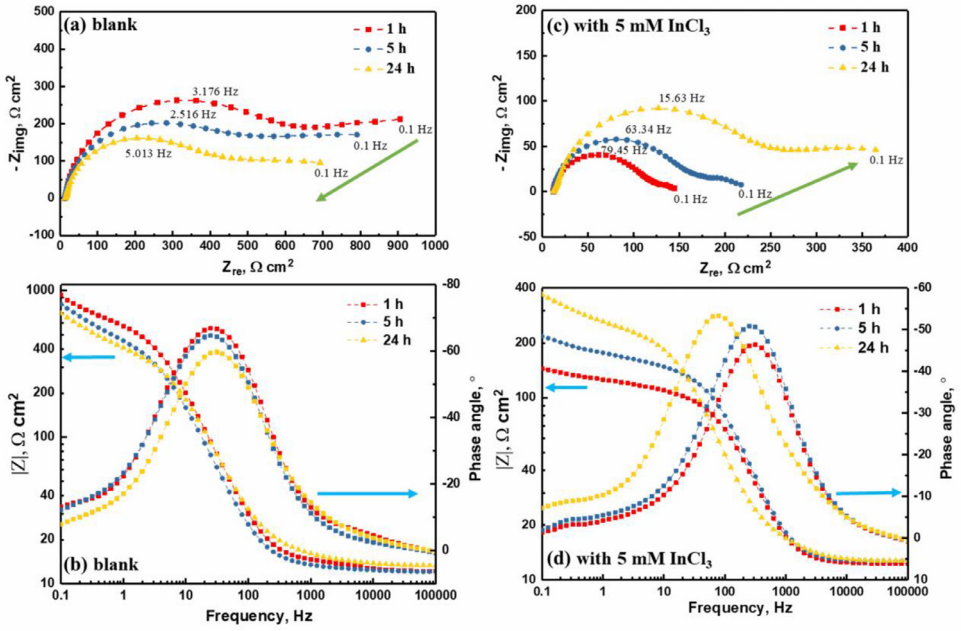

Fig. 2. EIS plots of Mg-0.15Ca anode measured after discharge at 1 mA cm^{-2} for different times in 3.5 wt.% NaCl solution (a) and (b) blank; (c) and (d) with 5 mM $InCl_3$. (For interpretation of the references to colour in this figure legend, the reader is referred to the web version of this article.)

The surface morphologies of the Mg-0.15Ca anode after discharge for varied periods in the solution with 5 mM $InCl_3$ additive are presented in Fig. 3. Fig. 3(a-c) indicate that the surface film formed after 24 h discharge is denser and more compact comparing to that after short time discharge, which is in agreement with the EIS data in Fig. 2c. The elemental mapping for the surface film formed after one-hour discharge (Fig. 3(d-g)) demonstrates some $In(OH)_3$ precipitates, occasionally found at the surface, while most of the surface is covered by $Mg(OH)_2$. Moreover, as illustrated by the elemental mapping depicted in Fig. 3(h-k), the coverage of $In(OH)_3$ on the anode surface after 5 h discharge increases. After 24 h discharge, the anode surface is almost fully covered by $In(OH)_3$ as shown in Fig. 3(l-o). The cross-sectional morphology and corresponding elemental mapping results exhibited in Fig. 3(p-s) shown that the In element enriches in the outmost layer, elucidating the film is composed of thin outer layer of mostly $In(OH)_3$ and thick inner layer of mainly $Mg(OH)_2$. The enhancement of impedance value amid the discharge process in the electrolyte with $InCl_3$ is contributed by the growth of this mixed surface film and consequently results in the positive shift of discharge potential.

The formation of the mixed surface film is attributed to the addition of $InCl_3$. As above mentioned, the initial pH of NaCl solution with 5 mM $InCl_3$ is 4.1 ± 0.1, which is more acidic than the non-buffered blank NaCl electrolyte with initial pH 5.6 ± 0.1. The pH decrease after $InCl_3$ addition is related to the hydrolysis of In^{3+} ions as indicated by the following reactions and the hydrolysis constant of In^{3+} are found in the literature [48],

$$In^{3+} + H_2O = InOH^{2+} + H^+; logK_1 = 10.0 \quad (6)$$

$$InOH^{2+} + H_2O = In(OH)_2^+ + H^+; \log K_2 = 10.18 \quad (7)$$

$$In(OH)_2^+ + H_2O = In(OH)_{3(s)} + H^+; \ \log K_3 = 9.42 \quad (8)$$

Moreover, the addition of $InCl_3$ is also capable to stabilize the pH of electrolyte even after 24 h discharge. The final pH of NaCl solution with 5 mM $InCl_3$ after 24 h discharging test is 4.3 ± 0.1. According to the thermodynamic equilibrium diagram shown in Fig. 4, stable $In(OH)_3$ precipitates form at pH above 4 in NaCl solution with 5 mM $InCl_3$, whereas stable $Mg(OH)_2$ precipitates from pH 10.3. The concentration of Mg^{2+} adopted for the thermodynamic calculation is deduced from the weight loss of Mg-0.15Ca

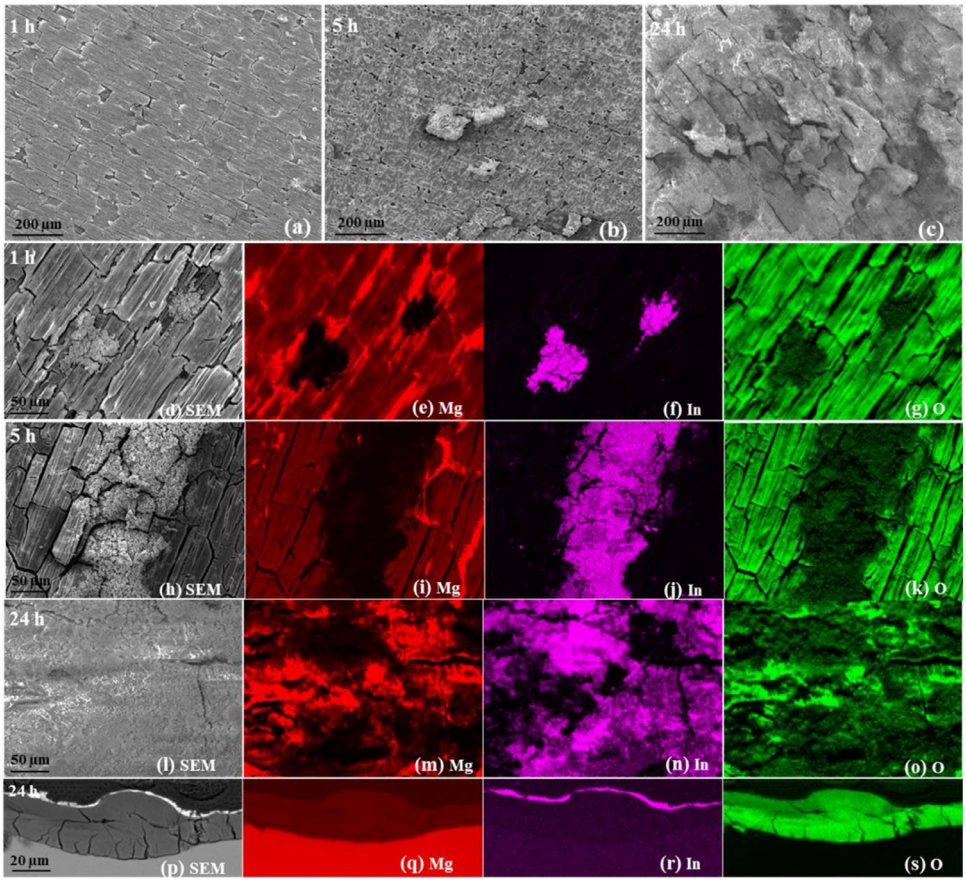

Fig. 3. Surface and cross-sectional morphologies of Mg-0.15Ca anode after discharge at 1 mA cm^{-2} in 3.5 wt.% NaCl solution with 5 mM $InCl_3$. Surface after (a)1 h; (b) 5 h; (c) 24 h. Elemental mapping for the surface after (d-g) 1 h; (h-k) 5 h; (l-o) 24 h. Cross section and corresponding elemental mapping after 24 h (p-s).

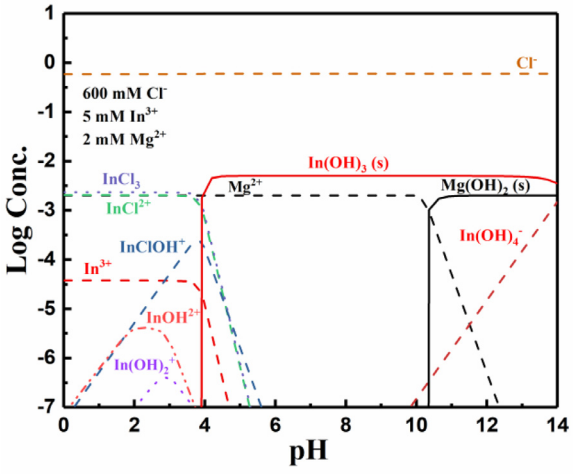

Fig. 4. Thermodynamic calculation of the equilibrium composition of relevant species in 3.5 wt.% NaCl solution with 5 mM In^{3+} and 2 mM Mg^{2+} via Hydra-Medusa program.

anode after 24 h discharge test in the electrolyte with 5 mM $InCl_3$. As above mentioned, the final pH of NaCl solution with 5 mM $InCl_3$ is 4.3, which seems to be too acidic for the formation of stable $Mg(OH)_2$ precipitation presented in Fig. 3. However, the final pH is referred to the final pH of bulk electrolyte, which is not representative for the local environment [35]. With the aim to clarify the influence of $InCl_3$ on the formation of discharge products film, the local pH on Mg-0.15Ca anode under galvanic polarization is measured and illustrated in Fig. 5.

As presented in Fig. 5a, the local pH on Mg-0.15Ca anode in blank NaCl solution increases immediately after discharge and stabilizes at around 10.3. The increase of pH in blank NaCl solution is due to the cathodic reaction,

$$2H_2O + 2e^- = H_2 + 2OH^- \quad (9)$$

In NaCl solution with 1 mM $InCl_3$, the local pH close to the electrode surface also increases rapidly within the initial 5 min from 4.3 to 9.7, which only shows marginal pH buffering effect of 1 mM $InCl_3$ comparing to that in blank NaCl. By contrast, 5 mM $InCl_3$ addition efficiently retards the increase of local pH in the region of 20 μm above Mg-0.15Ca anode, resulting in the pH stabilization at 4.6 even after 150 min discharge. Fig. 5b shows the gradients of pH on Mg-0.15Ca anode amid discharge, displaying the change of pH from 20 to 3000 μm above the anode surface. As presented in Fig. 5b, there is no significant difference between the local pH and bulk pH in the blank NaCl solution, both of which are alkaline. By comparison, the bulk pH of the $InCl_3$-containing electrolytes are both less than 5, which is consistent with the final bulk pH of $InCl_3$-containing electrolytes after 24 h half-cell discharge tests. However, the local pH in the electrolyte with different concentrations of $InCl_3$ is distinctly different. In this region of 20 μm above Mg-0.15Ca anode, the local pH in the electrolyte with 1 mM $InCl_3$ solution is 9.7 whilst that in 5 mM $InCl_3$-containing electrolyte, i.e. 4.6, is only slightly higher than bulk pH (4.4), indicating the addition of $InCl_3$ with different concentrations imparts remarkable impact on the local environment of Mg-0.15Ca anode during discharge. The local pH (9.7) in the electrolyte with 1 mM

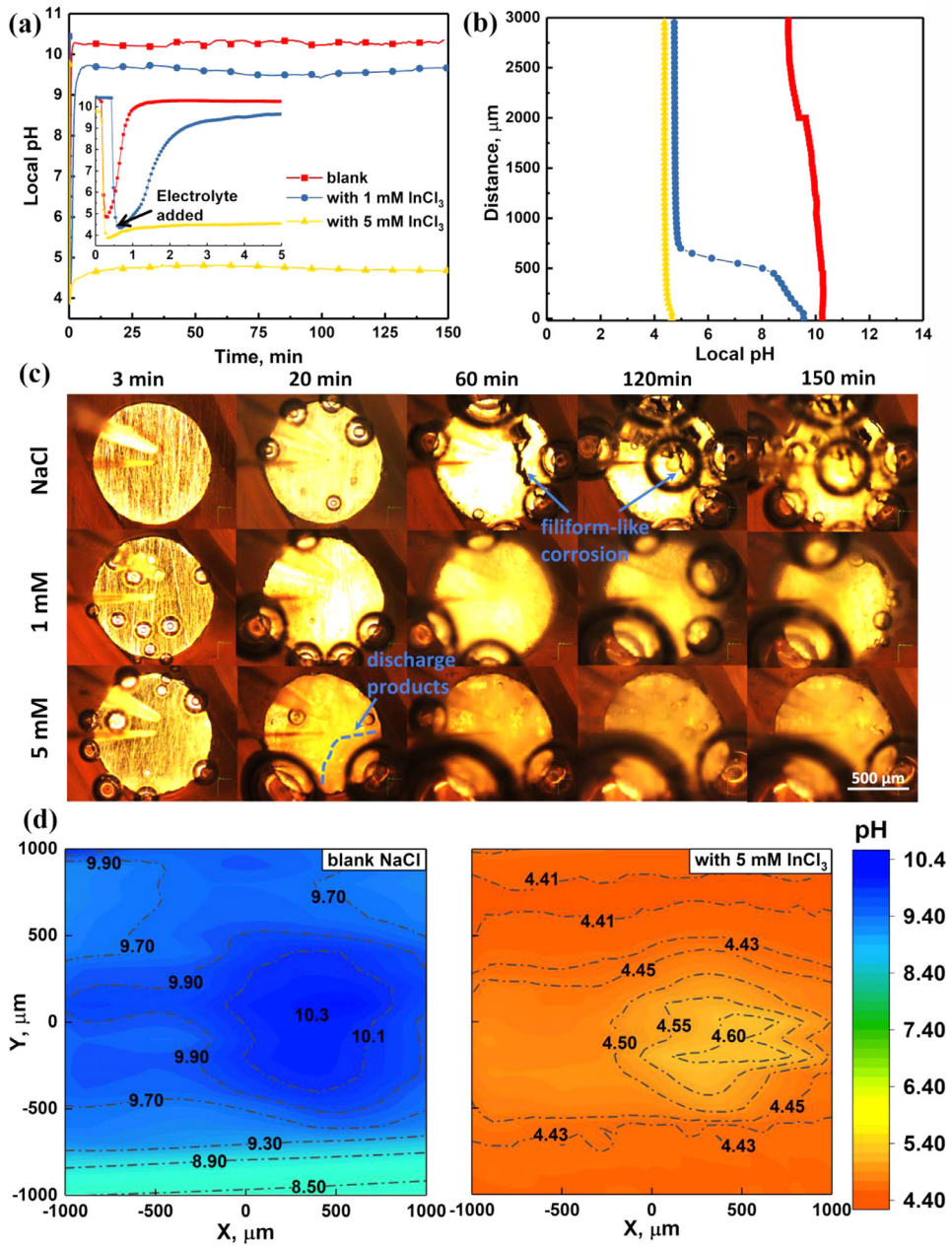

Fig. 5. (a) local pH above Mg-0.15Ca anode (20 μm); (b) vertical distribution of pH from Mg-0.15Ca anode surface to bulk environment; (c) the surface evolution of Mg-0.15Ca anode; and (d) horizontal distribution of local pH above Mg-0.15Ca anode (50 μm) at 1 mA cm^{-2} in blank NaCl and NaCl solution with 5 mM $InCl_3$.

$InCl_3$ solution is close to that in blank NaCl solution (10.3) and, thus, Mg-0.15Ca anode exhibits similar discharge behavior in these two electrolytes. In the electrolyte with 5 mM $InCl_3$, the concentration of In^{3+} decreases with the increase of discharge time via the hydrolysis reactions (Eq. (6-8)) and the precipitation reaction with OH^-generated by cathodic reaction. Thus, the discharge potential of Mg-0.15Ca in the electrolyte with 5 mM $InCl_3$ gradually shifts to a more positive value.

Fig. 5c exhibits the evolution of surface condition of Mg-0.15Ca anode during local pH measurements. After 20 min discharge, the products have already formed on the anode surface in the electrolyte with 5 mM $InCl_3$, whereas the discharge products in blank NaCl and 1 mM $InCl_3$-containing NaCl electrolyte cannot be visually observed. After 60 min discharge, filiform-like corrosion starts on the anode surface in blank NaCl solution. The surface of Mg-0.15Ca in the electrolyte with 5 mM $InCl_3$ is completely covered by fluffy discharge products. According to the local pH obtained from the region (4.6) and the equilibrium diagram presented in Fig. 4, these fluffy discharge products are most likely to be $In(OH)_3$, demonstrating that the local environment in this region is strongly influenced by the hydrolysis reaction of In^{3+}. Hence, the precipitation of stable $Mg(OH)_2$ is less pronounced in this region. As indicted in Fig. 3a, $Mg(OH)_2$ precipitation is the main component of the surface film on Mg-0.15Ca after 1 h discharge, revealing the growth of $Mg(OH)_2$ film is underneath the porous $In(OH)_3$ layer. Moreover, the structure of $Mg(OH)_2$ film shows less protectiveness due to the acidic environment introduced by the hydrolysis reaction of sufficient In^{3+}. Thus, the discharge potential of Mg-0.15Ca anode is improved by the addition $InCl_3$. Fig. 5d and 5e are presented to show the distribution of local pH above Mg-0.15Ca anode

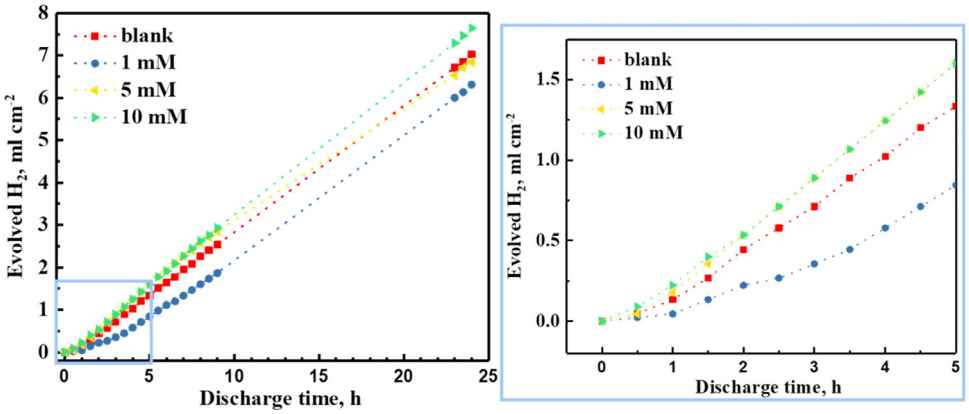

Fig. 6. Real-time hydrogen evolution of Mg-0.15Ca anode during discharge at 1 mA cm^{-2} in 3.5 wt.% NaCl solution with $InCl_3$ of different concentration.

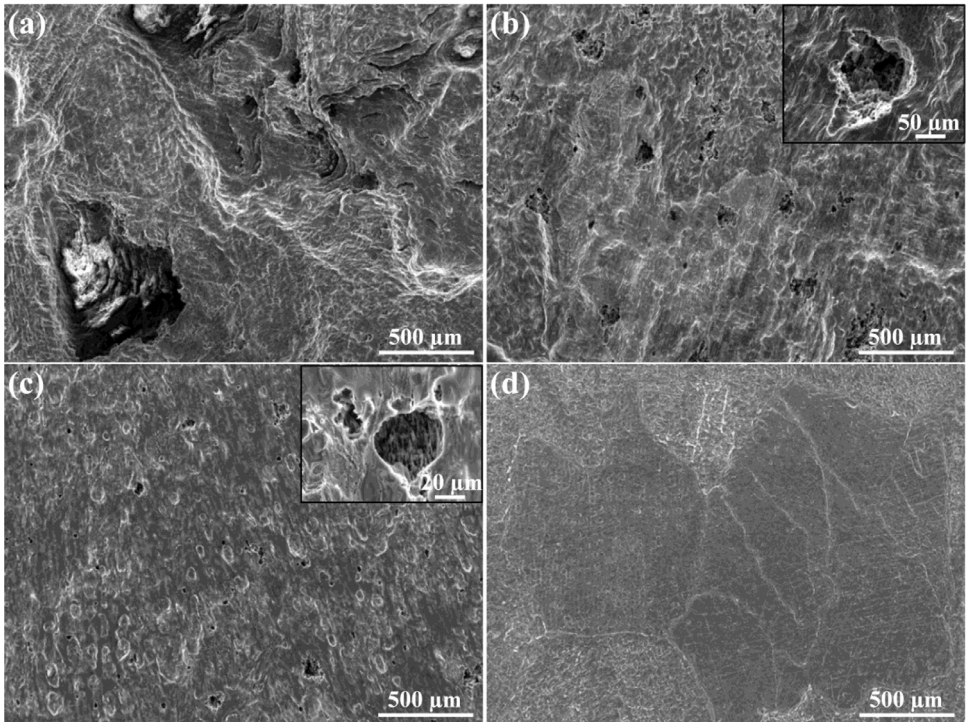

Fig. 7. Surface morphologies of Mg-0.15Ca anode after discharge at 1 mA cm^{-2} for 24 h and removal of discharge products in 3.5 wt.% NaCl solution with $InCl_3$: (a) blank; (b) 1 mM; (c) 5 mM; (d) 10 mM.

in order to exclude the influence of preferential localized corrosion, like the filiform-like corrosion happened in blank NaCl solution, on the results presented in Fig. 5a and 5b.

3.3. Self-corrosion and utilization efficiency

Fig. 6 presents the evolved hydrogen volume of Mg-0.15Ca anode during discharge at 1 mA cm^{-2} in the electrolyte with and without $InCl_3$. The real-time hydrogen evolution reflects the self-corrosion rate of anode amid discharge process. Apparently, the increment of $InCl_3$ concentration increases the self-corrosion of the Mg-0.15Ca anode. The addition of 1 mM $InCl_3$ suppresses the anode self-corrosion rate, while the addition of 10 mM $InCl_3$ results in a reverse effect. The overall self-corrosion rate within the 24 h discharge in the electrolyte with 5 mM $InCl_3$ additive is close to that in blank NaCl, in spite of one period with a higher self-corrosion rate at the beginning. It is remarkable that addition of low concentration (1 mM) of $InCl_3$ is able to decrease the self-corrosion rate of the Mg-0.15Ca anode, taking into consideration a common sense that lowering solution pH leads to higher corrosion rates of Mg-based materials at OCP condition [49-51]. Nevertheless, previous works have reported that the corrosion behavior of Mg at OCP condition might differ from the self-corrosion under polarization (or discharge) at varied current densities [9, 45], which is most probably because of the negative difference effect (NDE) [47] commonly found on Mg and Mg alloys. The inhibiting effect of 1 mM $InCl_3$ on the self-corrosion of Mg-0.15Ca under polarization is in agreement with that reported in the work of Gore et al.[45]., which did not show relevant results regarding the effect of higher $InCl_3$ concentration on Mg anode self-corrosion during discharge. In that work, the authors proposed that the deposition of $In(OH)_3/In_2O_3$ on Mg might be the reason for the unchanged cathodic kinetics of Mg as well as the inhibited self-corrosion during anodic polarization of Mg in 0.1 M NaCl solution with 1 mM $InCl_3$.

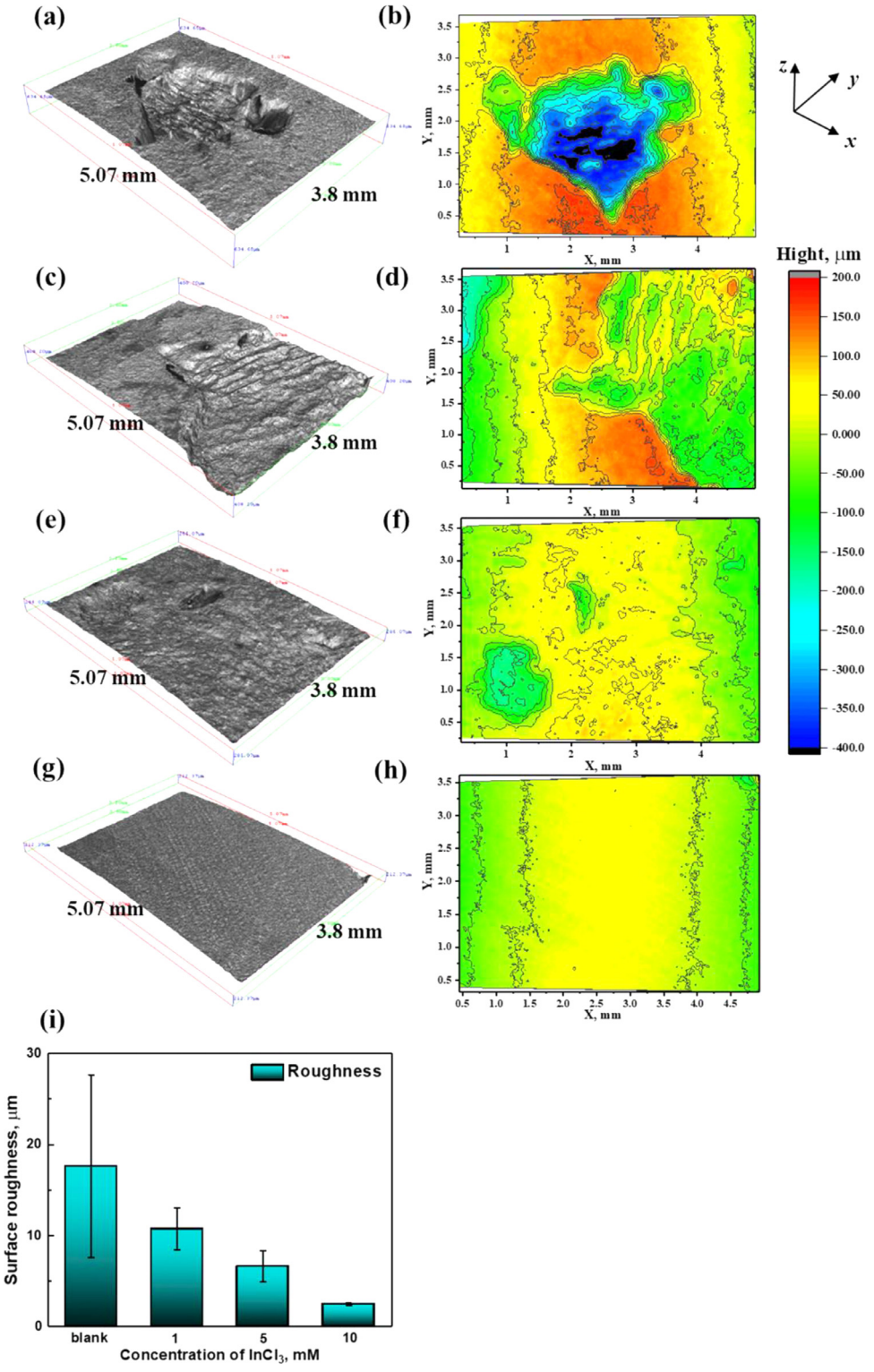

Fig. 8. 3D reconstruction and corresponding depth file for the Mg-0.15Ca anode topography without discharge products after discharge at 1 mA cm^{-2} for 24 h in 3.5 wt.% NaCl solution with $InCl_3$ of different concentration: (a, b) blank; (c, d) 1 mM; (e, f) 5 mM; (g, h) 10 mM; and (i) surface roughness of Mg-0.15Ca anode in 3.5 wt.% NaCl solution with $InCl_3$ of different concentration.

The provided results only show the existence of In species on Mg surface but the evolution of the $In(OH)_3/In_2O_3$ layer during anodic polarization and the interrelated inhibition effect of $In(OH)_3/In_2O_3$ has not been investigated yet.

According to the results obtained from local pH measurements, the addition of 1 mM $InCl_3$ is not capable to significantly change the local pH of Mg-0.15Ca anode under polarization in our work, which may not largely accelerate the dissolution of anode during discharge. The addition of 5 mM $InCl_3$ efficiently restricts the increase of local pH at the initial stage of discharge, which also accelerates the self-corrosion rate of Mg-0.15Ca anode at the beginning. After 24 h discharge, an uniform $In(OH)_3$ outer layer is formed on

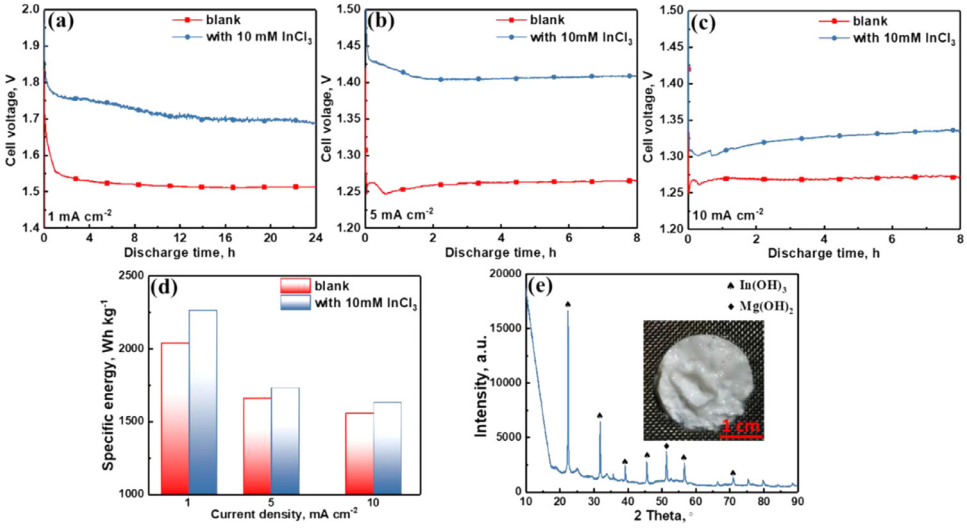

Fig. 9. Discharge curves of Mg-air battery with Mg-0.15Ca anode in 3.5 wt.% NaCl solution with and without 10 mM $InCl_3$ at (a) 1 mA cm^{-2}, (b) 5 mA cm^{-2}, and (c) 10 mA cm^{-2}; (d) specific energy and average cell voltage of Mg-air battery with Mg-0.15Ca anode in 3.5 wt.% NaCl solution with and without 10 mM $InCl_3$; (e) optical image and XRD diffraction pattern of the precipitation on air cathode after discharge.

Mg-0.15Ca anode in the electrolyte with 5 mM $InCl_3$ and, meanwhile, the self-corrosion rate slows down. It seems the growth of this $In(OH)_3$ layer may be the vital origin for the self-corrosion inhibition effect of $InCl_3$. However, the surface film formed in 5 mM $InCl_3$-containing electrolytes is always less protective than that formed in blank NaCl solution according to the EIS results. Moreover, there is no sign can be found in Fig. 2d that the $In(OH)_3$ layer leads to the formation of another time constant. Therefore, it is hard to directly attribute the self-corrosion inhibition effect of $InCl_3$ to the deposition of $In(OH)_3$. Further understanding of the origin of NDE effect for Mg and on the barrier / transport properties of the deposits is required to clarify the inhibition mechanism of $InCl_3$.

Interestingly, the change of utilization efficiency after adding $InCl_3$ (Fig. 1b) is not in accordance with the induced alteration on real time self-corrosion rate (Fig. 6). The Mg-0.15Ca anode in the solution with 5 mM $InCl_3$ shows a similar self-corrosion rate to that in blank NaCl solution, but possesses a higher utilization efficiency, 56.8% versus 51.4%. By contrast, adding 10 mM $InCl_3$ leads to an increased self-corrosion rate but does not render big difference to the utilization efficiency. This case must be related to the other form of self-corrosion, i.e. chunk effect, which is not fully included in the real-time hydrogen evolution. As demonstrated by Deng and co-workers [9], chunk effect, which refers to the detachment of secondary phases and undissolved matrix from anode substrate due to non-uniform dissolution, also causes large loss of anode utilization efficiency in some cases. Assuming hydrogen evolution is the dominating form of anode self-corrosion, the theoretical utilization efficiency can be calculated according to the real-time generation rate of hydrogen as displayed in Fig. 6 via the following equation.

$$\eta_{theo} = \frac{m_{dis}}{m_{dis} + m_H} \tag{10}$$

Where m_{dis} is the mass loss of anode due to applied discharge current, while m_H is the mass loss associated with cathodic hydrogen evolution reaction. Accordingly, the calculated theoretical efficiency is 60.6% in blank NaCl electrolyte and 61.2% in the electrolyte with 5 mM $InCl_3$. Thus, the contribution of chunk effect to the efficiency loss could be roughly estimated via comparing the actual and theoretical efficiency, indicating that of 9.2% and 4.4% for the blank solution and 5 mM $InCl_3$-containing solution, respectively. Anode efficiency loss because of chunk effect is reduced via $InCl_3$ addition.

Fig. 7 shows the surface morphology of the Mg-0.15Ca anode after discharge and removing discharge products. The anode surface after discharging in blank NaCl solution is uneven with large cavities (Fig. 7a). After 1 mM $InCl_3$ addition, the anode surface is relatively uniform, but shows some small holes (Fig. 7b). Such holes in smaller size are also found on the flat anode surface after discharging in the solution with 5 mM $InCl_3$ (Fig. 7c). By contrast, a generally flat and uniform surface without visible pits appears regarding 10 mM $InCl_3$ (Fig. 7d).

Fig. 8 displays the 3D reconstruction and corresponding depth profile for the anode topography after discharging after removal of discharge products. Obviously, flat anode surfaces with smaller roughness are obtained after using $InCl_3$ as an additive. Besides, the surface roughness decreases with the increment of $InCl_3$ concentration as shown in Fig. 8i. The results elucidate that $InCl_3$, as an additive, possesses the capability of homogenizing the dissolution of the Mg-0.15Ca anode, thus contributing to reduced chunk effect. With 10 mM $InCl_3$, the acceleration on hydrogen evolution during discharge is compensated by reduction of chunk effect, leading to similar utilization efficiency and capacity to those in blank electrolyte.

3.4. Mg-air battery testing

In the half-cell discharge testing, the addition of 10 mM $InCl_3$ significantly improves the discharge potential of Mg-0.15Ca alloy and maintains the effectiveness for 24 h discharging process. Besides, no negative effect is imparted to the anode utilization efficiency. Hence, we propose that 10 mM $InCl_3$ is a suitable electrolyte additive for aqueous Mg batteries. In this context, testing of aqueous Mg-air battery was done to evaluate its feasibility in a fully assembled battery system. Fig. 9(a-c) present the discharge curves of Mg-air battery in the electrolyte with and without 10 mM $InCl_3$ under different current densities. The addition of $InCl_3$ significantly improves the cell voltage in all cases. Amid discharge at 1 mA cm^{-2}, adding $InCl_3$ increases the cell voltage by 220 mV, namely, from 1.52 V to 1.74 V. During the initial 5 h discharging test at 5 mA cm^{-2}, the voltage of Mg-air battery in the electrolyte containing $InCl_3$ is 1.42 V, whereas the cell voltage in blank NaCl solution is 1.37 V. Nevertheless, the enhancement

of cell voltage induced by $InCl_3$ weakens after 8 h discharge and stabilized at 1.39 V. The addition of 10 mM $InCl_3$ also improves the cell voltage under 10 mA cm^{-2}, which is 50 mV higher than that in reference test. Fig. 9d summarizes the improvement of discharge performance by adopting 10 mM $InCl_3$ as electrolyte additives. As illustrated in Fig. 9d, the most significant enhancement regarding the specific energy is obtained under 1 mA cm^{-2}. With the increase of current density, the enhancement of discharge performance is decreasing. As displayed in Fig. 9e, a large amount of discharge products have precipitated and blocked the active surface of air cathode after discharging test, which may also give rise to the drop of cell voltage in the discharging test with high current density. As indicated in the XRD diffraction pattern, the precipitates on the air cathode are the mixed $In(OH)_3$ and $Mg(OH)_2$, which preferentially form on the air cathode because the cathodic reaction of Mg-air battery generates a large amount of OH^-. This problem can be addressed by applying selective permeable membrane, which should be considered in Mg-air battery configuration design for future works.

Conclusions

In this work, we evaluate the feasibility of $InCl_3$ as an electrolyte additive for aqueous Mg batteries. The half-cell discharge behavior, surface state evolution, self-corrosion rate during discharge of Mg-0.15 wt.% Ca anode and fully assembled aqueous Mg-air battery performance are determined in 3.5 wt.% NaCl solution with and without $InCl_3$. Following conclusions are drawn:

(1) Addition of $InCl_3$ improves the discharge potential of the anode. However, the enhancement weakens with discharge time. Higher $InCl_3$ concentration (10 mM) enables the anode with significantly more negative discharge potential and the enhancement lasts for a longer term, because the addition of In^{3+} is capable of retarding electrolyte alkalization during discharge due to its hydrolysis reaction, which leads to better discharge activity and less film-relevant potential drop.
(2) Local measurement reveals that the pH buffering effect induced by the addition of $InCl_3$ depends on its concentration. Addition of sufficient $InCl_3$ is able to hinder the increase of local pH close to the interface amid discharge. Nevertheless, 1 mM $InCl_3$ addition only shows pH buffering effect for the bulk environment, but the local pH is close to that in blank NaCl, resulting in similar discharge potential.
(3) 1 mM $InCl_3$ addition significantly decrease the self-corrosion rate of the Mg-0.15Ca anode amid discharge at 1 mA cm^{-2}. However, the self-corrosion rate is accelerated with the increment of $InCl_3$ concentration from 0.26 ml cm^{-2} h^{-1} (1 mM) to 0.32 ml cm^{-2} h^{-1} (10 mM).
(4) $InCl_3$ at a low concentration enhances the anode utilization efficiency, e.g. from ~51% to ~57% after adding 1 mM $InCl_3$. Addition of 10 mM $InCl_3$ homogenizes the anode dissolution, reducing anodic efficiency loss caused by chunk effect and maintaining the anode utilization efficiency to 52%.
(5) $InCl_3$ as electrolyte additive sufficiently improves the discharge performance of aqueous Mg-air battery, especially at lower current densities. The highest cell voltage and specific energy of aqueous Mg-air battery is achieved by adding 10 mM $InCl_3$ to 1.74 V and 2.26 kWh/kg (at 1 mA cm^{-2}). The improvement could be further enhanced via combination with battery configuration/cell design.

Author statement

Linqian Wang: Conceptualization, Investigation, Validation, Writing - original draft, Writing - review & editing.

Darya Snihirova: Supervision, Writing - review & editing, Funding acquisition, Project administration.

Min Deng: Conceptualization, Resources, Writing - review & editing.

Cheng Wang: Methodology, Writing - review & editing.

Daniel Höche: Conceptualization, Supervision, Writing - review & editing.

Sviatlana V. Lamaka: Conceptualization, Supervision, Methodology, Writing - review & editing.

Mikhail L. Zheludkevich: Conceptualization, Supervision, Writing - review & editing.

Declaration of Competing Interest

The authors declare that they have no known competing financial interests or personal relationships that could have appeared to influence the work reported in this paper.

Acknowledgement

The authors are grateful for the technical support of Mr. Gert Wiese, Mr. Ulrich Burmester and Mr. Volker Heitmann. Ms. Linqian Wang, Mr. Min Deng and Mr. Cheng Wang thank China Scholarship Council for the award of fellowship and funding (No. 201706370183, No. 201606370031, and No. 201806310128. Dr. Darya Snihirova acknowledges SeaMag project for financial support (MarTera ERA-NET cofund).

References

[1] David Linden, T.B. Reddy, Handbook of Batteries, McGraw-Hill, New York, 2002.
[2] C. Daniel, J. Besenhard, Handbook of Battery Materials, Wiley-VCH, Weinheim, 2012.
[3] M. Deng, D. Höche, D. Snihirova, L.Q. Wang, B. Vaghefinazari, S.V. Lamaka, M.L. Zheludkevich, Aqueous Mg batteries, in: M. Fichtner (Ed.), Magnesium Batteries: Research and Applications, Royal Society of Chemistry, United Kingdom, 2019, pp. 275–308.
[4] M. Deng, D. Höche, S.V. Lamaka, D. Snihirova, M.L. Zheludkevich, Mg-Ca binary alloys as anodes for primary Mg-air batteries, J. Power Sources 396 (2018) 109–118.
[5] X. Liu, S. Liu, J. Xue, Discharge performance of the magnesium anodes with different phase constitutions for Mg-air batteries, J. Power Sources 396 (2018) 667–674.
[6] N. Wang, Y. Mu, W. Xiong, J. Zhang, Q. Li, Z. Shi, Effect of crystallographic orientation on the discharge and corrosion behaviour of AP65 magnesium alloy anodes, Corrois. Sci. 144 (2018) 107–126.
[7] J.L. Wu, R.C. Wang, Y. Feng, C.Q. Peng, Effect of hot rolling on the microstructure and discharge properties of Mg-1.6wt%Hg-2wt%Ga alloy anodes, J. Alloys Compd. 765 (2018) 736–746.
[8] M. Deng, D. Höche, S.V. Lamaka, L. Wang, M.L. Zheludkevich, Revealing the impact of second phase morphology on discharge properties of binary Mg-Ca anodes for primary Mg-air batteries, Corros. Sci. 153 (2019) 225–235.
[9] M. Deng, L. Wang, D. Höche, S.V. Lamaka, D. Snihirova, B. Vaghefinazari, M.L. Zheludkevich, Clarifying the decisive factors for utilization efficiency of Mg anodes for primary aqueous batteries, J. Power Sources 441 (2019) 227201.
[10] X. Liu, J. Xue, P. Zhang, Z. Wang, Effects of the combinative Ca, Sm and La additions on the electrochemical behaviors and discharge performance of the as-extruded AZ91 anodes for Mg-air batteries, J. Power Sources 414 (2019) 174–182.
[11] N. Wang, W. Li, Y. Huang, G. Wu, M. Hu, G. Li, Z. Shi, Wrought Mg-Al-Pb-RE alloy strips as the anodes for Mg-air batteries, J. Power Sources 436 (2019) 226855.
[12] X. Chen, Q. Zou, Q. Le, J. Hou, R. Guo, H. Wang, C. Hu, L. Bao, T. Wang, D. Zhao, F. Yu, A. Atrens, The quasicrystal of Mg–Zn–Y on discharge and electrochemical behaviors as the anode for Mg-air battery, J. Power Sources 451 (2020) 227807.
[13] L. Wen, K. Yu, H. Xiong, Y. Dai, S. Yang, X. Qiao, F. Teng, S. Fan, Composition optimization and electrochemical properties of Mg-Al-Pb-(Zn) alloys as anodes for seawater activated battery, Electrochim. Acta 194 (2016) 40–51.
[14] J. Xu, Z. Wei, L. Tang, A. Wang, Y. Zhang, Y. Qiao, C. Chen, Effects of short pulse current on the voltage delay behavior of magnesium battery, J. Power Sources 454 (2020) 227869.
[15] M. Tsang, A. Armutlulu, A.W. Martinez, S.A.B. Allen, M.G. Allen, Biodegradable magnesium/iron batteries with polycaprolactone encapsulation: a microfabricated power source for transient implantable devices, Microsyst. Nanoeng. 1 (2015).
[16] M. Frei, J. Martin, S. Kindler, G. Cristiano, R. Zengerle, S. Kerzenmacher, Power supply for electronic contact lenses: abiotic glucose fuel cells vs. Mg/air batteries, J. Power Sources 401 (2018) 403–414.

[17] M. Liao, Y. Liu, E. Tian, W. Ma, H. Liu, Phosphorous removal and high-purity struvite recovery from hydrolyzed urine with spontaneous electricity production in Mg-air fuel cell, Chem. Eng. J. (2019) 123517.
[18] X.-J. Gu, W.-L. Cheng, S.-M. Cheng, H. Yu, Z.-F. Wang, H.-X. Wang, L.-F. Wang, Discharge behavior of Mg–Sn–Zn–Ag alloys with different Sn contents as anodes for Mg-air batteries, J. Electrochem. Soc. 167 (2020) 020501.
[19] J. Li, Z. Chen, J. Jing, J. Hou, Electrochemical behavior of Mg-Al-Zn-Ga-In alloy as the anode for seawater-activated battery, J. Mater. Sci. Technol. 41 (2020) 33–42.
[20] S.-m. Cheng, W.-l. Cheng, X.-j. Gu, H. Yu, Z.-F. Wang, H.-x. Wang, L.-f. Wang, Discharge properties of low-alloyed Mg–Bi–Ca alloys as anode materials for Mg–air batteries: influence of Ca alloying, J. Alloys Compd. 823 (2020) 153779.
[21] J. Ma, C. Qin, Y. Li, F. Ren, Y. Liu, G. Wang, Properties of reduced graphene oxide for Mg-air battery, J. Power Sources 430 (2019) 244–251.
[22] D. Höche, S.V. Lamaka, B. Vaghefinazari, T. Braun, R.P. Petrauskas, M. Fichtner, M.L. Zheludkevich, Performance boost for primary magnesium cells using iron complexing agents as electrolyte additives, Sci. Rep. 8 (2018) 7578.
[23] M.M. Dinesh, K. Saminathan, M. Selvam, S.R. Srither, V. Rajendran, Water soluble graphene as electrolyte additive in magnesium-air battery system, J. Power Sources 276 (2015) 32–38.
[24] M.A. Deyab, Decyl glucoside as a corrosion inhibitor for magnesium–air battery, J. Power Sources 325 (2016) 98–103.
[25] Y. Li, J. Ma, G. Wang, F. Ren, Y. Zhu, Y. Song, Investigation of sodium phosphate and sodium dodecylbenzenesulfunate as electrolyte additives for AZ91 magnesium-air battery, J. Electrochem. Soc. 165 (2018) A1713–A1717.
[26] B. Vaghefinazari, D. Höche, S.V. Lamaka, D. Snihirova, M.L. Zheludkevich, Tailoring the Mg-air primary battery performance using strong complexing agents as electrolyte additives, J. Power Sources 453 (2020) 227880.
[27] L. Wang, D. Snihirova, M. Deng, B. Vaghefinazari, S.V. Lamaka, D. Höche, M.L. Zheludkevich, Tailoring electrolyte additives for controlled Mg-Ca anode activity in aqueous Mg-air batteries, J. Power Sources 460 (2020) 228106.
[28] X. Zhao, L. Wang, X. Chen, W. Wang, H.L. Xin, X. Du, J. Yang, Ultrafine SmMn2O5-δ electrocatalysts with modest oxygen deficiency for highly-efficient pH-neutral magnesium-air batteries, J. Power Sources 449 (2020) 227482.
[29] Y. Xue, H. Miao, S. Sun, Q. Wang, S. Li, Z. Liu, Template-directed fabrication of porous gas diffusion layer for magnesium air batteries, J. Power Sources 297 (2015) 202–207.
[30] C. Shu, E. Wang, L. Jiang, Q. Tang, G. Sun, Studies on palladium coated titanium foams cathode for Mg–H_2O_2 fuel cells, J. Power Sources 208 (2012) 159–164.
[31] Y. Li, J. Ma, G. Wang, F. Ren, Y. Zhu, Y. Song, Investigation of sodium phosphate and sodium dodecylbenzenesulfonate as electrolyte additives for AZ91 magnesium-air battery, J. Electrochem. Soc. 165 (2018) A1713–A1717.
[32] D. Höche, C. Blawert, S.V. Lamaka, N. Scharnagl, C. Mendis, M.L. Zheludkevich, The effect of iron re-deposition on the corrosion of impurity-containing magnesium, Phys. Chem. Chem. Phys. 18 (2016) 1279–1291.
[33] S.V. Lamaka, B. Vaghefinazari, D. Mei, R.P. Petrauskas, D. Höche, M.L. Zheludkevich, Comprehensive screening of Mg corrosion inhibitors, Corros. Sci. 128 (2017) 224–240.
[34] S.V. Lamaka, D. Höche, R.P. Petrauskas, C. Blawert, M.L. Zheludkevich, A new concept for corrosion inhibition of magnesium: suppression of iron re-deposition, Electrochem. Commun. 62 (2016) 5–8.
[35] D. Snihirova, L. Wang, S.V. Lamaka, C. Wang, M. Deng, B. Vaghefinazari, D. Hoche, M.L. Zheludkevich, Synergistic mixture of electrolyte additives: a route to a high-efficiency Mg-air battery, J. Phys. Chem. Lett. (2020) 8790–8798.
[36] I.-J. Park, S.-R. Choi, J.-G. Kim, Aluminum anode for aluminum-air battery – part II: influence of In addition on the electrochemical characteristics of Al-Zn alloy in alkaline solution, J. Power Sources 357 (2017) 47–55.
[37] M. Pourgharibshahi, P. Lambert, The role of indium in the activation of aluminum alloy galvanic anodes, Mater. Corros. 67 (2016) 857–866.
[38] D.O. Flamini, S.B. Saidman, Electrochemical behaviour of Al–Zn–Ga and Al–In–Ga alloys in chloride media, Mater. Chem. Phys. 136 (2012) 103–111.
[39] J.B. Bessone, D.O. Flamini, S.B. Saidman, Comprehensive model for the activation mechanism of Al–Zn alloys produced by indium, Corros. Sci. 47 (2005) 95–105.
[40] X. Li, H. Lu, S. Yuan, J. Bai, J. Wang, Y. Cao, Q. Hong, Performance of Mg–9Al–1In Alloy as Anodes for Mg-Air Batteries in 3.5 wt% NaCl Solutions, J. Electrochem. Soc. 164 (2017) A3131–A3137.
[41] J. Li, B. Zhang, Q. Wei, N. Wang, B. Hou, Electrochemical behavior of Mg-Al-Zn-In alloy as anode materials in 3.5wt.% NaCl solution, Electrochim. Acta 238 (2017) 156–167.
[42] S. Yuan, H. Lu, Z. Sun, L. Fan, X. Zhu, W. Zhang, Electrochemical performance of Mg-3Al modified with Ga, In and Sn as anodes for Mg-air battery, J. Electrochem. Soc. 163 (2016) A1181–A1187.
[43] N. Wang, R. Wang, C. Peng, B. Peng, Y. Feng, C. Hu, Discharge behaviour of Mg-Al-Pb and Mg-Al-Pb-In alloys as anodes for Mg-air battery, Electrochim. Acta 149 (2014) 193–205.
[44] M. Deng, L. Wang, D. Höche, S.V. Lamaka, P. Jiang, D. Snihirova, N. Scharnagl, M.L. Zheludkevich, Ca/In micro alloying as a novel strategy to simultaneously enhance power and energy density of primary Mg-air batteries from anode aspect, J. Power Sources 472 (2020) 228528.
[45] P. Gore, S. Fajardo, N. Birbilis, G.S. Frankel, V.S. Raja, Anodic activation of Mg in the presence of In3+ ions in dilute sodium chloride solution, Electrochim. Acta 293 (2019) 199–210.
[46] M. Deng, L. Wang, D. Höche, S.V. Lamaka, C. Wang, D. Snihirova, Y. Jin, Y. Zhang, M.L. Zheludkevich, Approaching “stainless magnesium” by Ca micro-alloying, Mater. Horiz. (2020).
[47] G.L. Song, A. Atrens, Corrosion mechanisms of magnesium, Adv. Eng. Mater. 1 (1999) 11–33.
[48] L.e. Y.Y, Handbook of Analytical Chemistry, 6th ed., 1989 Himiya.
[49] A. Dhanapal, S. Rajendra Boopathy, V. Balasubramanian, Influence of pH value, chloride ion concentration and immersion time on corrosion rate of friction stir welded AZ61A magnesium alloy weldments, J. Alloys Compd. 523 (2012) 49–60.
[50] M.-C. Zhao, M. Liu, G.-L. Song, A. Atrens, Influence of pH and chloride ion concentration on the corrosion of Mg alloy ZE41, Corros. Sci. 50 (2008) 3168–3178.
[51] S. Johnston, Z. Shi, A. Atrens, The influence of pH on the corrosion rate of high-purity Mg, AZ91 and ZE41 in bicarbonate buffered Hanks’ solution, Corros. Sci. 101 (2015) 182–192.

6 Discussion

As the main component of aqueous Mg-air battery, Mg-based anode indeed plays a decisive role on defining the discharge performance of the battery. Nevertheless, electrolyte is also significant for the performance and the discharge behavior of both anode and cathode. According to the results presented in **Chapter 5**, the addition of electrolyte additives shows the capability of improving the discharge performance of AMABs from the aspects of cell voltage and anodic UE. The working mechanism of electrolyte additive is mainly based on regulating the interfacial condition between Mg anode and electrolyte, which can be partly detected by EIS measurement. Moreover, some of the electrolyte additives also exhibit the inhibition effect on the anomalous hydrogen evolution (AHE) under anodic polarization of Mg anode, also known as negative difference effect (NDE), which leads to the enhancement of anodic UE. Based on all the results presented in this dissertation, a general discussion is given in following for a better understanding on how various electrolyte additives influence the voltage and UE of Mg anodes.

6.1 Influence of electrolyte additives on the cell voltage

The theoretical voltage of AMAB is 3.1 V. The reactions taking place during discharge are:

$$\text{Anodic reaction: } 2\,Mg + 4\,OH^- \rightarrow 2\,Mg(OH)_2\downarrow + 4\,e^- \quad E_0 = -2.69\,V\ vs.SHE \tag{6-1}$$

$$\text{Cathodic reaction: } O_2 + 2\,H_2O + 4\,e^- \rightarrow 4\,OH^- \quad E_0 = 0.41\,V\ vs.SHE \tag{6-2}$$

$$\text{Overall reaction: } 2\,Mg + O_2 + 2\,H_2O \rightarrow 2\,Mg(OH)_2\downarrow \quad E = 3.1\,V \tag{6-3}$$

However, alkaline environment renders the Mg electrode passivated. As introduced in **Chapter 2**, the AMABs are normally in neutral electrolyte and the anodic reaction can be expressed as,

$$\text{Anodic reaction: } Mg \rightarrow Mg^{2+} + 2\,e^- \quad E_0 = -2.372\,V\ vs.SHE \tag{6-4}$$

Then the Mg^{2+} ions combine with the OH^- ions generated by cathodic reaction or parasitic HER to form $Mg(OH)_2$ precipitates on the top of anode surface.

$$\text{Formation of precipitation: } Mg^{2+} + 2\,OH^- \rightarrow Mg(OH)_2\downarrow \tag{6-5}$$

$$\text{Parasitic reaction: } Mg + 2\,H_2O \rightarrow Mg(OH)_2\downarrow + H_2\uparrow \tag{6-6}$$

The precipitated film formed during discharge is detrimental to the practical cell voltage in comparison with theoretical value. The practical cell voltage under a constant operating current

i, which can be expressed as follow [56, 57]:

$$E = OCV - \eta_a - \eta_c - iR_{int} \quad (6\text{-}7)$$

Where OCV represents the open circuit voltage of the battery. η_a and η_c represent the activation and concentration overvoltage related to anode and cathode, respectively, caused by charge transfer polarization and concentration polarization. iR_{int} is the ohmic drop caused by internal resistance R_{int} of AMAB, which is tightly affected by the electrolyte conductivity and surface film condition. Therefore, to obtain high battery voltage, the activation and concentration overvoltage need to be minimized and the OCV is required to be approaching the theoretical value. Meanwhile, low cell internal resistance should be fulfilled via adopting conductive electrolytes and appropriate battery design. From the anode side, alloying Mg anode with active elements leads to highly negative OCV and is capable of moderating the activation overvoltage. In terms of cathode, the reactants in cathodic reaction are O_2 and H_2O. The catalyst in air cathode is not consumed in the cathodic reaction (oxygen reduction reaction, ORR). Nevertheless, efficient catalyst for ORR is beneficial to decrease the activation overvoltage of cathode. Moreover, the reaction is diffusion controlled, thus, increasing the active surface area of air cathode is also really important. Both strategies from anode and cathode sides are conducive to increase the OCV and achieve high practical cell voltage. Electrolyte additives adopted in this work also do not directly take part in the discharge reaction, but their addition regulates the properties of surface film and induces fast dissolution kinetic of anode materials.

6.1.1 Surface film on Mg anode

According to Eq. 6-7, the cell voltage is closely related to the interfacial condition of Mg anode and electrolyte. The addition of Mg^{2+} complexing agents, e.g. 2,6-DHB, which are able to form soluble complexes with Mg^{2+} ions in the electrolyte, retard the formation of $Mg(OH)_2$ precipitates. Fig. 6-1 shows the surface morphologies and discharge curves of Mg-0.15Ca after 24 h discharge in 3.5 wt.% NaCl and 2,6-DHB containing electrolytes. The surfaces of Mg-0.15Ca anode in blank NaCl electrolyte and 0.05 M 2,6-DHB-containing electrolyte are completely covered by discharge products, whilst that in 0.1 M 2,6-DHB-containing solution is without any visible discharge products. As shown in Fig. 6-1d, 0.1 M 2,6-DHB addition shifts the discharge potential of Mg-0.15Ca to more negative value in comparison with that in blank NaCl electrolyte. Whereas, 0.05 M 2,6-DHB addition only improves the discharge activity of Mg-0.15Ca anode in the initial 16 h and then shifts to even more positive potential than that in blank NaCl electrolyte.

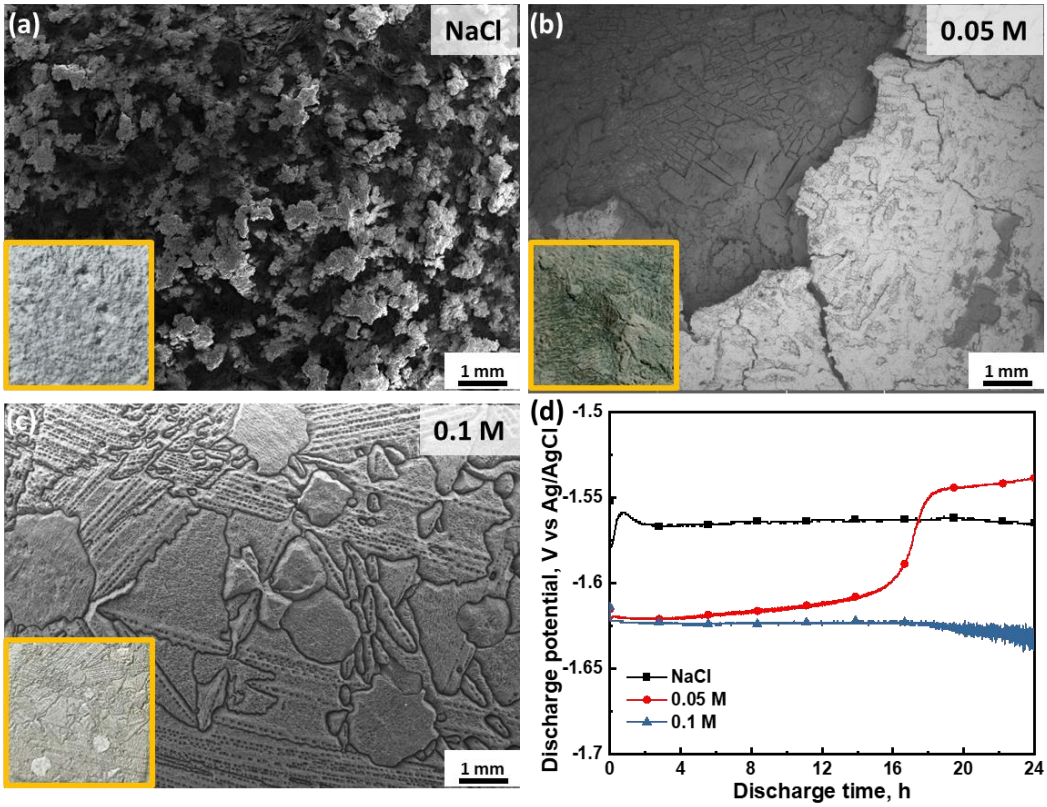

Fig. 6-1. Surface morphologies (a-c) and discharge curves (d) of Mg-0.15Ca after 24 h discharge in (a) blank NaCl solution, (b) 0.05 M and (c) 0.1 M 2,6-DHB-containing electrolytes (Applied current density, 5 mA cm^{-2})

Numerous literature adopted the morphologies of discharge product film on Mg anodes to interpret the effect of alloying elements [46, 55, 58-60], processing history [61-63] or electrolyte additives [24, 64, 65] on the discharge potential of Mg-based anode. However, the method applied for surface characterization is normally under *ex-situ* condition, which may give rise to inevitable changes on the characteristics of product film, such as, cracks or peeling of discharge products film. For instance, the macro-appearance of Mg-0.15Ca exhibited in the insertion of Fig. 6-1b seems to be complete and dense, however, during SEM characterization, a part of outer layer detached from the surface and big cracks formed due to the internal stress. Therefore, the explanation solely based on *ex-situ* surface characteristics may not be sufficient to draw reliable conclusions in some cases. EIS measurement is capable of detecting the minor changes happened on the electrode surface and correlated electrochemical processes at the electrode/electrolyte interface without changing the surface state. Therefore, EIS measurement amid discharge interval should be able to reveal *quasi-in-situ* anode surface evolution during discharge. The conventional Nyquist plot of Mg in NaCl solution is exhibited in Fig. 6-2a, which is mainly composed of two capacitive loops. There is much debate about the physical interpretations of these two capacitive loops. Some researchers deem that the HF capacitive

loop corresponds to the surface film capacitance in parallel with the charge transfer resistance. Here, the MF capacitive loop is associated to the mass transport process through the corrosion product film [48, 66]. Nevertheless, some other researchers suggest the HF capacitive loop originates from the surface film, while the MF capacitive loop is attributed to the charge transfer resistance in parallel with double layer capacitance [49, 67]. In addition, there are many researchers who believe that the HF capacitive loop is double layer capacitance in parallel with charge transfer resistance [68, 69].

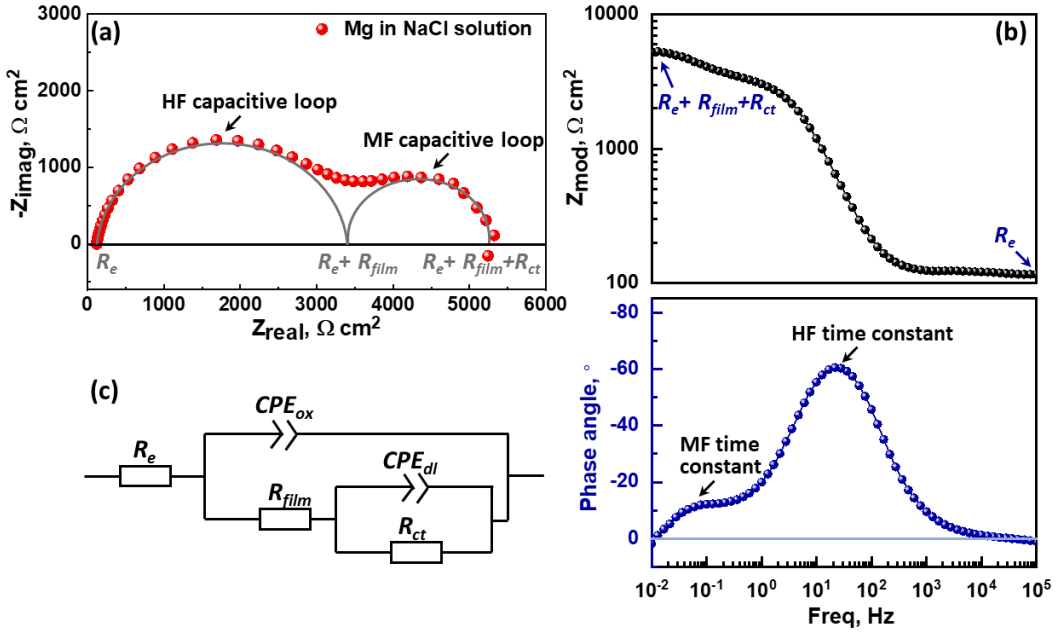

Fig. 6-2. Conventional (a) Nyquist plot, (b) Bode plot and (c) equivalent circuit for pure Mg in NaCl solution

According to the results presented in **Section 5.1** and **Section 5.2**, the physical interpretations regarding HF and MF time constants have been verified, which are presented as circuit elements in the equivalent circuit of Fig. 6-2c. The HF capacitive loop corresponding to the film-relevant behavior, whilst the MF capacitive loop originates from the resistance of charge transfer process in parallel with double layer capacitance. The total resistance of Mg/electrolyte interface can be expressed as,

$$R_{total} = R_e + R_{film} + R_{ct} \quad (6\text{-}8)$$

Where R_e refers to the electrolyte resistance. R_{film} and R_{ct} represent surface film resistance and charge transfer resistance, respectively. Through fitting procedure, these values can be extracted from the impedance spectra and then used to semi-quantitatively analyze the influence of interfacial condition between Mg/electrolyte on the discharge behavior of Mg electrode. Fig. 6-3 presents the results obtained by EIS measurement during intermittent

discharge of Mg-0.15Ca anodes in 3.5 wt.% NaCl and 2,6-DHB-containing electrolytes, which can be set as an instance to demonstrate this semi-quantitative analysis method.

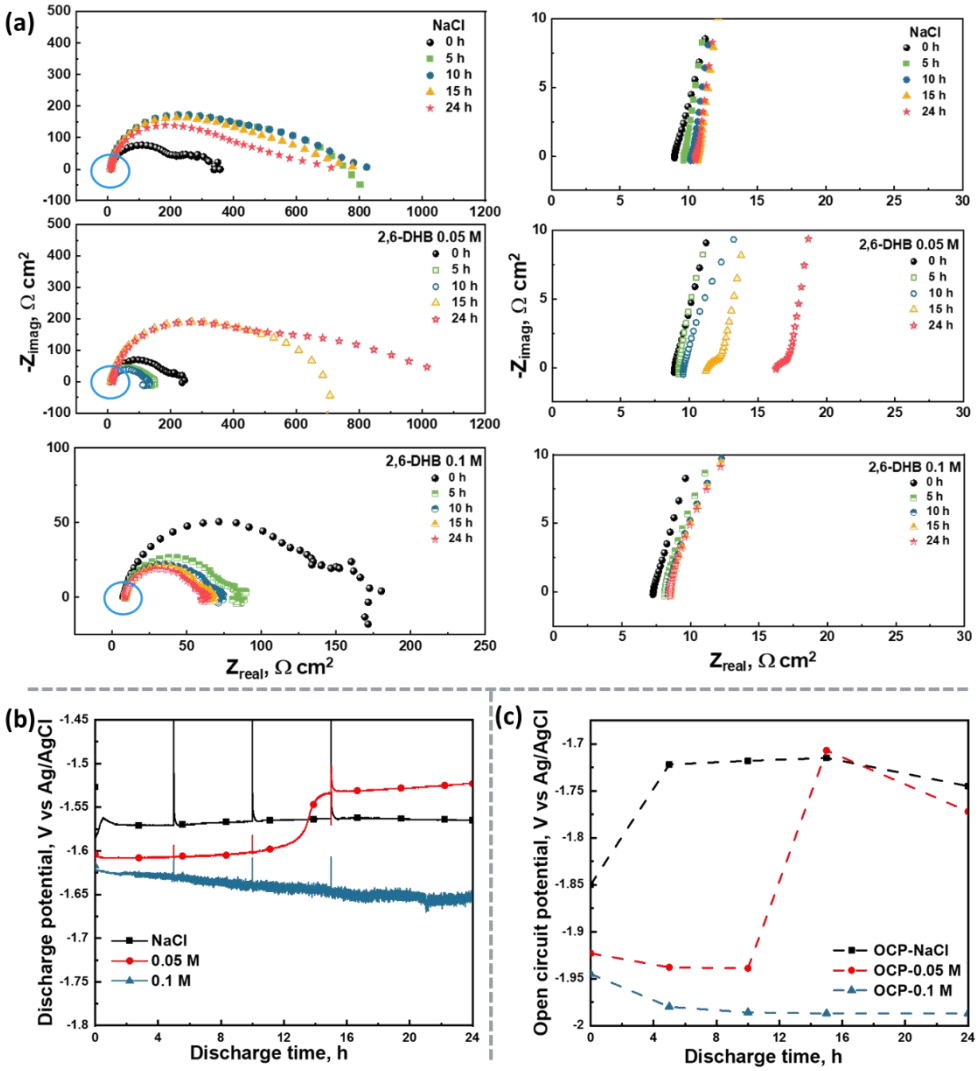

Fig. 6-3. (a) Nyquist plots, (b) discharge curve and (c) OCP of Mg-0.15Ca during intermittent discharge tests in blank NaCl and 2,6-DHB-containing electrolytes. (Applied current density, 5 mA cm^{-2})

The Nyquist plots obtained by EIS measurements during intermittent discharge interval are presented in Fig. 6-3a. The addition of 2,6-DHB leads to the shrinkage of HF and MF capacitive loops before discharge. The R_{total} in blank NaCl solution is around 400 Ω cm^2 and that in 0.1 M 2,6-DHB-containing electrolyte is around 175 Ω cm^2. When the discharge starts, the R_{total} in blank NaCl solution stabilizes at around 800 Ω cm^2, whilst the R_{total} in 0.1 M 2,6-DHB-containing electrolyte stabilizes at around 75 Ω cm^2.However, in 0.05 M 2,6-DHB-containing electrolyte, the R_{total} firstly declines to 150 Ω cm^2 and then increases to 1000 Ω cm^2. As shown in Fig. 6-2b and Fig. 6-2c, the addition of insufficient 2,6-DHB results in the accumulation of dense discharge products film, leading to the increment of η_a. Consequently, the discharge

potential of Mg-0.15Ca becomes more positive than that in blank NaCl solution. Moreover, it is also noteworthy that the high frequency part marked by blue circles roughly equals to the electrolyte resistance, R_e, and, in turn, also may shed lights on the evolution of $Mg(OH)_2$ film. As shown in Fig. 6-3a, the addition of 0.1 M 2,6-DHB significantly reduces the electrolyte resistance before discharge since the ionic concentration of this electrolyte is higher than that of blank NaCl solution (around 0.6 M). With the increase of discharge time, theoretically, the electrolyte should be more concentrated. However, all R_e after discharge shift to higher value than that before discharge. This phenomenon is counterintuitive, since the ionic centration of electrolyte should increase along with the discharging process. The increase of the high frequency part in 0.05 M 2,6-DHB-containing electrolyte is the most pronounced. The changes in the high frequency part after 15 h and 24 h discharge suggest a new relaxation process has taken place at the interface. As depicted in Fig. 6-1b, the surface of Mg-0.15Ca in 0.05 M 2,6-DHB-containing electrolyte is indeed discrepant to that in blank NaCl and in 0.1 M 2,6-DHB-containing electrolyte with double layer structure. It is highly likely that this new relaxation process is related to the formation of the outer layer. Fig. 6-3b and Fig. 6-3c displays the discharge potential and OCP of Mg-0.15Ca in the intermittent discharge test. The discharge potential and OCP of Mg-0.15Ca in blank NaCl solution keeps stable after the initially increase, even though the surface is fully covered by discharge products (Fig. 6-1a). In 0.1 M 2,6-DHB-containing electrolyte, Mg-0.15Ca always possesses more negative discharge potential than that in blank NaCl solution, which is in line with the negative OCP and low R_{total} observed in impedance spectra comparing to that in blank solution. Similarly, the evolution of OCP and R_{total} observed in 0.05 M 2,6-DHB-containing electrolyte is consistent with that of discharge potential and reflects the change of anode surface condition, suggesting EIS measurement amid discharge interval possess the ability to detect and correlate the changes in the Mg/electrode interfacial condition change with the anode discharge behavior. Furthermore, the EIS results indicate that sufficient 2,6-DHB addition is not only shifts the OCP of Mg-0.15Ca anode to negative value, but also decrease the surface film relevant potential drop.

6.1.2 Growth of the $Mg(OH)_2$ in presence of additives

In addition to the effect of Mg^{2+} complexing agents on hindering the precipitation of $Mg(OH)_2$, the electrolyte additives are also able to influence the kinetics of the reactions occuring in AMABs. Fig. 6-4 illustrates the chemical equilibria in blank NaCl solution and additive-containing electrolytes (0.1 M CIT and 0.1 M 3,4-DHB), which were calculated by Hydra-Medusa software. For illustration and comparison reason, the concentrations of Mg^{2+} in these

three systems were set as 0.01 M. As shown in Fig. 6-4a, the formation of insoluble $Mg(OH)_2$ in blank NaCl solution takes place at pH 9.9, whereas the critical pH for $Mg(OH)_2$ precipitation in CIT-containing electrolyte is 10.5 (Fig. 6-4b). When 0.1 M 3,4-DHB is introduced into NaCl solution (Fig. 6-4c), the precipitation of $Mg(OH)_2$ is shifted from pH 9.9 to pH 13.1. From Fig. 6-4c, soluble $Mg(C_7H_3O_4)_2^{4-}$ complexes dominate a wide pH range at least from pH 8 to 13. Hence, there are only a trace amount of free Mg^{2+} in this 3,4-DHB-containing electrolyte in comparison with that in blank NaCl solution, even the setting values are the same.

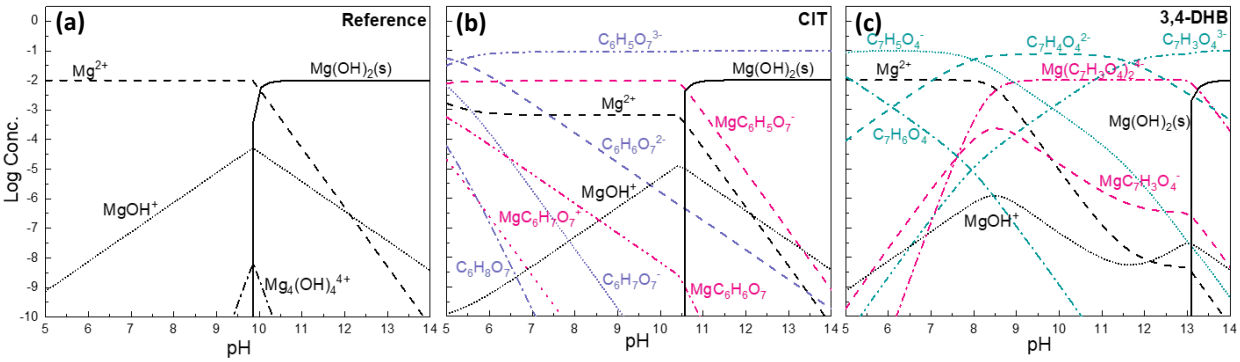

Fig. 6-4. Thermodynamic calculation of the equilibrium composition of relevant species in (a) blank NaCl; and the same electrolyte with 0.1 M (b) CIT; and (c) 3,4-DHB. (Total concentration of Mg^{2+} species: 0.01 M)

Both CIT and 3,4-DHB are Mg^{2+} complexing reagents, whilst their complexation abilities are different and are defined by the stability constant of the complexes listed in Table. 6-1. The stability constant for Mg-CIT is 3.45 and that for Mg-$(3,4\text{-DHB})_2$ is 9.84. Higher stability constant represents stronger complexation ability, and, in turn, less possibility for the formation of $Mg(OH)_2$ precipitates and less film-relevant potential drop under discharging condition, which is beneficial for the improvement of power density of AMABs. Nevertheless, when the complexation ability of selected additive is too strong, the additives will additionally promote the dissolution of Mg to Mg^{2+} and consume it via the following complexation reaction,

$$\text{Complexation reaction: } Mg^{2+} + Ligand^{x-} \rightarrow Mglig^{2-x} \quad (6\text{-}9)$$

Eventually, it leads to the reduction of anodic UE. Hence, choosing Mg^{2+} complexing agents as additives should always consider applied conditions (e.g. discharge load). The addition of organic acid will also introduce another reaction into the AMABs, i.e. the disassociation reaction of organic acid,

$$\text{Dissociation reaction: } H_3A \rightarrow H_2A^- + H^+ \quad (6\text{-}10)$$

The disassociation constants for CIT and 3,4-DHB are also listed in Table. 6-1. In order to make the results more comparable to that obtained in blank NaCl solution. All organic acid-

containing electrolytes were neutralized to pH 7. CIT is fully deprotonated but only the carboxylate proton of 3,4-DHB is dissociated. Thus, 3,4-DHB addition is also able to consume the OH^- ions and hinder the formation of $Mg(OH)_2$, which also can result in accelerated dissolution of Mg. As shown in Table 6-1, the final pH of blank NaCl after 24 h hydrogen evolution test is 10.7 and that of CIT-containing electrolyte is 11.4 owing to the accelerated hydrogen evolution and Mg dissolution, whereas the final pH of 3,4-DHB-containing electrolyte is 9.5. Combining strong Mg^{2+} complexation ability and the pH buffering effect, 3,4-DHB accelerates the kinetics of Mg dissolution reaction, reduces the film relevant potential drop, achieves the most negative discharge potential of Mg-Ca anode in both low and high current densities (Table. 6-1).

Table 6-1 Stability constants of Mg^{2+} complexes produced by selected electrolyte additives and disassociation constants of selected additives and electrolyte pH after 24 h HET and discharge potential of Mg-Ca [70, 71].

Complexing agent	Stability constants	Disassociation constants		pH after 24 h of HET (initial pH 7)	Discharge potential of Mg-Ca (V vs Ag/AgCl)	
	$logKMg^{2+}$	LogKa	Ref.		1 mA cm^{-2}	10 mA cm^{-2}
NaCl	-	-	-	10.7	-1.62	-1.51
CIT	ML/M.L 3.45	5.70	[70]	11.4	-1.80	-1.50
	MHL/M.HL 1.81	4.35				
	MH2L/M. H2L 0.7	2.90				
3,4-DHB	ML2/M.L2 9.84	12.2	[71]	9.5	-1.95	-1.55
	ML/M.L 5.67	8.70				
		4.34				

In spite of the disassociation reactions of organic acids possess pH buffering effect, the hydrolysis effect of some metallic ions is also able to moderate the electrolyte alkalization during discharge. In^{3+} ions, adopted in ***paper 5***, exhibit strong pH buffering effect and are capable of controlling both local and bulk pH, depending on the applied concentration. According to the results presented in ***paper 5***, 10 mM $InCl_3$ addition enables Mg-0.15Ca anode to maintain -1.76 V vs Ag/AgCl in comparison with -1.61 V vs Ag/AgCl in 3.5 wt.% NaCl solution at 1 mA cm^{-2}. The hydrolysis reactions of In^{3+} ions are as follows,

$$In^{3+} + H_2O = InOH^{2+} + H^+ \quad (6\text{-}11)$$

$$InOH^{2+} + H_2O = In(OH)_2^+ + H^+ \quad (6\text{-}12)$$

$$In(OH)_2^+ + H_2O = In(OH)_{3(s)} + H^+ \quad (6\text{-}13)$$

which are able to neutralize the OH^- ions generated by parasitic and cathodic reactions. Hence, the addition of In^{3+} ions keeps the electrolyte pH below to 5 even after 24 h discharge at 1 mA cm^{-2}, and subsequently, improves the discharge activity of Mg-0.15Ca anode.

6.2 Influence of electrolyte additive on the utilization efficiency

As above mentioned, the addition of selected additives may also introduce inverse effect on the anodic UE depending on the applied condition. Anodic UE is one of the decisive parameters in the evaluation of AMAB systems, which plays a vital role for the specific capacity, energy density and cell life of AMABs. Searching for Mg anodes with high UE and alleviating self-discharge via adding inorganic or organic compounds are always the emphasis of novel AMAB systems development. Anodic UE is a physical value indicating the difference between the theoretical weight loss and the actual weight loss of anode materials. As shown in Eq. 4-3, the theoretical weight loss depends on the applied current, discharge duration and some physical constants for specific Mg-based anode. The actual weight loss includes the theoretical loss, the loss caused by "chunk effect", and the loss owing to self-discharge or so-called self-corrosion. Strictly, chunk effect (CE) also belongs to one kind of self-discharge behavior of Mg-based anodes, which refers to the detachment of metallic chunk from anode surface during discharge. As reported in [37, 72], the ratio of weight loss caused by chunk effect may exceed 50% for heavy alloyed Mg-based anode materials, e. g. ZE41. In this work, the self-discharge behavior of Mg-based anode specifically refers to the negative difference effect (NDE), which is also knowns as anomalous hydrogen evolution (AHE).

6.2.1 Non-uniform dissolution of Mg-based anode

The known origins of chunk effect is non-uniform and localized dissolution of Mg-based anodes during discharge, which may initiated from second phases, impurities or grain boundaries in Mg-based anodes. Fig. 6-5 exhibits the cross sections of Mg-0.04Ca in blank NaCl, 0.1 M CIT- and 3,4-DHB-containing electrolytes. As illustrated in Fig. 6-5a, Mg-0.04 Ca suffers from serious non-uniform dissolution. Several channels form and extend to the matrix. When it forms a closed loop, the metallic chunks surrounded by channels will completely lose contact with matrix and no longer contribute to energy supply. The addition of CIT and 3,4-DHB alleviate the non-uniform dissolution of Mg-0.04Ca in different extents. In

the magnified view of Mg-0.04Ca in CIT-containing electrolyte (Fig. 6-5d), there are still several undissolved metallic pieces in the discharge product film. Whereas, 3,4-DHB addition significantly eliminates the localized dissolution of Mg-0.04Ca and retards the precipitation of discharge products as shown in Fig. 6-5e and Fig. 6-5f.

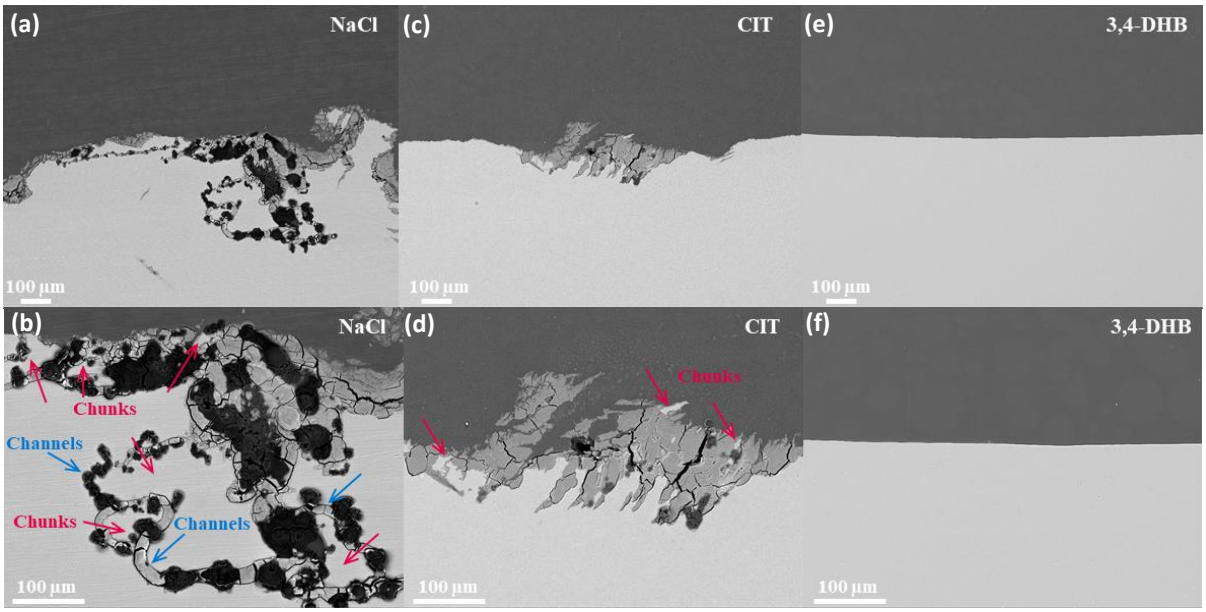

Fig. 6-5. Cross-section images(BSE mode) of Mg-0.04Ca after 24 h discharge at 5 mA cm^{-2} in: (a-b) blank NaCl; (c-d) 0.1 M CIT-containing ; and (e-f) 0.1 M 3,4-DHB-containing electrolytes.

The uniform dissolution of Mg-0.04Ca anode in CIT- and 3,4-DHB-containing electrolytes should also be attributed to their ability to form soluble complexes with Mg^{2+}, which accelerates the reaction kinetics of anode dissolution and reduce the chance for the occurrence of localized corrosion. Consequently, the UE loss caused by CE should be alleviated via adding Mg^{2+} complexing agents. Nevertheless, as aforementioned, the effect of selected additives on the discharge performance of AMABs also depends on the discharge condition. In spite of its significant effect on elimination of CE, 3,4-DHB is too strong for low load application (e.g. 1 mA cm^{-2}), leading to undesirable UE, 9% in comparison with 53% for blank NaCl solution under 1 mA cm^{-2} (Fig. 6-6). The reduction of UE introduced by 3,4-DHB is because the excessed Mg^{2+} complexation ability and pH buffering effect of 3,4-DHB accelerate the self-discharge of Mg-0.04Ca anode. With the increase of applied current density, the UE of Mg-0.04Ca in 3,4-DHB-containing electrolyte greatly enhances, which is the highest under 10 mA cm^{-2} among that in NaCl and CIT-containing electrolytes.

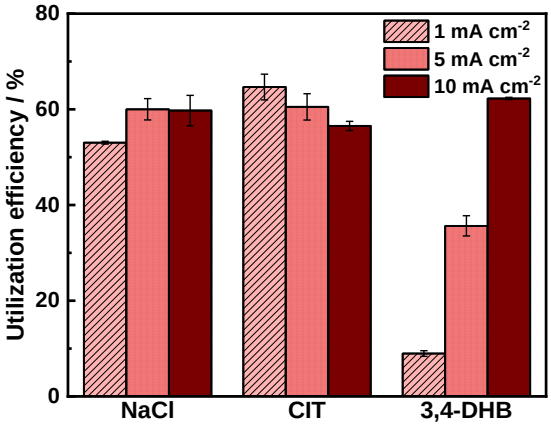

Fig. 6-6. Utilization efficiencies of Mg-0.04Ca after 24 h discharge at 1, 5 and 10 mA cm^{-2} in blank NaCl, 0.1 M CIT-containing, and 0.1 M 3,4-DHB-containing electrolytes.

Similarly, In^{3+} addition also exhibits the capability of inducing uniform dissolution of Mg anode during discharge. As shown in Fig. 6-7, more uniform surface of Mg-0.15Ca is observed in more concentrated $InCl_3$ electrolytes, suggesting less efficiency loss caused by chunk effect.

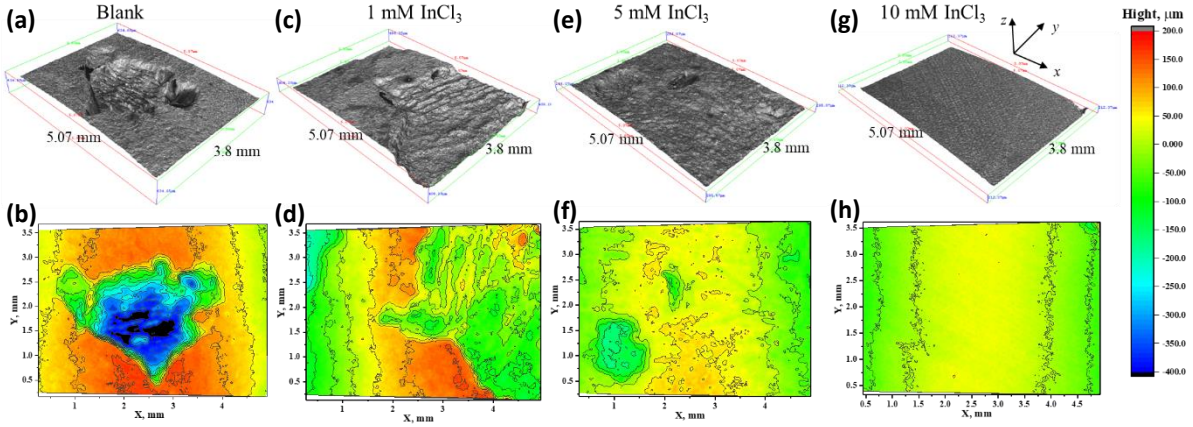

Fig. 6-7. 3D reconstruction and corresponding depth file for the Mg-0.15Ca anode topography without discharge products after discharge at 1 mA cm^{-2} for 24 h in 3.5 wt.% NaCl solution with $InCl_3$ of different concentration: (a, b) blank; (c, d) 1 mM; (e, f) 5 mM; and (g, h) 10 mM.

6.2.2 Self-discharge of Mg-based materials

The self-discharge of Mg-based materials is also known as NDE or AHE, referring to the anomalous hydrogen evolution reaction (Eqs. 6-14 and 6-15) happened on Mg electrode surface under anodic polarization. The traditional hydrogen evolution reaction is a cathodic reaction,

Hydrogen evolution reaction: $2\,H^+ + 2\,e^- \rightarrow H_2$ (in acidic environment) (6-14)

or,

$$2\,H_2O\ +\ 2\,e^-\ \rightarrow\ H_2\ +\ 2\,OH^-\ \text{(in non-acidic environment)} \qquad (6\text{-}15)$$

During galvanostatic discharge mode, Mg-based anodes are under anodic polarization, and theoretically, the cathodic hydrogen evolution reaction should be suppressed. However, the experimentally observed hydrogen evolution from Mg-based anode during discharge is even more intensive than that under OCP. This abnormal phenomenon is called NDE. Many attempts have been made to clarify the origin and mechanism of NDE during last decade [73-77]. Nevertheless, the discussion and arguments concerning this topic have not been stopped. Even though the interpretations regarding NDE are still controversial, there are already solid evidences that NDE is related to the alloy categories [37] and electrolyte compositions [78]. As shown in Fig. 6-8, the addition of $InCl_3$ and 2,6-DHB with various concentrations is able to moderate the hydrogen evolution of Mg-0.15Ca under different current densities. 1 mM $InCl_3$ and 0.1 M 2,6-DHB addition show the lowest hydrogen evolution rate under 1 and 5 mA cm^{-2} current densities, respectively. The results are in line with the UEs of Mg-0.15Ca obtained in $InCl_3$- and 2,6-DHB-containing electrolytes, since chunk effect is not serious in Mg-0.15Ca anode. It is noteworthy that 0.05 M 2,6-DHB and 10 mM $InCl_3$ addition introduce less evident or even negative effect on inhibiting self-discharge of Mg-0.15Ca. The electrolyte additives are capable of hindering the self-discharge of Mg-based anodes but their concentration is an important parameter for their effect on self-discharge inhibition. Hence, the electrolyte additive, which simultaneously decreases self-discharge and alleviates chunk effect under proper applied condition, would greatly improve the UE of Mg-based anodes.

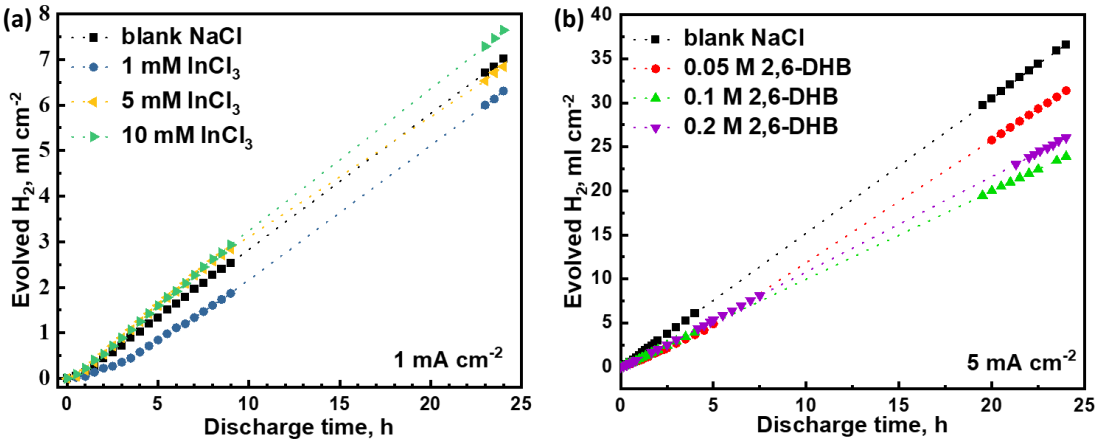

Fig. 6-8. Real-time hydrogen evolution of Mg-0.15Ca anode during discharge (a) at 1 mA cm^{-2} for 24 h in blank NaCl and different concentration $InCl_3$-containing electrolytes, and (b) at 5 mA cm^{-2} for 24 h in blank NaCl and different concentration 2,6-DHB-containing electrolytes.

7 Summary and outlook

This work aims to fill the gap between the practical and theoretical performance of AMABs via optimizing the electrolyte system for novel Mg-Ca anode. Mg^{2+} complexing agents have been proposed as potential electrolyte additives to boost the discharge performance of aqueous Mg-air batteries. The influence of Mg^{2+} complexing agents with diverse complexation abilities on discharge performance of Mg-Ca based AMABs was investigated, which exhibits strong regulating capability to interfacial conditions between Mg-Ca anode and electrolyte. With the aim to clarify the correlations between the anode/electrolyte interfacial condition and the discharge behavior of Mg anode, EIS measurements were performed. In order to accurately analyze the surface evolution of Mg detected by EIS measurement, the physical interpretations of HF and MF time constants (capacitive loops) were thoroughly investigated. Thereafter, the effects and working mechanisms of 2,6-DHB and $InCl_3$ as electrolyte additives for AMABs were investigated. Accordingly, some main conclusions are drawn below:

1) HF capacitive loop in Mg impedance spectra is proven to be related to the surface film resistance in parallel with the MgO film capacitance. The thicknesses of MgO films formed in NaCl solution with various pH are calculated from the fitted EIS results in HF range and compared with the actual surface conditions characterized by TEM. The EIS results indicate that Mg possess the least film resistance but the thickest MgO film in 0.05 M NaCl solutions with pH 3 than that in 0.05 M NaCl solution with 5.6 and 11, which are consistent with the surface film morphologies observed by TEM.

2) Tribo-EIS measurements confirm that the HF time constant in Mg impedance spectra stems from the barrier properties of MgO-based surface film and the MF time constant originates from the charge transfer process. EIS measurements are capable of monitoring Mg electrode surface evolution.

3) Abrasion introduced by tribometer dramatically increases film-free sites on Mg in NaCl solution and affects HF and MF time constants differentially. The resistance reduction of the HF time constant is associated with the ratio of the abraded surface area to the total exposed surface area of Mg, which is consistent with the expectation for the change of surface film resistance caused by abrasion. The influence of abrasion on the MF time constant is more significant than that of the HF time constant. The MF time constant possess extremely small resistance in the scratch, which is in line with the charge transfer resistance and shows the non-polarizable feature of Mg.

4) Mg^{2+} complexing agents improve the discharge potential of Mg-0.04Ca efficiently. The average discharge potential of Mg-0.04Ca in NaCl solution with 0.1 M 3,4-DHB reaches -1.95 V at 1 mA cm^{-2}, which is 320 mV more negative than that in blank NaCl solution. The addition of Mg^{2+} complexing agents are capable of hindering the precipitation of discharge products on anode surface and providing more active areas for discharge reaction. Hence, the addition of Mg^{2+} complexing agents decreases the film-relevant potential drop and leads to negative discharge potential for Mg anode.

5) Moderate Mg^{2+} complexing agents are proven to enhance anodic UE of Mg-0.04Ca in this work. The highest value of 67.2% is achieved for Mg-0.04Ca anode in 0.1 M 2,6-DHB-containing electrolyte at 10 mA cm^{-2}, with simultaneously improved discharge activity. The addition of moderate Mg^{2+} complexing agents eliminates the weight loss caused by chunk effect and alleviates self-discharge of Mg-based anodes.

6) Mg^{2+} complexing agents overall have positive effects on the discharge performance of AMABs with novel Mg-0.04Ca anode. Nevertheless, different additives should be used for various discharge loads to obtain optimal effect, according to their complexation abilities with Mg^{2+}. For low discharge current, moderate Mg^{2+} complexing agents, such as CIT and SAL, stimulate the ideal performance of Mg-0.04Ca based AMABs. The peak specific energy appears at 1 mA cm^{-2} in NaCl with 0.1 M CIT and reaches 3.0 kWh kg^{-1} (vs. 2.1 kWh kg^{-1} in blank NaCl). At high discharge loads, better performance is achieved when using the additives with stronger complexation ability, such as 3,4-DHB and 5-sulfoSAL. At 10 mA cm^{-2}, the specific energy of Mg-0.04Ca based AMABs in 0.1 M 5-sulfoSAL-containing electrolyte is the highest, achieving 1.9 kWh kg^{-1} (vs. 1.6 kWh kg^{-1} in blank NaCl).

7) Addition of 2,6-DHB simultaneously improves the discharge potential and utilization efficiency of Mg-0.15Ca anode. The results of EIS measurement amid intermittent discharge indicate that sufficient amount of 2,6-DHB hinders the formation of discharge products and improves the discharge activity of Mg-0.15Ca. The results of real-time hydrogen evolution elucidate that 2,6-DHB addition is able to moderate the self-discharge of Mg-0.15Ca anode.

8) 2,6-DHB is proven to be a versatile electrolyte additive for AMABs based on diverse metallic Mg anodes (HP-Mg, Mg-0.15Ca, AZ31, and AM50 Mg alloys). Sufficient amount of 2,6-DHB (e.g 0.2 M) mainly improves the battery performance in terms of cell voltage and power dnesity for low discharge load (1 mA cm^{-2}), while for high current densities (e.g. 10 mA cm^{-2}), the enhancement of the specific energy is significant. The highest specific energy is

achieved in Mg-0.15Ca based AMAB with 2,6-DHB-containing electroylte, as 2.0 kWh kg^{-1}.

9) Addition of $InCl_3$ improves the discharge potential of Mg-0.15Ca anode. The addition of 10 mM $InCl_3$ shifts the discharge potential of Mg-0.15Ca from -1.61 V to -1.76 V at 5 mA cm^{-2}. The improvement is caused by the hydrolysis reactions of In^{3+}, which retards the electrolyte alkalization during discharge and leads to better discharge activity. 1 mM $InCl_3$ addition only shows pH buffering effect for the bulk environment under 1 mA cm^{-2} applied current density, whilst the local pH is close to that in blank NaCl, resulting in similar discharge potential. 10 mM $InCl_3$ is able to hinder the increase of local pH during discharge and keep discharge activity of Mg-0.15Ca anode.

10) $InCl_3$ addition with different concentrations improves the UE of Mg-0.15Ca via different mechanisms. 1 mM $InCl_3$ addition significantly decrease the self-discharge of Mg-0.15Ca during discharge. Addition of 10 mM $InCl_3$ homogenizes the anode dissolution, reducing anodic efficiency loss caused by chunk effect.

11) $InCl_3$ as electrolyte additive sufficiently improves the discharge performance of AMABs, especially at low current density. The highest cell voltage and specific energy of Mg-0.15Ca are obtained in 10 mM $InCl_3$-containing electrolyte at 1 mA cm^{-2}, 1.74 V and 2.3 kWh kg^{-1}, respectively.

The results obtained in this work elucidate that adopting suitable electrolyte additive is an efficient method to boost the discharge performance of AMABs. The addition of organic compounds (e.g. 2,6-DHB) or inorganic compounds (e.g. $InCl_3$) is capable of regulating the Mg/electrolyte interfacial condition and influencing the discharge behavior of Mg anode. In this work, only five organic compound and one inorganic compound were systematically investigated. Numerous potential electrolyte additives are waiting to be explored. Meanwhile, it is also worthy to look forward that the performance enhancement of AMABs through using additive mixture. The combination of metallic cations and organic compounds is reported to be efficient electrolyte additives for aqueous Al-air batteries in terms of improving the UE and cell voltage [41, 79]. The research on commercial pure Mg anode indicates that the UE of commercial pure Mg anode can be significantly improved to 82% by adding the mixture of SAL and NO_3^- [13]. Therefore, finding other potential electrolyte additives and employing additive mixtures are essential to improve the discharge performance of AMABs. Nevertheless, screening the vast amount of potentially effective organic and inorganic compounds as electrolyte additives for AMABs solely through experimental methods is tremendously time-

and resource-consuming. There are two possible strategies to screen the potential compounds efficiently for future work. The first one is choosing the potential compounds based on a better mechanistic understanding of the discharge behavior of Mg anode. Another strategy is selecting efficient Mg corrosion inhibitors via the computer-assisted methods. For instance, the data driven machine learning methods have been used to predict the corrosion inhibition efficiency of organic compounds [80-83]. Both strategies will facilitate the process of finding effective electrolyte additives. In addition, the combination of efficient electrolyte additive with novel Mg-based anodes, such as Mg-Ca-In [19] and Mg-Ca-Ge [11], should also be promising for achieving high-performance AMABs. Except for the influence of electrolyte additive on anode, the interaction of electrolyte additive with other components of AMABs is also worth investigating, for example, the possible effect of the additives on the performance of catalysts in air-cathode. Future works on screening electrolyte additives need to comprehensively consider the impact of electrolyte additives on all components of AMABs. Moreover, in spite of the large number of published works, the practical application of AMABs with electrolyte additive may encounter the problems associated with scale-up. Therefore, a rational design of AMAB is practically valuable.

References

[1] Q. Liu, Z. Pan, E. Wang, L. An, G. Sun, Aqueous metal-air batteries: Fundamentals and applications, Energy Storage Materials, 27 (2020) 478-505.

[2] J. Fu, Z.P. Cano, M.G. Park, A. Yu, M. Fowler, Z. Chen, Electrically Rechargeable Zinc-Air Batteries: Progress, Challenges, and Perspectives, Adv Mater, 29 (2017).

[3] F. Cheng, J. Chen, Metal-air batteries: from oxygen reduction electrochemistry to cathode catalysts, Chem Soc Rev, 41 (2012) 2172-2192.

[4] J.-S. Lee, S. Tai Kim, R. Cao, N.-S. Choi, M. Liu, K.T. Lee, J. Cho, Metal-Air Batteries with High Energy Density: Li-Air versus Zn-Air, Advanced Energy Materials, 1 (2011) 34-50.

[5] Y. Li, J. Lu, Metal–Air Batteries: Will They Be the Future Electrochemical Energy Storage Device of Choice?, ACS Energy Letters, 2 (2017) 1370-1377.

[6] Y. Sun, X. Liu, Y. Jiang, J. Li, J. Ding, W. Hu, C. Zhong, Recent advances and challenges in divalent and multivalent metal electrodes for metal–air batteries, Journal of Materials Chemistry A, 7 (2019) 18183-18208.

[7] D. Höche, S.V. Lamaka, B. Vaghefinazari, T. Braun, R.P. Petrauskas, M. Fichtner, M.L. Zheludkevich, Performance boost for primary magnesium cells using iron complexing agents as electrolyte additives, Scientific Reports, 8 (2018) 7578.

[8] M. Deng, D. Höche, S.V. Lamaka, D. Snihirova, M.L. Zheludkevich, Mg-Ca binary alloys as anodes for primary Mg-air batteries, Journal of Power Sources, 396 (2018) 109-118.

[9] X. Liu, J. Xue, P. Zhang, Z. Wang, Effects of the combinative Ca, Sm and La additions on the electrochemical behaviors and discharge performance of the as-extruded AZ91 anodes for Mg-air batteries, Journal of Power Sources, 414 (2019) 174-182.

[10] L. Wang, D. Snihirova, M. Deng, B. Vaghefinazari, S.V. Lamaka, D. Höche, M.L. Zheludkevich, Tailoring electrolyte additives for controlled Mg-Ca anode activity in aqueous Mg-air batteries, Journal of Power Sources, 460 (2020) 228106.

[11] M. Deng, L. Wang, D. Höche, S.V. Lamaka, D. Snihirova, P. Jiang, M.L. Zheludkevich, Corrosion and discharge properties of Ca/Ge micro-alloyed Mg anodes for primary aqueous Mg batteries, Corrosion Science, 177 (2020) 108958.

[12] B. Vaghefinazari, D. Höche, S.V. Lamaka, D. Snihirova, M.L. Zheludkevich, Tailoring the Mg-air primary battery performance using strong complexing agents as electrolyte additives, Journal of Power Sources, 453 (2020) 227880.

[13] D. Snihirova, L. Wang, S.V. Lamaka, C. Wang, M. Deng, B. Vaghefinazari, D. Hoche, M.L. Zheludkevich, Synergistic Mixture of Electrolyte Additives: A Route to a High-Efficiency Mg-Air Battery, Journal of Physical Chemistry Letters, (2020) 8790-8798.

[14] N. Wang, W. Li, Y. Huang, G. Wu, M. Hu, G. Li, Z. Shi, Wrought Mg-Al-Pb-RE alloy strips as the anodes for Mg-air batteries, Journal of Power Sources, 436 (2019) 226855.

[15] X. Chen, Q. Zou, Q. Le, J. Hou, R. Guo, H. Wang, C. Hu, L. Bao, T. Wang, D. Zhao, F. Yu, A. Atrens, The quasicrystal of Mg–Zn–Y on discharge and electrochemical behaviors as the anode for Mg-air battery, Journal of Power Sources, 451 (2020) 227807.

[16] T. Zhang, Z. Tao, J. Chen, Magnesium–air batteries: from principle to application, Materials Horizons, 1 (2014) 196-206.

[17] M. Deng, D. Höche, D. Snihirova, L. Wang, B. Vaghefinazari, S.V. Lamaka, M.L. Zheludkevich, Aqueous Mg Batteries, in: Magnesium Batteries, 2019, pp. 275-308.

[18] K.W. Leong, Y. Wang, W. Pan, S. Luo, X. Zhao, D.Y.C. Leung, Doubling the power output of a Mg-air battery with an acid-salt dual-electrolyte configuration, Journal of Power Sources, 506 (2021) 230144.

[19] M. Deng, L. Wang, D. Höche, S.V. Lamaka, P. Jiang, D. Snihirova, N. Scharnagl, M.L. Zheludkevich, Ca/In micro alloying as a novel strategy to simultaneously enhance power and energy density of primary Mg-air batteries from anode aspect, Journal of Power Sources, 472 (2020) 228528.

[20] L. Wang, D. Snihirova, M. Deng, C. Wang, D. Höche, S.V. Lamaka, M.L. Zheludkevich, Indium chloride as an electrolyte additive for primary aqueous Mg batteries, Electrochimica Acta, 373 (2021) 137916.

[21] X. Zhao, L. Wang, X. Chen, W. Wang, H.L. Xin, X. Du, J. Yang, Ultrafine SmMn2O5-δ electrocatalysts with modest oxygen deficiency for highly-efficient pH-neutral magnesium-air batteries, Journal of Power Sources, 449 (2020) 227482.

[22] Y.-C. Zhao, G.-S. Huang, G.-l. Gong, T.-Z. Han, D.-B. Xia, F.-S. Pan, Improving the Intermittent Discharge Performance of Mg–Air Battery by Using Oxyanion Corrosion Inhibitor as Electrolyte Additive, Acta Metallurgica Sinica (English Letters), 29 (2016) 1019-1024.

[23] Y.C. Zhao, G.S. Huang, C. Zhang, C. Peng, F.S. Pan, Effect of phosphate and vanadate as electrolyte additives on the performance of Mg-air batteries, Materials Chemistry and Physics, 218 (2018) 256-261.

[24] Y. Li, J. Ma, G. Wang, F. Ren, Y. Zhu, Y. Song, Investigation of sodium phosphate and sodium dodecylbenzenesulfonate as electrolyte additives for AZ91 magnesium-air battery, Journal of the Electrochemical Society, 165 (2018) A1713.

[25] M. Mayilvel Dinesh, K. Saminathan, M. Selvam, S.R. Srither, V. Rajendran, K.V.I.S. Kaler, Water soluble graphene as electrolyte additive in magnesium-air battery system, Journal of Power Sources, 276 (2015) 32-38.

[26] Y. Feng, W. Xiong, J. Zhang, R. Wang, N. Wang, Electrochemical discharge performance of the Mg–Al–Pb–Ce–Y alloy as the anode for Mg–air batteries, Journal of Materials Chemistry A, 4 (2016) 8658-8668.

[27] X. Liu, S. Liu, J. Xue, Discharge performance of the magnesium anodes with different phase constitutions for Mg-air batteries, Journal of Power Sources, 396 (2018) 667-674.

[28] N. Wang, R. Wang, Y. Feng, W. Xiong, J. Zhang, M. Deng, Discharge and corrosion behaviour of Mg-Li-Al-Ce-Y-Zn alloy as the anode for Mg-air battery, Corrosion Science, 112 (2016) 13-24.

[29] Z.L. Wang, D. Xu, J.J. Xu, X.B. Zhang, Oxygen electrocatalysts in metal-air batteries: from aqueous to nonaqueous electrolytes, Chem Soc Rev, 43 (2014) 7746-7786.

[30] X. Zhang, Y. Li, M. Jiang, J. Wei, X. Ding, C. Zhu, H. He, H. Lai, J. Shi, Engineering the coordination environment in atomic Fe/Ni dual-sites for efficient oxygen electrocatalysis in Zn-air and Mg-air batteries, Chemical Engineering Journal, 426 (2021) 130758.

[31] C. Zhao, Y. Jin, W. Du, C. Ji, X. Du, Multi-walled carbon nanotubes supported binary PdSn nanocatalyst as effective catalytic cathode for Mg-air battery, Journal of Electroanalytical Chemistry, 826 (2018) 217-224.

[32] F.W. Richey, B.D. McCloskey, A.C. Luntz, Mg anode corrosion in aqueous electrolytes and implications for Mg-Air batteries, Journal of the Electrochemical Society, 163 (2016) A958.

[33] T. Khoo, A. Somers, A.A.J. Torriero, D.R. MacFarlane, P.C. Howlett, M. Forsyth, Discharge behaviour and interfacial properties of a magnesium battery incorporating trihexyl(tetradecyl)phosphonium based ionic liquid electrolytes, Electrochimica Acta, 87 (2013) 701-708.

[34] M.A. Deyab, Decyl glucoside as a corrosion inhibitor for magnesium–air battery, Journal of Power Sources, 325 (2016) 98-103.

[35] F. Tong, S. Wei, X. Chen, W. Gao, Magnesium alloys as anodes for neutral aqueous magnesium-air batteries, Journal of Magnesium and Alloys, (2021).

[36] X. Chen, X. Liu, Q. Le, M. Zhang, M. Liu, A. Atrens, A comprehensive review of the development of magnesium anodes for primary batteries, Journal of Materials Chemistry A, 9 (2021) 12367-12399.

[37] M. Deng, L. Wang, D. Höche, S.V. Lamaka, D. Snihirova, B. Vaghefinazari, M.L. Zheludkevich, Clarifying the decisive factors for utilization efficiency of Mg anodes for primary aqueous batteries, Journal of Power Sources, 441 (2019) 227201.

[38] A. Mitha, A.Z. Yazdi, M. Ahmed, P. Chen, Surface Adsorption of Polyethylene Glycol to Suppress Dendrite Formation on Zinc Anodes in Rechargeable Aqueous Batteries, ChemElectroChem, 5 (2018) 2409-2418.

[39] K.E. Sun, T.K. Hoang, T.N. Doan, Y. Yu, X. Zhu, Y. Tian, P. Chen, Suppression of Dendrite Formation and Corrosion on Zinc Anode of Secondary Aqueous Batteries, ACS Appl Mater Interfaces, 9 (2017) 9681-9687.

[40] H. Jiang, S. Yu, W. Li, Y. Yang, L. Yang, Z. Zhang, Inhibition effect and mechanism of inorganic-organic hybrid additives on three-dimension porous aluminum foam in alkaline Al-air battery, Journal of Power Sources, 448 (2020) 227460.

[41] Q.X. Kang, T.Y. Zhang, X. Wang, Y. Wang, X.Y. Zhang, Effect of cerium acetate and L-glutamic acid as hybrid electrolyte additives on the performance of Al–air battery, Journal of Power Sources, 443 (2019) 227251.

[42] M.A. Deyab, Effect of nonionic surfactant as an electrolyte additive on the performance of aluminum-air battery, Journal of Power Sources, 412 (2019) 520-526.

[43] S.J. Banik, R. Akolkar, Suppressing Dendritic Growth during Alkaline Zinc Electrodeposition using Polyethylenimine Additive, Electrochimica Acta, 179 (2015) 475-481.

[44] D. Cao, L. Wu, G. Wang, Y. Lv, Electrochemical oxidation behavior of Mg–Li–Al–Ce–Zn and Mg–Li–Al–Ce–Zn–Mn in sodium chloride solution, Journal of Power Sources, 183 (2008) 799-804.

[45] P. Zhang, Q. Li, L.Q. Li, X.X. Zhang, Z.W. Wang, A study of environment-friendly synergistic inhibitors for AZ91D magnesium alloy, Materials and Corrosion, 66 (2015) 31-34.

[46] M.C. Lin, C.Y. Tsai, J.Y. Uan, Electrochemical behaviour and corrosion performance of Mg–Li–Al–Zn anodes with high Al composition, Corrosion Science, 51 (2009) 2463-2472.

[47] L. Fan, H. Lu, The effect of grain size on aluminum anodes for Al–air batteries in alkaline electrolytes, Journal of Power Sources, 284 (2015) 409-415.

[48] M.P. Gomes, I. Costa, N. Pébère, J.L. Rossi, B. Tribollet, V. Vivier, On the corrosion mechanism of Mg investigated by electrochemical impedance spectroscopy, Electrochimica Acta, 306 (2019) 61-70.

[49] M. Deng, L. Wang, D. Höche, S.V. Lamaka, C. Wang, D. Snihirova, Y. Jin, Y. Zhang, M.L. Zheludkevich, Approaching “stainless magnesium” by Ca micro-alloying, Materials Horizons, (2020).

[50] M. Curioni, F. Scenini, T. Monetta, F. Bellucci, Correlation between electrochemical impedance measurements and corrosion rate of magnesium investigated by real-time hydrogen measurement and optical imaging, Electrochimica Acta, 166 (2015) 372-384.

[51] M. Esmaily, J.E. Svensson, S. Fajardo, N. Birbilis, G.S. Frankel, S. Virtanen, R. Arrabal, S. Thomas, L.G. Johansson, Fundamentals and advances in magnesium alloy corrosion, Progress in Materials Science, 89 (2017) 92-193.

[52] I.-J. Park, S.-R. Choi, J.-G. Kim, Aluminum anode for aluminum-air battery – Part II: Influence of In addition on the electrochemical characteristics of Al-Zn alloy in alkaline solution, J. Power Sources 357 (2017) 47-55.

[53] M. Pourgharibshahi, P. Lambert, The role of indium in the activation of aluminum alloy galvanic anodes, Mater. Corros. , 67 (2016) 857-866.

[54] J. Li, K. Wan, Q. Jiang, H. Sun, Y. Li, B. Hou, L. Zhu, M. Liu, Corrosion and Discharge Behaviors of Mg-Al-Zn and Mg-Al-Zn-In Alloys as Anode Materials, Metals, 6 (2016) 65.

[55] N. Wang, R. Wang, C. Peng, B. Peng, Y. Feng, C. Hu, Discharge behaviour of Mg-Al-Pb and Mg-Al-Pb-In alloys as anodes for Mg-air battery, Electrochimica Acta, 149 (2014) 193-205.

[56] David Linden, T.B. Reddy, Handbook of Batteries, McGraw-Hill, New York, 2002.

[57] C Daniel, J. Besenhard, Handbook of Battery Materials, Wiley-VCH, Weinheim, 2012.

[58] M. Yuasa, X. Huang, K. Suzuki, M. Mabuchi, Y. Chino, Discharge properties of Mg–Al–Mn–Ca and Mg–Al–Mn alloys as anode materials for primary magnesium–air batteries, Journal of Power Sources, 297 (2015) 449-456.

[59] M. Deng, R.-c. Wang, Y. Feng, N.-g. Wang, L.-q. Wang, Corrosion and discharge performance of Mg–9%Al–2.5%Pb alloy as anode for seawater activated battery, Transactions of Nonferrous Metals Society of China, 26 (2016) 2144-2151.

[60] T. Zheng, Y. Hu, Y. Zhang, S. Yang, F. Pan, Composition optimization and electrochemical properties of Mg-Al-Sn-Mn alloy anode for Mg-air batteries, Materials & Design, 137 (2018) 245-255.

[61] N. Wang, R. Wang, C. Peng, Y. Feng, B. Chen, Effect of hot rolling and subsequent annealing on electrochemical discharge behavior of AP65 magnesium alloy as anode for seawater activated battery, Corrosion Science, 64 (2012) 17-27.

[62] G. Huang, Y. Zhao, Y. Wang, H. Zhang, F. Pan, Performance of Mg–air battery based on AZ31 alloy sheet with twins, Materials Letters, 113 (2013) 46-49.

[63] B. Xiao, G.-L. Song, D. Zheng, F. Cao, A corrosion resistant die-cast Mg-9Al-1Zn anode with superior discharge performance for Mg-air battery, Materials & Design, 194 (2020) 108931.

[64] J. Ma, G. Wang, Y. Li, W. Li, F. Ren, Influence of Sodium Silicate/Sodium Alginate Additives on Discharge Performance of Mg–Air Battery Based on AZ61 Alloy, Journal of Materials Engineering and Performance, 27 (2018) 2247-2254.

[65] J. Ma, C. Qin, Y. Li, F. Ren, Y. Liu, G. Wang, Properties of reduced graphene oxide for Mg-air battery, Journal of Power Sources, 430 (2019) 244-251.

[66] G. Baril, G. Galicia, C. Deslouis, N. Pébère, B. Tribollet, V. Vivier, An impedance investigation of the mechanism of pure magnesium corrosion in sodium sulfate solutions, Journal of The Electrochemical Society, 154 (2007) C108-C113.

[67] G.-L. Song, K.A. Unocic, The anodic surface film and hydrogen evolution on Mg, Corrosion Science, 98 (2015) 758-765.

[68] S. Yin, W. Duan, W. Liu, L. Wu, J. Yu, Z. Zhao, M. Liu, P. Wang, J. Cui, Z. Zhang, Influence of specific second phases on corrosion behaviors of Mg-Zn-Gd-Zr alloys, Corrosion Science, 166 (2020) 108419.

[69] Y. Shi, C. Peng, Y. Feng, R. Wang, N. Wang, Enhancement of discharge properties of an extruded Mg-Al-Pb anode for seawater-activated battery by lanthanum addition, Journal of Alloys and Compounds, 721 (2017) 392-404.

[70] A.E. Martell, R.M. Smith, Critical stability constants: second supplement, Springer, 1989.

[71] A.E. Martell, R.M. Smith, Critical stability constants: other organic ligands, Springer, 1974.

[72] M. Deng, L. Wang, B. Vaghefinazari, W. Xu, C. Feiler, S.V. Lamaka, D. Höche, M.L. Zheludkevich, D. Snihirova, High-energy and durable aqueous magnesium batteries: recent advances and perspectives, Energy Storage Materials, (2021).

[73] S. Fajardo, C.F. Glover, G. Williams, G.S. Frankel, The Source of Anodic Hydrogen Evolution on Ultra High Purity Magnesium, Electrochimica Acta, 212 (2016) 510-521.

[74] J. Huang, G.-L. Song, A. Atrens, M. Dargusch, What activates the Mg surface—A comparison of Mg dissolution mechanisms, Journal of Materials Science & Technology, 57 (2020) 204-220.

[75] T. Würger, C. Feiler, G.B. Vonbun-Feldbauer, M.L. Zheludkevich, R.H. Meißner, A first-principles analysis of the charge transfer in magnesium corrosion, Scientific Reports, 10 (2020).

[76] D. Höche, C. Blawert, S.V. Lamaka, N. Scharnagl, C. Mendis, M.L. Zheludkevich, The effect of iron re-deposition on the corrosion of impurity-containing magnesium, Physical Chemistry Chemical Physics, 18 (2016) 1279-1291.

[77] S.H. Salleh, S. Thomas, J.A. Yuwono, K. Venkatesan, N. Birbilis, Enhanced hydrogen evolution on Mg (OH)2 covered Mg surfaces, Electrochimica Acta, 161 (2015) 144-152.

[78] P. Gore, S. Fajardo, N. Birbilis, G.S. Frankel, V.S. Raja, Anodic activation of Mg in the presence of In3+ ions in dilute sodium chloride solution, Electrochimica Acta, 293 (2019) 199-210.

[79] D. Wang, H. Li, J. Liu, D. Zhang, L. Gao, L. Tong, Evaluation of AA5052 alloy anode in alkaline electrolyte with organic rare-earth complex additives for aluminium-air batteries, Journal of Power Sources, 293 (2015) 484-491.

[80] C. Feiler, D. Mei, B. Vaghefinazari, T. Würger, R.H. Meißner, B.J.C. Luthringer-Feyerabend, D.A. Winkler, M.L. Zheludkevich, S.V. Lamaka, In silico screening of modulators of magnesium dissolution, Corrosion Science, (2019) 108245.

[81] T. Würger, D. Mei, B. Vaghefinazari, D.A. Winkler, S.V. Lamaka, M.L. Zheludkevich, R.H. Meißner, C. Feiler, Exploring structure-property relationships in magnesium dissolution modulators, npj Materials Degradation, 5 (2021).

[82] T. Würger, C. Feiler, F. Musil, G.B.V. Feldbauer, D. Höche, S.V. Lamaka, M.L. Zheludkevich, R.H. Meißner, Data Science Based Mg Corrosion Engineering, Frontiers in Materials, 6 (2019).

[83] C. Feiler, D. Mei, B.J.C. Luthringer-Feyerabend, S.V. Lamaka, M.L. Zheludkevich, Rational Design of Effective Mg Degradation Modulators, Corrosion, 77 (2020) 204-208.

Appendix

1. Glossary

2,6-DHB	2,6-dihydroxybenzoate
3,4-DHB	3,4-dihydroxybenzoate
5-sulfoSAL	5-sulfosalicylate
8-HQ	8-hydroxyquinoline
AABs	Al-air batteries
AAS	atomic absorption spectroscopy
AEEA	2-(2-aminoethylamino) ethanol
AHE	anomalous hydrogen evolution
AM50	Mg-4.85 wt.% Al-0.43 wt.% Mn
AMAB	aqueous Mg-air battery
AMABs	aqueous Mg-air batteries
APG	alkyl polyglucoside
AZ31	Mg-2.97 wt.% Al-0.73 wt.% Zn
BF	bright field
BMIMBF4	1-butyl-3-methyl imidazolium tetrafluoroborate
BSE	backscattered-electron
CE	chunk effect
CIT	citrate
CMC	carboxymethyl cellulose
CPE_{dl}	electric double layer capacitance
CPE_{ox}	oxide film capacitance
CP-Mg	commercial purity Mg
CTAB	cetyl trimethyl ammonium bromide
CV	cyclic voltammetry
DDAB	dihexadecyl dimethyl ammonium bromide
DDBAB	dodecyl dimethyl benzyl ammonium bromide
DE	dimethyl amine epoxy propane
DG	Decyl glucoside
EC	equivalent circuit

EDS	energy-dispersive X-ray spectroscopy
EDTA	ethylenediaminetetraacetic acid
EVs	electric vehicles
EIS	electrochemical impedance spectroscopy
F	Faraday constant
FABs	Fe-air batteries
FIB	focused ion beam system
GAFAC RA 600	polyoxyethylene alkyl phosphate ester acid
HAADF	high angle annular dark field
HER	hydrogen evolution reaction
HET	hydrogen evolution test
HF	high frequency
HP-Mg	high purity magnesium
HP-Mg-24	high purity magnesium with 24 ppm Fe
HP-Mg-51	high purity magnesium with 51 ppm Fe
I	applied current
IL	ionic liquid
IMZ	imidazole
LIBs	Li-ion batteries
LSM	laser scanning microscope
MABs	Mg-air batteries
MEA	monoethanolamine
MF	middle frequency
Mg-0.04Ca	Mg-0.04 wt.% Ca
Mg-0.15Ca	Mg-0.15 wt.% Ca
m_i	atomic weight
NDE	negative difference effect
n_i	ionic valence
NTA	nitrilotriacetic acid disodium salt
OCP	open circuit potential
OCV	open circuit voltage
OPS	oxide polishing suspension
ORR	oxygen reduction reaction

PANI	polyaniline
PDP	potentiodynamic polarization
PE	polyethylene
PEG	polyethylene glycol
PEG DiAcid 600	poly(ethylene glycol) bis (carboxymethyl) ether
PEI	polyethylenimine
$PP_{14}TFSI$	1-Ethyl-3-Methylimidazolium Bis(Trifluoromethylsulfonyl)Imide
PSS	poly (sodium 4-styrenesulfonate)
PTFE	polytetrafluorethylene
PZ	piperazine
QSPR	quantitative structure property relationship
R_{ct}	charge transfer resistance
R_e	electrolyte resistance
R_{film}	surface film resistance
RGO	reduced graphene oxide
R_{int}	internal resistance of aqueous Mg-air battery
rms	root mean square
R_{total}	total resistance
SA	sodium alginate
SAL	salicylate
SC	specific capacity
SDBS	sodium dodecyl benzene sulfonate
SD-OES	spark discharge optical emission spectrometry
SDS	sodium dodecyl sulfate
SE	secondary electron
SEM	scanning electron microscope
SHE	standard hydrogen electrode
SIET	scanning ion-selective electrode technique
STEM	scanning transmission electron
t	discharge time
TAAHs	Tetrea-alkyl ammonium hydroxides
TBAB	tetrabutylammonium bromide
TEM	transmission electron microscope

Trion	4,5-dihydroxy-1,3-benzenedisulfonic acid disodium salt monohydrate
Tribo-EIS	tribo-electrochemical impedance spectroscopy
Tribo-PDP	Tribo-potentiodynamic polarization
Tween 20	poly-sorbate 20
U	cell voltage
UAV	unmanned aerial vehicle
UE	utilization efficiency
UEs	utilization efficiencies
W_{theo}	theoretical weight loss of anode
WSG	water soluble graphene
x_i	mass fraction
XRD	X-ray diffraction analysis
ZABs	Zn-air batteries
ΔW	actual weight loss of anode
η_a	activation overvoltage of anode
η_c	activation overvoltage of cathode
$[P_{6,6,6,14}][Cl]$	trihexyl(tetradecyl)phosphoium chloride

2. Publications during candidature

Peer-reviewed papers

1) **L. Wang**, D. Snihirova, M. Deng, B. Vaghefinazari, S.V. Lamaka, D. Höche, M.L. Zheludkevich, Tailoring electrolyte additives for controlled Mg-Ca anode activity in aqueous Mg-air batteries, Journal of Power Sources, 460 (2020) 228106.

2) **L. Wang**, D. Snihirova, M. Deng, C. Wang, D. Höche, S.V. Lamaka, M.L. Zheludkevich, Indium chloride as an electrolyte additive for primary aqueous Mg batteries, Electrochimica Acta, 373 (2021) 137916.

3) **L. Wang**, D. Snihirova, M. Deng, C. Wang, B. Vaghefinazari, G. Wiese, M. Langridge, D. Höche, S.V. Lamaka, M.L. Zheludkevich, Insight into physical interpretation of high frequency time constant in electrochemical impedance spectra of Mg, Corrosion Science, 187 (2021) 109501.

4) **L. Wang**, D. Snihirova, M. Deng, B. Vaghefinazari, D. Höche, S.V. Lamaka, M.L. Zheludkevich, Enhancement of discharge performance for aqueous Mg-air batteries in 2,6-dihydroxybenzoate-containing electrolyte, Chemical Engineering Journal, 429 (2022) 132369.

5) **L. Wang**, D. Snihirova, M. Deng, B. Vaghefinazari, D. Höche, S.V. Lamaka, M.L. Zheludkevich, Revealing physical interpretation of time constants in electrochemical impedance spectra of Mg via Tribo-EIS measurements, Electrochimica Acta, 404 (2022) 139582.

6) M. Deng, **L. Wang**, B. Vaghefinazari, Wen Xu, Christian Feiler, S.V. Lamaka, D. Höche, M.L. Zheludkevich, D. Snihirova, High-energy and durable aqueous magnesium batteries: recent advances and perspectives, Energy Storage Materials, 43 (2021), 238-247. (As co-corresponding author)

7) M. Deng, **L. Wang**, D. Höche, S.V. Lamaka, P. Jiang, D. Snihirova, M.L. Zheludkevich, Corrosion and discharge properties of Ca/Ge micro-alloyed Mg anodes for primary aqueous Mg batteries, Corrosion Science, 177 (2020) 108958. (As co-corresponding author)

8) J. Yang, S. Di, C. Blawert, S.V. Lamaka, **L. Wang**, B. Fu, P. Jiang, L. Wang, M.L. Zheludkevich, Enhanced Wear Performance of Hybrid Epoxy-Ceramic Coatings on Magnesium Substrates, ACS Applied Materials & Interfaces, 10, 36 (2018) 30741-30751.

9) M. Deng, D. Höche, S.V. Lamaka, **L. Wang**, M.L. Zheludkevich, Revealing the impact of second phase morphology on discharge properties of binary Mg-Ca anodes for primary Mg-air batteries, Corrosion Science, 153 (2019) 225-235.

10) M. Deng, **L. Wang**, D. Höche, S.V. Lamaka, D. Snihirova, B. Vaghefinazari, M.L. Zheludkevich, Clarifying the decisive factors for utilization efficiency of Mg anodes for primary aqueous batteries, Journal of Power Sources, 441 (2019) 227201.

11) D. Snihirova, **L. Wang**, S.V. Lamaka, C. Wang, M. Deng, B. Vaghefinazari, D. Höche, M.L. Zheludkevich, Synergistic Mixture of Electrolyte Additives: A Route to a High-Efficiency Mg-Air Battery, The Journal of Physical Chemistry Letters, 11(20), 8790-8798.

12) M. Deng, **L. Wang**, D. Höche, S.V. Lamaka, P. Jiang, D. Snihirova, N. Scharnagl, M.L. Zheludkevich, Ca/In micro-alloying as a novel strategy to simultaneously enhance power and energy density of primary Mg-air batteries from anode aspect, Journal of Power Sources, 472 (2020) 228528.

13) C. Wang, D. Mei, G. Wiese, **L. Wang**, M. Deng, S.V. Lamaka, M.L. Zheludkevich, High rate oxygen reduction reaction during corrosion of ultra-high-purity magnesium, NPJ Materials Degradation 4, 42 (2020).

14) M. Deng, L**. Wang**, D. Höche, S.V. Lamaka, C. Wang, D. Snihirova, Y. Jin, Y. Zhang, M.L. Zheludkevich, Approaching “stainless magnesium” by Ca micro-alloying, Materials Horizons, 8(2), 589-596.

Book chapter

1) M. Deng, D. Höche, D. Snihirova, **L. Wang**, B. Vaghefinazari, S.V. Lamaka, M.L. Zheludkevich, Aqueous Mg batteries, in: M. Fichtner (Ed.) Magnesium Batteries: Research and Applications, Royal Society of Chemistry, United Kingdom, 2019, pp. 275-308.

3. Own contribution to publications and manuscripts included in this dissertation

1) **L. Wang**, D. Snihirova, M. Deng, B. Vaghefinazari, W. Xu, D. Höche, S.V. Lamaka, M.L. Zheludkevich, Electrolyte for Aqueous metal-air batteries. (Incorporated in **Chapter 2**)

L. Wang designed the outline and structure of this literature review in discussion with D. Snihirova and M. Deng. The writing and modification of this literature review was implemented by L. Wang according to the comments and corrections made by all authors.

2) **L. Wang**, D. Snihirova, M. Deng, C. Wang, B. Vaghefinazari, G. Wiese, M. Langridge, D. Höche, S.V. Lamaka, M.L. Zheludkevich, Insight into physical interpretation of high frequency time constant in electrochemical impedance spectra of Mg, Corrosion Science, 187 (2021) 109501. (Incorporated in **Section 5.1**)

L. Wang conceived and planed this work in discussion with D. Snihirova, S.V. Lamaka, D. Höche and M.L. Zheludkevich. Experiments included in this work were carried out by L. Wang (EIS measurements), C. Wang (Local pH & DO measurement), G. Wiese (SEM & FIB), M. Langridge (TEM). M.L. Zheludkevich and D. Snihirova gave guidance and advices on the data analysis and results interpretation. L. Wang conducted the paper writing and modification according to all comments and corrections made by all authors.

3) **L. Wang**, D. Snihirova, M. Deng, B. Vaghefinazari, D. Höche, S.V. Lamaka, M.L. Zheludkevich, Revealing physical interpretation of time constants in electrochemical impedance spectra of Mg via Tribo-EIS measurements, Electrochimica Acta, 404 (2022) 139582. (Incorporated in **Section 5.2**)

L. Wang conceived and planed this work in discussion with D. Snihirova and M.L. Zheludkevich. Experiments included in this work were carried out by L. Wang. D. Snihirova, M. Deng and B. Vaghefinazari gave valuable advices on the experimental design. D. Höche, S.V. Lamaka and M.L. Zheludkevich gave constructive suggestions on the data analysis and results interpretation. L. Wang conducted the paper writing and modification according to all comments and corrections made by all authors.

4) **L. Wang**, D. Snihirova, M. Deng, B. Vaghefinazari, S.V. Lamaka, D. Höche, M.L. Zheludkevich, Tailoring electrolyte additives for controlled Mg-Ca anode activity in aqueous Mg-air batteries, Journal of Power Sources, 460 (2020) 228106. (Incorporated in **Section 5.3**)

L. Wang conceived the conceptual design of this work. D. Snihirova, M. Deng and B. Vaghefinazari gave valuable advices on the experimental design. Experiments included in this work were carried out by L. Wang. D. Höche, S.V. Lamaka and M.L. Zheludkevich gave constructive suggestions on the data analysis and results interpretation. L. Wang conducted the paper writing and modification according to all comments and corrections made by all authors.

5) **L. Wang**, D. Snihirova, M. Deng, B. Vaghefinazari, D. Höche, S.V. Lamaka, M.L. Zheludkevich, Enhancement of discharge performance for aqueous Mg-air batteries in 2,6-dihydroxybenzoate-containing electrolyte, Chemical Engineering Journal, 429 (2022) 132369. (Incorporated in **Section 5.4**)

L. Wang conceived the conceptual design of this work. M. Deng, D. Snihirova and B. Vaghefinazari gave valuable advices on the experimental design. Experiments included in this work were carried out by L. Wang. D. Höche, S.V. Lamaka and M.L. Zheludkevich gave helpful suggestions on the data analysis and results interpretation. L. Wang conducted the paper writing and modification according to all comments and corrections made by all authors.

6) **L. Wang**, D. Snihirova, M. Deng, C. Wang, D. Höche, S.V. Lamaka, M.L. Zheludkevich, Indium chloride as an electrolyte additive for primary aqueous Mg batteries, Electrochimica Acta, 373 (2021) 137916. (Incorporated in **Section 5.5**)

L. Wang conceived and designed this work in discussion with M. Deng and D. Snihirova. L. Wang carried out most experiments included in this work. C. Wang and S.V. Lamaka gave constructive suggestions on the data analysis for localized measurements. All authors contributed to the data analysis and results interpretation. L. Wang conducted the paper writing and modification according to all comments and corrections made by all authors.

Acknowledgement

After four years of working and living in Geesthacht, it is my pleasure to be able to express my sincere gratitude in this special way to all those who have helped me during the last four years. The thesis would not be accomplished in such a successful manner without their kind support and encouragement.

First of all, I would like to show my sincere gratitude to my supervisor, Prof. Mikhail Zheludkevich, for giving me this great opportunity to conduct my PhD work in this vibrant and excellent research group. In ancient Chinese poetry, we describing teachers and supervisors as people who are willing to propagate doctrine, impart professional knowledge, and resolve doubts. My supervisor is always willing to share his knowledge to all group members as much as possible. I will never forget those days that he spent the whole afternoon answering my questions and sharing his constructive advices. His rigorous attitude to academic issues and his gentle attitude to people will have a profound impact on my future career.

Many thanks to my daily supervisor, Dr. Darya Snihirova, a talented young scientist. She is not only my daily supervisor, but in most cases, she is like a big sister, who always encouraged me and took care of me. Without her help, I would not have been able to adapt and integrate into our battery team in a short time. I would also like to thank Dr. Sviatlana Lamaka and Dr. Daniel Höche. At every regular battery meeting, they always share their insightful suggestions based on their valuable experience and expertise, which is significant for me to solve problems and make improvements. Special thanks are given to Mr. Bahram Vaghefinazari, who is always eager to help newcomers in the lab. I received a lot of help from him in my Lab life. Thank you to all the members of our battery team.

I would like to pass on my acknowledgement to Mr. Ulrich Burmester, Mr. Gert Wiese, Ms. Petra Fischer, Mr. Volker Heitman, Dr. Mark Langridge and Mr. Daniel Strerath regarding all the assistance on materials preparation, characterization and chemical analysis. My research work would not go well without their kind collaboration and support. Besides, I would like to thank all my previous and current officemates, Ms. Ting Wu, Mr. Cheng Wang, Ms. Wen Xu, Dr. Nuria Pulido-González, Dr. Gen Zhang, Dr. Xun Ma, Dr. Junjie Yang, Dr. Wanying Liu. I really enjoy the days that we spent together in Room 328. I would like to thank Dr. Christian Feiler, Dr. Silva Campos and all the colleagues in MO institute.

I would like to thank all my Chinese friends for sharing happiness and sorrows during my PhD. Special thanks to our poker game team (Dr. Pingli Jiang, Dr. Hong Yang, Dr. Yiming Jin, Dr.

Di Mei, Dr. Xun Zeng, etc.). I have countless great and joyful moments with them, allowing me to forget my worries. I do enjoy all the time playing, chatting and hanging out with them. I would like to express my appreciation to my lovely friend, Dr, Jing Zeng. The space distance and time difference have not affect our relationship. We have given each other endless support in the most difficult moments.

I sincerely appreciate the fellowship from China Scholarship Council (CSC) for the financial support for my PhD study in Germany.

Last but not at least, I would like to express my deepest gratitude to my family for their unconditional love, support and encouragement. I am very lucky to be my mom's daughter. She has always respected my thoughts and supported me in every possible way in every decision I have made. Many thanks to my father for treating me as his own daughter, even though we are not related by blood. Thank you so much for accompanying mom on these days when I could not be there. Many special thanks are given to Dr. Deng for always helps, comforts and cheers me up when I am feeling down. I have never felt alone in this country because of him. He is my best friend and partner in my working and living life. Thanks for every meal he prepared that makes him not only a good scientist but also a great cook. I hope we will be the most trustworthy and reliable partners on the road of our life.